



The University of
Nottingham

UNITED KINGDOM • CHINA • MALAYSIA

*Preparation and Characterisation of
Photoactive Supramolecular Soft Materials*

Shaun M. Smith

School of Chemistry

Thesis submitted to the University of Nottingham
for the Degree of Doctor of Philosophy

September 2023

Abstract

Soft material systems containing photosensitizers have been prepared and studied both for their use as photodynamic therapy agents and to investigate single molecule diffusion phenomena at the microscale. Gemini imidazolium amphiphiles were used to prepare supramolecular gels that possessed a liquid phase containing various ratios of water and ethanol. Photoactive compounds such as phthalocyanines and porphyrins were incorporated into the gels during preparation to yield a photoactive supramolecular material. Partly, this work outlines an investigation into the aggregation and fluorescence properties of these photoactive compounds both in solution and as part of the gel material as relates to their ability to generate singlet oxygen for antimicrobial photodynamic therapy, where significant enhancement of singlet oxygen generation of a water-soluble phthalocyanine was measured. Further, investigation into the molecular diffusion characteristics of these photoactive compounds confined to gel fibres was conducted using total internal reflection fluorescence microscopy and the results were statistically analysed. Changes in photon flux and the protonation state of a phthalocyanine altered its movement, as measured by mean instantaneous velocity calculations and mean square displacement analysis. This study provides important insights into the fundamental mechanism of molecular diffusion in gels and may have practical implications in the development of novel materials for optoelectronic and sensing applications. Glycopolymers containing a repeating unit of a modified galactose ring were also incorporated with the gel to form a gelator-glycopolymer hybrid hydrogel. A disruption of gel morphology brought about by increasing glycopolymer concentration was seen as analysed through electron and fluorescence microscopy. Confocal fluorescence microscopy of the imidazolium gels containing a range of fluorophores was attempted to correlate with total internal reflection fluorescence microscopy, along with a study of the dynamics of diketopyrrolopyrrole derivatives. Migratory behaviour of these diketopyrrolopyrrole compounds from outside to within the fibre was observed and studied. Finally, cryogenic scanning electron microscopy was employed to potentially correlate the gel morphology observed both in the dried state as seen with conventional scanning electron microscopy and in the hydrated state as seen with fluorescence microscopy. In cryogenically frozen imidazolium gels containing diketopyrrolopyrrole derivatives, thinner fibre widths were observed. In a concentration study, fibre width increased when moving from zero to 100 μM of zinc phthalocyanine tetrasulfonic acid within the cryogenically frozen gel but increasing the concentration to 500 μM had no further effect on fibre width. This is different from conventional SEM imaging of dried fibres,

where increasing zinc phthalocyanine tetrasulfonic acid concentration from 100 μM to 500 μM led to significant changes in gel morphology, making the fibres no longer visible. The studies of the imidazolium gels reported in this work could contribute to potential applications in photodynamic therapy and provide further important foundational information about photoactive soft materials.

Acknowledgements

I would like to express my deepest gratitude and appreciation to the individuals who have been instrumental in my academic journey and the completion of my PhD.

First and foremost, I would like to thank my former supervisor, Prof. David Amabilino, for his guidance and expertise. His constructive feedback and insights have been instrumental in shaping my work and helping me to produce a thesis of which I am proud. I would also like to thank Graham Newton for picking up my supervisorship and supporting me towards the end of my PhD. I would also like to express my gratitude to my co-supervisors, Lluïsa Pérez-García and Giuseppe Mantovani, whose multidisciplinary perspectives enriched this thesis, making it more comprehensive and well-rounded. I am also indebted to all of the lab mates I had the pleasure of knowing in both the Amabilino group, and the NAMI group, whose camaraderie and assistance have been a constant source of encouragement and motivation.

I also want to thank my mum and dad for their unwavering support and encouragement throughout this process, even if I could never successfully explain what my PhD was actually about. I would also like to thank Leicester City Football Club for reminding me that however bad things may get, they can always get worse.

Finally, I want to express my heartfelt gratitude to my girlfriend Bethan. Her love, support, and encouragement have been a constant source of strength throughout my journey. She has been there for me through the good and the bad, providing support and helping me to stay motivated even when the going got tough. I could not have done this without her by my side.

DECLARATION

The work described in this thesis was conducted at the School of Chemistry at the University of Nottingham between the dates of October 2019 and April 2023. I, Shaun Smith, declare that the work is my own and has not been submitted for a degree at another university.

List of Abbreviations

Φ_{SO}	Singlet Oxygen Quantum Yield
λ_{exc}	Wavelength of Excitation
λ_{filter}	Wavelength of Fluorescence Filter
λ_{irr}	Wavelength of Irradiation
1.2Cl	1,3-Bis[(3-octadecyl-1-imidazolium)methyl]benzene di-chloride
1.2Br	1,3-Bis[(3-octadecyl-1-imidazolium)methyl]benzene di-bromide
ABMA	9,10-Anthracenedyl-bis(methylene)dimalonic Acid
AFM	Atomic Force Microscopy
AIBN	Azobisisobutyronitrile
ALA	5-Amino Levulinic Acid
aPDT	Antimicrobial Photodynamic Therapy
ATRP	Atom-Transfer Radical Polymerisation
AuNP	Gold Nanoparticle
Azo	Azobenzene
BSE	Back-Scattered Electron
CG	Chain-Growth
CLSM	Confocal Laser Scanning Microscope
Cryo-SEM	Scanning Electron Cryomicroscopy
CSA	Camphorsulfonic Acid
CTA	Chain-Transfer Agent
CTAB	<i>N,N,N</i> -Trimethylhexadecan-1-aminium Bromide
CuPc	Copper Phthalocyanine
DAPI	4',6-Diamidino-2-phenylindole
DMSO	Dimethyl Sulfoxide
DOG	Difference of Gaussians
DPP	Diketopyrrolopyrrole
EDS	Energy-Dispersive x-ray Spectroscopy
Endo-O ₂ -ABMA	9,10-Anthracenedyl-bis(methylene)dimalonic Acid Endoperoxide
FEG	Field-Emission Gun

FIB	Focused Ion Beam
G+	Gram-positive
G-	Gram-negative
H ₂ Pc	Non-metalated Phthalocyanine
HOMO	Highest-Occupied Molecular Orbital
LDH	Layered Double Hydroxide
LAP	Linear Assignment Problem
LMW	Low Molecular Weight
LUMO	Lowest-Unoccupied Molecular Orbital
MIV	Mean Instantaneous Velocity
MSD	Mean Square Displacement
NIR	Near-IR
NMP	Nitroxide-Mediated Polymerisation
PDT	Photodynamic Therapy
PE	Primary Electron
P _{irr}	Power of Irradiation Source (Laser)
PPIX	Protoporphyrin IX
ppm	Parts Per Million
PS	Photosensitizer
PTSA	4-Toluenesulfonic Acid
PXRD	Powder X-Ray Diffraction
RAFT	Reversible Addition-Fragmentation Chain-Transfer
RDRP	Reversible-Deactivation Radical Polymerisation
RI	Refractive Index
ROI	Region Of Interest
ROS	Reactive Oxygen Species
SA	Staphylococcus Aureus
SE	Secondary Electron
SEC	Size-Exclusion Chromatography
SG	Step-Growth

SO	Singlet Oxygen
STORM	Single Molecule Localisation Microscopy
TCPP	Tetrakis(4-carboxyphenyl)porphyrin
TFA	Trifluoroacetic Acid
THF	Tetrahydrofuran
TLC	Thin-Layer Chromatography
TPPS	5,10,15,20-(Tetra-4-sulfonatophenyl)porphyrin
TIRF	Total Internal Reflection Fluorescence
ZnPc	Zinc(II) Phthalocyanine
ZnPcS8	Octasulfonate Zinc(II) Phthalocyanine
ZnPcSO ₂ Me	Tetrakis(methylsulfonyl)phthalocyaninato Zinc(II)
ZnPcTS	Zinc(II) Phthalocyanine Tetrasulfonic Acid

Table of Contents

Chapter 1	i
1.1 Soft materials	1
1.1.1. Gels	1
1.1.2. Photodynamic therapy.....	6
1.1.3. Porphyrinoid photosensitizers.....	12
1.2. Photoactive soft materials	16
1.3. Objectives	18
1.4. References.....	19
Chapter 2.....	24
2.1. Background.....	25
2.2. Gemini bis-imidazolium gelator (1.2Br/1.2Cl) synthesis	27
2.3. Zinc(II) phthalocyanine tetrasulfonic acid (ZnPcTS)	28
2.3.1. ZnPcTS solution characterisation	29
2.3.2. ZnPcTS@Gel preparation and characterisation.....	34
2.3.3. ZnPcTS singlet oxygen generation	41
2.3.4. Further additives and conditions study	46
2.4. Zinc(II) tetrakis(methylsulfonyl)phthalocyanine	52
2.4.1. ZnPcSO ₂ Me solution characterisation	53
2.4.2. ZnPcSO ₂ Me gel preparation and characterisation	55
2.4.3. ZnPcSO ₂ Me singlet oxygen generation	57
2.5. Conclusion	58
2.6. Experimental.....	59
2.6.1. General procedures	59
2.6.2. Synthetic procedures.....	61
2.7. References.....	63
Chapter 3.....	66
3.1. Background.....	67
3.2. Zinc(II) phthalocyanine tetrasulfonic acid (ZnPcTS)	69
3.2.1. High-loading morphology and dynamics.....	74
3.2.2. Low loading fluorophore dynamics	77
3.2.3. Light and acid-controlled speed/encapsulation modulation.....	81
3.3. 5,10,15,20-(Tetra-4-sulfonatophenyl)porphyrin (TPPS)	93
3.3.1. Fibre morphology and fluorophore dynamics.....	95
3.4. Mixed system (TCPP and ZnPcTS).....	98

3.5.	Zinc(II) phthalocyanine tetrasulfonatomethyl (ZnPcSO ₂ Me).....	102
3.6.	Conclusion	105
3.7.	Experimental.....	107
3.7.1.	General procedures	107
3.8.	References.....	110
Chapter 4.....		112
4.1.	Background.....	113
4.2.	Glycopolymer and chain-transfer agent synthesis	118
4.2.1.	CTA synthesis (sodium 3-{[(1-oxo-1-prop-2-yn-1-ylamino-propan-2-yl-thio)carbonothioyl]thio} propane-1-sulfonate).....	118
4.2.2.	Galactose monomer synthesis (β -D-galactopyranosyloxyethyl acrylamide).....	121
4.2.3.	Glycopolymer synthesis.....	122
4.3.	Characterisation of Glycopolymer@Gel system.....	126
4.3.1.	Macroscopic and SEM characterisation of Glycopolymer@Gel system.....	126
4.3.2.	ZnPcTS@PolymerGel.....	129
4.3.3.	ZnPcTS@PolymerGel TIRF study	131
4.4.	Conclusion	138
4.5.	Experimental.....	139
4.5.1.	General procedures	139
4.5.2.	Synthetic procedures	141
4.6.	References.....	147
Chapter 5.....		149
5.1.	Background.....	150
5.2.	Zinc(II) phthalocyanine tetrasulfonic acid (ZnPcTS) and 5,10,15,20-(Tetra-4-sulfonatophenyl)porphyrin.....	154
5.3.	DPP@Gels	157
5.3.1.	PyranDPP.....	158
5.3.2.	CO ₂ HDPP.....	161
5.3.3.	Pyridine/PyridiniumDPPs	164
5.4.	Conclusion	179
5.5.	Experimental.....	180
5.5.1.	General procedures	180
5.6.	References.....	181
Chapter 6.....		183
6.1.	Background.....	184
6.2.	Preliminary FIB experiments	188
6.3.	Fibre Analysis & Drying effects / Confocal comparison.....	191
6.4.	Phthalocyanine concentration investigation.....	202

6.5. Conclusion	206
6.6. Experimental.....	207
6.6.1. General procedures	207
6.7. References.....	208
Chapter 7.....	210
7.1. Summary	211
7.2. Limitations	213
7.3. Further work.....	214
Appendix.....	217

Chapter 1

Introduction

1.1 Soft materials

Soft materials comprise a group of substances that can exhibit distinctive mechanical, optical, electrical, or thermal properties. Various types of gels (hydrogels, organogels, low-molecular weight gels), biomaterials, foams, and elastomers can all be considered soft materials (Fig. 1.1).¹⁻⁴ The advantages of such materials arise from their intrinsic weakness and poor resistance to stress, which in turn renders them dynamic and adaptable to an array of applications. This is especially true for supramolecular materials in general, where weak intermolecular forces are the driving force behind assembly and can be relatively easily broken.

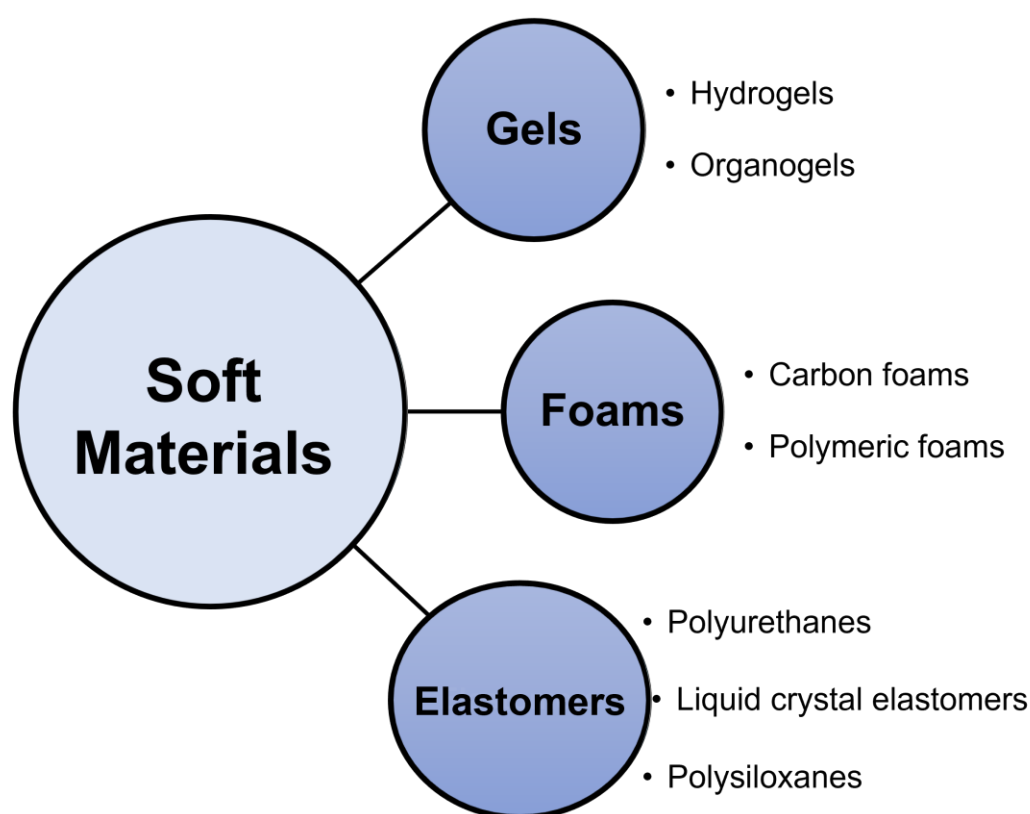


*Fig. 1.1. A non-exhaustive representation of some soft materials.*⁵

In this context, ‘soft’ tends to refer to the poor ability of materials to resist applied stress. The elastic modulus, which is a measure of the ease of deformation, of soft materials is significantly lower than that of their harder counterparts. For example, gels broadly tend to have elastic moduli of less than 10 MPa.⁶ This value is considerably lower than that of typical materials such as wood (~ 1100 MPa) and the polymers that constitute plastics (~ 2500 MPa).

1.1.1. Gels

Gels are an example of a soft material that can be defined as a minority solid phase dispersed within a majority fluid phase to form a colloidal suspension in which the fluid phase is confined to the material principally by surface tension.⁷ Gels are found abundant in consumer products,

particularly in healthcare, food, and cosmetics.⁸⁻¹⁰ **Figure 1.2** represents the microstructure of a typical gel, with the solid phase forming a three-dimensional network throughout the majority fluid phase. Rheologically, gels can also be defined as materials that exhibit no flow (i.e. act solid-like) up to their yield point, at which point they break apart.

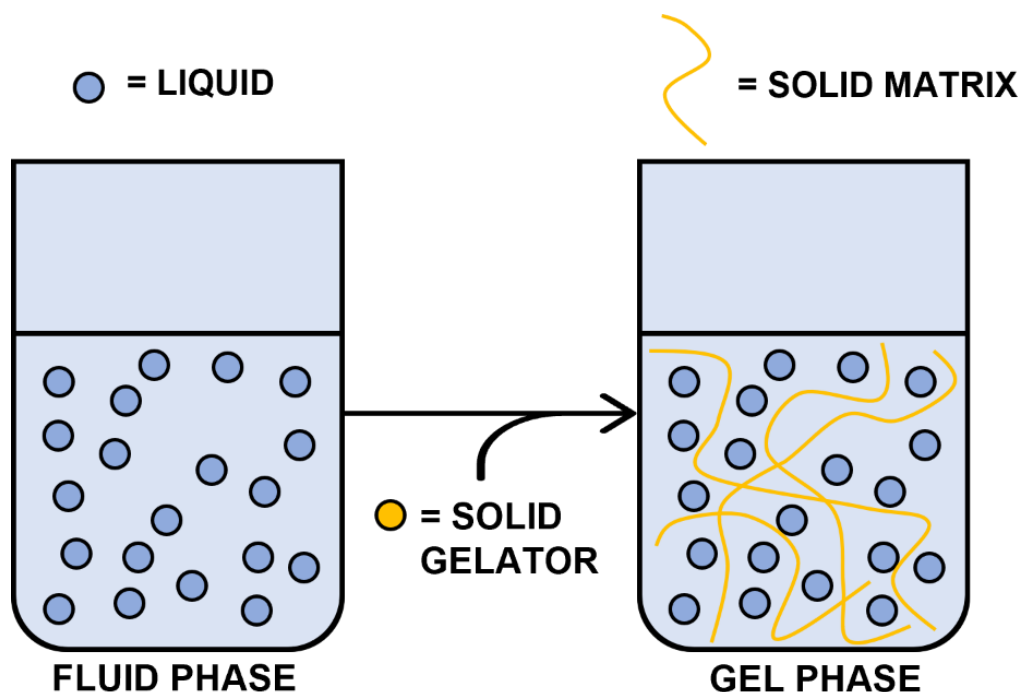


Fig. 1.2. Representation of the formation of a three-dimensional fibrous network that immobilises the solvent resulting in a gel. The solid gelator (yellow circles) undergoes self-assembly in the presence of the fluid phase (blue circles) forming the solid matrix (yellow lines).

Whilst all gels are a solid dispersed within a liquid, the constituent liquid tends to dictate how the given gel is classified. When the liquid phase is an organic solvent (e.g. THF, hexane, DMSO), the gel is classified as an organogel. Within the class of organogels, there are two further distinctions that can be made based on the form of the dispersed solid phase. Self-assembly of low molecular weight (LMW) gelators within organic solvent results in LMW organogels.¹¹ When the dispersed solid phase takes the form of a polymeric gelator, what results is a polymeric organogel where the three-dimensional solid matrix is bound together chemically (covalently crosslinked polymer) or physically (entangled polymeric chains), with the latter generally possessing greater thermoreversibility than the former.¹² An example of a LMW organogel is that of lecithin when mixed with an organic solvent followed by addition of a polar solvent.¹³ Lecithin is a glycerophospholipid found in animal and plant tissues which

can be processed and is widely used in food industries and biotechnology.^{14,15} The lecithin initially undergoes reverse micellation in the pure organic solvent, a process commonly seen with phospholipid-type amphiphiles.¹⁶ With the gradual addition of a polar solvent, the reverse micelles begin to form cylindrical micelles. These cylindrical micelles then grow and entangle, forming a three-dimensional fibrous network resulting in an organogel.

Hydrogels are a subclass of gels possessing a liquid phase of that is made up of water, though some gels containing a minority amount of ethanol in addition to water can be considered hydrogels. A common example of a product found in the world around us crafted using hydrogels is contact lenses. These lenses make use of hydrogels due to their elevated water content, enhancing breathability and comfort for the eyes. Additionally, their soft and flexible nature contributes to overall comfort during wear. Hydrogels have been long studied for their applications in medicinal and pharmaceutical areas.¹⁷⁻¹⁹ Clinically approved injectable hydrogels are largely macromolecular polymer-based and many naturally occurring polymers such as collagen are being developed for these ends.²⁰ Combining a polymeric approach with the use of LMW gelators has been used to prepare hybrid hydrogel materials with desirable properties.^{21,22} For applications like 3D printing, the reversibility of LMW gel systems provides an obstacle to their use. By combining an imidazolium LMW gelator with a range of photopolymerized acrylate polymers, the mechanical properties desired for effective 3D printing have been shown to be improved whilst also limiting the prevalence of issues relating to mechanical anisotropy in purely photopolymerized systems.²³

Alluded to in the section about lecithin organogels, the process of gel formation is often conducted by manipulating the solvent environment in which the solid gelator is situated. A commonly used technique involves changing the temperature of a solvent in which a given gelator is partially soluble. Increasing the temperature of a suspension results in gelator dissolution, and upon cooling, the dissolved gelator can self-assemble as its solubility decreases. This self-assembly then results in the three-dimensional solid matrix that characterises a gel.⁷ Such a technique has been used for the gel screening of sugar-based LMW gelators such as sorbitol, potentially opening up applications in personal care and energy technologies.²⁴ Generally, the intrinsic driving force for self-assembly is the minimisation of the free energy of the system until an equilibrium is reached. The reversible nature of this process renders it a thermodynamic process. Self-assembly therefore stands in contrast to typical crystallisation, as in the latter, the formation of stronger and irreversible bonds during nucleation and growth may favour the production of kinetic products - essentially, the

structures that form most rapidly. Another method for preparing gels is by using a solvent-antisolvent technique. Here, a gelator is dissolved in a solvent in which it is soluble and upon the addition of an antisolvent, the gelator precipitates out in a similar fashion to the cooling method as a fibrous matrix immobilising the liquid and forming a gel. This method of gel preparation is commonly used and possesses an advantage over temperature-based gel preparation as properties of the gel can be tuned by varying the amount of antisolvent compared with solvent.^{25,26}

Gemini imidazolium amphiphile LMW gelators are an example of molecules that self-assemble into hydrogels by use of the solvent-antisolvent technique and show promise in the area of drug delivery.²⁷ These imidazolium gels form upon the addition of water to an ethanolic solution of the LMW gelator, with the fibre thickness and distribution heavily influenced by the ratio of water to ethanol, which can be seen in **Fig. 1.3** where a specific gelator with an alkyl chain length of 18 (**1.2Br**) self-assembles with a fibre distribution considerably altered at a water-ethanol ratio of 7:3 compared with 5:5 as measured by atomic force microscopy (AFM).

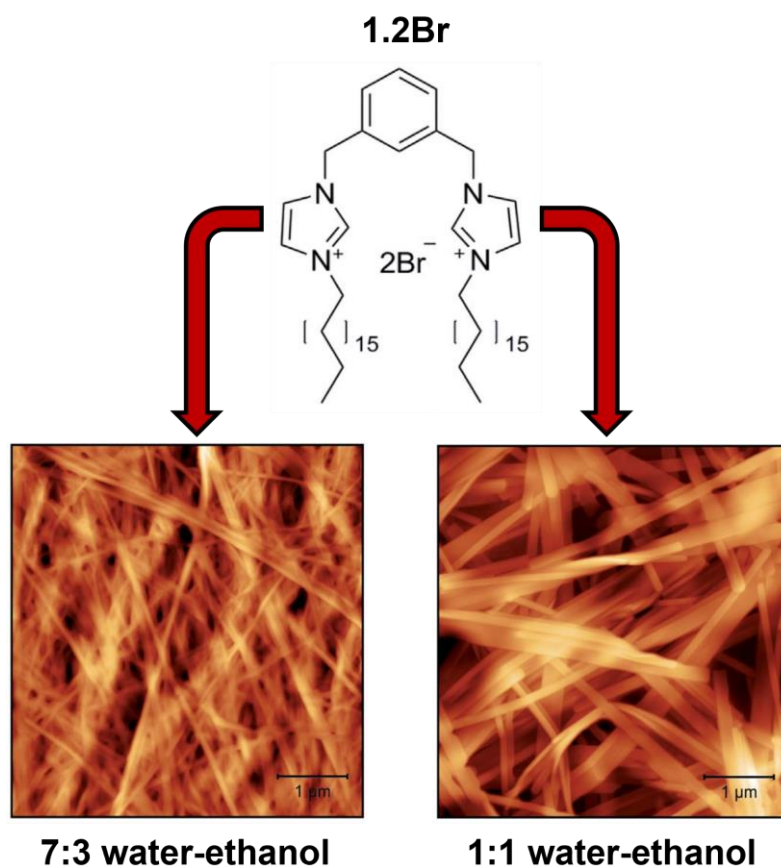


Figure 1.3. The fibre thickness and thickness distribution of gemini imidazolium LMW gelator **1.2Br** is considerably changed when final water-ethanol ratio is altered. Image adapted from Ref. 26 with permission from the Royal Society of Chemistry.

Whilst having been shown to be effective capping agents for gold nanoparticles (AuNP's), these imidazolium gelators have also been shown to provide a scaffold in which AuNP's can be prepared.²⁸⁻²⁹ AuNP size distributions were narrower when prepared inside the gel, displaying an example of how supramolecular materials can provide scaffolds for controlled reactions.

Another subclass of gels are multicomponent supramolecular gels. In the case of a multicomponent gel, more than one type of LMW gelator participates in the self-assembly process.³⁰⁻³² Each component may contribute different functional groups or properties to the resulting gel. In multicomponent gels, self-sorting or co-assembly can occur.³² If a two-component gel system is imaged, self-sorting refers to the process of one of the individual components interacting with components of the same type to form homo-aggregates. Co-assembly is the process by which components of distinct types interact with one another,

resulting in the formation of hetero-aggregates. Whether a specific multicomponent system undergoes self-sorting or co-assembly is dictated by the components themselves as well as external conditions such as solvent, pH, and temperature.³³ Diversity in components allows tuning of the properties of the gel, permitting further functionalisation opportunities in the materials formed. When utilising multiple LWM gelators, the resulting gel system is often sensitive to variations in the relative quantities of the components. In a study by Adams *et al.*, the interaction between a naphthalene-based dipeptide gelator and two naphthalene diimides (of which only one forms gels) was investigated.³⁴ It was found that the method of sample preparation affected visual colour, molecular packing, and aggregation in both solutions and the gel state, consequently influencing the microscale and bulk properties. Furthermore, variations were observed when compounds were mixed in a solution compared to when they were combined in a solid state. Another key factor in multicomponent gels is the selective choice of components based on enantioselectivity. Research conducted by Smith *et al.* demonstrated that in a two-component gel system consisting of an L-lysine carboxylic acid dendron and a chiral amine, the L-amino acid is preferably incorporated into the supramolecular structure as a consequence of its higher stability compared to the gel formed by the interaction between the same L-lysine carboxylic acid dendron and the D-amino acid.³⁵

1.1.2. Photodynamic therapy

Photodynamic therapy (PDT) refers to the process of irradiating a photosensitizer with light near its absorption maximum and subsequently forming reactive oxygen species (ROS) by energy transfer with molecular oxygen.³⁶⁻³⁹ Among the varieties of ROS, singlet oxygen (SO) is the most prevalent, although hydroxyl radicals ($\bullet\text{OH}$) and superoxide anions (O_2^-) can form depending on the photosensitizer and local conditions.^{40,41} When a photosensitizer generates ROS, two processes can occur, named Type I and Type II. Type I refers to the formation of hydroxyl radicals, whereas Type II describes the formation of SO. Localising ROS generation inside a tumour can subsequently have a therapeutic effect as a consequence of the apoptosis and necrosis of cancer cells.⁴² Analogously, localisation of ROS within bacteria can result in a bactericidal effect.⁴³ Under normal conditions, molecular oxygen is in its triplet state and is relatively unreactive compared with SO. **Figure 1.4** displays a simplified Jablonski diagram of the formation of SO through a type II process. Upon excitation of a photosensitizer from the ground state to an excited state (and after internal conversion), two main processes can occur: fluorescence emission from the excited photosensitizer to the ground state, or intersystem crossing (ISC). ISC results in the formation of a photosensitizer in an excited triplet

state, constituting a formally forbidden process due to its violation of the spin selection rule. However, the presence of heavy atoms introducing spin-orbit coupling can promote ISC. Additionally, when the vibrational levels of the excited species overlap, ISC becomes more favourable. An excited photosensitizer in its triplet state can then reach the ground state *via* phosphorescence or by interaction with molecular oxygen. It is this interaction and subsequent energy transfer that converts the triplet molecular oxygen to the reactive SO.

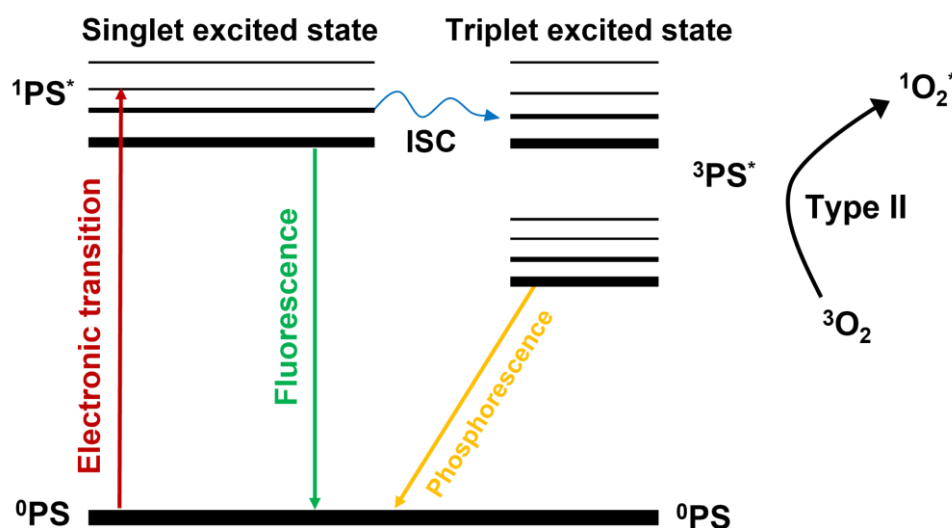


Figure 1.4. Jablonski diagram for the formation of SO. Light is absorbed by the photosensitizer (PS) which (after internal conversion) undergoes ISC to form the triplet excited state. This triplet excited state then undergoes an energy transfer with triplet oxygen to yield SO.

Molecular oxygen has two excited singlet states above the ground triplet state: the ¹Δ_g and the ¹Σ_g⁺ states. Primitive electron diagrams of these states are shown in **Fig. 1.5**. Both conversions from the ¹Δ_g and ¹Σ_g⁺ states to the triplet ground state are formally forbidden as a consequence of the spin selection rule ($\Delta S = 0$), though the higher energy ¹Σ_g⁺ state has a shorter lifetime than the ¹Δ_g state as a result of the occurrence of its non-radiative transition from the former to the latter. Gas phase radiative lifetimes of the ¹Δ_g state are 45 minutes whereas the ¹Σ_g⁺ lifetime ranges from 7-12 seconds.⁴⁴ In solution, the radiative lifetimes of both the ¹Δ_g and ¹Σ_g⁺ states are drastically shorter than in the gas phase, with ¹Δ_g and ¹Σ_g⁺ having a measured lifetime range from 10⁻⁶ – 10⁻³ seconds and 10⁻¹¹ – 10⁻⁹ seconds, respectively.⁴⁵

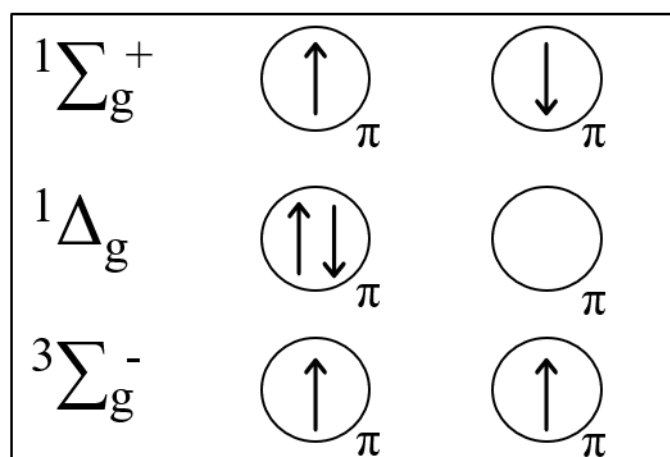


Figure 1.5. A simplified representation of the lowest singlet states and triplet state of molecular oxygen. Image adapted from Ref. 38 with permission from Elsevier.

Upon the formation of SO, both physical and chemical quenching can occur. Physical quenching occurs where an interaction, often spin-orbit coupling or triplet energy transfer, between SO and quenching substrate results in no new products other than the conversion of SO to the ground state. Common SO quenchers include β -carotene, azide, and 1,4-diazabicyclo-[2.2.2]-octane (DABCO).⁴⁶ Chemical quenching is a process whereby a new product is formed after the interaction between a substrate and is where SO finds its main uses.

The first clinically approved photosensitizers for PDT are known as ‘first generation’ photosensitizers. The most well-known first-generation photosensitizer was Photofrin, a haematoporphyrin mixture developed between the 1960’s and 1970’s shown in **Fig. 1.6.**⁴⁷

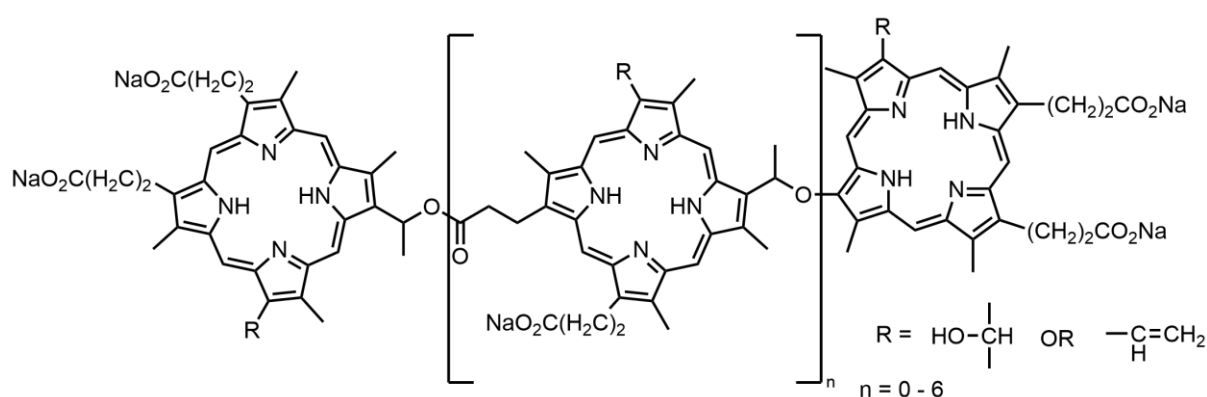


Figure 1.6. Structure of the haematoporphyrin oligomer known as Photofrin, the first clinically approved photosensitizer for PDT.

Second-generation photosensitizers were those made in the late 1980’s and are mainly porphyrinoid-based.⁴⁸ 5-Aminolevulinic acid (ALA), shown in **Fig. 1.7,** is an example of a

second-generation photosensitizer. Whilst intrinsically not a photosensitizer as an isolated molecule, ALA is a natural precursor to protoporphyrin IX (PPIX) which itself is a precursor to haemoglobin and chlorophyll. ALA is first converted to porphobilinogen *via* the enzyme ALA dehydratase. Porphobilinogen is mono-pyrrole compound which then cyclises to form the tetrapyrrole compound ‘uroporphyrinogen III’. Uroporphyrin III is then converted in two steps to PPIX. One significant advantage of ALA is its ability to penetrate tumour cell membranes, a feat not achievable by PPIX itself.⁴⁹ The key condition that renders ALA well-suited to cancer therapeutics is the lack of ferrochelatase in cancer cells. Ferrochelatase converts PPIX into haem B and thus its absence leads to an accumulation of PPIX inside the cancerous cells. Excitation of the absorption bands of PPIX at 505 nm and 630 nm results in efficient SO generation and therefore a positive therapeutic effect.⁵⁰

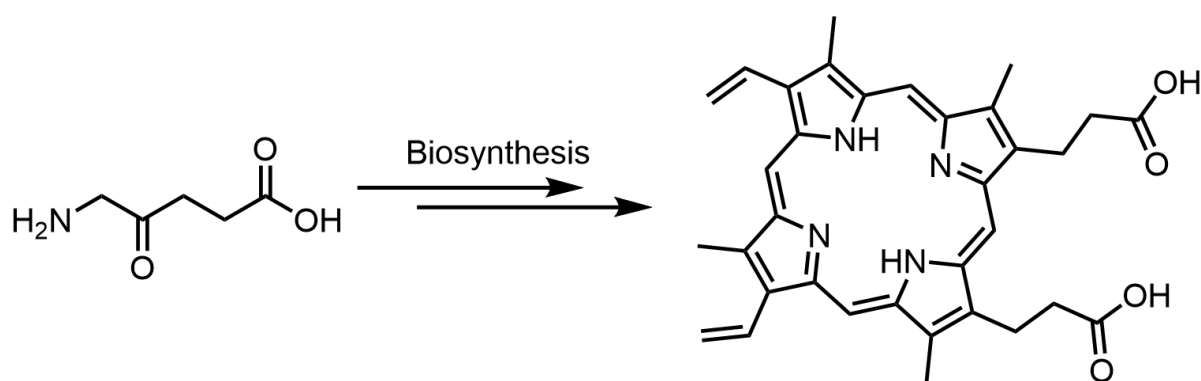


Figure 1.7. ALA (left) is metabolised into protoporphyrin IX (right), which then preferentially accumulates in tumours.

Third-generation photosensitizers often contain a supramolecular component in their system, and this can often be based around the use of nanoparticles, or the classes of gels described previously. Tuning the responsivity of supramolecular photosensitizers can impart beneficial properties in terms of delivery, targeting, and modulating ROS generation. Since the year 2000, the extent of research into supramolecular materials for PDT has increased markedly.⁵¹ ROS-switchable supramolecular photosensitizers are systems of great interest whereby the photodynamic activity of the photosensitizer can be modulated. This modulation between the photosensitizer’s “ON” (ROS generating) state and “OFF” (non-ROS generating) state can be prompted by external stimuli. This strategy is attractive as it can limit the phototoxicity of the photosensitizer to healthy cells and allows for a greater quantity of photosensitizer to be delivered. pH-responsive supramolecular photosensitizers are popular systems for achieving ROS-switchability, mainly owing to the relative acidity of cancerous cells (pH 6.5 – 7.4) in

comparison with healthy cells.⁵² This pH difference has already been exploited for cancer diagnosis and drug delivery.⁵³ Polysaccharide/drug conjugates consisting of hydrophilic (containing poly(ethylene glycol) groups) and hydrophobic (containing a chlorin-e6, a porphyrinoid derivative as the photosensitising moiety) sections mounted upon a glycol chitosan backbone were developed by Lee *et al.* and shown to possess weak acid responsiveness.⁵⁴ Within normal cells (pH = 7.4), irradiation of this conjugate results in no cell death, indicating that self-quenching of SO generation is occurring. Upon irradiating the conjugate within epithelial carcinoma (HeLa) cells (pH = 6.8 – 7.4), high phototoxicity is observed. This responsiveness was owed to conformational change of the conjugate under mildly acidic conditions. This polysaccharide/drug conjugate showed higher tumour selectivity than free chlorin-e6. A different type of acid-responsiveness was described by Yoon *et al.*, whereby incorporation of a functionalised zinc phthalocyanine (ZnPcS8) upon a layered double hydroxide (LDH) (**Fig. 1.8**) displayed a vast disparity in phototoxicity between pH 6 → pH 6.5 → pH 7.4.⁵⁵ When situated upon the LDH at neutral conditions, the SO generation of ZnPcS8 is quenched as a result of photoinduced electron transfer (PET) between itself and the LDH upon irradiation. The electrostatic interactions between ZnPcS8 and the LDH depart under acidic conditions, allowing the free zinc phthalocyanine to be released from the LDH and no longer be quenched by PET.

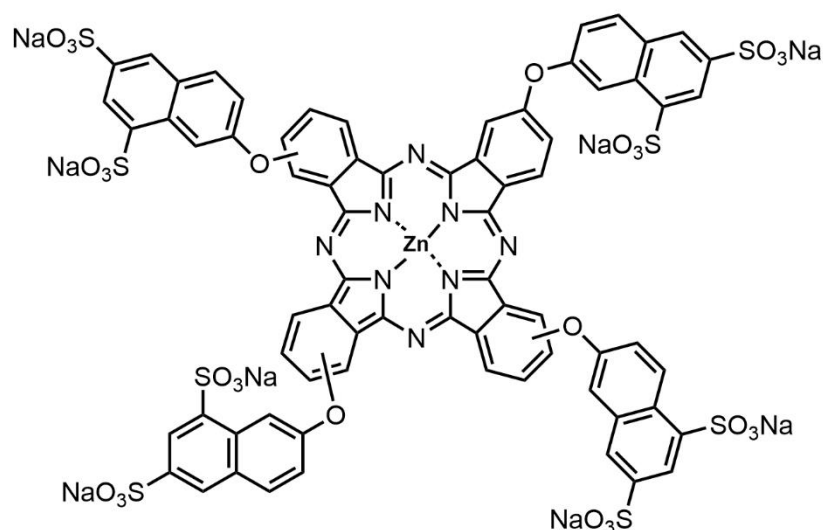


Figure 1.8. ZnPcS8 was situated upon an LDH, affording a system whereby much higher phototoxicity was displayed under acidic conditions owing to the release of free ZnPcS8.

Antimicrobial PDT (aPDT) is a promising area of research for neutralising certain pathogens that cause disease. This technique is based on the same principle as anticancer PDT, whereby a photosensitizer is localised in the vicinity of target and excited to cause death *via* the

generation of ROS. In particular, aPDT provides an alternative to habitual antibiotics at a time when antibiotic resistance is rising alarmingly.⁵⁶ As opposed to anticancer PDT, where development has been ongoing for several decades, development of photosensitizers suited for aPDT has not been as thorough or in-depth. This is partially due to the success that antibiotics have had over recent decades, somewhat negating the need for a novel modality for the treatment of bacterial infection. A significant advantage of aPDT over conventional antibiotics is that the efficacy of a photosensitizer is independent of the antibiotic resistance of the target bacteria. aPDT also has the potential to be much more versatile than conventional antibiotics, with a single photosensitizer conceivably being able to act on bacteria, fungi, yeasts, and parasites.⁵⁷

The efficacy of aPDT photosensitizers is in large part governed by the type of bacteria targeted. The difference in cell membrane structures of Gram-positive (G+) and Gram-negative (G-) bacteria (**Fig. 1.9**) lead to differing degrees of photosensitizer uptake. The cell walls of G+ bacteria tend to be permeable to most photosensitizers. G- bacteria, however, possess lipopolysaccharides on their outer membrane, which render the membrane strongly negatively charged. This negative charge yields a G- outer membrane that is impermeable to anionic and neutral compounds.⁵⁸ As a result, specific research into the development of cationic photosensitizers has been carried out, which can permeate both G+ and G- outer membranes.

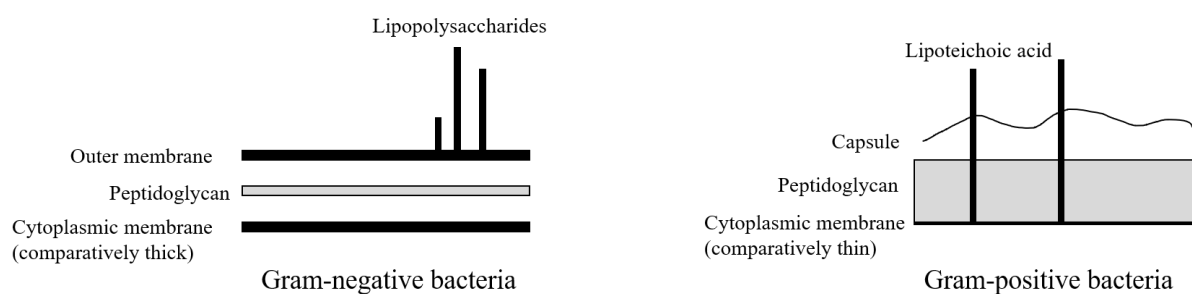


Figure 1.9. Cell wall diagrams of G+ and G- bacteria. The negative charge brought about by lipopolysaccharides renders the outer membrane of G- bacteria impermeable to anionic and neutral photosensitizers. The greater thickness of the G- cytoplasmic membrane also presents a barrier to aPDT.

The difference in efficacy of anionic versus cationic photosensitizers is exemplified in a study by Minnock *et al.*, where both anionic (tetrasulfonated) and cationic (pyridinium) functionalised zinc phthalocyanines were tested as to their photodynamic efficacy against G- bacteria.⁵⁹ The survival rates of *E. coli* show a large difference between the anionic and cationic

derivatives despite the chromophore being unchanged. This difference was clearly a result of differences in cellular uptake, demonstrating the importance of photosensitizer charge for G-aPDT efficacy.

A consequence of the poor permeability of G- outer membranes is that more studies have focused on the deactivation of G+ bacteria. *Staphylococcus aureus* (SA), a common G+ bacteria, is well documented to be able to develop multidrug resistance.⁶⁰ This resistance has spurred interest into the photodynamic deactivation of SA *via* aPDT. Methylene blue and toluidine blue are common and well-studied photosensitizers which were shown to completely eradicate the SA bacteria examined when irradiated with a 664 nm diode laser.⁶¹ Incubation of SA with ALA also demonstrated the complete inactivation of MRSA (a strain of SA) upon irradiation at 407-420 nm.⁶² Complete inactivation of other MRSA strains was also seen upon irradiation of a disulfonated aluminium phthalocyanine by 673 nm light.⁶³ Photosensitivity of the MRSA strains occurred immediately, indicating rapid uptake of an aluminium phthalocyanine within the MRSA cells. Aluminium phthalocyanines have been much studied for photodynamic therapy because of their favourable optical properties, biocompatibility, and functionalisation opportunities.⁶⁴

1.1.3. Porphyrinoid photosensitizers

Most photosensitizers share certain important characteristics such as strong absorption, appropriate triplet energy level, high SO quantum yield, long triplet state lifetime, and photostability. There are, however, other considerations which render some photosensitizers more attractive than others. An absorption maximum in the red to near-IR (NIR) region is widely sought after in photosensitizers for use in PDT applications. Shown in **Fig. 1.10** is a comparison of skin-penetration distances as a function of wavelength. When moving into the red to NIR region, tissue penetration increases until tailing off after 870 nm. Maximising tissue penetration is therefore achievable by tuning the photosensitizer to absorb at as far into the red to NIR regions as possible. Limitations to PDT efficacy are therefore brought about by low tissue penetration levels as a result of the inability of the irradiating light to reach areas in which the photosensitizers are situated.

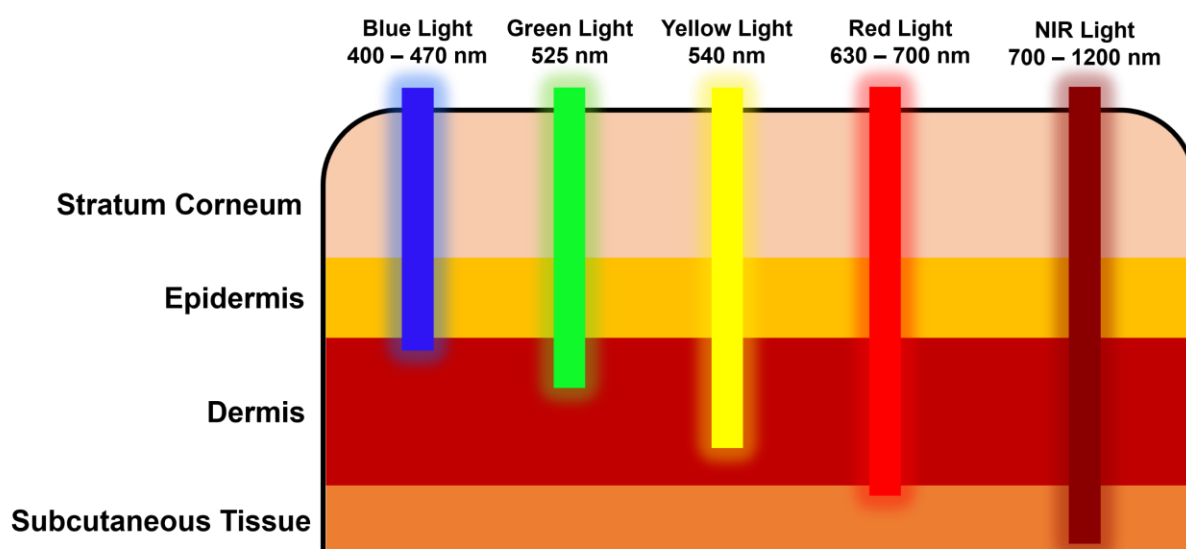


Figure 1.10. Approximate tissue penetration depth dependency on wavelength. Figure adapted from Ref. 65 with permission from Springer Nature.

Porphyrinoid compounds generally, and phthalocyanines more specifically, fulfil many requirements for an effective photosensitizer. As referred to, the first clinically available photosensitizer was the haematoporphyrin derivative Photofrin. Many second-generation photosensitizers are of the porphyrinoid-type, with porphyrins and phthalocyanines being the most studied.⁴⁸

Phthalocyanines are macrocyclic compounds that are a synthetic analogue of the naturally occurring porphyrin. As seen in **Fig. 1.11**, phthalocyanines and porphyrins share the same base structure of four pyrrolic units linked *via* carbon atoms (in the case of porphyrin) or nitrogen atoms (phthalocyanine). The other difference is the pyrrole units of porphyrin are replaced by isoindole units in phthalocyanine. Whilst the basic structure of phthalocyanines is similar to that of porphyrins, different functionalisation can be achieved with the former. Functionalising the substituents on the exterior of the isoindole unit can confer certain desirable characteristics (e.g. solubility, absorption, and electrochemical behaviour) and allow for a degree of control over the supramolecular structures adopted by the molecules.⁶⁶ The two positions on the isoindole accessible for functionalisation are often labelled the peripheral and non-peripheral positions.

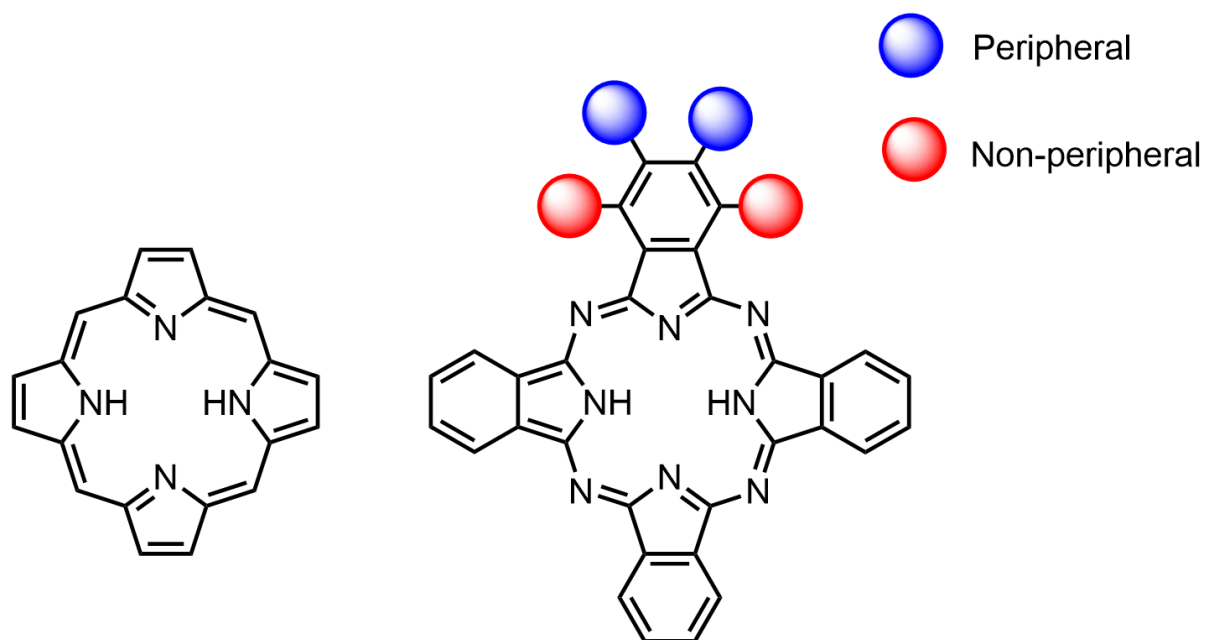


Figure 1.11. Second generation photosensitizers such as porphyrin (left) and phthalocyanine (right), with the functionalisable peripheral and non-peripheral positions labelled on the phthalocyanine.

Phthalocyanines were an accidental discovery by the German chemists Braun and Tcherniac in 1907 after forming an unknown, coloured compound during an attempted synthesis of *o*-cyanobenzamide.⁶⁷ However, it took a further twenty years before the properties of phthalocyanines were investigated. In 1927, chemists Henri de Diesbach and Edmond von der Weid made the fortuitous discovery of a ‘complex product containing copper and pyridine’.⁶⁸ They describe the remarkable physical and chemical stability of what was copper phthalocyanine (CuPc). It was this stability along with striking colour that made them ideal materials for dyes and colourants. The CuPc discovered by de Diesbach and von der Weid is still currently used in pigments and paints.

The stability of phthalocyanines, and porphyrinoid compounds in general, arises from several contributing factors. Being an aromatic species, phthalocyanines exhibit resistance to reactions that could disrupt the conjugated system. Metallated phthalocyanines are stable as a consequence of the macrocyclic effect. The macrocyclic effect is related to the chelate effect, with the latter referring to the entropy-driven binding of a metal species in solution by a multidentate ligand (in this case a phthalocyanine) and the former arising from the pre-organisation of the cyclic ring and low associated entropic cost of metal binding.

Many functionalisation do opportunities exist for phthalocyanines, despite their stability. Firstly, the two hydrogen atoms present at the centre of metal-free phthalocyanines can be

replaced by an array of metal centres. Whilst the most commonly used metals are Cu and Zn, phthalocyanines have been made using over seventy different metal ions.⁶⁹ The metal-centred phthalocyanine investigated depends strongly on the properties sought after for certain applications. Derivatives of Zn and Al phthalocyanines are commonly used in SO generation and PDT studies. Cu and Zn are often the metal centres of choice when investigating their use in organic photovoltaic devices whereas more exotic centres such as ruthenium and titanium are often seen in the study of the three-dimensional nanostructures formed by phthalocyanines.^{70,71} These larger transition metal elements are often too large to sit within the plane of the phthalocyanine macrocycle, so protrude outside the plane.⁶⁹ This non-planarity has consequences for the packing of the compounds in the solid state.⁶⁹ Secondly and as displayed in **Fig. 1.11**, the positions on the exterior of the isoindole units can be functionalised to tune the property of the resultant material, which is done by functionalising the phthalonitrile precursor before cyclisation. As a result of the generally poor solubility of phthalocyanines, groups containing long alkyl chains are commonly introduced in these positions in order to solubilise the compound in organic solvents.⁷² The solubilising effect of alkyl substituents is vital for making films *via* spin-coating or drop casting as the material must be solution-processable. Water-solubility can also be conferred by introducing ionic or hydrophilic units into the structure.^{73,74} In some systems, a further functionalisation opportunity is available for exploitation. For certain metal centres, axial co-ordination is available and thus axial ligands can be introduced allowing for further tuning of the properties of the phthalocyanine. The axial ligand functionalisation of silicon phthalocyanine, for example, has been the subject of much research.^{75,76} The solubility, electronic absorption, and aggregation behaviour has been modified *via* the addition of axial ligands such as sulfonates, esters, and ethers.⁷⁷ Phthalocyanines are thus incredibly attractive as photoactive materials as a result of the plethora of functionalisation opportunities, allowing for the tuning of a wide range of properties to suit the application in question.

The photophysical properties of phthalocyanines are the essential characteristic to their applications in PDT, organic photovoltaics, and catalysis. Phthalocyanines generally contain two distinct absorption bands, the Soret band (or B-band) ($\pi \rightarrow \pi^*$) and Q-band ($n \rightarrow \pi^*$). The Soret band is generally found between 300 – 400 nm and the Q-band between 600 – 700 nm. It is this latter Q-band which is crucial for PDT applications, as its location in the red-to-NIR region renders it well-matched to light sources that have relatively deep skin penetration. The

position and shape of the Q-band are extremely dependent on the solvent environment, any additives, or molecular functionalisation.⁷⁸⁻⁸⁰

1.2. Photoactive soft materials

In general, soft materials provide a foundation to build photoactive systems that are useful in many applications. Given the already discussed susceptibility of many soft materials to thermal changes, incorporation of photothermal molecules into such structures (or building an intrinsically photothermally active material) provides an opportunity to produce thermoresponsive materials. Photothermal agents emit heat after light absorption, and examples of which can be seen with both organic and inorganic materials and compounds.^{81,82} The obvious application for such materials is in photothermal therapy, a treatment whereby light excitation by the photothermal system results in heat emission and the subsequent delivery of a therapeutic effect.⁸³⁻⁸⁵ An interesting example of such a system is the class of porphysomes, shown in **Fig. 1.12**. Porphysomes are spherical nanovesicles which are produced by the self-assembly of porphyrin lipids.⁸⁶ Upon excitation in their micellar form, relaxation predominately occurs through non-radiative pathways, resulting in the emission of heat. The porphysomes functioned as effective photothermal agents in *in vivo* environments, eclipsing the effect of Photofrin and the porphysome PDT in laser and dose-matched studies.

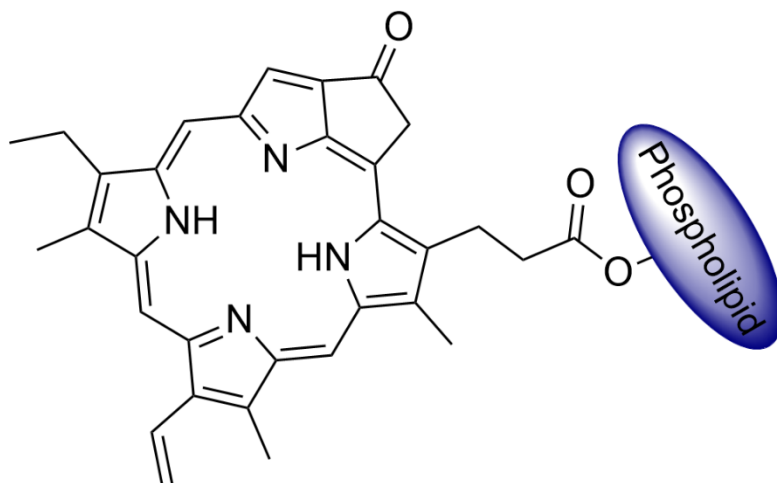


Figure 1.12. This phospholipid-functionalised porphyrin self-assembles to form micelles in the presence of cholesterol.

Photothermal gel systems have also been studied. Polymeric hydrogels developed by Zheng *et al.* partially contained platinum nanoparticles as photothermal agents and displayed significant mechanical and rheological stiffening under irradiation with NIR light.⁸⁷ In addition, the presence of a UV-responsive photoisomerisable azobenzene derivative also

encapsulated within the gel resulted in mechanical and rheological softening under UV irradiation. This example is an elegant demonstration of a dual-responsive photoactive gel.

The use of a light-triggered heat response can also be used to result in encapsulation or release of a molecular load. This effect is clearly applicable in the field of controlled release, where a molecular load is intended to be delivered in specific locations and under certain conditions.⁸⁸ In such systems, supramolecular structures are commonly prepared containing a one or more photoresponsive groups. A common example of such a group is a photocleavable side group present on a polymer.^{89,90} Polymeric nanoparticles developed by Fomina *et al.* were prepared from a polymer containing a self-immolative quinone-methide groups.⁹¹ Upon irradiation with UV and NIR light, the previously encapsulated photosensitizer Nile Red was released through degradation of the polymeric nanoparticle carriers.

Gels have been formed through the cross-linking of diblock copolymers containing two photoresponsive groups.⁹² The gels were initially formed by cross-linking in the presence of > 310 nm UV irradiation whilst cooling through dimerisation of one of the photoresponsive groups present, coumarin. When irradiated by < 260 nm UV light, reverse photocleavage of the other photoresponsive group (cyclobutane) reduced the cross-linking density of the gel and thus led to significant swelling of the gel. Adams *et al.* conducted research on hydrogels that demonstrate a photothermal effect, allowing the gels to generate heat when exposed to specific light wavelengths. This phenomenon was primarily attributed to the formation of the perylene bisimide radical anion. Their work serves as a noteworthy example of a self-assembled photoactive supramolecular system.⁹³

Photoactivity is not just limited to applications on the macroscale, as microscale changes in brought about by photoresponsivity have shown to significantly alter low-dimensional processes. Azobenzene derivatives are well-known for their ability to photoisomerise under UVA-Visible irradiation and/or thermal stimulus. This photoswitching has been exploited to manipulate porphyrin aggregation and alter rheological properties of gels.^{94,95} Imidazolium gels described previously based on the amphiphile **1.2Br** (**Fig. 1.3**) have been shown to provide a fibre scaffold through which tetracarboxylated porphyrin (**TCPP**) molecular travellers have exhibited motion, as measured by fluorescence microscopy.⁹⁶ However, this movement shown in **Fig. 1.13** required the presence of an azobenzene molecular switch to induce **TCPP** motion upon heat emission caused by photoisomerisation. This movement manifests itself as a fibre 'going dark' as the fluorescent porphyrin moves out from the fibre in view.

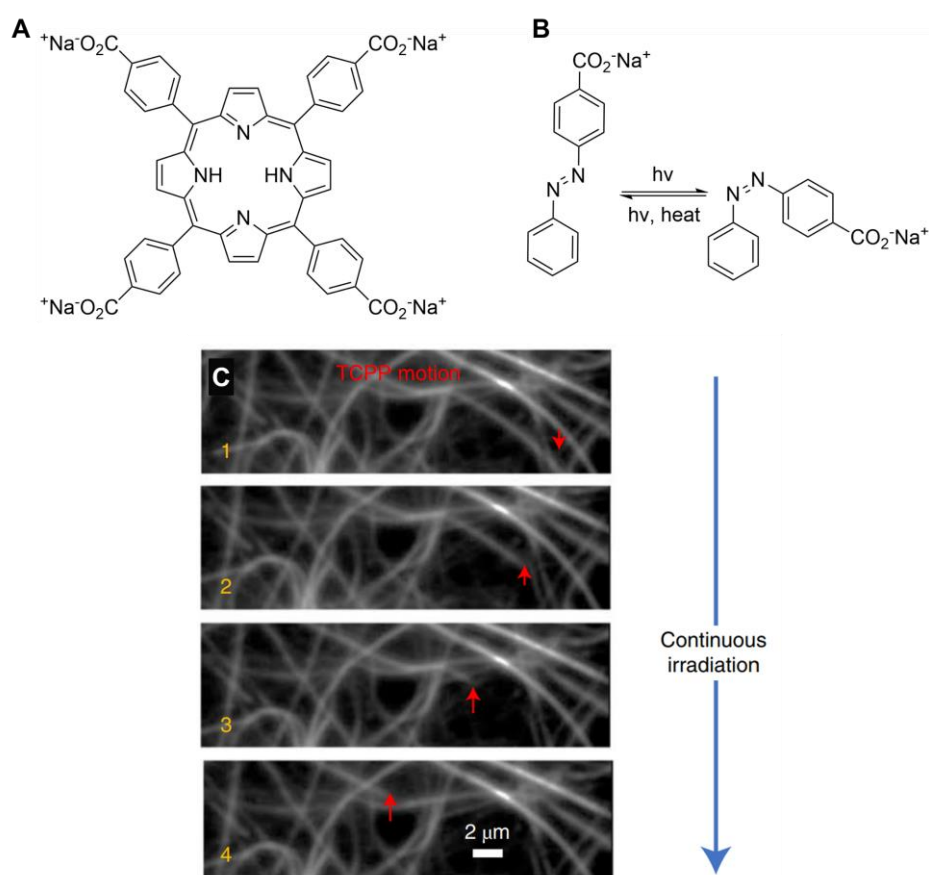


Figure 1.13. *TCPP* travellers moving through a gel scaffold via heat generated by photoisomerisation of an azobenzene derivative. (A) *TCPP* traveller used in the study. (B) Water-soluble azobenzene derivative that caused molecular motion. (C) Visual representation of porphyrin movement seen as fluorescence intensity loss. Image adapted from Ref. 96 with permission from Springer Nature.

This imidazolium gel containing **TCPP** also provides another example of a photoactive soft material for PDT applications. Incorporation of the **TCPP** within gel fibres as seen in the study relating to molecular motion (without azobenzene) led to a significant enhancement of SO generation when compared with that of **TCPP** in solution.⁹⁷ This enhancement is attributed to geometries adopted by **TCPP** under its immobilisation within the gel fibres.

1.3. Objectives

Third-generation photosensitizer systems can exploit the significant advantages of intrinsic photosensitizer compounds whilst diminishing to the greatest extent their downsides. It is therefore an aim of this work to prepare novel third-generation photosensitizer systems based predominately on imidazolium based gelators containing photosensitizer compounds, with an emphasis on phthalocyanines. Upon their preparation, the ability of these photosensitizer

systems to generate SO within the supramolecular structure of the gels will be compared with that of the isolated photosensitizers in solution. The microscale structure of these systems will also be explored, with characterisation and quantification of any molecular motion as seen in analogous systems.⁹⁶ In addition to the individual gel systems, glycopolymer-gel hybrid materials will be prepared and characterized as to their unique microstructure and properties. Glycopolymers were chosen for their ability to introduce carbohydrate moieties into the gel system, offering the potential for enhanced targeting and biocompatibility in applications such as drug delivery and PDT.

This research aims to demonstrate the use of photoactive soft materials, displaying their wide range of potential applications and providing new avenues for future exploration in diverse fields.

1.4. References

1. D. B. Amabilino, D. K. Smith, J. W. Steed, *Chem. Soc. Rev.*, 2017, 46, 2404 – 2420.
2. R. Parenteau-Bareil, R. Gauvin, F. Bethod, *Materials*, 2010, 3, 1863 – 1887.
3. N. Brun, S. Ungureanu, H. Deleuze, R. Backov, *Chem. Soc. Rev.*, 2011, 40, 771 – 788.
4. A. Fletcher, M. C. Gupta, K. L. Dudley, E. Vedeler, *Compos. Sci. Technol.*, 2010, 70, 953 – 958.
5. J. Li, W. Wong, X. Tao, *Nanoscale*, 2020, 12, 1281 – 1306.
6. P. Calvert, *Adv. Mater.*, 2009, 21, 743 – 756.
7. P. Terech, R. G. Weiss, *Chem. Rev.*, 1997, 97, 3133 – 3160.
8. B. Liu, H. Yang, C. Zhu, J. Xiao, H. Cao, J. Simal-Gandara, Y. Li, D. Fan, J. Deng, *Crit. Rev. Food Sci. Nutr.*, 2022, 12, 1 – 23.
9. M. C. Koetting, J. T. Peters, S. D. Steichen, N. A. Peppas, *Mater. Sci. Eng. R Rep.*, 2015, 93, 1 – 49.
10. A. Wynne, M. Whitefield, A. Dixon, S. Anderson, *J. Dermatol. Treat.*, 2009, 13, 61 – 66.
11. A. Vintiloiu, J. Leroux, *J. Control. Release*, 2008, 125, 179 – 192.
12. L. Z. Rogavina, V. G. Vasil'ev, E. E. Braudo, *Polym. Sci. Ser. C*, 2008, 50, 85 – 92.
13. Y. A. Shchipunov, *Russ. Chem. Rev.*, 1997, 66, 301.
14. D. Guzey, D. J. McClements, *Adv. Colloid Interface Sci.*, 2006, 128 – 130, 227 – 248.
15. F. Donsì, M. Annunziata, M. Vincensi, G. Ferrari, *J. Biotechnol.*, 2011, 159, 342 – 350.
16. J. Kim, M. Kim, J. Lee, *Food Sci.*, 2018, 261, 194 – 200.

17. A. K. Yetisen, I. Naydenova, F. D. Vasconcellos, J. Blyth, C. R. Lowe, *Chem. Rev.*, 2014, 114, 10654 – 10696.
18. J. H. Lee, *Biomater. Res.*, 2018, 22, 27.
19. A. Mellati, S. Dai, J. Bi, B. Jin, H. Zhang, *RSC Adv.*, 2014, 4, 63951 – 63961.
20. A. Mandal, J. R. Clegg, A. C. Anselmo, S. Mitragotri, *Bioeng. Transl. Med.*, 2020, 5, e10158.
21. D. J. Cornwell, D. K. Smith, *Mater. Horiz.*, 2015, 2, 279 – 293.
22. D. J. Cornwell, B. O. Okesola, D. K. Smith, *Soft Matter*, 2013, 9, 8730 – 8736.
23. Z. Zhou, M. Samperi, L. Santu, G. Dizon, S. Aboarkaba, D. Limón, C. Tuck, L. Pérez-García, D. J. Irvine, D. B. Amabilino, R. Wildman, *Mater. Des.*, 2021, 206, 109792.
24. G. C. Dizon, G. Atkinson, S. P. Argent, L. T. Santu, D. B. Amabilino, *Soft Matter*, 2020, 16, 4640 – 4654.
25. J. Raeburn, C. Mendoza-Cuenca, B. N. Cattoz, M. A. Little, A. E. Terry, A. Z. Cardoso, P. C. Griffiths, D. J. Adams, *Soft Matter*, 2015, 11, 927 – 935.
26. M. Samperi, L. Pérez-García, D. B. Amabilino, *Chem. Sci.*, 2019, 10, 10256 – 10266.
27. M. Rodrigues, A. C. Calpena, D. B. Amabilino, M. L. Garduño-Ramírez, L. Pérez-García, *J. Mater. Chem. B*, 2014, 2, 5419 – 5429.
28. L. Casal-Dujat, M. Rodrigues, A. Yagüe, A. C. Calpena, D. B. Amabilino, J. González-Linares, M. Borràs, L. Pérez-García, *Langmuir*, 2012, 28, 2368 – 2381.
29. M. Rodrigues, A. Genç, J. Arbiol, D. B. Amabilino, L. Pérez-García, *J. Colloid Interface Sci.*, 2015, 446, 53 – 58.
30. L. E. Buerkle, S. J. Rowan, *Chem. Soc. Rev.*, 2012, 41, 6089 – 6102.
31. A. R. Hirst, D. K. Smith, *Chem. Eur. J.*, 2005, 11, 5496 – 5508.
32. E. R. Draper, D. J. Adams, *Chem. Soc. Rev.*, 2018, 47, 3395 – 3405.
33. S. Panja, B. Dietrich, A. J. Smith, A. Seddon, D. J. Adams, *ChemSystemsChem*, 2022, 4, e202200008.
34. R. I. Randle, R. E. Ginesi, O. Matsarskaia, R. Schweins, E. R. Draper, *Macromol. Rapid Commun.*, 2022, 44, 2200709.
35. W. Edwards, D. K. Smith, *J. Am. Chem. Soc.*, 2014, 136, 1116 – 1124.
36. I. J. Macdonald, T. J. Dougherty, *J. Porp. Phthalocyanines*, 2001, 5, 105 – 129.
37. A. P. Castano, P. Mroz, M. R. Hamblin, *Nat. Rev. Cancer*, 2006, 6, 535 – 545.
38. M. C. DeRosa, R. J. Crutchley, *Coord. Chem. Rev.*, 2002, 233 – 234, 351 – 371.
39. B. W. Henderson, T. J. Dougherty, *Photochem. Photobiol.*, 1992, 55, 145 – 157.
40. M. Hayyan, M. A. Hashim, I. M. Alnashef, *Chem. Rev.*, 2016, 116, 3029 – 3085.

41. B. Halliwell, A. Adhikary, M. Dingfelder, M. Dizdaroglu, *Chem. Soc. Rev.*, 2021, 50, 8355 – 8360.
42. B. Perillo, M. Di Donato, A. Pezone, E. Di Zazzo, P. Giovannelli, G. Galasso, G. Castoria, A. Migliaccio, *Exp. Mol. Med.*, 2020, 52, 192 – 203.
43. F. Vatanserver, W. C. M. A. de Melo, P. Avci, D. Vecchio, M. Sadasivam, A. Gupta, R. Chandran, M. Karimi, N. A. Parizotto, R. Yin, G. P. Tegos, M. R. Hamblin, *FEMS Microbiol. Rev.*, 2013, 37, 955 – 989.
44. S. J. Arnold, M. Kubo, E. A. Ogryzlo, *Advances in Chemistry*, ACS Publications, Vol 77, 1968.
45. P. B. Merkel, D. R. Kearns, *J. Am. Chem. Soc.*, 1972, 94, 1029 – 1030.
46. F. Wilkinson, W. P. Helman, A. B. Ross, *J. Phys. Chem. Ref. Data*, 1995, 24, 663 – 677.
47. T. J. Dougherty, *J. Clin. Laser Med. Surg.*, 1996, 14, 219 – 221.
48. J. Kou, D. Dou, L. Yang, *Oncotarget*, 2017, 8, 81591 – 81603.
49. E. Erdtman, D. J. V. A. dos Santos, L. Löfgren, L. A. Eriksson, *Chem. Phys. Lett.*, 2008, 463, 178 – 182.
50. T. Nishimura, K. Hara, N. Honda, S. Okazaki, H. Hazama, K. Awazu, *Lasers Med. Sci.*, 2020, 35, 1289 – 1297.
51. X. Li, S. Lee, J. Yoon, *Chem. Soc. Rev.*, 2018, 47, 1174 – 1118.
52. R. A. Gatenby, R. J. Gillies, *Nat. Rev. Cancer*, 2004, 4, 891 – 899.
53. J. Liu, Y. Huang, A. Kumar, A. Tan, S. Jin, A. Mozhi, X. Liang, *Biotechnol. Adv.*, 2014, 32, 693 – 710.
54. S. Y. Park, H. K. Baik, Y. T. Oh, K. T. Oh, Y. S. Youn, E. S. Lee, *Angew. Chem., Int. Ed. Engl.*, 2011, 50, 1644 – 1647.
55. X. Li, B. Zheng, M. Ke, Y. Zhang, J. Huang, J. Yoon, *Theranostics*, 2017, 7, 2746 – 2756.
56. C. L. Ventola, *Pharmacol. Ther.*, 2015, 40, 277 – 283.
57. G. Jori, C. Fabris, M. Soncin, S. Ferro, O. Coppellotti, D. Dei, L. Fantetti, G. Chiti, G. Ronucci, *Lasers Surg. Med.*, 2006, 38, 468 – 481.
58. T. Dai, Y. Huang, M. R. Hamblin, *Photodiagnosis Photodyn. Ther.*, 2009, 6, 170 – 188.
59. A. Minnock, D. I. Vernon, J. Schofield, J. Griffiths, J. H. Parish, S. T. Brown, *J. Photochem. Photobiol. B*, 1996, 32, 159 – 164.
60. K. Hiramatsu, Y. Katayama, M. Matsuo, T. Sasaki, Y. Morimoto, A. Sekiguchi, T. Baba, *J. Infect. Chemother.*, 2014, 20, 593 – 601.

61. M. N. Usacheva, M.C. Teichert, M. A. Biel, *Lasers Surg. Med.*, 2001, 29, 165 – 173.
62. Y. Nitzan, M. Salmon-Divon, E. Shporen, Z. Malik, *Photochem. Photobiol. Sci.*, 2004, 3, 430 – 435.
63. M. A. Griffiths, B. W. Wren, M. Wilson, *J. Antimicrob. Chemother.*, 1997, 40, 873 – 876.
64. N. Sekkat, H. van den Bergh, T. Nyokong, N. Lange, *Molecules*, 2011, 17, 98 – 144.
65. E. Sorbellini, M. Rucco, F. Rinaldi, *Lasers Med. Sci.*, 2018, 33, 1431 – 1439.
66. N. A. Kuznetsova, N. S. Gretsova, O. A. Yuzhakova, V. M. Negrimovskii, O. L. Kaliya, E. A. Luk'yanets, *Russ. J. Gen. Chem.*, 2001, 71, 36 – 41.
67. A. Braun, J. Tcherniac, *Ber. Dtsch. Chem. Ges.*, 1907, 40, 2709 – 2714.
68. H. de Diesbach, E. von der Weid, *Helv. Chim. Acta*, 1927, 10, 886 – 888.
69. C. C. Leznoff, A. B. P. Lever, *Phthalocyanines: properties and applications*, Weinheim, Cambridge, Vol 1, 1989.
70. A. M. Paoletti, G. Pennesi, G. Rossi, A. Generosi, B. Paci, V. Rossi Albertini, *Sensors*, 2009, 9, 5277 – 97.
71. A. Generosi, B. Paci, V. Rossi Albertini, P. Perfetti, G. Pennesi, G. Rossi, R. Caminiti, *Appl. Phys. Lett.*, 2005, 87, 181904.
72. M. J. Cook, *Chem. Rec.*, 2002, 2, 225 – 236.
73. H. Li, T. J. Jensen, F. R. Fronczek, M. G. H. Vicente, *J. Med. Chem.*, 2008, 51, 502 – 511.
74. J. T. Ferreira, J. Pina, C. A. F. Ribeiro, R. Fernandes, J. P. C. Tomé, M. S. Rodríguez-Morgade, T. Torres, *J. Mater. Chem. B*, 2017, 5, 5862 – 5869.
75. X. Chen, D. Ma, K. Cai, S. Pan, Y. Wang, T. Zhang, Z. Huang, H. Yang, Y. Peng, *J. Coord. Chem.*, 2014, 68, 732 – 740.
76. K. Mitra, M. C. T. Hartman, *Org. Biomol. Chem.*, 2021, 19, 1168 – 1190.
77. S. A. Mikhailenko, L. I. Solov'eva, E. A. Luk'yanets, *Russ. J. Gen. Chem.*, 2004, 74, 451 – 459.
78. T. Furuyama, K. Satoh, T. Kushiya, N. Kobayashi, *J. Am. Chem. Soc.*, 2014, 136, 765 – 776.
79. K. Nakai, J. Usami, N. Kobayashi, *J. Porp. Phthalocyanines*, 2007, 11, 222 – 227.
80. K. Liu, Y. Wang, J. Yao, Y. Luo, *Chem. Phys. Lett.*, 2007, 438, 36 – 40.
81. Z. Qin, J. C. Bischof, *Chem. Soc. Rev.*, 2012, 41, 1191 – 1217.
82. G. Baffou, R. Quidant, *Laser Photonics Rev.*, 2012, 7, 171 – 187.

83. S. Nomura, Y. Morimoto, H. Tsujimoto, M. Arake, M. Harada, D. Saitoh, I. Hara, E. Ozeki, A. Satoh, E. Takayama, K. Hase, Y. Kishi, H. Ueno, *Sci. Rep.*, 2020, 10, 9765.
84. X. Song, Q. Chen, Z. Liu, *Nano Res.*, 2015, 8, 340 – 354.
85. J. Wang, J. Qiu, *Cancer Res. Front.*, 2016, 2, 67 – 84.
86. J. F. Lovell, C. S. Jin, E. Huynh, T. D. MacDonald, W. Cao, G. Zheng, *Angew. Chem. Int. Ed. Engl.*, 2012, 51, 2429 – 2433.
87. Z. Zheng, J. Hu, H. Wang, J. Huang, Y. Yu, Q. Zhang, Y. Cheng, *ACS Appl. Mater. Interfaces*, 2017, 9, 24511 – 24517.
88. M. Bruneau, S. Bennici, J. Brendle, P. Dutournie, L. Limousy, S. Pluchon, *J. Control. Release.*, 2019, 294, 355 – 371.
89. E. Cabane, V. Malinova, S. Menon, C. G. Palivan, W. Meier, *Soft Matter*, 2011, 7, 9167 – 9176.
90. J. Xuan, D. Han, H. Xia, Y. Zhao, *Langmuir*, 2014, 30, 410 – 417.
91. N. Fomina, C. McFearin, M. Sermsakdi, O. Edigin, A. Almutairi, *J. Am. Chem. Soc.*, 2010, 132, 9540 – 9542.
92. J. He, X. Tong, Y. Zhao, *Macromolecules*, 2009, 42, 4845 – 4852.
93. L. Thomson, R. E. Ginesi, D. D. Osborne, E. R. Draper, D. J. Adams, *Chem. Eur. J.*, 2023, 29, e202300663.
94. F. L. Callari, S. Sortino, *Chem. Commun.*, 2008, 6179 – 6181.
95. I. Lee, O. Dobre, D. Richards, C. Ballestrem, J. M. Curran, J. A. Hunt, S. M. Richardson, J. Swift, L. Wong, *ACS Appl. Mater. Interfaces*, 2018, 10, 7765 – 7776.
96. M. Samperi, B. Bdiri, C. D. Sleet, R. Markus, A. R. Mallia, L. Pérez-García, D. B. Amabilino, *Nat. Chem.*, 13, 1200 – 1206.
97. M. Samperi, D. Limón, D. B. Amabilino, L. Pérez-García, *Cell Rep. Phys. Sci.*, 2020, 1, 100030.

Chapter 2

Photophysical Investigation of Photosensitizer Incorporated Gels

2.1. Background

Phthalocyanines can be rendered water-soluble by functionalising the exterior of the macrocycle with hydrophilic, including ionic, moieties.¹ Water-solubility is often desired in photosensitizers generally, especially in areas of medicinal and clinical interest. Despite their solubility, water-soluble phthalocyanines are often susceptible to aggregation in aqueous environments.^{2,3} This aggregation increases the likelihood of non-radiative relaxation pathways during excitation, resulting in a lowered fluorescence and a poorer ability to generate singlet oxygen (SO) under irradiation. The degree of phthalocyanine aggregation in solution can be estimated by the relative intensity of peaks present in the Q-band. The non-aggregated phthalocyanine Q-band peak generally falls at 670 – 690 nm, whilst dimer and higher-order aggregate peaks possess a hypsochromic shift to 620 – 650 nm.⁴ The Q-band maximum of an aggregated phthalocyanine is at a higher energy (shorter wavelength) as a consequence of the formation of H-aggregates (cofacial stacking), where the highest-occupied molecular orbital (HOMO) and lowest-unoccupied molecular orbital (LUMO) are coupled by intermolecular charge transfer, resulting in a higher energy transition.

SO generation can be measured using a variety of techniques. Advanced studies use *in vitro* and *in vivo* methods to examine the efficacy of a given photosensitizer.^{5,6} Before these studies can be carried out, it is prudent to conduct measurements of SO generation in non-biological conditions. A common method used to measure SO generation rate is to measure the phosphorescence signal of the SO as it relaxes to the ground state after being generated by a photosensitizer.⁷ This wavelength of this phosphoresced light from SO lies at ~ 1270 nm, and thus falls out of the range of many commercial spectrophotometers. Another possibility is to use a molecular probe as a scavenger for the SO generated by a photosensitizer under irradiation.^{8,9} The compound 9,10-anthracenedyl-bis(methylene)dimalonic acid (**ABMA**) is an example of a fluorescent water-soluble molecular probe used in studies of SO generation.^{10,11} In aqueous solution, **ABMA** (shown in **Fig. 2.1**) has an absorption maximum at ~ 380 nm. Under irradiation with 380 nm light, three **ABMA** fluorescent emission peaks are present at ~ 400 nm, ~ 430 nm, and ~ 460 nm. **ABMA** reacts with SO to form an endoperoxide compound (**endo-O₂-ABMA**), as shown in **Fig. 2.1**. **Endo-O₂-ABMA** is not fluorescent when irradiated at 380 nm light, meaning the fluorescence decay of **ABMA** can be used as a direct proxy for SO generation. It is by tracking the intensity decrease of the central peak at ~ 430 nm, which is usually the most intense, that the generation rate of SO can be measured.

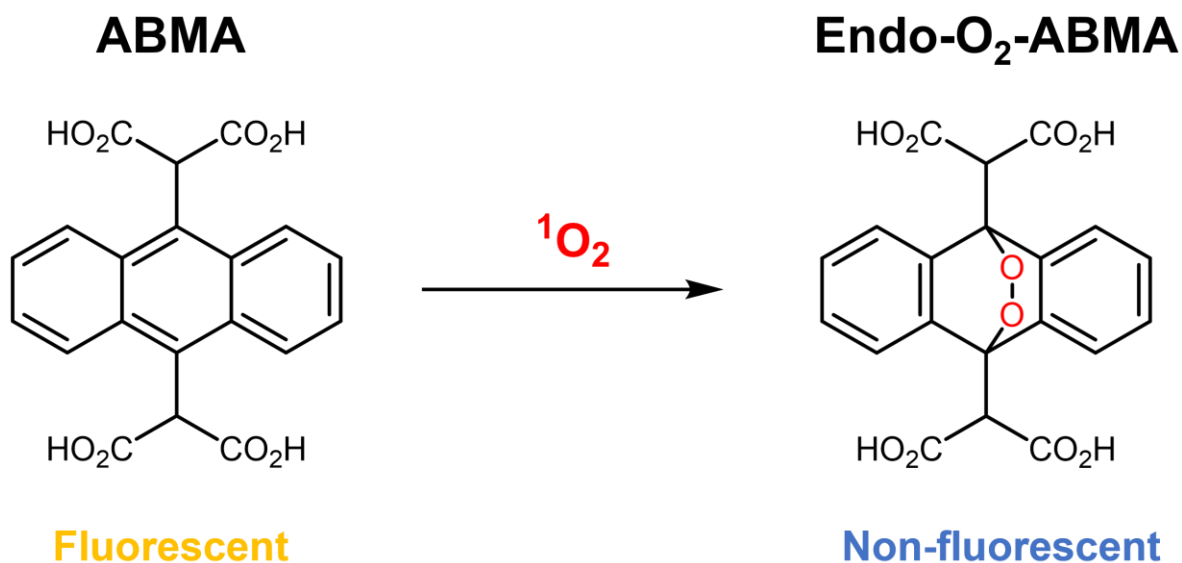


Figure 2.1. The fluorescent *ABMA* molecular probe reacts with *SO* to form *endo-O₂-ABMA*, a compound not fluorescent under 380 nm excitation. Fluorescence decay used as proxy for *SO* generation.

As explored in the introduction chapter, third-generation photosensitisers are systems that incorporate certain immune- or nanotechnologies.¹² Photosensitisers incorporated into gels are a common example of third-generation photosensitisers containing a supramolecular moiety. A diverse array of gels has been explored in the pursuit of effective third-generation photosensitisers.^{13,14} Here, 1,3-bis[(3-octadecyl-1-imidazolium)methyl]benzene di-bromide (**1.2Br**) gelators self-assemble into a three-dimensional fibrous network constituting a gel when mixed with various water-ethanol mixtures.¹⁵ The alkyl chains interdigitate (**Fig. 2.2**) and leave the cationic heads facing away from the alkyl tails. The bromide counter-ions lie between cationic layers, a position significant for its ability to encapsulate other guest molecules.¹⁶ Anionic compounds are easily encapsulated and locked into **1.2Br** gel fibres, with negligible release over the course of days.¹⁷ Neutral compounds have also been encapsulated, though do show release profiles as a consequence of weaker electrostatic binding between the cationic layers.

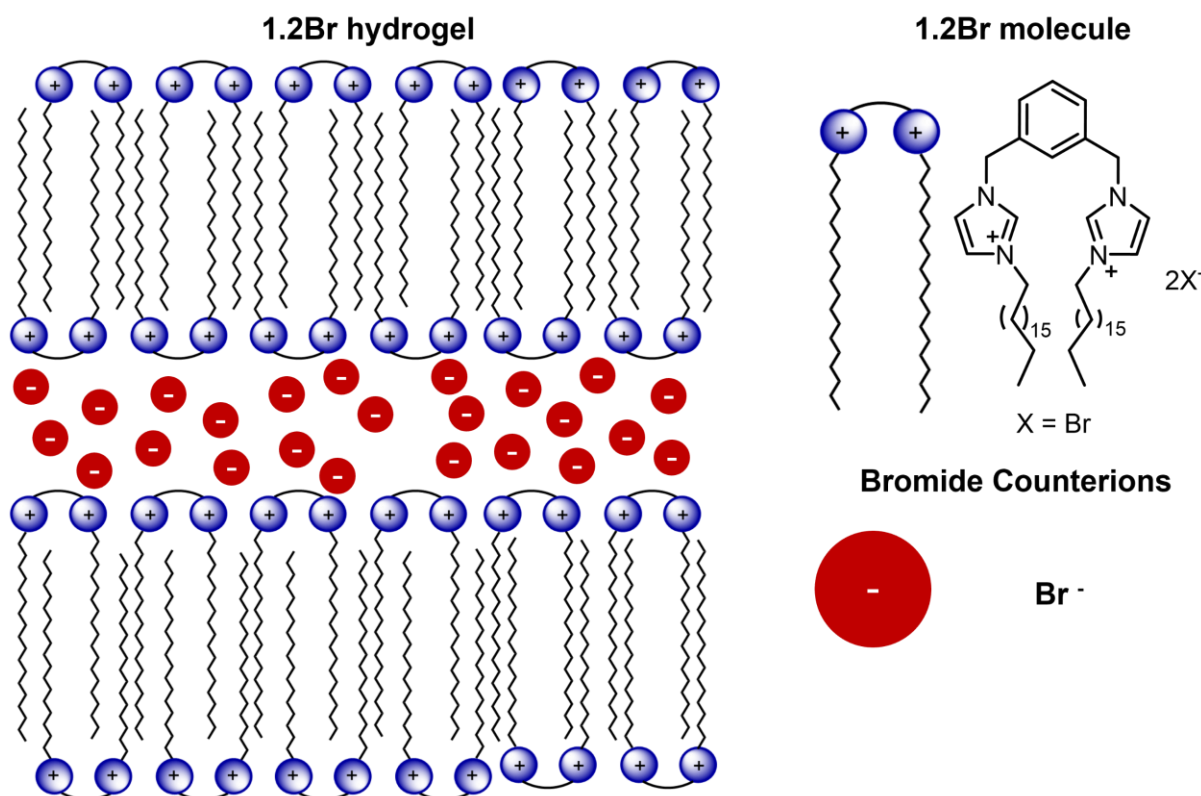


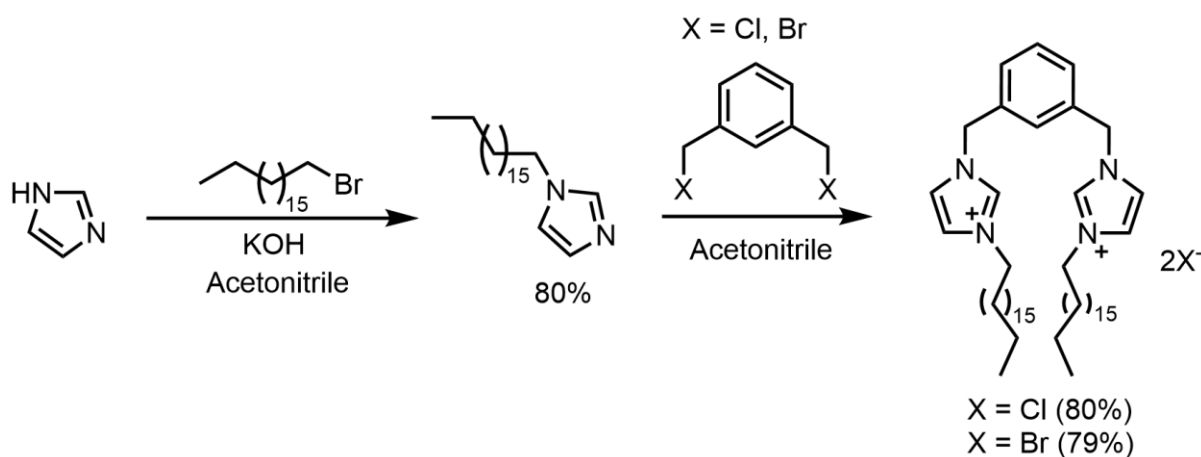
Figure 2.2. A subsection of the fibre structure of a **1.2Br** hydrogel. Alkyl chains form a lamellar structure and in between cationic imidazolium layers lie the bromide counter-ions. Note: sizes are not to scale.

Here, **1.2Br** and the 1,3-bis[(3-octadecyl-1-imidazolium)methyl]benzene di-chloride (**1.2Cl**) gelators will be synthesized for their use in the preparation of hydrogels. A water-soluble tetrasulfonic acid zinc phthalocyanine (**ZnPcTS**) will be characterized in solution as to its photophysical properties and its rate of SO generation compared with that of **ZnPcTS** incorporated inside a **1.2Br** hydrogel. A neutral zinc tetrasulfonatomethyl phthalocyanine (**ZnPcSO₂Me**), structurally similar to **ZnPcTS** but containing sulfonatomethyl groups rather than sulfonic acid groups, will also be characterized in solution and incorporated into a **1.2Br** gel. It could be imagined that the **1.2Br** gel could provide an altered local environment for the phthalocyanine, potentially reducing aggregation and promoting increased singlet oxygen production. Storing the photosensitizer within the gel could also prove advantageous for potential clinical applications.

2.2. Gemini bis-imidazolium gelator (**1.2Br/1.2Cl**) synthesis

The **1.2Br** and **1.2Cl** gelators were synthesized *via* the reaction of an alkylated imidazole with 1,3-bis(bromomethyl) benzene or 1,3-bis(chloromethyl) benzene, respectively (**Scheme 2.1**). The first step involved alkylation of the imidazole ring, which was achieved by heating

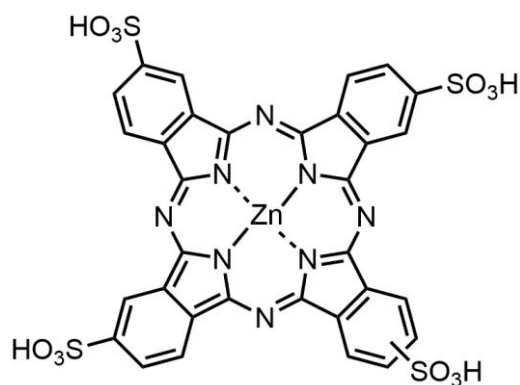
imidazole with 1-bromooctadecane in acetonitrile over fifteen hours. Purification through column chromatography yielded the 1-octadecyl-1*H*-imidazole in 80% yield. Subsequently, the reaction of 1-octadecyl-1*H*-imidazole with either 1,3-bis(bromomethyl)benzene (to form **1.2Br**) or 1,3-bis(chloromethyl)benzene (to form **1.2Cl**) by stirring overnight at 80 °C gave the final **1.2Br** and **1.2Cl** gelators. Upon precipitation, the final pure **1.2Br** and **1.2Cl** gelator compounds were obtained in 79% yield and 80% yield, respectively.



Scheme 2.1. Synthetic route to the **1.2Br** and **1.2Cl** gelators.

2.3. Zinc(II) phthalocyanine tetrasulfonic acid (**ZnPcTS**)

ZnPcTS is a water-soluble phthalocyanine containing sulfonic acid substituents on the peripheral positions of its isoindole rings. Like most phthalocyanines, **ZnPcTS** has been shown to generate SO when its Q-band is irradiated in the presence of oxygen. This property has resulted in much of the research into **ZnPcTS** being based on its potential use for photodynamic therapy (PDT) and antimicrobial photodynamic therapy (aPDT) applications. In 1994, Griffiths *et al.* investigated the *in vivo* photodynamic efficacy of **ZnPcTS** on fibrosarcoma tumours in rats.¹⁸ The main finding of this study was that the Q-band absorption of **ZnPcTS** changes markedly from solution to the cell-bound state, likely a consequence of a differing aggregation states in the latter. Whilst irradiation of **ZnPcTS** at 630 nm and 680 nm had a minimal effect on tumour growth rate, irradiation at 692 nm suppressed the growth rate markedly. It should be noted that **ZnPcTS** is synthesized largely as a mixture of regioisomers, and thus the **ZnPcTS** used in this study exists as a mixture of regioisomers.



ZnPcTS

Further studies have investigated the SO generation characteristics of **ZnPcTS** in solution phase. Kuznetsova *et al.* examined the SO quantum yield (Φ_{SO}) of **ZnPcTS** along with other zinc phthalocyanines that possessed differing degrees of sulfonation (mono-, bis-, tri-, and tetra-substituted).¹⁹ Φ_{SO} refers to the efficiency with which photons of excitation light generate molecules of singlet oxygen and was measured by comparing the rate of decay of an SO scavenger with respect to a known reference photosensitizer. The Φ_{SO} of **ZnPcTS** in aqueous solution was as low as ≤ 0.01 , which is a consequence of the aggregation of **ZnPcTS** in aqueous media. In the same study, the non-ionic surfactant Triton X-100 was added to the aqueous solution of **ZnPcTS** in an attempt to limit aggregation. This suppression of **ZnPcTS** aggregation resulted in a much higher Φ_{SO} of 0.30. In dimethylsulfoxide (DMSO), where **ZnPcTS** does not aggregate, Φ_{SO} was as high as 0.68.

Though soluble as a neutral compound, **ZnPcTS** has been shown to possess different photophysical properties when in its tetrasulfonate form.²⁰ To explore these possibilities, **ZnPcTS** formulations containing 0 to 4 eq. of sodium hydroxide (NaOH) relative to the phthalocyanine (with 4 eq. being a single hydroxide unit per sulfonic acid). It is therefore possible to investigate the behaviour of the phthalocyanine in multiple states. Further base and salt additives will also be incorporated to study how these influence **ZnPcTS** behaviour when incorporated into a gel.

2.3.1. **ZnPcTS** solution characterisation

Figure 2.3A displays the absorption spectrum of **ZnPcTS** in water (with and without 4 eq. NaOH) and in DMSO. The lack of **ZnPcTS** aggregation in DMSO is evidenced by the sharp peak at 679 nm, which corresponds to the non-aggregated **ZnPcTS** absorption maximum. This corroborates earlier work by Kuznetsova *et al.*¹⁹ The absorption spectrum of **ZnPcTS** in water without NaOH shows a Q-band centred at ~ 636 nm, and that of **ZnPcTS** in water with

NaOH reveals a similar Q-band shape similar to the spectrum without base but containing a shoulder at ~ 679 nm. This observation indicates a lesser degree of aggregation of **ZnPcTS** in the presence of NaOH. The difference in aggregation tendency observed in solution is likely brought about by electrostatic interactions between the sodium cations and the anionic sulfonate group present upon the exterior of **ZnPcTS** in the presence of NaOH, and potential hydrogen bonding between sulfonic acid groups of neighbouring phthalocyanines without the presence of NaOH. The pK_a of the **ZnPcTS** sulfonic acids is approximately -2 and therefore we expect that the protons are largely dissociated in neutral water.^{21,22} It is not immediately clear that within the **ZnPcTS** aggregates in water that all of the acid protons will dissociate because of the local environment in the assembly, and it could be that hydrogen bonding between neighbouring stacked phthalocyanines takes place, and for this reason the addition of the base has such a large impact upon the absorption and fluorescence characteristics of the phthalocyanine.

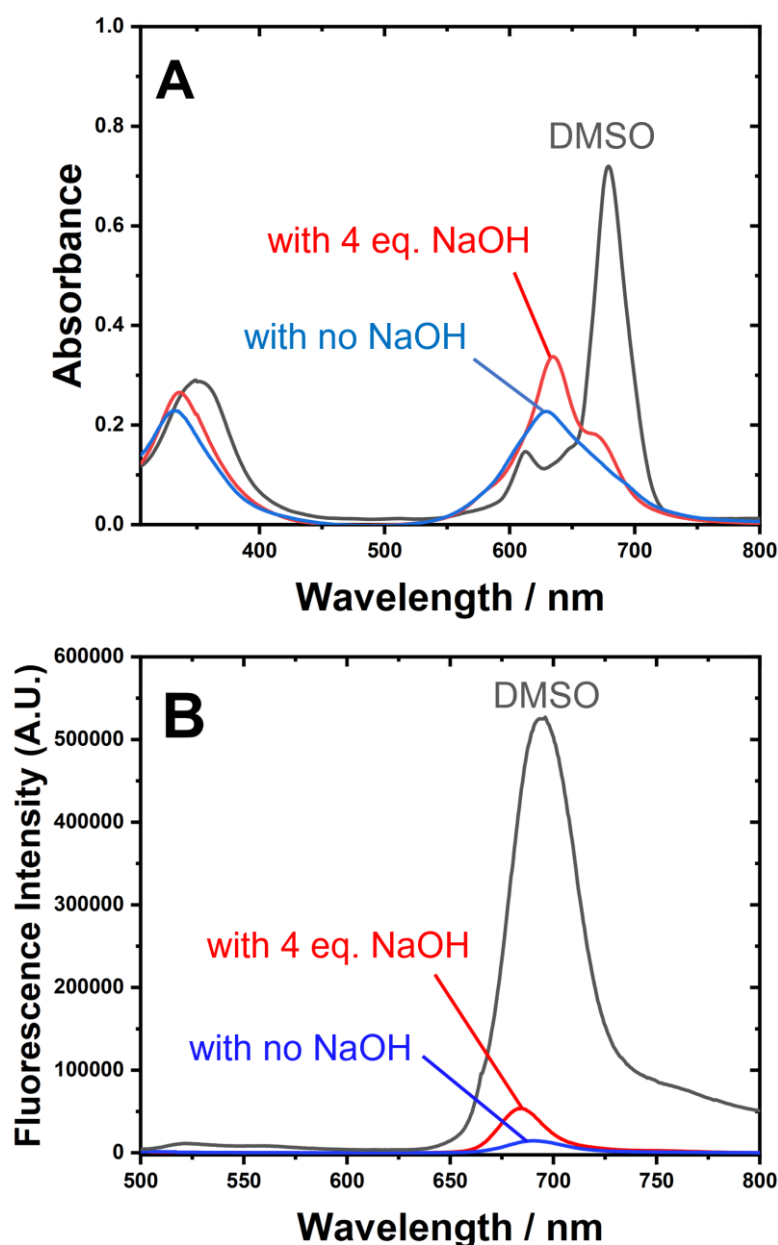


Figure 2.3. (A) Absorption spectrum of **ZnPcTS** at a concentration of 10 μM in DMSO (black), water with 4 eq. NaOH (red), and water without NaOH (blue). (B) Fluorescence emission spectrum of **ZnPcTS** at a concentration of 10 μM in DMSO (black), water with 4 eq. NaOH (red), and water without NaOH (blue). $\lambda_{exc.} = 300 \text{ nm}$ and $\lambda_{filter} = 330 \text{ nm}$ for all three measurements.

This aggregation also has the effect of quenching fluorescence emission of **ZnPcTS** in aqueous solution which can be seen in **Fig 2.3B**, where the fluorescence emission spectra of **ZnPcTS** in DMSO and in water (with and without 4 eq. NaOH) is shown. As a result of the short lifetime of the second excited singlet state of **ZnPcTS**, only one significant emission peak resulting from the first excited state is observed when exciting the Soret band (~ 350 nm) or the Q-band

in the red to far-red region (600-700 nm). A low-intensity peak between 500-550 nm is seen with **ZnPcTS** in DMSO and corresponds to the minimal emission from the second excited state brought about by its short lifetime.²³ Although relative fluorescence intensities between samples cannot be quantitatively compared without conducting the necessary calibrations, **ZnPcTS** in DMSO results in a significantly larger fluorescence than **ZnPcTS** in aqueous solution. The position of the emission maxima also varies depending on both solvent and presence of base. The emission maximum of **ZnPcTS** in DMSO is located at 695 nm, and that of **ZnPcTS** in water (with and without 4 eq. NaOH) is present at 685 nm and 691 nm, respectively.

Another commonly used method to prevent aggregation of hydrophobic core-containing molecules is to introduce surfactants into the system. The compound *N,N,N*-trimethylhexadecan-1-aminium bromide (**CTAB**) (shown in **Fig. 2.4A**), a cationic surfactant, has been shown to inhibit aggregation in water-soluble phthalocyanines.²⁴ **Fig. 2.4** shows the absorption spectra of **ZnPcTS** in water with 4 eq. NaOH (**Fig. 2.4A**) and in water without NaOH (**Fig. 2.4B**). In each spectrum, the effect of increasing the **CTAB** concentration from 0 to 1 μM to 10 μM can be seen. The effect of disaggregation that can be seen by the increase of the **ZnPcTS** monomer Q-band at ~ 679 nm is observed both in the presence of base and without but is more pronounced in the solutions containing 4 equivalents of NaOH. This disparity in effect is probably a consequence of the anionic character of the deprotonated **ZnPcTS** and its more significant interaction with the cationic **CTAB**. As seen from the fluorescence emission spectra (**Fig. 2.4C**), fluorescence intensity increases (as predicted) with the addition of **CTAB** at a concentration of 1 μM but is almost completely quenched at a concentration of 10 μM . This complete reduction of fluorescence could be result of the heavy atom effect brought about by the bromide anions, which have been shown to reduce the fluorescence of anthracene derivatives by increasing their triplet state lifetimes.²⁵

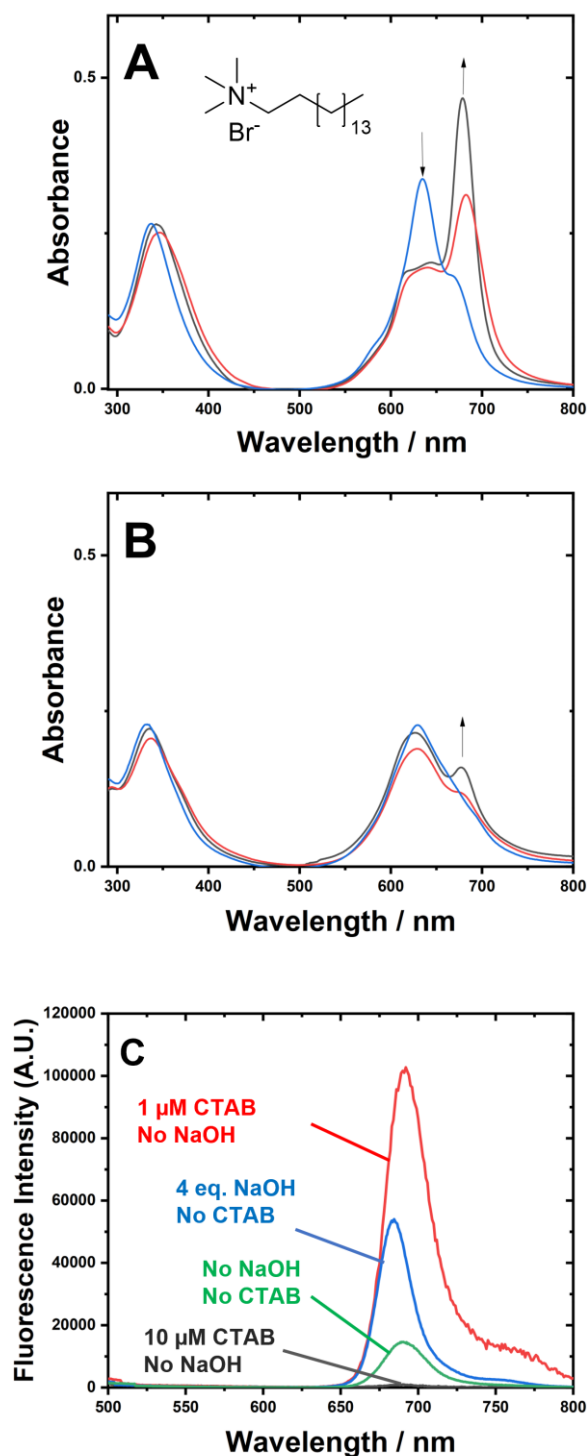


Figure 2.4. (A) Absorption spectra of ZnPcTS (10 μM) with 4 eq. NaOH containing no CTAB (blue), 1 μM CTAB (red), and 10 μM CTAB (grey). CTAB structure shown. (B) Absorption spectra of ZnPcTS (10 μM) with no NaOH containing no CTAB (blue), 1 μM CTAB (red), and 10 μM CTAB (grey). (C) Fluorescence emission spectra of ZnPcTS (10 μM) with no NaOH and no CTAB (green), with 4 eq. NaOH and no CTAB (blue), with no NaOH and 1 μM CTAB (red), and with no NaOH and 10 μM CTAB (grey). $\lambda_{\text{exc}} = 300 \text{ nm}$ and $\lambda_{\text{filter}} = 330 \text{ nm}$ for all fluorescence measurements.

2.3.2. ZnPcTS@Gel preparation and characterisation

The gels comprising the gelator, phthalocyanine and base - abbreviated **ZnPcTS_nEqBase@Gels** - were prepared using the solvent-antisolvent method whereby **1.2Br** dissolved in ethanol was added to the aqueous phthalocyanine solution (with NaOH where applicable) to give a mixture consisting of a 1:1 water-ethanol ratio and final **1.2Br** concentration of 12 mM within the gel as displayed in **Fig. 2.5**. In order to investigate the effect of **ZnPcTS** incorporation in the gel as the tetrasulfonic acid and as the corresponding salt derivative, stock solutions which contained 0-4 equivalents of NaOH relative to **ZnPcTS** (0 to 1 equivalent per sulfonic acid group). Gels prepared with n equivalents of NaOH are subsequently labelled **ZnPcTS_nEqBase@Gel**. After the mixture of the aqueous and ethanolic solutions, gelation generally occurred within one minute irrespective of the concentrations of **ZnPcTS**. No appreciable difference in gelation time was observed between the gels containing differing concentrations of NaOH and the prepared gels were both robust and stable over several months at room temperature.

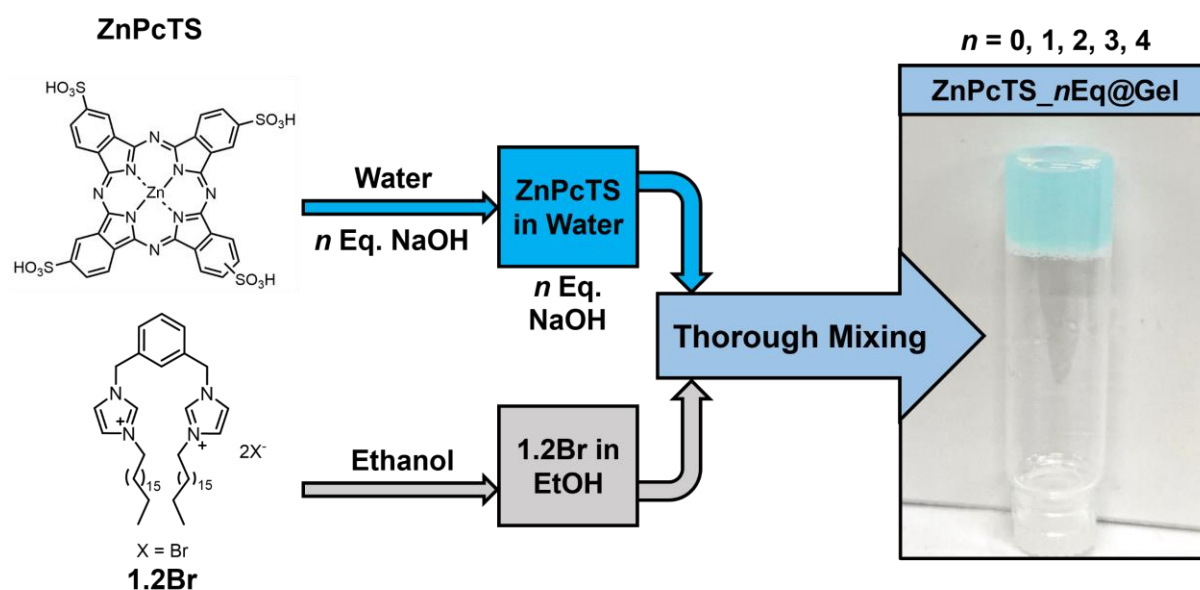


Figure 2.5. Procedure for preparation of gels from an equal volume of **ZnPcTS** with n equivalents of NaOH in water and **1.2Br** in ethanol.

FT-IR spectra of the pristine **1.2Br** xerogel (dried gel), **ZnPcTS_0EqBase@Gel** and **ZnPcTS_4EqBase@Gel** xerogels were collected and compared with **ZnPcTS** in the solid state are shown in **Fig. 2.6**. Xerogels were formed *via* drying a sample of the hydrated gel overnight under vacuum. The O-H stretch of the sulfonic acid found at 3205 cm^{-1} in the spectrum of the solid state **ZnPcTS** is not seen to the same extent in the **ZnPcTS_nEqBase@Gel**. The lack of

a strong O-H stretch in the **ZnPcTS_0EqBase@Gel** xerogel indicates that there is a degree of deprotonation of the sulfonic acid groups even without the addition of base, at least in the dried form of the gel. Another characteristic peak is found at 1403 cm^{-1} and corresponds to the S=O stretch, which is not seen in the **1.2Br** xerogel spectrum, thus corresponding to the encapsulated phthalocyanine.

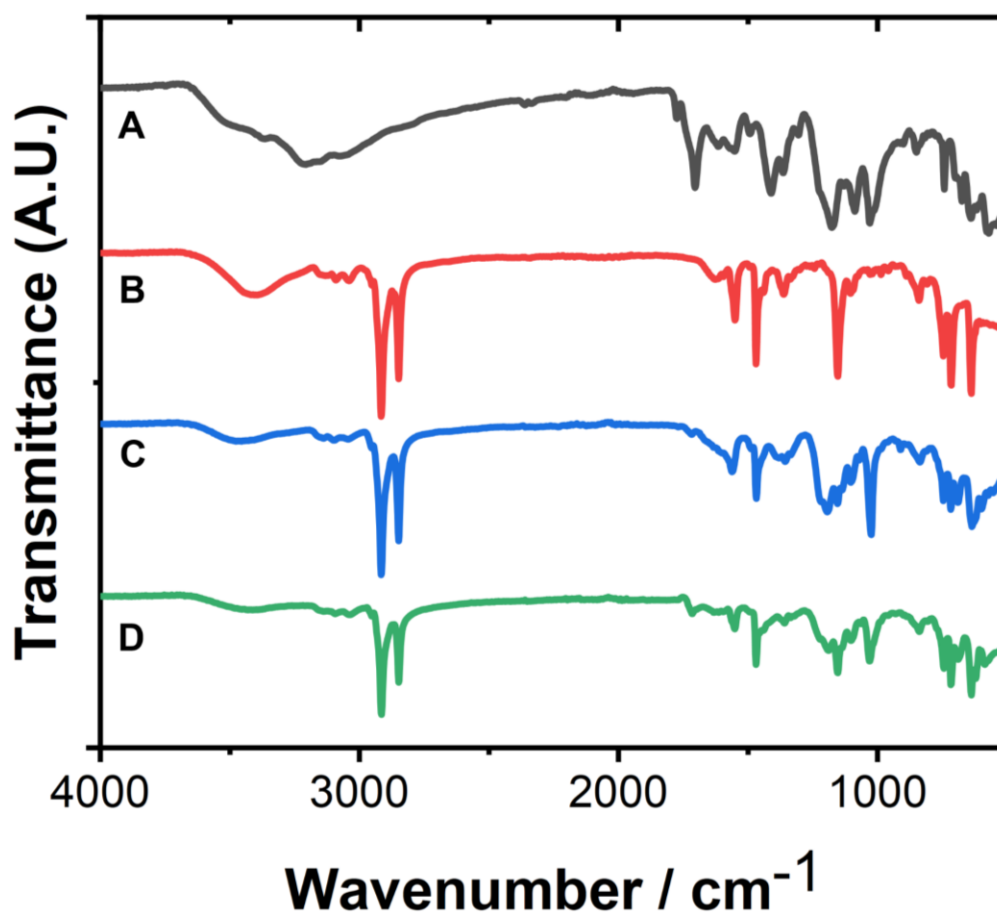


Figure 2.6. FT-IR comparison of solid state **ZnPcTS**, pristine **1.2Br** xerogel and **ZnPcTS** xerogels. (A) Solid state **ZnPcTS**. (B) Pristine **1.2Br** xerogel, $[1.2Br] = 12\text{ mM}$, 1:1 water ethanol. (C) **ZnPcTS_4EqBase@Gel** xerogel, $[1.2Br] = 12\text{ mM}$, 1:1 water ethanol, $[ZnPcTS] = 100\text{ }\mu\text{M}$, $[NaOH] = 400\text{ }\mu\text{M}$. (D) **ZnPcTS_0EqBase@Gel** xerogel, $[1.2Br] = 12\text{ mM}$, 1:1 water ethanol, $[ZnPcTS] = 100\text{ }\mu\text{M}$. All concentrations are the final concentrations within each dried gel.

To better understand the microscale structure of the newly formed gels, SEM imaging was employed. **ZnPcTS_nEqBase@Gel** xerogel samples were prepared with no base and increasing concentrations of **ZnPcTS** (no phthalocyanine; $12\text{ }\mu\text{M}$; $120\text{ }\mu\text{M}$ and 1.2 mM) with the gelator concentration kept constant at 12 mM . Further samples were prepared with the same concentrations of **ZnPcTS** but also including 4 eq. of NaOH to investigate the potential effect of base upon the microscale structure. SEM images (**Fig. 2.7**) reveal that when no **ZnPcTS** is

present within the gels, the gel fibres are relatively well-defined, irrespective of the presence of base. Increasing the **ZnPcTS** concentration to 12 μM within the gel does not influence the fibres to a considerable extent. However, upon increasing to 120 μM and finally 1.2 mM, significant changes to the fibre morphology occur, moving from predominantly straight fibres (**Fig. 2.7A-D**) and upon increasing **ZnPcTS** loading, beginning to appear less straight and well-defined and cluster into areas of high fibre density (**Fig. 2.7E-H**). This trend towards greater morphological disturbance with greater photosensitizer loading is observed also with identical concentrations of a tetracarboxylated porphyrin.¹⁷

[ZnPcTS]



0 mM

With 4 eq. NaOH

With no NaOH

0.012 mM

0.12 mM

1.2 mM

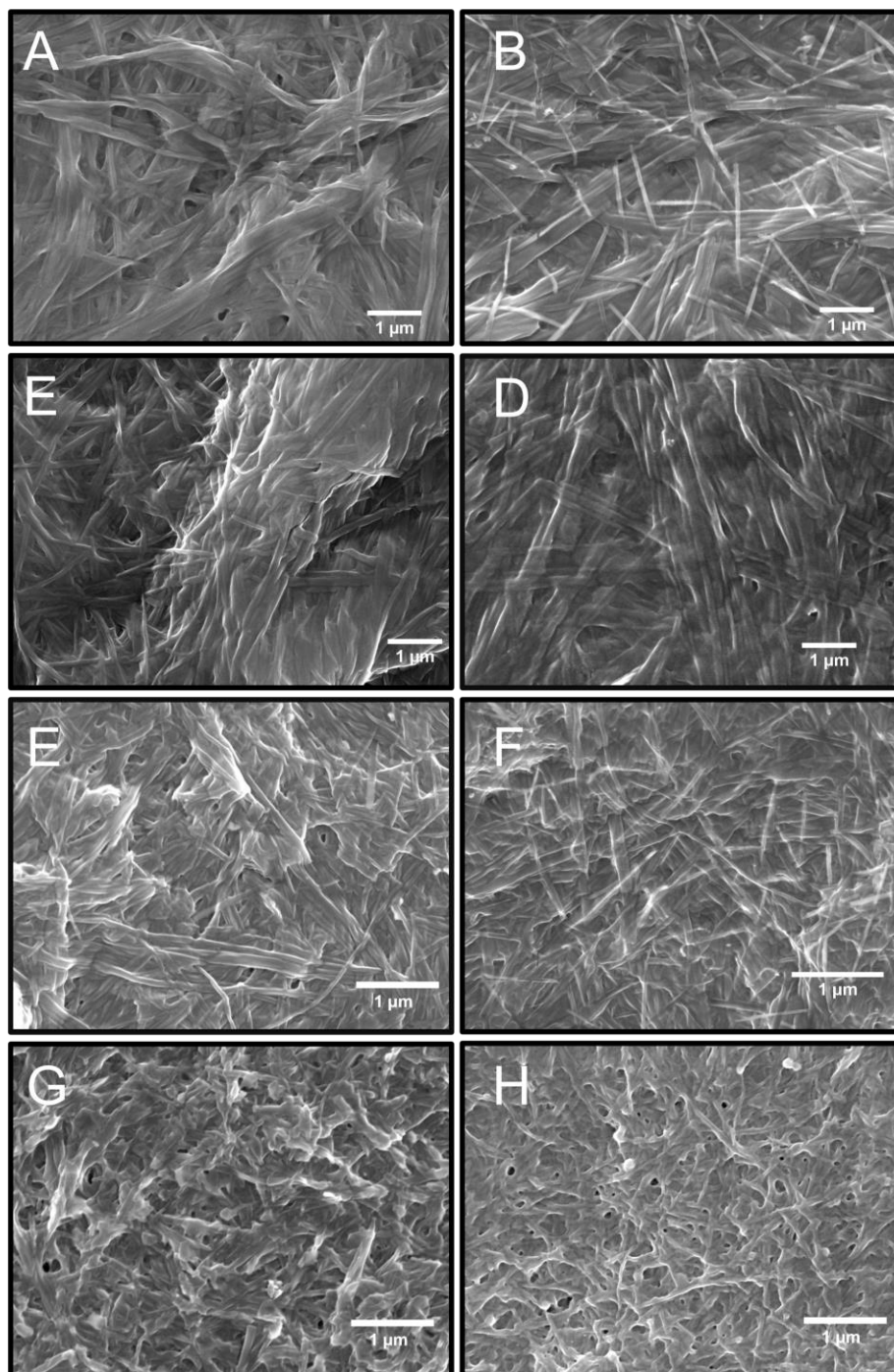


Figure 2.7. SEM images xerogels of **1.2Br** gels formed in a 1:1 water-ethanol ratio and covered with a 5-nm-thick layer of iridium. **ZnPcTS** concentration is increased by a factor of ten until the final concentration of 1.2 mM. No discernible difference is observed between the samples containing 4 eq. and no base. Scale corresponds to 1 μm .

Rheological characterisation (**Fig. 2.8**) revealed the prevalence of the storage modulus (elastic modulus, G') over the loss modulus (G''), indicating that **1.2Br** gels have a solid-like feature

rather than a liquid behaviour independently of the presence of the phthalocyanine, which is in agreement with previous reports on other guests in the gel.^{17,26} In the published work supporting this study, it was found that the incorporation of the **ZnPcTS** or the corresponding salt form increased both the gel resistance to deformation and the resistance to rupture, observing a greater influence in the case of **ZnPcTS** rather than the corresponding salt form.²⁷ The increased resistance to deformation (G' and G'' values) and the increased resistance to rupture (Critical stress values) are shown in **Table 2.1**. It has been previously shown that an increasing loading of a tetracarboxylated porphyrin within a **1.2Br** framework was correlated to an augmented resistance to rupture.¹⁷ In this work, it is reported that **ZnPcTS** can induce a similar effect, but to a lower extent for the organic salt. There is a distinct contribution of the ionic and non-ionic **ZnPcTS** structure on the **1.2Br** gel assembly that affects the gel strength. It could be imagined that the deprotonated **ZnPcTS** in **ZnPcTS_4EqBase@Gel** would interact more strongly with the cationic heads of the **1.2Br** gel, resulting in a weakening of the bulk structure as measured using rheological analysis.

Table 2.1. Critical stress values from oscillation amplitude sweep (crossover points when $G' = G''$). [Work carried out by D. Limón at Universitat de Barcelona]

Sample	G'^*	G''^*	Critical stress (Pa)
1.2Br gel	2059	410	15.52
ZnPcTS_0EqBase@Gel	8707	1808	57.02
ZnPcTS_4EqBase@Gel	3072	859	37.04

*Denotes average values at the linear viscoelastic region (0.1-1.0 Pa)

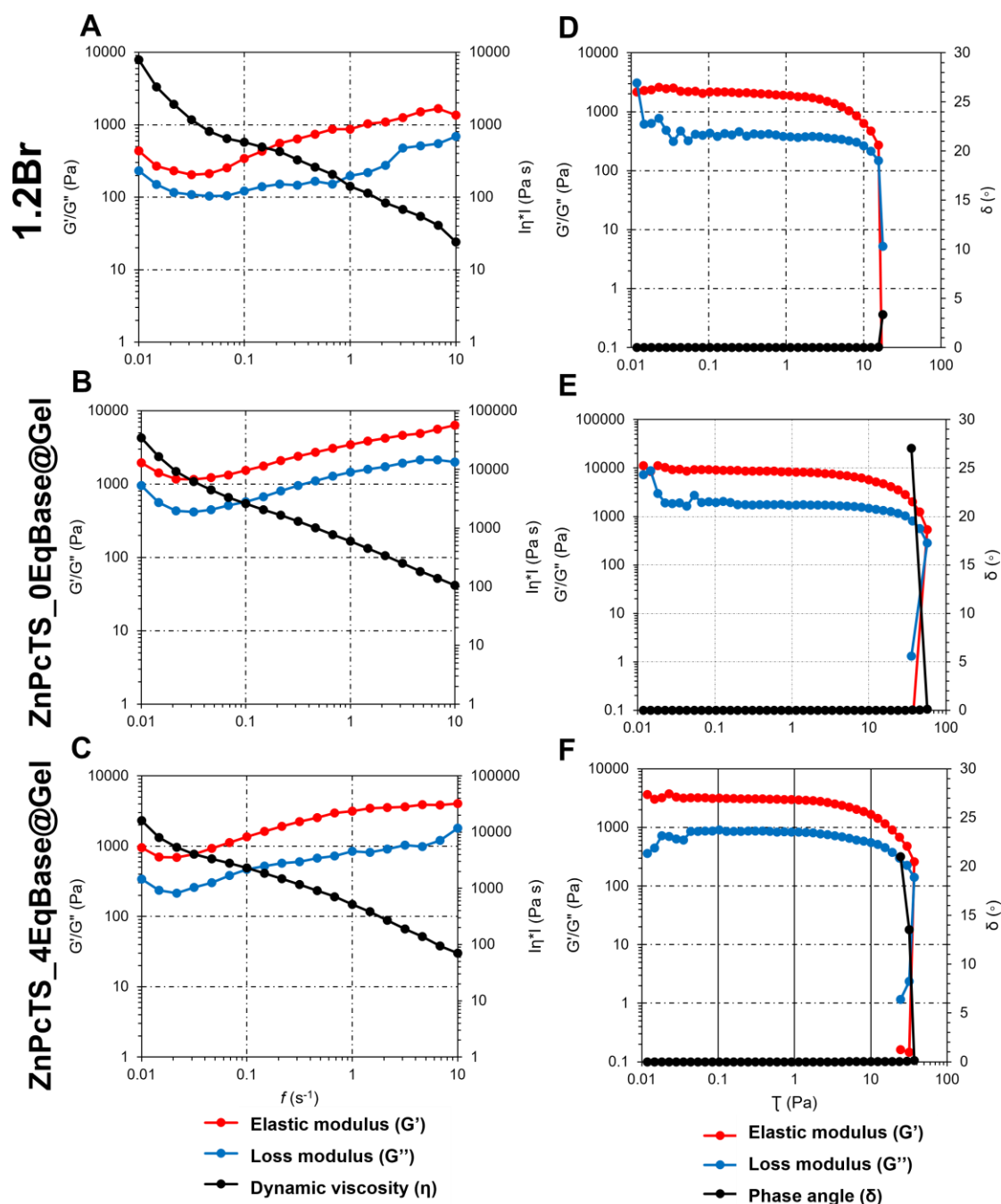


Figure 2.8. Frequency sweep (A, B, C) and amplitude sweep (D, E, F) profiles of 1.2Br gel (A, D), ZnPcTS_0EqBase@Gel (B, E) and ZnPcTS_4EqBase@Gel (C, F). [Work conducted by D. Limón at Universitat de Barcelona]

The absorption characteristics of ZnPcTS when incorporated into the gel were also influenced by the presence of NaOH. **Figure 2.9A** shows the absorption spectra of ZnPcTS_4EqBase@Gel and ZnPcTS_0EqBase@Gel. ZnPcTS_4EqBase@Gel has a greater extinction coefficient in the Q-band region than ZnPcTS_0EqBase@Gel along with a different Q-band shape. This disparity in absorbance could be explained by the varying extents

of aggregation of **ZnPcTS** within the gel with and without the presence of base. Fluorescence emission spectra (**Fig. 2.9B**) of gels containing an intermediate amount (1, 2, 3 eq. NaOH) of base show an initial decrease in emission intensity and a bathochromic shift in the position of the emission maximum from 0 to 1 eq. of NaOH, followed by hypsochromic shifts from 1 to 4 eq. NaOH. This decrease in fluorescence intensity upon the addition of 1 eq. of NaOH was not expected, as lowering aggregation tends to increase fluorescence activity, though this result is discussed further in the context of the singlet oxygen generation experiments. In order to mimic the solvent composition within the gel, the absorption and emission spectra of **ZnPcTS** in 1:1 water-ethanol solution were characterized (**Fig. 2.9C,D**). Again, **ZnPcTS** in the presence of base in this 1:1 water-ethanol solution exhibits greater absorbance and an extinction coefficient which is more than double that of **ZnPcTS** in 1:1 water-ethanol without the presence of base. The Q-band of **ZnPcTS** with 4 eq. NaOH in 1:1 water-ethanol strongly resembles that of **ZnPcTS** in DMSO, indicating that the **ZnPcTS** is not aggregated in 1:1 water-ethanol when 4 eq. of NaOH are present. When base is not present, the Q-band shape is more complicated with the two peaks split into four. This Q-band splitting pattern is observed in the free base phthalocyanine H₂Pc but also seen in metalated phthalocyanines.²⁸ Splitting of this type is intrinsic to H₂Pc and is caused by the asymmetry of the isoindole nitrogens in the phthalocyanine ring. This asymmetry causes the HOMO and the LUMO to be non-degenerate, resulting in two different transitions in the Q-band region.²⁹ Absorption spectra of **ZnPcTS@Gel** samples containing 1-3 equivalents of NaOH show intermediate Q-band shapes between that of the 0 eq. and 4 eq. NaOH samples. The extinction coefficients and absorption maxima of **ZnPcTS** in solution/gel (**Table 2.2**) reveal that **ZnPcTS** with 4 eq. NaOH has a higher absorption than that of the counterpart without NaOH.

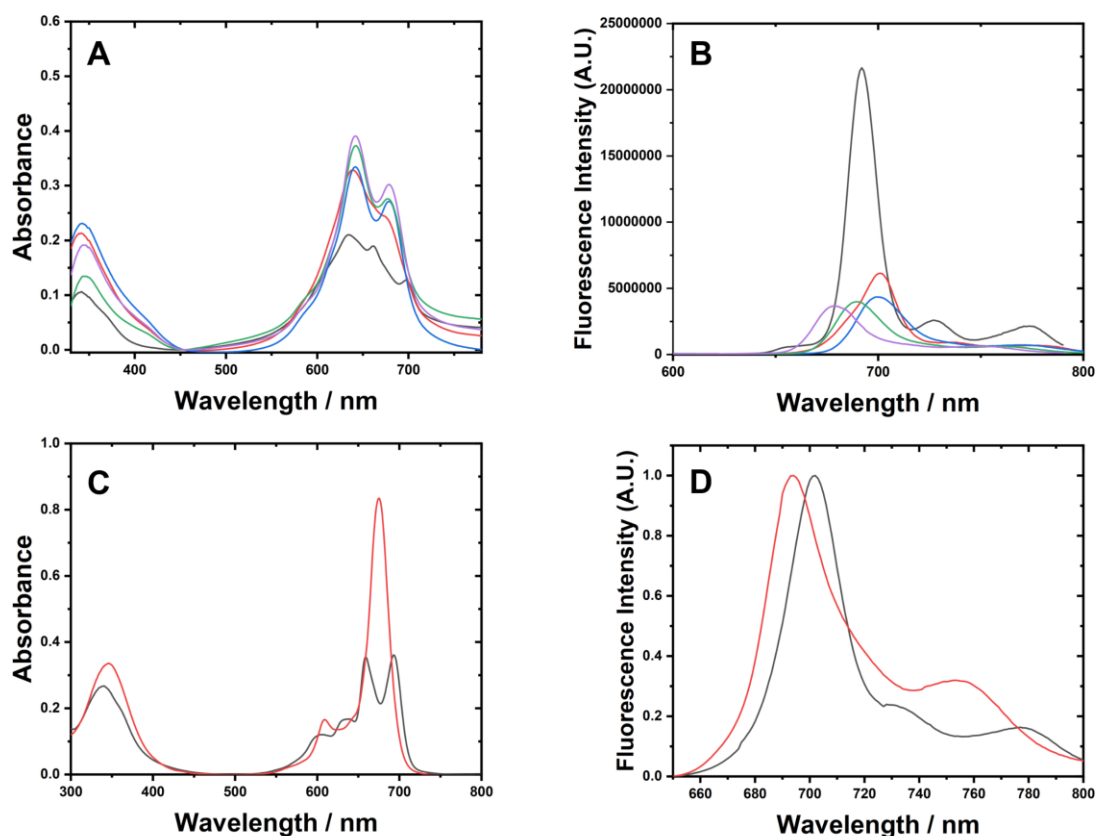


Figure 2.9. (A) Absorption spectra of **ZnPcTS_nEqBase@Gels**, $n = 0$ (grey), $n = 1$ (red), $n = 2$ (blue), $n = 3$ (green), $n = 4$ (lilac), $[\text{ZnPcTS}] = 100 \mu\text{M}$. (B) Fluorescence emission spectra of **ZnPcTS_nEqBase@Gels**, $n = 0$ (grey), $n = 1$ (red), $n = 2$ (blue), $n = 3$ (green), $n = 4$ (lilac), $[\text{ZnPcTS}] = 10 \mu\text{M}$. (C) Absorption spectra of **ZnPcTS** ($10 \mu\text{M}$) in 1:1 water-ethanol with 4 eq. NaOH (red) and no NaOH (grey). (D) Fluorescence emission spectra of **ZnPcTS** ($10 \mu\text{M}$) in 1:1 water-ethanol with 4 eq. NaOH (red) and no NaOH (grey). $\lambda_{\text{exc}} = 625 \text{ nm}$ and $\lambda_{\text{filter}} = 645 \text{ nm}$ for these fluorescence measurements.

Table 2.2. Extinction coefficients of **ZnPcTS** in different systems.

ZnPcTS_nEqBase	Extinction Coefficient (ϵ)		
	Water	1:1 Water-Ethanol	1.2Br Gel
$n = 4$	34000	83000	39000
$n = 0$	22000	36000	21000

2.3.3. **ZnPcTS** singlet oxygen generation

The SO-generating ability of the gels was assessed using **ABMA**, a fluorescent probe which reacts with singlet oxygen producing a non-fluorescent (in visible spectrum) endoperoxide compound and reducing the overall **ABMA** fluorescence emission between $\sim 400 - 500 \text{ nm}$. A diode laser of 660 nm was used to excite the Q-band of **ZnPcTS**, and subsequently generate

SO. A comparison of the **ZnPcTS** in solution and within the gel would confirm whether aggregation had a considerable effect upon the SO generating ability, along with how the presence of base influences SO generation. **Figure 2.10** shows overlaid fluorescence spectra of **ABMA** over fifteen minutes of irradiation in the presence of **ZnPcTS** ($10\ \mu\text{M}$) in water and with 4 eq. NaOH. To quantify the **ABMA** decay, the intensity of the emission peak at $\sim 430\ \text{nm}$ was tracked over the fifteen minutes to yield values corresponding to percentage of **ABMA** decayed. Plotting the relative intensities of this **ABMA** emission peak over time yields information relating to the rate of SO generation along with the associated kinetics. **Figure 2.11A** displays **ABMA** decay plots of **ZnPcTS** ($10\ \mu\text{M}$), one with 4 eq. NaOH (blue line) and one with no NaOH in water (red line). The SO generation of **ZnPcTS** both with and without base in aqueous media is modest, with roughly a 10% decrease in **ABMA** intensity after 15 minutes. A control **ABMA** plot without any **ZnPcTS** is also shown in **Fig. 2.11A**, as there is a small inherent decay of **ABMA** fluorescence over time. Again, this poor SO generation rate is largely a consequence of the significant aggregation in the aqueous solvent.

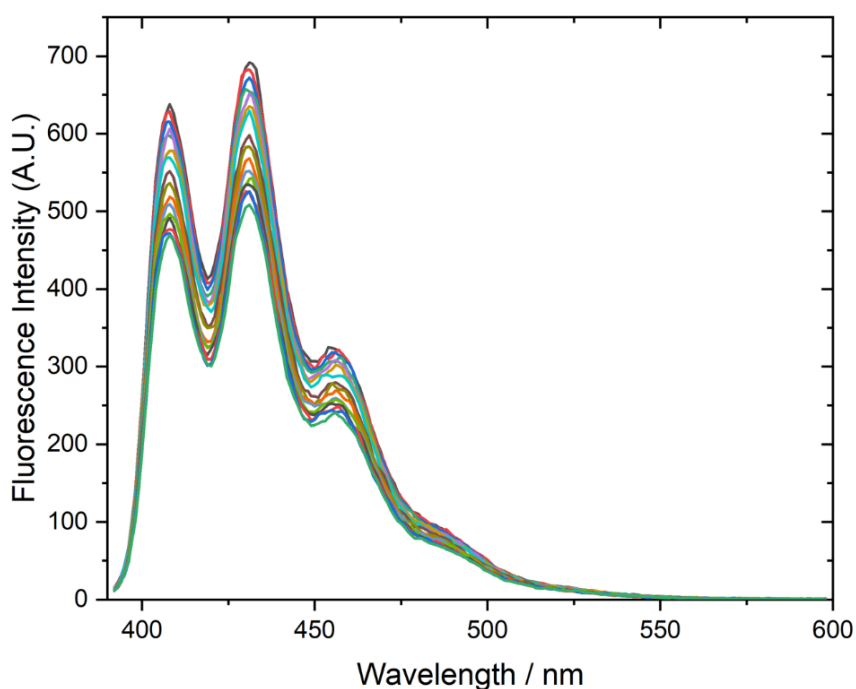


Figure 2.10. A total of sixteen **ABMA** fluorescence emission spectra in which the intensity of $\sim 430\ \text{nm}$ maximum can be seen to decrease under irradiation with a red laser in the presence of **ZnPcTS** ($10\ \mu\text{M}$) and 4 eq. NaOH in aqueous solution. $\lambda_{\text{irr}} = 660\ \text{nm}$, $P_{\text{irr}} = 50\ \text{mW}$. $\lambda_{\text{exc}} = 380\ \text{nm}$.

Figure 2.11A also shows **ABMA** decay plots of **ZnPcTS_0EqBase@Gel** and **ZnPcTS_4EqBase@Gel** dispersed in water. An enhancement in SO-generating ability is clearly seen for both gels tested, **Fig. 2.12** shows the fluorescence emission decay of **ABMA** for the measurements with **ZnPcTS_4EqBase@Gel**, where a clear qualitative difference can be seen in comparison with **Fig. 2.10**. Fitting pseudo first order kinetics results in a rate enhancement (with respect to aqueous solution) of 17x and 9x for **ZnPcTS_4EqBase@Gel** and **ZnPcTS_0EqBase@Gel**, respectively. Whilst encapsulation in the **1.2Br** gel clearly enhances SO generation, a disparity between **ZnPcTS_4EqBase@Gel** and **ZnPcTS_0EqBase@Gel** exists. Increased aggregation of **ZnPcTS** within the gel containing no NaOH, along with a potential influence of the heavy atom effect may be contributing to this difference. This disparity is explained by the observed reduced fluorescence of **ZnPcTS_4EqBase@Gel** compared with **ZnPcTS_0EqBase@Gel**. With the triplet excited state of the former being stabilised by the heavy atom effect, fluorescence should decrease as a result in more intersystem crossing, which we observe as enhanced SO generation. To further evaluate the effect of NaOH, similar measurements were obtained for **ZnPcTS@Gels** containing 1, 2, and 3 equivalents of NaOH. **Fig. 2.11B** shows the **ABMA** decay curves for **ZnPcTS@Gels** with 0 to 4 equivalents of base. Largely within error, the **ZnPcTS_1,2,3EqBase@Gels** yield **ABMA** decay curves that lie in between that of **ZnPcTS_0EqBase@Gel** and **ZnPcTS_4EqBase@Gel**, indicating that increasing NaOH content induces an increase in SO generation through the gradual increase in amount of non-aggregated phthalocyanine species.

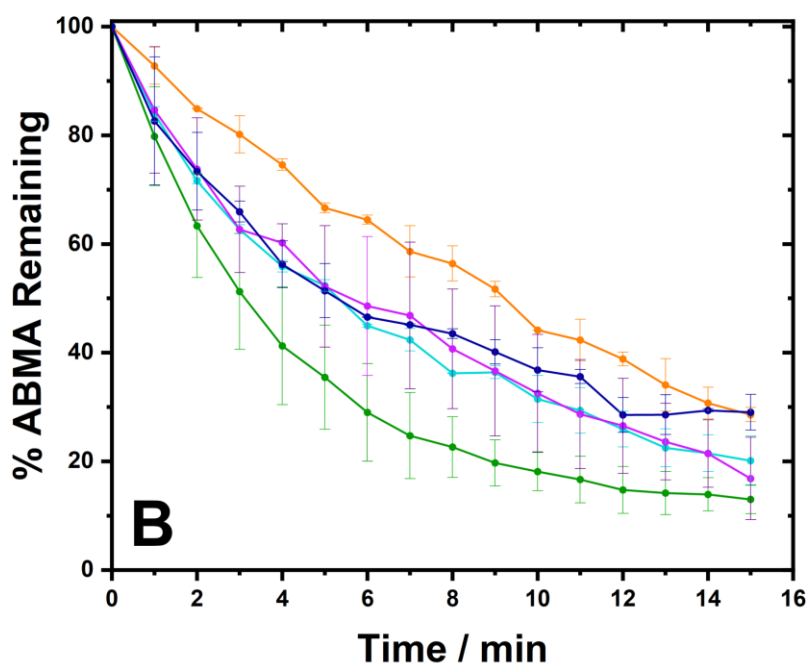
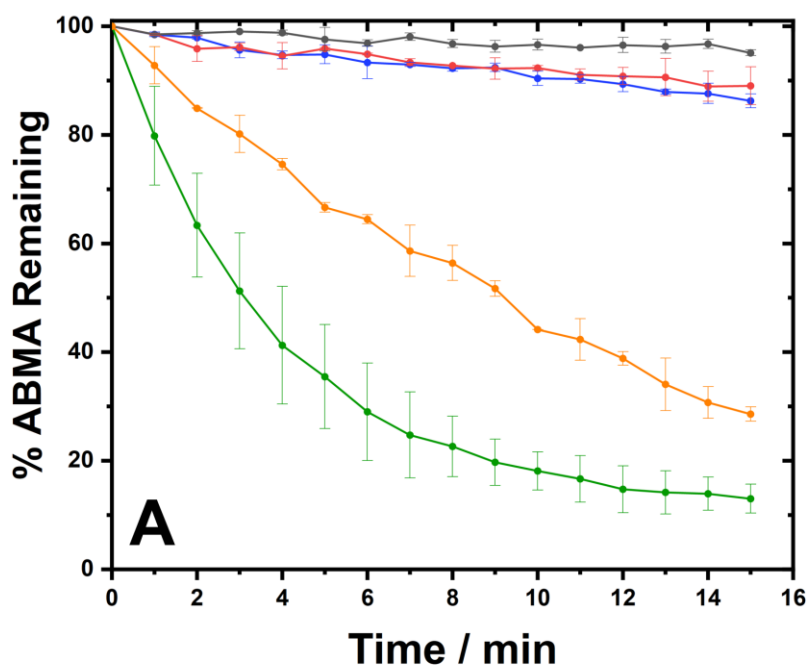


Figure 2.11. (A) ABMA decay plot without ZnPcTS (grey line), ZnPcTS (10 μM) with no NaOH (red line) in aqueous solution, ZnPcTS (10 μM) with 4 eq. NaOH (blue line) in aqueous solution, ZnPcTS_0EqBase@Gel (orange) and ZnPcTS_4EqBase@Gel (green) (B) ABMA decay plot of ZnPcTS_0EqBase@Gel (orange), ZnPcTS_1EqBase@Gel (cyan), ZnPcTS_2EqBase@Gel (dark blue), ZnPcTS_3EqBase@Gel (magenta), and ZnPcTS_4EqBase@Gel (green). In all gel samples, final [ZnPcTS] = 2 μM . λ_{exc} = 380 nm.

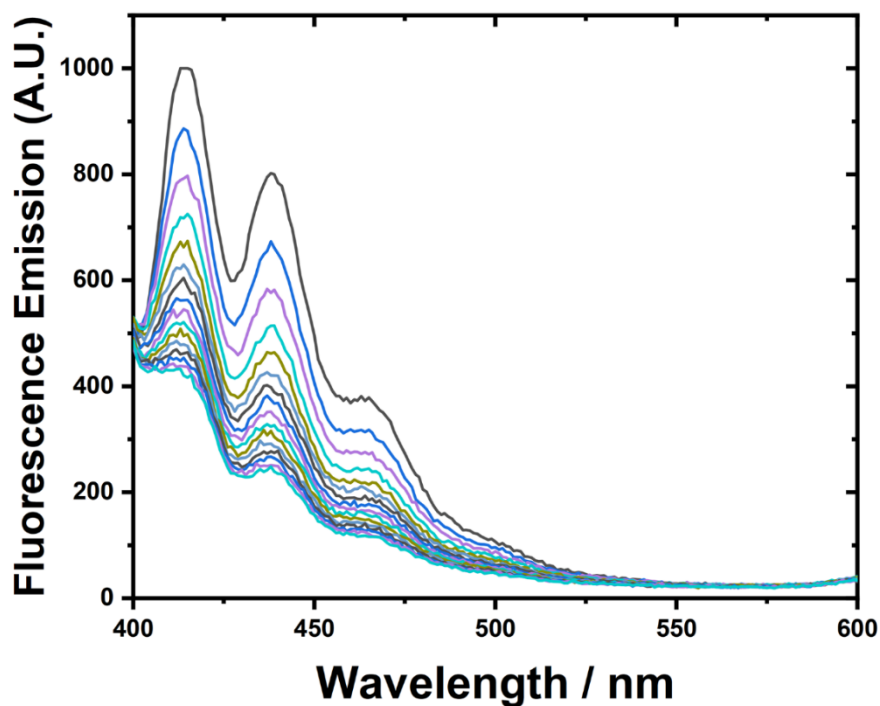


Figure 2.12. Sixteen *ABMA* fluorescence emission spectra in which the intensity of ~ 430 nm maximum can be seen to decrease under irradiation with a red laser in the presence of *ZnPcTS_4EqBase@Gel* ($2 \mu\text{M}$) dispersed in water. $\lambda_{\text{irr}} = 660$ nm, $P_{\text{irr}} = 50$ mW. $\lambda_{\text{exc}} = 380$ nm.

CTAB was shown to decrease **ZnPcTS** aggregation at a concentration of $1 \mu\text{M}$ in aqueous solution. This is corroborated by the SO generation of **ZnPcTS** in said system (**Fig. 2.13**). Whilst the effect is relatively small, an increase in SO generation over fifteen minutes is observed. Similarly to the fluorescence quenching of **ZnPcTS** by **CTAB**, the fluorescence of **ABMA** is also completely quenched by the addition of $10 \mu\text{M}$ **CTAB**, prohibiting SO generation measurements with this probe.

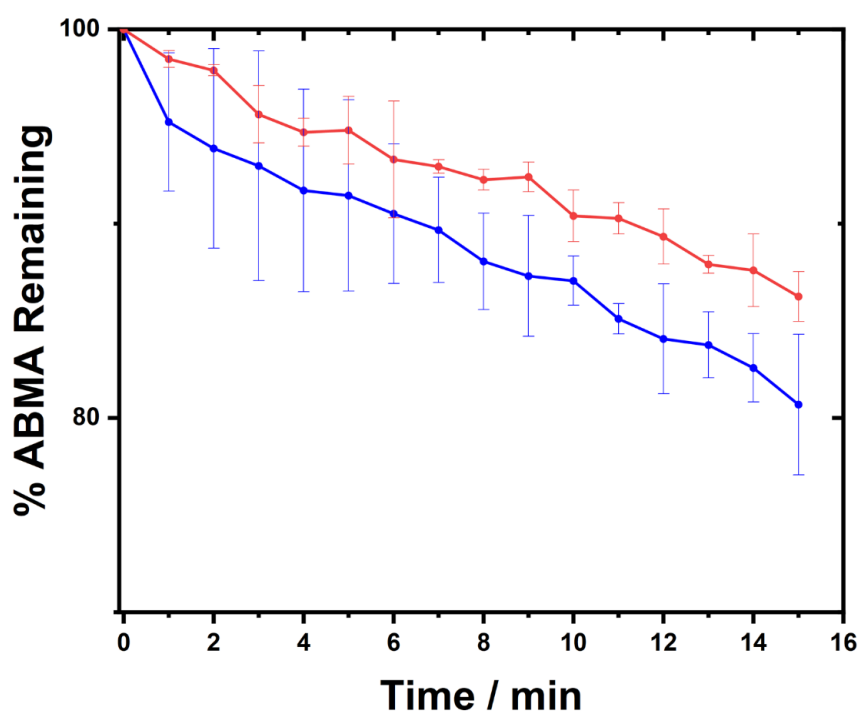


Figure 2.13. ABMA decay plots for ZnPcTS (40 μM) in water (red) and ZnPcTS (40 μM) in water with 1 μM CTAB (blue).

2.3.4. Further additives and conditions study

To further understand the role of base in providing enhanced SO generation, identical gel systems containing caesium hydroxide were prepared. CsOH is a basic compound with a $\text{p}K_{\text{a}}$ value of 15.76, making it fractionally more basic than NaOH which has a $\text{p}K_{\text{a}}$ of 15.70 although this difference is not likely to have a significant effect upon the gel system. More importantly, Cs^+ cations are significantly larger (167 pm) than Na^+ cations (116 pm).³⁰ The influence of potential adherence of these differently sized cations to the phthalocyanine's deprotonated anionic sulfonate groups could influence aggregation state, resulting in increased SO generation.

Figure 2.14 displays the absorption and fluorescence emission spectra for ZnPcTS_4EqCsOH@Gel at a concentration of 100 μM . The Q-band shape for ZnPcTS in this system is indistinguishable from that of ZnPcTS_4EqNaOH@Gel, indicating that the aggregation state of ZnPcTS is not influenced by the presence of the larger Cs^+ cations. The fluorescence emission peak also lies at the same wavelength, indicating that the hydroxide ions have the predominant effect upon aggregation as a result of deprotonation of the phthalocyanine.

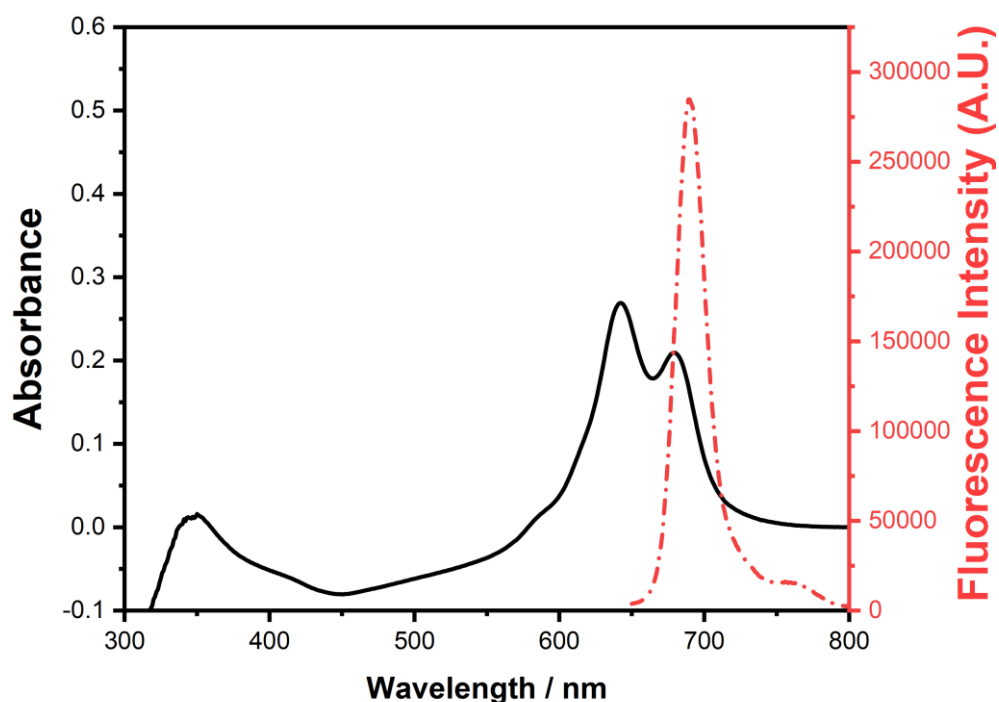


Figure 2.14. UV-Visible absorption (black solid line, $[\text{ZnPcTS}] = 100 \mu\text{M}$) and fluorescence emission (red dotted line, $[\text{ZnPcTS}] = 10 \mu\text{M}$) spectra of $\text{ZnPcTS_4EqCsOH@Gel}$. $\lambda_{\text{exc}} = 625 \text{ nm}$ and $\lambda_{\text{filter}} = 645 \text{ nm}$ for the fluorescence measurement.

The similarities of $\text{ZnPcTS_4EqCsOH@Gel}$ to $\text{ZnPcTS_4EqNaOH@Gel}$ are not solely limited to absorption and fluorescence characteristics. **Figure 2.15** shows the ABMA decay plot for $\text{ZnPcTS_4EqCsOH@Gel}$ compared with that of $\text{ZnPcTS_4EqNaOH@Gel}$. When overlain, the two gels show a remarkably similar rate of SO generation. This provides further evidence that the choice of base cation has no effect upon the aggregation state of ZnPcTS as part of the **1.2Br** gel.

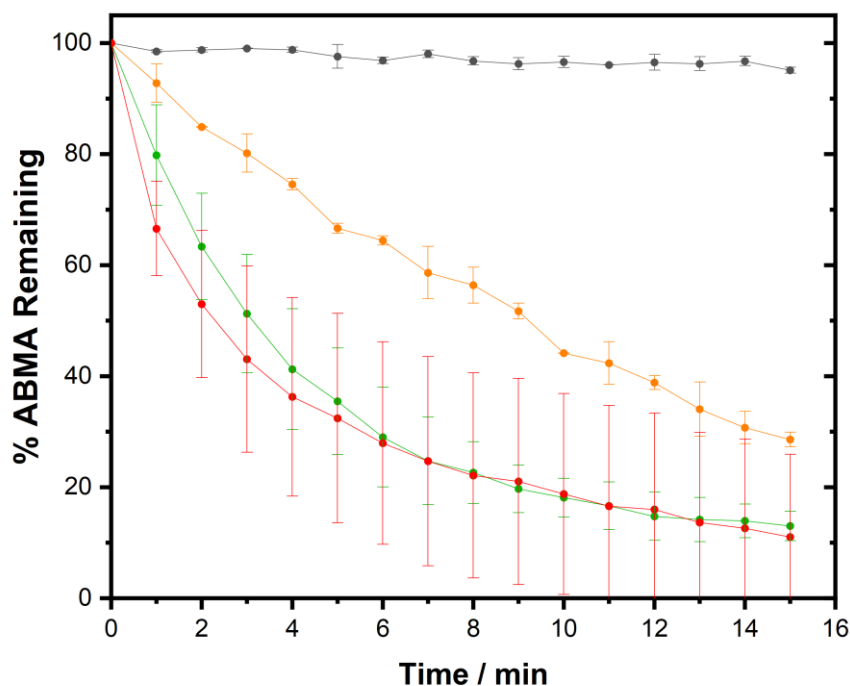


Figure 2.15. ABMA decay plots of *ZnPcTS_4EqCsOH@Gel* (red) as compared with *ZnPcTS_0EqNaOH@Gel* (orange) and *ZnPcTS_4EqNaOH@Gel* (green) and an ABMA control (black). In all gel samples, final $[ZnPcTS] = 2 \mu M$. $\lambda_{irr} = 660 \text{ nm}$, $P_{irr} = 50 \text{ mW}$. $\lambda_{exc} = 380 \text{ nm}$.

The inverse experiment to changing the cation can be carried out by adding a non-basic sodium salt. Given the results relating to CsOH, the addition of NaCl should have a different effect on the photophysical characteristics of **ZnPcTS** when incorporated into the gel compared with that of **ZnPcTS** in the presence of base (CsOH, NaOH). **Fig. 2.16A** shows absorption spectra of *ZnPcTS_4EqNaCl@Gel*, *ZnPcTS_0EqNaOH@Gel*, and *ZnPcTS_4EqNaOH@Gel*, where a typical aggregated phthalocyanine Q-band shape can be seen in each spectrum. As expected, **ZnPcTS** appears more aggregated in the presence of NaCl rather than NaOH owing to less thorough deprotonation with the former. Interestingly, the absorption profile of **ZnPcTS** is changed by the presence of NaCl when compared with *ZnPcTS_0EqNaOH@Gel*. The absorption spectrum of *ZnPcTS_4EqNaCl@Gel* appears to be an intermediate shape between that of 0 equivalents of NaOH and 4 equivalents of NaOH. This suggests that the chloride anions may be influencing aggregation. A possibility is that chloride anions are displacing the bromide counterions (from **1.2Br**) between the cationic layers wherein the **ZnPcTS** resides. This displacement may have an effect upon fibre structure at the microscale resulting in altered aggregation. **Figure 2.16B** shows a comparison of the fluorescence emission spectra of

ZnPcTS_4EqNaCl@Gel with **ZnPcTS_4EqNaOH@Gel**, where a small bathochromic shift can be seen in the former.

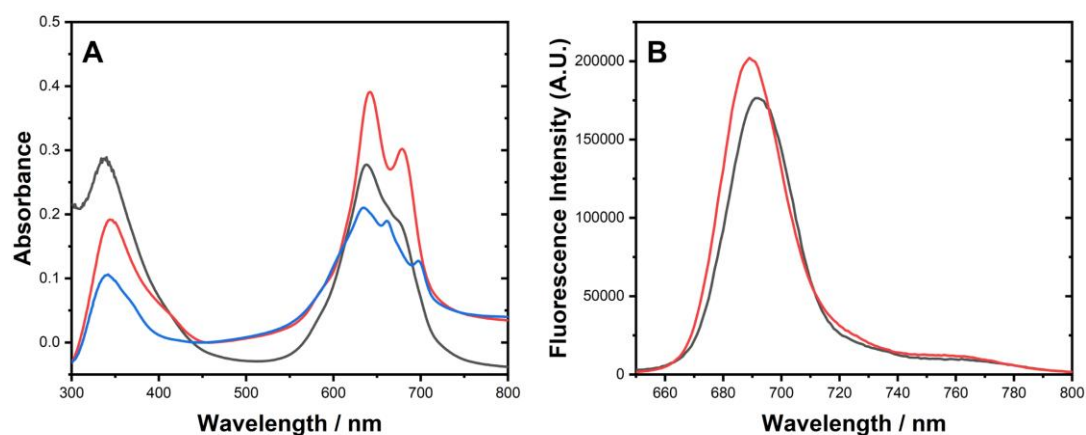


Figure 2.16. (A) Absorption spectra of **ZnPcTS_4EqNaCl** (black), **ZnPcTS_0EqNaOH@Gel** (blue), and **ZnPcTS_4EqNaOH** (red). $[ZnPcTS] = 100 \mu M$ for all three spectra. (B) Fluorescence emission spectra of **ZnPcTS_4EqNaCl@Gel** (black) and **ZnPcTS_4EqNaOH** (red). $[ZnPcTS] = 10 \mu M$ for both fluorescence spectra. $\lambda_{exc} = 625 \text{ nm}$ and $\lambda_{filter} = 645 \text{ nm}$ for these fluorescence measurements.

Figure 2.17 shows ABMA decay plots of **ZnPcTS_4EqNaCl@Gel**, **ZnPcTS_0EqNaOH@Gel**, and **ZnPcTS_4EqNaOH@Gel**. The SO generation rate of **ZnPcTS_4EqNaCl@Gel** lies roughly in between that of **ZnPcTS_0EqNaOH@Gel** and **ZnPcTS_4EqNaOH@Gel**, but closer to **ZnPcTS_0EqNaOH@Gel**. This trend corroborates the finding that the absorption profile of **ZnPcTS_4EqNaCl@Gel** represents an intermediate degree of aggregation between that of **ZnPcTS_0EqNaOH@Gel** and **ZnPcTS_4EqNaOH@Gel**.

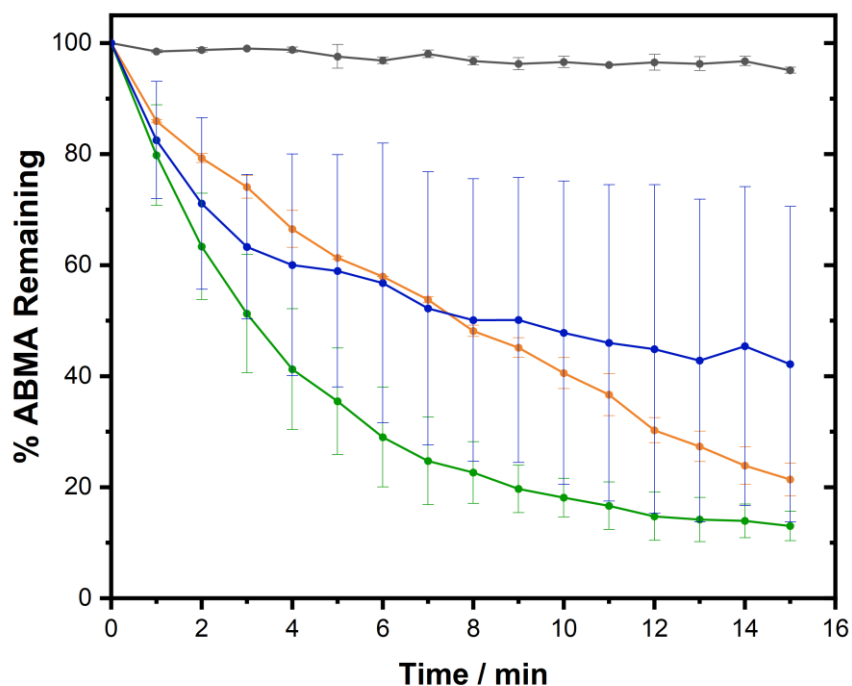


Figure 2.17. *ABMA decay plots of $\text{ZnPcTS}_{4\text{EqNaCl}}@\text{Gel}$ (dark blue) as compared with $\text{ZnPcTS}_{0\text{EqNaOH}}@\text{Gel}$ (orange) and $\text{ZnPcTS}_{4\text{EqNaOH}}@\text{Gel}$ (green) and an ABMA control (black). In all gel samples, final $[\text{ZnPcTS}] = 2 \mu\text{M}$. $\lambda_{\text{irr}} = 660 \text{ nm}$, $P_{\text{irr}} = 50 \text{ mW}$. $\lambda_{\text{exc}} = 380 \text{ nm}$.*

As a general procedure, the addition of gel to the aqueous **ABMA** solutions was done through injecting through a needle and dispersing. This was viewed as the optimal method to ensure that the greatest possible amount of gel surface area was exposed to **ABMA**. The lifetime of SO in solution is very short, so there is little time for the generated SO to diffuse through the solution or indeed out of the gel.³¹ To test this, an experiment was conducted whereby an equal volume (compared with the dispersed solutions) of solid **ZnPcTS@Gel** was formed at the bottom of a cuvette. An **ABMA** solution was then added on top of this gel before the SO measurements were carried out as described before. As the same amount of **ZnPcTS** was present overall, any change in SO generation characteristics must be a result of the solid gel formulation. **Fig. 2.18** displays a visual representation of this setup.

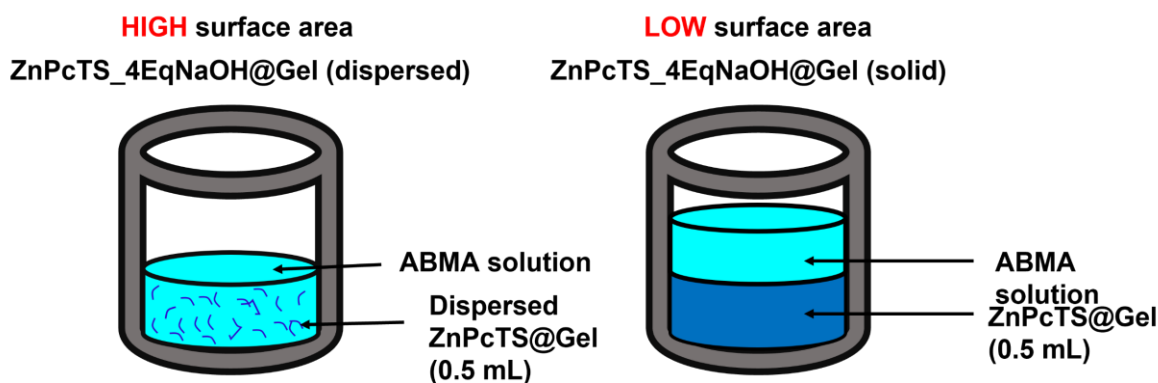


Figure 2.18. Visual representation of the dispersed gel used in the previous measurements (left) and the solid gel configuration (right).

Figure 2.19 displays the **ABMA** decay plots for both **ZnPcTS_4EqNaOH@Gel** dispersed into solution and **ZnPcTS_4EqNaOH@Gel** formed as a solid section of gel at the bottom of the fluorescence cuvette. It is immediately clear that gel dispersal is essential to result in any appreciable amount of **ABMA** decay. Two factors could be influencing this. As mentioned, the dispersed gel has a greater surface area of gel in contact with the **ABMA** in solution, meaning that generated **SO** can react with **ABMA** before decaying more often than with the solid gel. In the solid gel example, it is possible that **SO** is being formed throughout the gel. Given the low lifetimes of singlet oxygen in the liquid phase (in the microsecond to nanosecond scale), only the surface of the gel in contact with the **ABMA** solution has any chance of having its generated **SO** react with the **ABMA** before decaying. However, it could be that the solid gel acts as a block on the laser beam, meaning that the bulk of the gel is not able to generate **SO**. It is likely that both effects combine to yield a poor photosensitizer system. This difference in **SO** generation rate has ramifications for potential applications and *in vitro/in vivo* experiments in aPDT. For the system to work effectively, having a single block of gel in contact with either a bacterial solution or bacteria in general may not result in a significant antibacterial effect. Given our soft material scaffold for the photosensitizer, however, this may not be a terminal problem as the breaking up of the supramolecular system is easily carried out (e.g. rubbing onto a wound). It is unknown why there is an increase in **ABMA** intensity in the case of the solid gel. Though samples were left to equilibrate before measurement, further equilibration may have been required for the solid gel sample. This observed effect still supports the conclusion that negligible **ABMA** decay is seen with this sample.

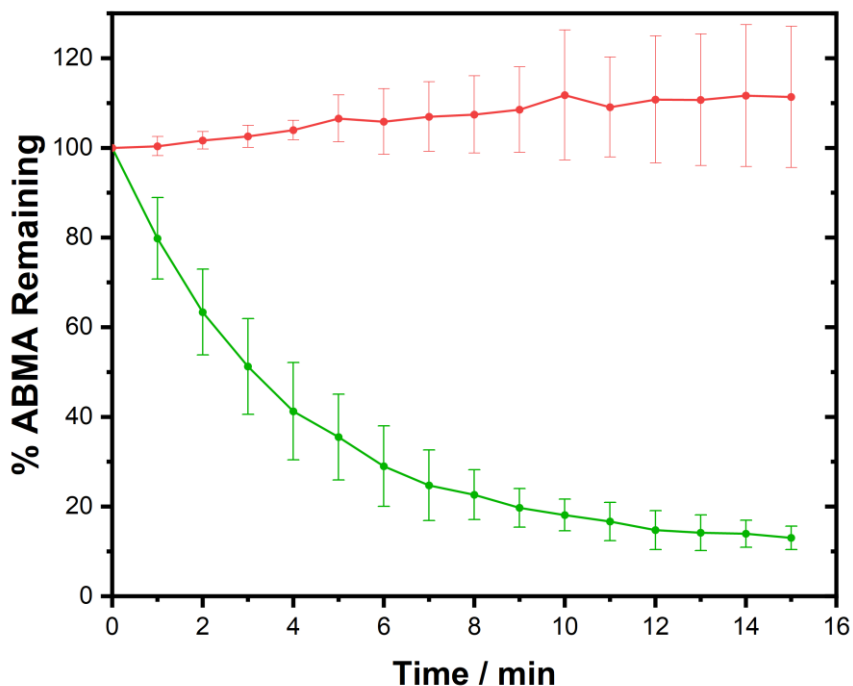
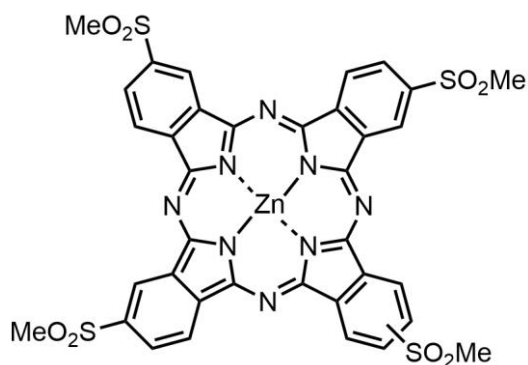


Figure 2.19. ABMA decay plots of *ZnPcTS_4EqNaOH@Gel* (dispersed) (green) and *ZnPcTS_4EqNaOH@Gel* (solid) (red). In all gel samples, final $[ZnPcTS] = 2 \mu\text{M}$. $\lambda_{irr} = 660 \text{ nm}$, $P_{irr} = 50 \text{ mW}$. $\lambda_{exc} = 380 \text{ nm}$.

2.4. Zinc(II) tetrakis(methylsulfonyl)phthalocyanine

ZnPcSO₂Me is a water-insoluble phthalocyanine that has been synthesized by Dumoulin *et al.* for use in aPDT.³² Being structurally similar to **ZnPcTS**, it can be used to investigate how slightly altering the peripheral units might affect photophysical properties.



ZnPcSO₂Me

ZnPcSO₂Me can be prepared through the heating of sulfanatomethyl phthalonitrile with a zinc salt in DMF. The phthalocyanine's absorption characteristics in DMSO at a concentration of

10 μM are typical of a non-aggregated phthalocyanine, with a Q-band consisting of an intense peak at ~ 680 nm and a shoulder at ~ 620 nm. Its fluorescence emission is slightly red shifted with respect to the unsubstituted zinc(II) phthalocyanine (ZnPc). **ZnPcSO₂Me** has been shown to display highly effective antibacterial behaviour when irradiated with 600 – 700 nm red light, with a greater effect on gram-positive *staphylococcus aureus* than on gram-negative *E-coli*.

2.4.1. ZnPcSO₂Me solution characterisation

Given the hydrophobic nature of **ZnPcSO₂Me**, photophysical characterisation in neat aqueous solution was not possible as a consequence of the phthalocyanine's insolubility in such a solvent. A solvent system of 1:1 water-ethanol (as seen within the gel), shows that the phthalocyanine is heavily aggregated as seen in **Fig. 2.20**. The main peak in the Q-band lies at 635 nm, indicating the presence of dimers and higher order aggregates. In addition to this, the poor baselines of the spectra, caused by Rayleigh scattering (where light interacts with particles or molecules that are much smaller than the wavelength of the incident light), indicate that full dissolution is not achieved in this solvent system.

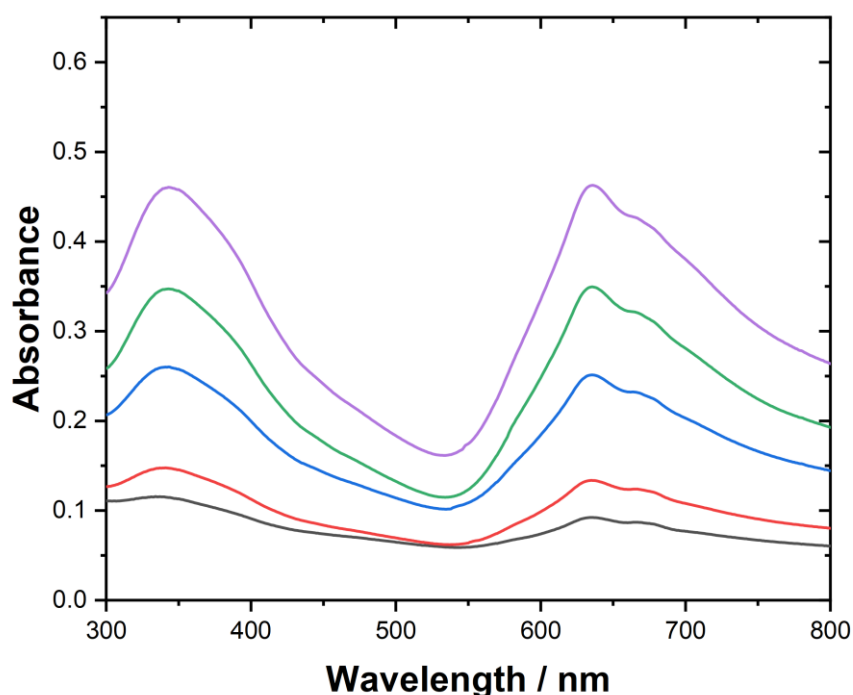


Figure 2.20. UV-Visible absorption spectrum of **ZnPcSO₂Me** in 1:1 water-ethanol at a concentration of 10 μM (black), 20 μM (red), 40 μM (blue), 60 μM (green), 80 μM (lilac).

Upon altering the water-ethanol ratio to 5:95, the absorption profile changes in a manner that suggests aggregation is reduced. **Figure 2.21** suggests also that full **ZnPcSO₂Me** is not achieved at this ethanol content, with significant Rayleigh scattering resulting in a poor baseline.

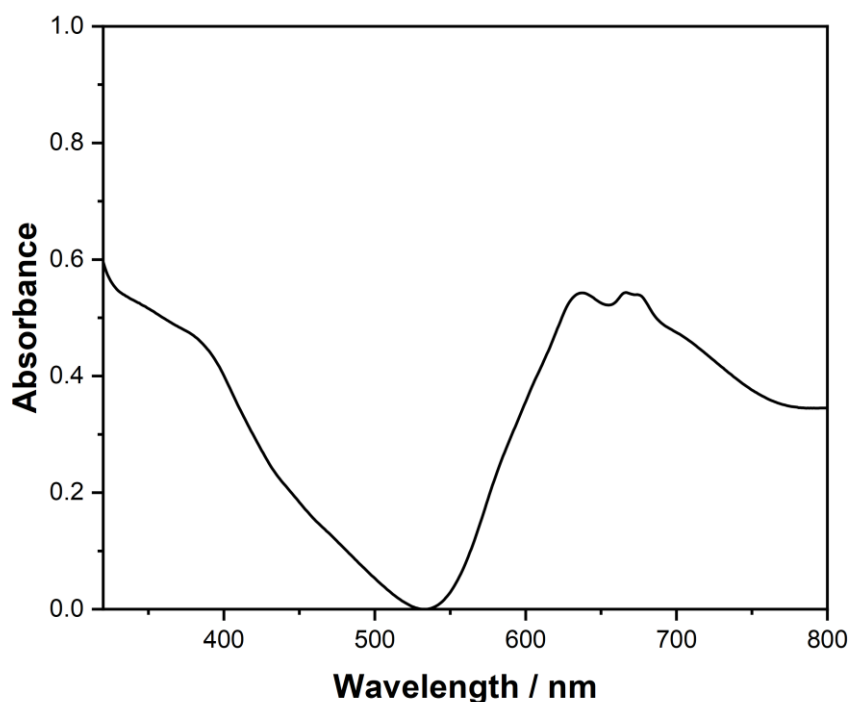


Figure 2.21. UV-Visible absorption spectrum of **ZnPcSO₂Me** in 5:95 water-ethanol at a concentration of 80 μ M.

The fluorescence emission (**Fig. 2.22**) of **ZnPcSO₂Me** in both 1:1 and 5:95 water-ethanol displays a typical phthalocyanine emission spectrum with an emission maximum present at \sim 681 nm and 679 nm for the former and latter respectively when excited at 630 nm.

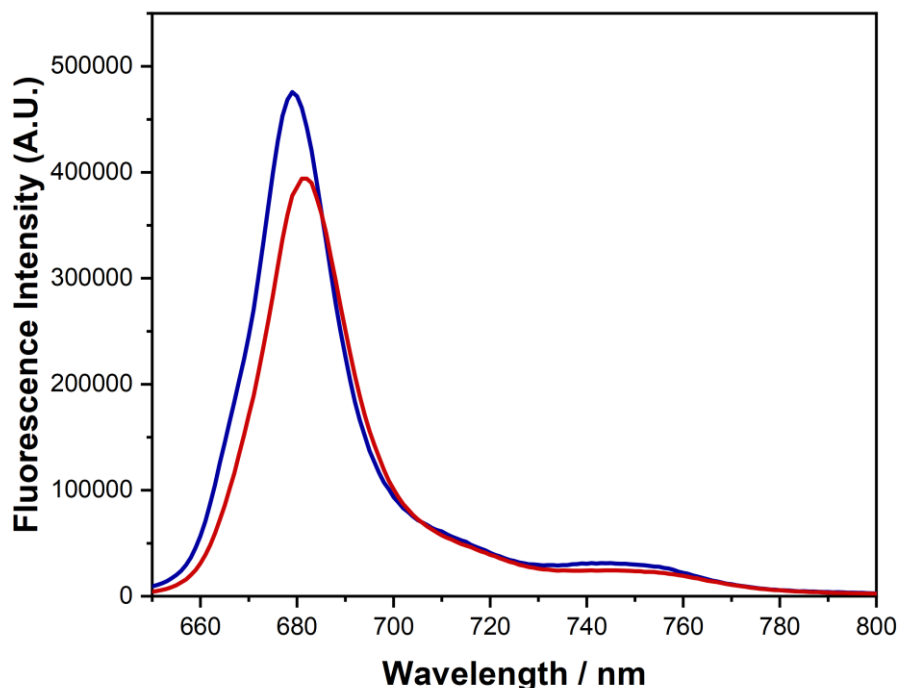


Figure 2.22. Fluorescence emission of **ZnPcSO₂Me** in 1:1 water-ethanol (red) and 5:95 water-ethanol (blue) with $[\text{ZnPcSO}_2\text{Me}] = 80 \mu\text{M}$ for both measurements. $\lambda_{\text{exc}} = 625 \text{ nm}$ and $\lambda_{\text{filter}} = 645 \text{ nm}$ for both fluorescence measurements.

2.4.2. **ZnPcSO₂Me** gel preparation and characterisation

A significant difference relating to gel experiments involving **ZnPcSO₂Me** was that the phthalocyanine had to be part of the ethanolic phase along with the **1.2Br** gelator prior to gel formation. Other than this, there were no differences in macroscopic gel formation or gelation time. Absorption spectroscopy of **ZnPcSO₂Me@Gel** is shown in **Fig. 2.23** and contrasts strongly **ZnPcSO₂Me** in the aqueous solution phase. The aggregation of **ZnPcSO₂Me** seen in 1:1 water-ethanol solution appears to be severely curtailed when incorporated into a 1:1 water-ethanol **1.2Br** gel. This reduction of aggregation somewhat matches that seen in the case of **ZnPcTS**.

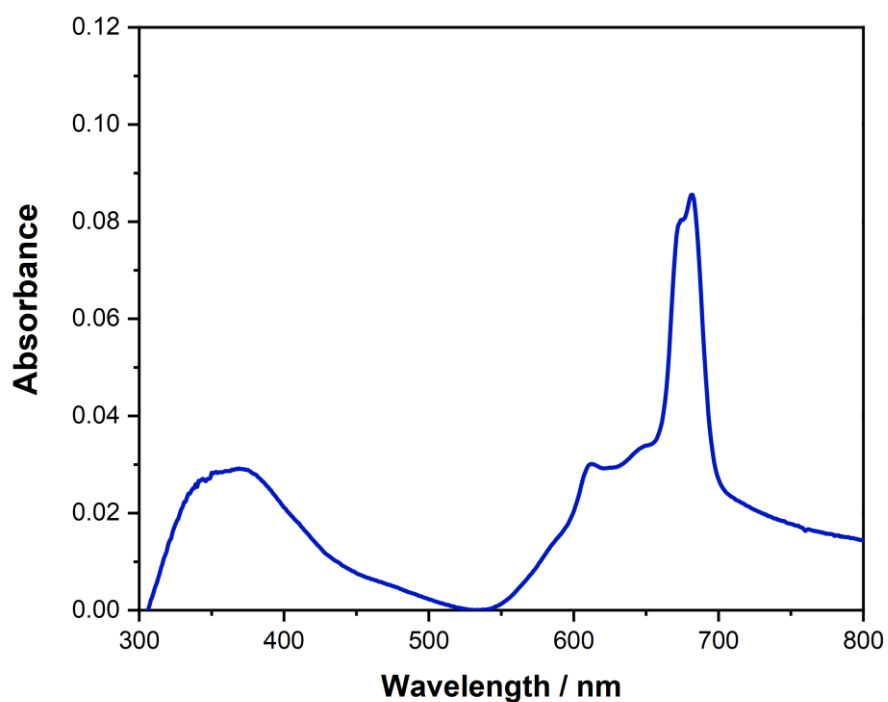


Figure 2.23. UV-Visible absorption spectrum of **ZnPcSO₂Me@Gel** with $[\text{ZnPcSO}_2\text{Me}] = 100 \mu\text{M}$, $[\text{1.2Br}] = 12 \text{ mM}$, 1:1 water-ethanol.

The position of the fluorescence emission of **ZnPcSO₂Me** is largely unchanged within the gel when compared with the phthalocyanine in 1:1 water-ethanol (**Fig. 2.24**). The emission peak is slightly hypsochromically shifted by $\sim 3 \text{ nm}$.

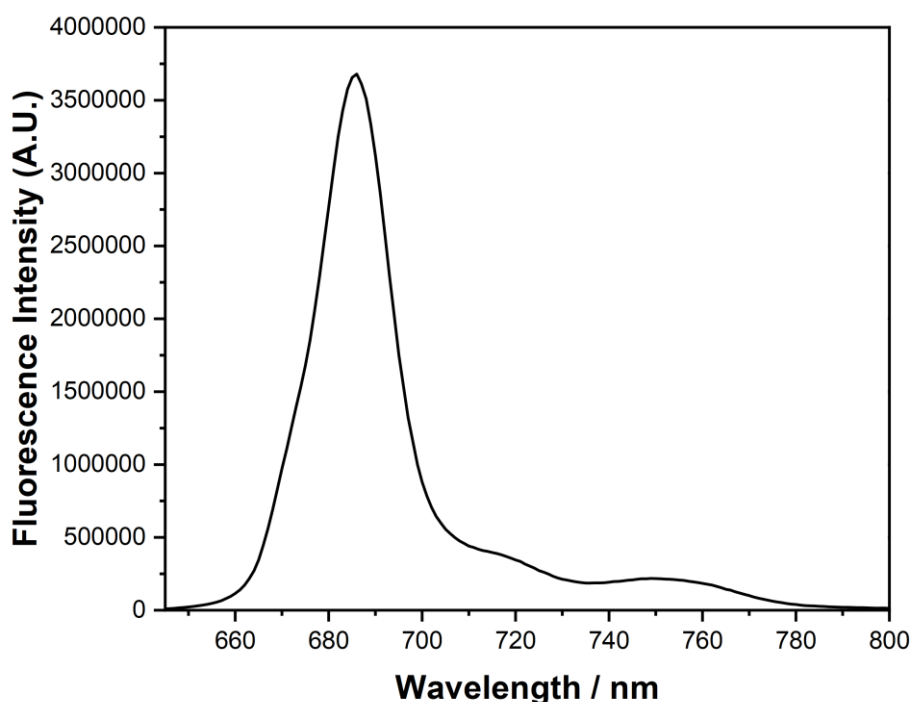


Figure 2.24. Fluorescence emission of **ZnPcSO₂Me@Gel** with $[\text{ZnPcSO}_2\text{Me}] = 100 \mu\text{M}$. $\lambda_{\text{exc}} = 625 \text{ nm}$ and $\lambda_{\text{filter}} = 645 \text{ nm}$ for this fluorescence measurement.

2.4.3. **ZnPcSO₂Me** singlet oxygen generation

For the following SO measurements, a different irradiation source was used. This new laser possessed a power of 5 mW and emission wavelength of 635 nm. This is $\sim 10\text{x}$ weaker than the laser used in the previous study with **ZnPcTS**, meaning results are not immediately comparable. In addition, the time taken to observe significant **ABMA** degradation was considerably longer. Here, **ABMA** fluorescence measurements were taken every fifteen minutes for a total of 2 hours in order to see substantial **ABMA** decay.

Firstly, solution phase studies on the SO generation of **ZnPcSO₂Me** were carried out. **Figure 2.25** displays **ABMA** decay plots of **ZnPcSO₂Me** in 1:1 water-ethanol (blue) and in 5:95 water-ethanol (green). **ZnPcSO₂Me** in 5:95 water-ethanol does not exhibit considerably greater SO generation than **ZnPcSO₂Me** in 1:1 water-ethanol, meaning the lesser amount of aggregation in the latter does not translate into increased SO generation at least on the timescales explored in this study.

As seen in the photophysical studies, **ZnPcSO₂Me** is much less aggregated when incorporated into the **1.2Br** gel compared to when solvated in 1:1 water-ethanol. This claim is further

corroborated by SO generation measurements of **ZnPcSO₂Me@Gel**, where the rate of SO generation is enhanced significantly (Fig. 2.25). **ZnPcSO₂Me@Gel** also displayed a greater amount of SO generation than **ZnPcTS_0EqNaOH@Gel** in similar conditions. This disparity can be explained by the much greater non-aggregation of **ZnPcSO₂Me** within the gel when compared to that of **ZnPcTS** in the same conditions.

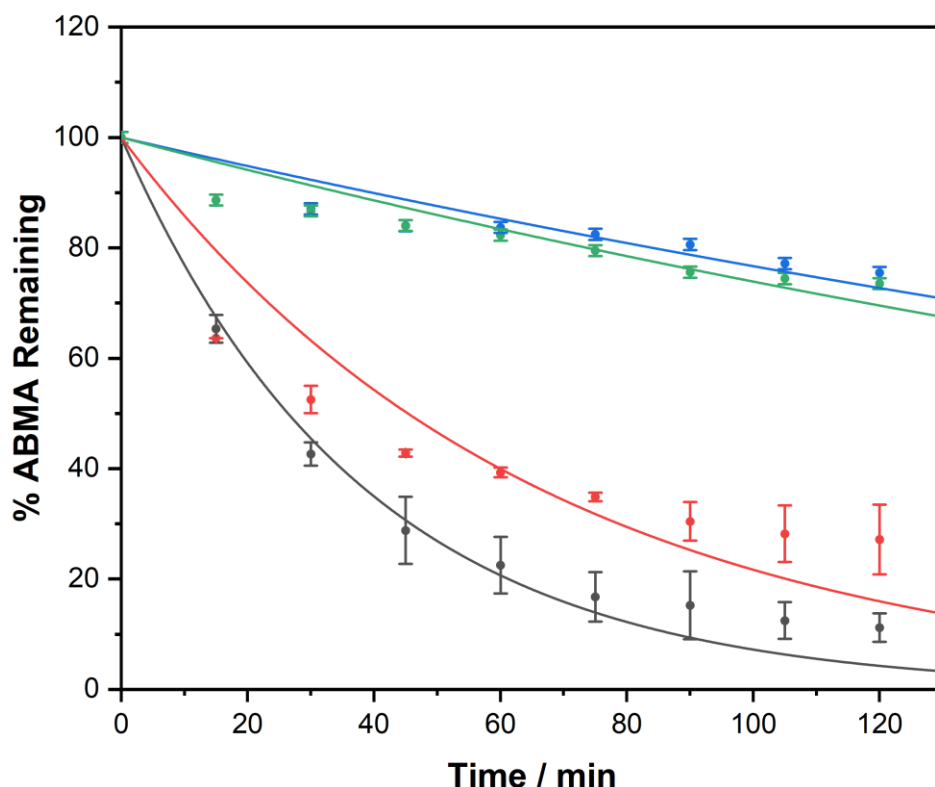


Figure 2.25. ABMA decay plots of **ZnPcSO₂Me** in 1:1 water-ethanol (blue), **ZnPcSO₂Me** in 5:95 water-ethanol (green), **ZnPcSO₂Me@Gel** (black), and **ZnPcTS_0EqNaOH@Gel** (red). In all solutions and gels, final $[\text{ZnPcSO}_2\text{Me}] = 2 \mu\text{M}$. $\lambda_{\text{irr}} = 635 \text{ nm}$, $P_{\text{irr}} = 5 \text{ mW}$. $\lambda_{\text{exc}} = 380 \text{ nm}$.

2.5. Conclusion

In summary, aggregation of **ZnPcTS** in aqueous solution has been shown to considerably quench SO generation. In a mixed water-ethanol solvent system, the water-soluble phthalocyanine predominantly exists in its unaggregated form. The creation of a water-ethanol microenvironment within an excess of water through dispersion of a water-ethanol **1.2Br** gel has allowed the photosensitizer to retain its non-aggregated form and subsequently possess the ability to generate a significantly increased amount of SO compared with the same phthalocyanine in aqueous solution. The presence of base has also been shown to affect

ZnPcTS aggregation both in aqueous solution and as part of the gel by limiting aggregation. Also, a similar enhancement in the rate of SO generation was seen with a hydrophobic zinc phthalocyanine **ZnPcSO₂Me**. Incorporation of **ZnPcSO₂Me** into the **1.2Br** gel resulted in significant disaggregation with respect to **ZnPcSO₂Me** in solution, as seen with absorption spectroscopy. This lowered aggregation manifested itself as considerably enhanced SO generation. **ZnPcSO₂Me** displayed a higher rate of SO generation in **1.2Br** when compared with **ZnPcTS** in the same gel system. This disparity is also a consequence of the reduced aggregation of the former. This study demonstrates the effectiveness of supramolecular encapsulation in soft materials for realising the potential of photosensitizers that are highly susceptible to aggregation in aqueous environments.

2.6. Experimental

Imidazole ($\geq 99\%$), 1-bromooctane (99%), 1,3-bis(bromomethyl) benzene (97%), 1,3-bis(chloromethyl) benzene $\geq 98.0\%$ was purchased from Sigma Aldrich. Zinc phthalocyanine tetrasulfonic acid (**ZnPcTS**) was purchased from PorphyChem. Zinc tetrasulfonatomethyl phthalocyanine (**ZnPcSO₂Me**) was provided by Acıbadem Mehmet Ali Aydınlar Üniversitesi (collaboration). The other commonly used reagents purchased from a range of different suppliers and used without any further purification. Preparation of the dicationic amphiphile gelator (**1.2Br**) was carried out through an established synthetic procedure.²⁹ Chromatography purifications were performed using Sigma-Aldrich Silica Gel (pore size 60Å, particle size 40 – 63 μm) and thin-layer chromatography (TLC) was carried out on E. Merck silica gel plates irradiated using 365 nm UV light. NMR spectra were acquired on a Bruker AV400 spectrometer and NMR spectra were recorded at room temperature. All chemical shifts are reported in δ parts per million (ppm), using the solvent residual signal as an internal standard and the coupling constant values (J) are reported in Hertz (Hz). The following abbreviations are used for signal multiplicities: s, singlet; d, doublet; t, triplet; m, multiplet; and b, broad.

2.6.1. General procedures

Unless explicitly stated otherwise, gels were prepared at a 1:1 water-ethanol ratio with a final gelator concentration of 12 mM. A total of five aqueous **ZnPcTS** 2.4 mM stock solutions (containing 0, 1, 2, 3, 4 equivalents of NaOH relative to the concentration of **ZnPcTS**) were prepared to achieve the desired concentration in the gel. Similar stock solutions were made for **ZnPcTS** containing 4 equivalents of CsOH or NaCl. For the **1.2Br** gels, an equal volume of 24 mM gelator solution in absolute ethanol was added to the diluted **ZnPcTS** solution in MilliQ

water (including NaOH where noted) *via* micropipette and mixed vigorously and rapidly. This preparation led to robust gels which were stable over the timescale of months at room temperature (approximately 18-25 °C). For experiments involving **ZnPcSO₂Me**, the phthalocyanine stock solution had to be made up in an ethanolic solution and mixed with the ethanolic **1.2Br** solution prior to gel formation.

The rheological assessment of gel samples was performed in a HAAKE RheoStress 1 rheometer (Thermo Scientific) according to a literature procedure.³⁰ Briefly, a sensor with 60 mm diameter (PP60) was used with a 3 mm gap between plates and the characterisation was performed at 36 ± 1 °C. For the oscillatory amplitude sweep test, the amplitude of deformation (shear stress) was varied (0-100 Pa) while the frequency was kept constant at 1 Hz; while for the frequency sweep test, the shear frequency was varied (10.00 – 0.01 Hz) and the amplitude of the shear stress was set at 0.50 Pa. Rheological analysis for this Chapter was carried out by D. Limón at Universitat de Barcelona. UV-Visible absorption spectroscopy measurements were taken with quartz cuvettes of path length 10 mm or 1 mm in a Cary UV-Visible NIR Spectrometer. Absorption measurements of gel samples containing **ZnPcTS** had to contain the photosensitizer at a higher concentration than samples used in the SO studies to be able to see through the heavy scattering brought about by the gel. Fluorescence emission of gel (1 mm cuvette) and solutions (10 mm cuvette) was characterized using a FLS 980 spectrometer (Edinburgh Instruments) equipped with a front face sample holder. For gel fluorescence measurements, the use of long pass filters and front face geometry allow to remove the effect of scattering (the beam hits the cuvette surface and enters the detector). Fourier-transform infrared spectroscopy (FT-IR) was carried out on a Bruker Tensor 27 instrument equipped with a Pike GladiATR attachment with a diamond crystal and was performed in dried gel samples. SEM images were acquired with a JEOL 7100F FEG-SEM system on samples cast on aluminium stubs, dried under vacuum and coated with a 5-nm-thick layer of iridium. Image acquisition was performed using a working distance of 6 mm and 10 kV accelerating voltage.

SO generation rate of **ZnPcTS** photosensitizer systems were measured by monitoring the fluorescence decrease of **ABMA** in water with the presence of **ZnPcTS** and **ZnPcTS_nEqBase@Gels** upon irradiation with a 50 mW 660 nm laser. The sample in a 10 mm quartz cuvette was irradiated for 1 minute intervals using the diode laser. The **ABMA** fluorescence was characterized using a FLS 980 spectrometer. Quantitative **ABMA** decay analysis was done by comparing the fluorescence intensity $I(\mathbf{ABMA})_t$ with the initial **ABMA**

concentration $I(\text{ABMA})_{t_0}$ according to **Equation 2.1**. For each sample, two experiments were carried out and the mean calculated, and range plotted as y-axis error bars.

$$\text{Eq(2.1).} \quad \% \text{ ABMA Decay } (t) = \frac{I(\text{ABMA})_{t_0}}{I(\text{ABMA})_t}$$

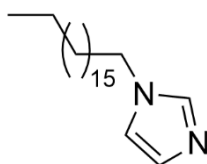
In a typical SO experiment, a 0.5 mL sample of gel containing the **ZnPcTS** at a concentration of 10 μM was prepared in a syringe which, upon gelation, was dispersed into to 2 mL of a 146 μM **ABMA** solution to yield a suspension with final working concentrations of 2 μM (**ZnPcTS**), 117 μM (**ABMA**) and a final ethanol content of 10% in 2.5 mL sample volume. Two SO generation experiments were carried out and the average emission decay of **ABMA** plotted as a function of irradiation time. All **ABMA** decay plots were fit to pseudo first order kinetics (**Equation 2.2**) to determine rate constants.

$$\text{Eq(2.2).} \quad [A] = [A]_0 * e^{-kt}$$

In the SO measurements of the neutral **ZnPcSO₂Me**, a 5 mW 635 nm laser was used. In a typical SO experiment, a 0.5 mL sample of gel containing the **ZnPcSO₂Me** at a concentration of 10 μM was prepared in a syringe which, upon gelation, was dispersed into to 2 mL of a 146 μM **ABMA** solution to yield a suspension with final working concentrations of 2 μM (**ZnPcSO₂Me**), 117 μM (**ABMA**) and a final ethanol content of 10% in 2.5 mL sample volume. The sample in a 10 mm quartz cuvette was irradiated for 15 minute intervals using the diode laser. Two SO generation experiments were carried out and the average emission decay of **ABMA** plotted as a function of irradiation time.

2.6.2. Synthetic procedures

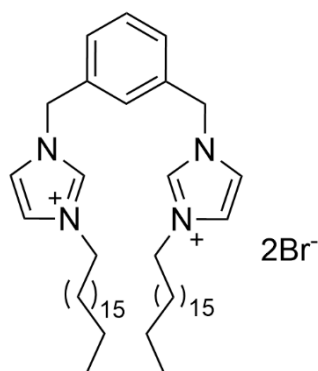
1-Octadecyl-1*H*-imidazole



Acetonitrile (60 mL) and KOH (2.52 g, 44.9 mmol) were added to a flask and stirred until full dissolution of KOH. To this flask, imidazole (2.72 g, 40 mmol) was added and stirred at room temperature for 2 h. To a separate flask was added 1-bromooctadecane (13.30 g, 39.9 mmol) along with acetonitrile (40 mL). This separate flask was then stirred at 50 °C for 15 min. After

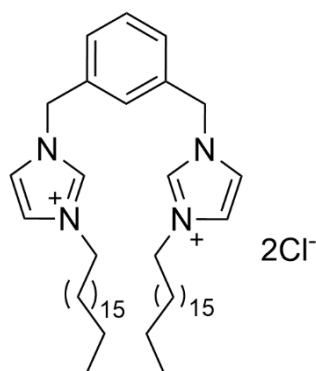
this time, the separate flask containing 1-bromooctadecane in acetonitrile was added to the flask containing imidazole. This combined mixture was stirred at room temperature for 24 h. Solvent removed *in vacuo* to yield a crude off-white solid. Solid was dissolved in DCM and filtered. Subsequent filtrate was concentrated *in vacuo* to yield a waxy off-white solid which was then purified on silica gel (9% MeOH in DCM) to yield a waxy white solid (10.22 g, 80%). ¹H NMR (400 MHz, CDCl₃) δ/ppm 7.57 (s, 1H, Im-H (2)), 7.08 (t, *J* = 1.2 Hz, 1H, Im-H(5)), 6.92 (t, *J* = 1.2 Hz, 1H, Im-H(4)), 3.95 (t, *J* = 7.2 Hz, 2H, N-CH₂), 1.78 (m, 2H, N-CH₂-CH₂), 1.46 – 1.09 (m, 32H, (CH₂)₁₅), 0.89 (t, *J* = 7.2 Hz, 3H, CH₃). ¹³C NMR (101 MHz, CDCl₃) δ/ppm 136.9 (Im-C(2)), 128.9 (Im-C(5)), 118.8 (Im-C(4)), 47.2 (N-CH₂), 31.9 (N-CH₂-CH₂), 31.1-22.7 ((CH₂)₁₅), 14.1 (CH₃). IR ν max ATR/cm⁻¹: 2916 (S, Asym. Aliph. C-H stretch), 2849 (S, Sym. Aliph. C-H stretch), 1508 (M, Aliph. C-H scissor), 1462 (M, Aliph. C-H bend).

1,3-Bis[(3-octadecyl-1-imidazolium)methyl]benzene di-bromide (**1.2Br**)



1-Octadecyl-1*H*-imidazole (2.26 g, 7.05 mmol) was added to acetonitrile (60 mL) and stirred at room temperature for 10 min. The compound 1,3-bis(bromomethyl) benzene (0.93 g, 3.52 mmol) was then added and mixture gently stirred at 80 °C for 19 h. Solvent was removed *in vacuo* and resulting off-white powder was dissolved in DCM and precipitated with diethyl ether to yield a white solid (2.52 g, 79 %) characterized as **1.2Br**. ¹H NMR (400 MHz, CDCl₃) δ/ppm 10.39 (s, 2H, Im-H(2)), 8.11 (t, 2H, Im-H(5)), 8.07 (s, 1H, Ar-H(2)), 7.58 (dd, *J* = 7.7 Hz, *J* = 1.7 Hz, 2H, Ar-H(4,6)), 7.24 (d, 2H, Im-H(4)), 7.20 (t, *J* = 7.7 Hz, 1H, Ar-H(5)), 5.63 (s, 4H, CH₂), 4.28 (t, *J* = 7.5 Hz, 4H, N-CH₂), 1.90 (p, *J* = 7.5 Hz, 4H, N-CH₂-CH₂), 1.33-1.24 (m, 60H, (CH₂)₁₅), 0.89 (t, 6H, CH₃). ¹³C NMR (101 MHz, CDCl₃) δ/ppm 136.8 (Im-C(2)), 134.6 (Ar-C(1,3)), 130.4 (Ar-C(2)), 129.9 (Ar-C(4, 5, 6)), 123.5 (Im-C(5)), 121.7 (Im-C(4)), 52.5 (CH₂), 50.3 (N-CH₂), 31.9- 22.7 ((CH₂)₁₅), 14.1 (CH₃). IR ν max ATR/cm⁻¹: 2916 (S, Asym. Aliph. C-H stretch), 2849 (S, Sym. Aliph. C-H stretch), 1562 (M, Aliph. C-H scissor), 1469 (M, Aliph. C-H bend).

1,3-Bis[(3-octadecyl-1-imidazolio)methyl]benzene di-chloride (1.2Cl)



1-Octadecyl-1*H*-imidazole (3.22 g, 10.0 mmol) added to acetonitrile (70 mL) and stirred at room temperature for 10 min. The compound 1,3-bis(chloromethyl) benzene (0.88 g, 5.00 mmol) was then added and mixture gently stirred at 80 °C for 18 h. Solvent removed *in vacuo* and the resulting off-white powder was dissolved in DCM and precipitated with diethyl ether to yield a white solid (3.23 g, 80 %) characterized as **1.2Cl**. ¹H NMR (400 MHz, CDCl₃) δ/ppm 10.52 (s, 2H, Im-H(2)), 8.09 (t, 2H, Im-H(5)), 8.05 (s, 1H, Ar-H(2)), 7.54 (dd, *J* = 7.7 Hz, *J* = 1.7 Hz, 2H, Ar-H(4,6)), 7.24 (d, 2H, Im-H(4)), 7.21 (t, *J* = 7.7 Hz, 1H, Ar-H(5)), 5.61 (s, 4H, CH₂), 4.27 (t, *J* = 7.5 Hz, 4H, N-CH₂), 1.90 (p, *J* = 7.5 Hz, 4H, N-CH₂-CH₂), 1.35-1.21 (m, 60H, (CH₂)₁₅), 0.89 (t, *J* = 4.0 Hz, 6H, CH₃). ¹³C NMR (101 MHz, CDCl₃) δ/ppm 137.2 (Im-C(2)), 134.7 (Ar-C(1,3)), 130.5 (Ar-C(2)), 129.9 (Ar-C(4, 5, 6)), 123.4 (Im-C(5)), 121.5 (Im-C(4)), 52.7 (CH₂), 50.3 (N-CH₂), 31.9-22.7 ((CH₂)₁₅), 14.1 (CH₃). IR ν max ATR/cm⁻¹: 2918 (S, Asym. Aliph. C-H stretch), 2849 (S, Sym. Aliph. C-H stretch), 1562 (M, Aliph. C-H scissor), 1470 (M, Aliph. C-H bend).

2.7. References

1. F. Dumoulin, M. Durmuş, V. Ahsen and T. Nyokong, *Coord. Chem. Rev.*, 2010, 254, 2792 – 2847.
2. D. B. Berezin, V. V. Makarov, S. A. Znoyko, V. E. Mayzlish, A. V. Kustov, *Mendeleev Commun.*, 2020, 30, 621 – 623.
3. H. Isago, H. Fujita, *J. Porp. Phthalocyanines*, 2018, 22, 1 – 10.
4. K. Palewska, J. Sworakowski, J. Lipiński, *Opt. Mater.*, 2012, 34, 1717 – 1724.
5. J. R. Kanofsky, *J. Photochem. Photobiol.*, 2010, 87, 14 – 17.
6. O. Mollins-Molina, R. Brescolí-Obach, G. Garcia-Lainez, I. Andreu, S. Nonell, M. A. Miranda, M. C. Jiménez, *J. Phys. Org. Chem.*, 2017, 30, e3722.
7. D. Beri, M. Jakoby, D. Busko, B. S. Richards, A. Turshatov, *Front. Chem.*, 2020, 8, 567.

8. R. S. Bodannes, P. C. Chan, *FEBS Lett.*, 1979, 105, 195 – 196.
9. M. Schaefer, R. Hardeland, *J. Pineal Res.*, 2009, 46, 40 – 52.
10. B. Sharma, A. Jain, L. Pérez-García, J. A. Watts, F. J. Rawson, G. R. Chaudhary, G. Kaur, *J. Mat. Chem. B*, 2022, 10, 2160 – 2170.
11. N. A. Kuznetsova, N. S. Gretsova, O. A. Yuzhakova, V. M. Negrimovskii, O. L. Kaliya, E. A. Lukyanets, *Russ. J. Gen. Chem.*, 2001, 71, 36 – 41.
12. I. S. Mfouo-Tynga, L. D. Dias, N. M. Inada, C. Kurachi, *Photodiagnosis Photodyn. Ther.*, 2021, 34, 102091.
13. C. R. Fontana, D. S. dos Santos Jr, J. M. Bosco, D. M. Spolidorio, R. A. C. Marcantonio, *Drug Deliv.*, 2008, 15, 417 – 422.
14. H. Chen, H. Zhang, J. Wang, X. Zhu, *J. Mater. Res.*, 2023, DOI: 10.1557/s43578-023-01256-7.
15. M. Samperi, L. Pérez-García, D. B. Amabilino, *Chem. Sci.*, 2019, 10, 10256 – 10266.
16. M. Rodrigues, A. C. Calpena, D. B. Amabilino, M. L. Garduño-Ramírez, L. Pérez-García, *J. Mat. Chem. B*, 2014, 2, 5419 – 5429.
17. M. Samperi, D. Limón, D. B. Amabilino, L. Pérez-García, *Cell Rep.*, 2020, 1, 100030.
18. J. Griffiths, J. Cruse-Sawyer, S. R. Wood, J. Schofield, S. B. Brown, B. Dixon, *J. Photochem. Photobiol. B*, 1994, 24, 195 – 199.
19. N. A. Kuznetsova, N. S. Gretsova, V. M. Derkacheva, O. L. Kaliya, E. A. Lukyanets, *J. Porp. Phthalocyanines*, 2003, 7, 147 – 154.
20. K. Bernauer, S. Fallab, *Helv. Chim. Acta*, 1961, 44, 1287 – 1292.
21. H. Dong, H. Du, S. R. Wickramasinghe, X. Qian, *J. Phys. Chem. B*, 2009, 113, 14094 – 14101.
22. J. P. Guthrie, *Can. J. Chem.*, 1977, 56, 2342 – 2354.
23. L. Howe, J. Z. Zhang, *J. Phys. Chem. A*, 1997, 101, 3207 – 3213.
24. X. Li, X. He, A. C. H. Ng, C. Wu, D. K. P. Ng, *Macromolecules*, 2000, 33, 2119 – 2123.
25. T. Wolff, *Ber. Bunsenges. Phys. Chem.*, 1982, 86, 1132 – 1134.
26. M. Samperi, B. Bdiri, C. D. Sleet, R. Markus, A. R. Mallia, L. Pérez-García, D. B. Amabilino, *Nat. Chem.*, 2021, 13, 1200 – 1206.
27. S. M. Smith, T. F. Abelha, D. Limón, M. Samperi, B. Sharma, K. Plaetzer, F. Dumoulin, D. B. Amabilino, L. Pérez-García, *J. Porp. Phthalocyanines*, 2023, 27, 434 – 443.
28. N. Kobayashi, K. Nakai, *Chem. Comm.*, 2007, 4077 – 4092.
29. H. Isago, in *Optical Spectra of Phthalocyanines and Related Compounds*, ed. 1, Springer Tokyo, pp 41 – 106.

30. R. D. Shannon, *Acta Cryst.*, 1976, 32, 751 – 767.
31. P. B. Merkel, D. R. Kearns, *J. Am. Chem. Soc.*, 1972, 94, 1029 – 1030.
32. Ü. İsci, M. Beyreis, N. Tortik, S. Z. Topal, M. Glueck, V. Ahsen, F. Dumoulin, T. Kiesslich, K. Plaetzer, *Photodiagnosis Photodyn. Ther.*, 2016, 13, 40 – 47.

Chapter 3

**Investigation into confined molecular
diffusion of fluorophores along gel fibres**

3.1. Background

Total internal reflection fluorescence (TIRF) microscopy is a type of fluorescence microscopy developed in the early years of the 1980's.^{1,2} TIRF microscopy is widely used in bioimaging as a result of its intrinsically high signal-to-noise ratio along with its ability to excite a relatively thin section of a given sample. TIRF microscopy differs from conventional epifluorescence microscopy techniques, where excitation light is shone straight through a sample. In epifluorescence mode, excitation of the entirety of the sample often leads to a low signal-to-noise ratio as fluorescence emission arises from each point in the sample which can dramatically lower contrast.³ TIRF relies on total internal reflection, an optical phenomenon that occurs when light propagating in a material with refractive index (RI) of n_1 hits a material with a different RI (n_2) at or above the critical angle (θ_c) (Eq. 3.1) as governed by Snell's Law.

$$\text{Equation 3.1} \quad \theta_c = \arcsin\left(\frac{n_2}{n_1}\right)$$

Within a TIRF microscope, incident excitation light is passed through immersion oil and onto a cover slip. Upon total internal reflection, an evanescent wave propagates perpendicular to the coverslip and into the sample. As the evanescent wave is exponentially decaying, the wave only penetrates into a thin subsection of the sample before completely dissipating. This type of excitation results in surface selectivity for fluorophores close to the interface between sample and coverslip as shown in **Fig. 3.1**. The penetration depth of the evanescent wave (usually between 35 – 300 nm) is dependent on the wavelength of light, respective RI's of the immersion oil and coverslip, and the angle at which the excitation light is incident upon the coverslip. The penetration depth (d) for light of wavelength λ_{exc} incident upon a coverslip with RI n_2 at an angle θ can be calculated mathematically by use of Eq. 3.2.⁴

$$\text{Equation 3.2} \quad d = \frac{\lambda_{exc}}{4\pi n_2 \sqrt{\sin^2(\theta) - \sin^2(\theta_c)}}$$

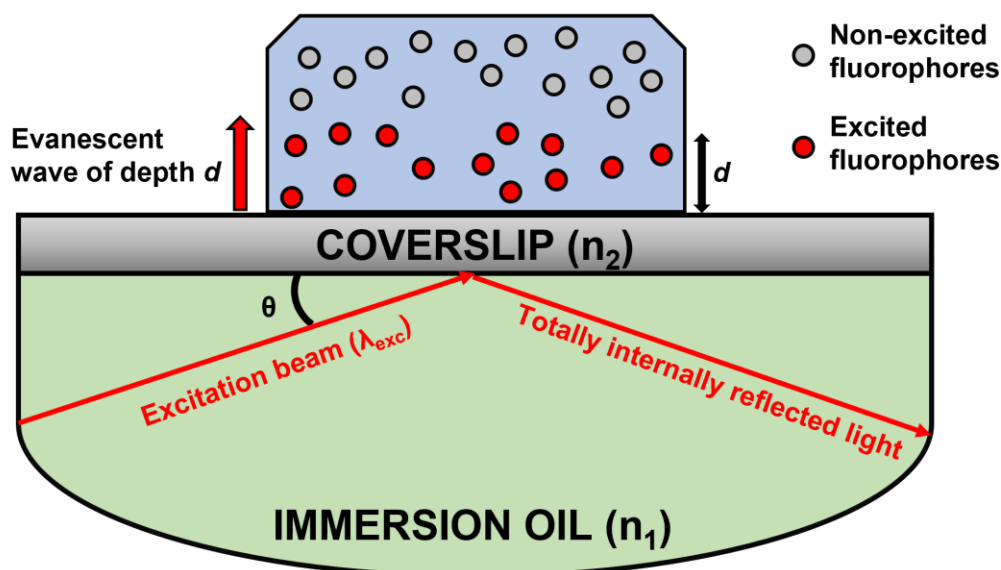


Figure 3.1. Diagram of a typical TIRF microscope set-up. Excitation light of wavelength λ_{exc} is directed at angle θ (where $\theta > \theta_c$) to the coverslip and undergoes total internal reflection. An evanescent wave propagates perpendicular to the normal to a penetration depth of length d . Fluorophores localized within distance d to the coverslip undergo fluorescence emission whilst those above distance d remain in the ground state.

In addition to bioimaging, where TIRF finds its predominant usage, TIRF microscopy has been employed to characterize supramolecular fibrous systems. A supramolecular structure was developed by Magana *et al.* where cationic cyanine derivatives, fluorescent in their monomer form, form polyaminated fibres which act as supramolecular scaffolds for silicic acid condensation when undergoing self-assembly in water.⁵ In this polyaminated form, the fluorescence of the cyanine dyes is quenched, though silicic acid condensation leads to partial recovery of the cyanine fluorescence. TIRF microscopy assisted in monitoring this condensation through the gradual increase in fluorescence intensity over time to reveal a range of fibrous structures. A further example of TIRF-aided characterisation of fibrous systems was in a polycaprolactone-coated polysulfone/poly(ether sulfone) material developed by Xue *et al.*⁶ When fluorescent oxygen-sensitive porphyrinoid derivatives were incorporated into the nanofibres of such a system (formed through electrospinning), imaging of these composite fibres was carried out. The modulation of fluorescence brought about by changing of oxygen content in the system was seen in individual fibres under TIRF conditions.

TIRF microscopy has also been used to measure microscale and nanoscale diffusion of fluorescent compounds.⁷⁻¹⁰ Diffusion refers to the net movement over a period of time often through a concentration gradient. Specifically, the movement of ions is essential in energy generation and storage, chemical signalling, and information processing. In biological systems,

the preeminent case of ionic diffusion concerns the movement of cations and anions through ion channels, which govern cell signalling, dictate action potential, and are therefore critical for a vast number of biological functions.¹¹⁻¹³ In synthetic systems, the harnessing of ionic diffusion has been undertaken to advance photovoltaic and energy storage devices.¹⁴⁻¹⁷ The development of synthetic materials that provide channels through which anions can permeate has been notable in the improvement of microbial fuel cells, with novel anion exchange membrane configurations enabling high power densities.^{18,19} Ionic conductivity is also important in polymer hydrogels that are used in a number of materials.²⁰ The complete understanding of different types of ion diffusion in these and other systems is still being understood from a fundamental level.²¹ In natural and synthetic systems, diffusion can be investigated by mean-square displacement analysis and consequently can lead to classifications of diffusion as directed, random (Brownian), or confined.^{22,23} This chapter describes results that may help to comprehend some of these processes at the molecular level by providing an essentially one-dimensional path for diffusion.

In this chapter, a supramolecular system is described where zinc(II) phthalocyanine tetrasulfonic acid (**ZnPcTS**), a fluorescent compound containing four peripheral sulfonic acid groups diffuses along a pathway formed by the bis-imidazolium gelator compound 1,3-bis[(3-octadecyl-1-imidazolium)methyl]benzene di-bromide (**1.2Br**), which forms fibres that encapsulate the fluorophore. The motion of the anionic phthalocyanine was monitored by TIRF microscopy at both ensemble and single molecule level. A **ZnPcTS** concentration of 10 μM within the gel made possible the clear imaging of fibre morphology whilst still allowing observation of molecular diffusion. Using a lower **ZnPcTS** concentration of 0.1 μM allowed for the monitoring of individual phthalocyanines shuttling along gel fibres. Furthermore, tracking analysis was used to quantify movement in terms of average velocity and diffusion coefficients. Modulation of excitation laser intensity was performed to investigate the relationship between irradiance and average fluorophore speed. Further modulation of movement behaviour was induced by the presence of two acids within the gel: camphorsulfonic acid (**CSA**) and 4-toluenesulfonic acid (**PTSA**). This chemical modulation influenced both the movement characteristics and encapsulation of the phthalocyanine fluorophores.

3.2. Zinc(II) phthalocyanine tetrasulfonic acid (ZnPcTS)

As discussed in chapter 2, zinc(II) phthalocyanine tetrasulfonic acid is a water-soluble fluorophore. In this work it has been discovered that, in aqueous solution, aggregation of this

fluorophore leads to quenched fluorescence. Incorporation into a **1.2Br** gel to an extent limits this aggregation resulting in greater fluorescence emission, presumably by blocking dimer formation within the dimensions of the fibres. The sulfonic acid groups present at the peripheral positions of **ZnPcTS** render the compound soluble in aqueous media because of ionisation. The ionisation provides the driving force for **ZnPcTS** to be encapsulated within the cationic gel fibres (**Fig. 3.2**).

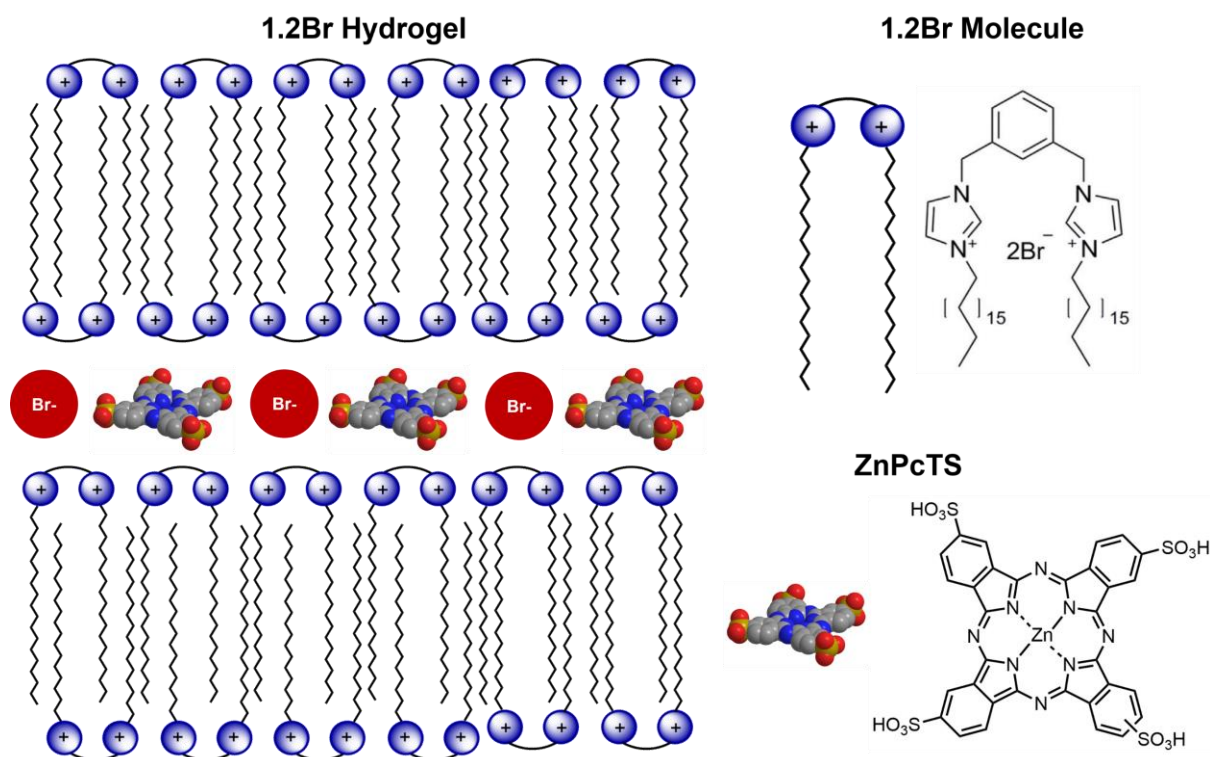


Figure 3.2. Representation of **1.2Br** gelator scaffold and the position of the fluorophore **ZnPcTS**. **ZnPcTS** is electrostatically confined between cationic imidazolium heads. Note: Bromide charges are illustrative and therefore do not match the cationic charge.

To understand the nature of the anionic **ZnPcTS** when incorporated into the cationic gel fibres, the newly formed material was characterized spectroscopically. Infrared spectroscopy of the **ZnPcTS@Gel** xerogels indicates that **ZnPcTS** exists in its deprotonated form in the gel fibres (**Fig. 3.3**). This situation might be expected, given the low pK_a of **ZnPcTS** (-2 approximately). The presence of ethanol within the gel has been shown to lower the pK_a of functional groups including sulfonic acids.²⁴ Scanning electron microscopy (SEM) (**Fig. 3.4**) and atomic force microscopy (AFM) (**Fig. 3.5**) show a gel morphology that is fibrillar, and similar in general features to the pure gelator and other composite gels of this type.²⁵⁻²⁷

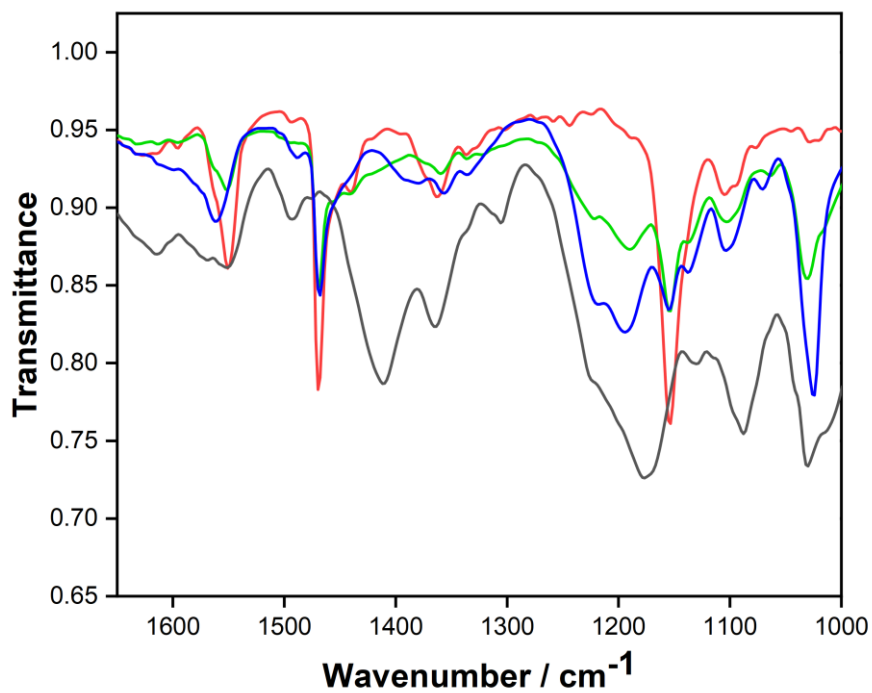


Figure 3.3. Magnified infrared spectra of **ZnPcTS** and **ZnPcTS@Gel** xerogels. Solid state **ZnPcTS** (black). Pristine **1.2Br** xerogel (red), $[1.2Br] = 12 \text{ mM}$, 1:1 water ethanol. **ZnPcTS@Gel** xerogel containing 4 equivalents of NaOH (blue), $[1.2Br] = 12 \text{ mM}$, 1:1 water ethanol, $[ZnPcTS] = 100 \text{ }\mu\text{M}$, $[NaOH] = 400 \text{ }\mu\text{M}$. **ZnPcTS@Gel** xerogel (green), $[1.2Br] = 12 \text{ mM}$, 1:1 water ethanol, $[ZnPcTS] = 100 \text{ }\mu\text{M}$. All concentrations are the final concentrations within each dried gel.

ZnPcTS@Gel

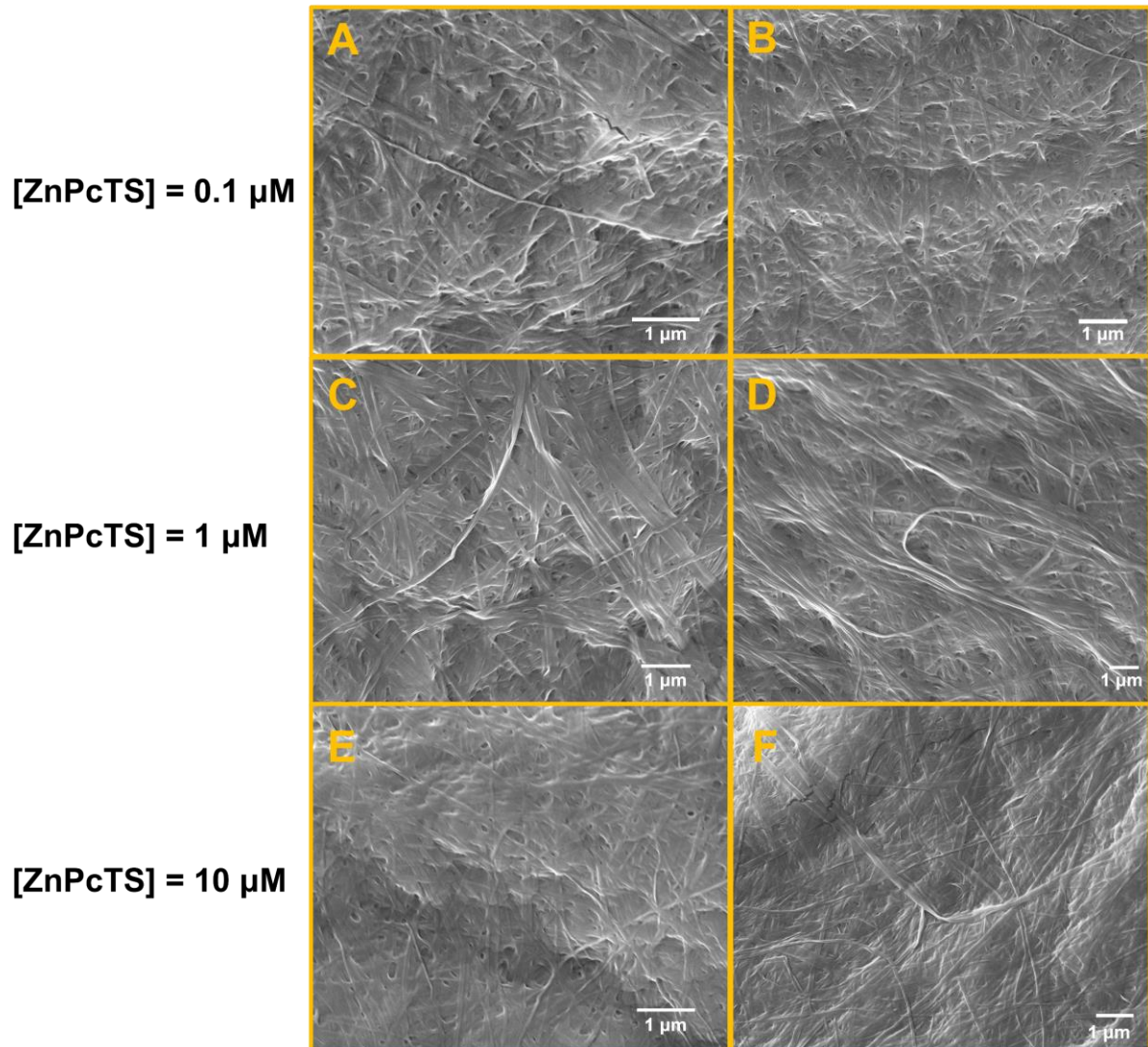


Figure 3.4. SEM images of **ZnPcTS@Gel** xerogels containing different **ZnPcTS** concentrations. (A-B) $[ZnPcTS] = 0.1 \mu M$. (C-D) $[ZnPcTS] = 1 \mu M$. (E-F) $[ZnPcTS] = 10 \mu M$.

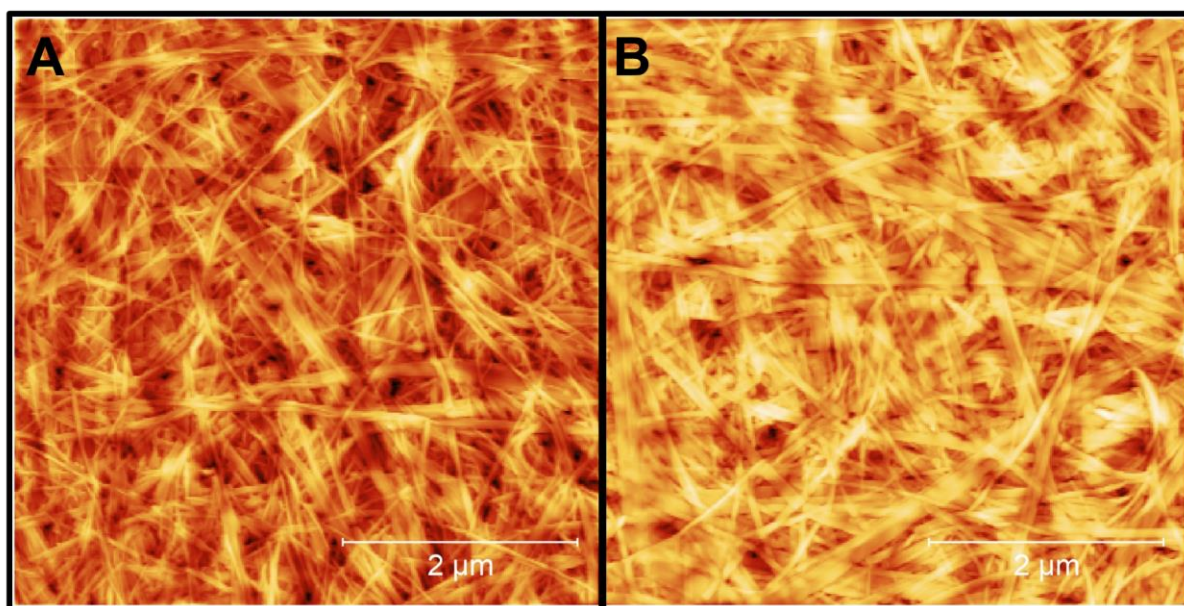


Figure 3.5. AFM images of **ZnPcTS@Gel** xerogels containing different **ZnPcTS** concentrations. (A) $[\text{ZnPcTS}] = 0.1 \mu\text{M}$. (B) $[\text{ZnPcTS}] = 10 \mu\text{M}$.

Given the phthalocyanine in the gel is fluorescent (**Fig. 3.6**), the system can be imaged using TIRF microscopy. TIRF can locate the approximate positions of fluorophores within the structure under investigation, and in real time.²⁸ Therefore, while SEM/AFM image the surface of dry samples here, TIRF allows dynamic measurement of the gel in its solvated form, typically within 150 nm of the base of the sample at its interface with the glass slide.^{26,29}

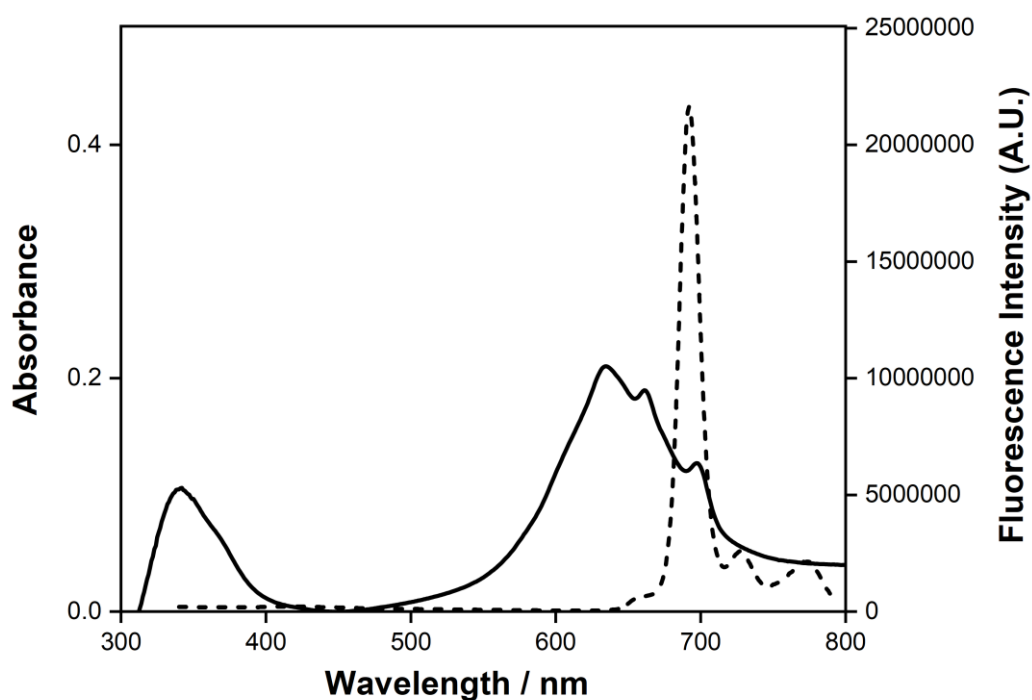


Figure 3.6. Absorption (solid line) and emission (dotted line) spectra of **ZnPcTS@Gel**, $[ZnPcTS] = 100 \mu M$, $[1.2Br] = 12 mM$, 1:1 water ethanol.

3.2.1. High-loading morphology and dynamics

TIRF samples were prepared directly in a 10-well compartmentalisation block, which allowed for the formation of the gel in situ and to perform the imaging directly without any further sample manipulation. To capture images, a laser wavelength of 642 nm was used to excite the Q-band of **ZnPcTS** within the hydrated gel. Emission beyond 650 nm was observed using a low pass (LP) filter. At a **ZnPcTS** concentration of 10 μM (**Fig. 3.7**), gel fibres can be identified in both individual frames and the average projection. This average projection indicates that **ZnPcTS** is wholly confined to the gel fibres, negligibly in interstices, and that most gel fibres appear relatively straight with little bending. The most noteworthy feature of this system is the observation of movement of the fluorophore travellers along gel fibres, seen as flickering of the linear features. The phthalocyanine displayed consistent fluorescence intensity with minimal photobleaching over the course of the experiments, even at 100% laser power. This precluded the use of stochastic optical reconstruction microscopy (STORM), though movement of fluorophores allowed for the imaging of morphology by use of maximum and average projections as described above. Previously, a tetracarboxylate porphyrin was incorporated in the fibres, no dynamics were observed under similar conditions.^{26,29} The

movement observed in the present case is attributed to motion of the fluorophore within the fibres that is possible because of the relatively weak electrostatic interactions between the sulfonate groups of **ZnPcTS** with the cationic gelator (sulfonates are readily displaced by carboxylates in these systems), although these interactions still ensure that the phthalocyanine is retained in the fibres.³⁰

10 μM **ZnPcTS@Gel**

Frame from video

Average Image

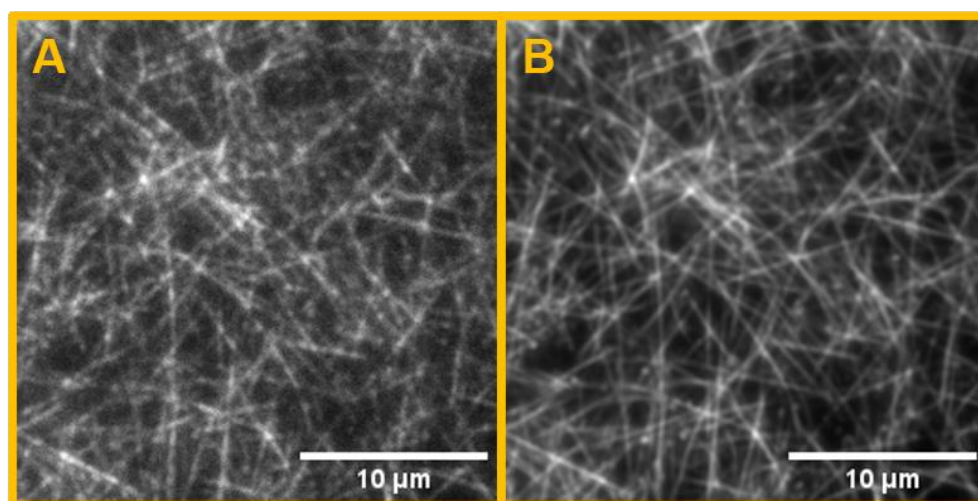


Figure 3.7. Single-frame and average projection of 10 μM **ZnPcTS@Gel**. (A) A single frame from the raw video captured at a **ZnPcTS** concentration of 10 μM . (B) Average projection of a full video over 600 frames. Imaging details: laser 642 nm, emission filter LP 650 nm.

Lowering the **ZnPcTS** concentration to 1 μM has a significant effect on the TIRF appearance of the gels and movement of fluorophores (**Fig. 3.8**). In isolation, the fluorophores appear to move randomly throughout the region analysed over the course of the video and it is not possible to readily identify the presence of gel fibres as easily as in the sample with a greater concentration of **ZnPcTS**. However, the average projections from the videos reveal acicular objects and thereby confirms that the fluorophores are indeed confined to the gel fibres in the same manner as in the 10 μM **ZnPcTS** sample.

1 μM ZnPcTS@Gel

Frame from video Average Image

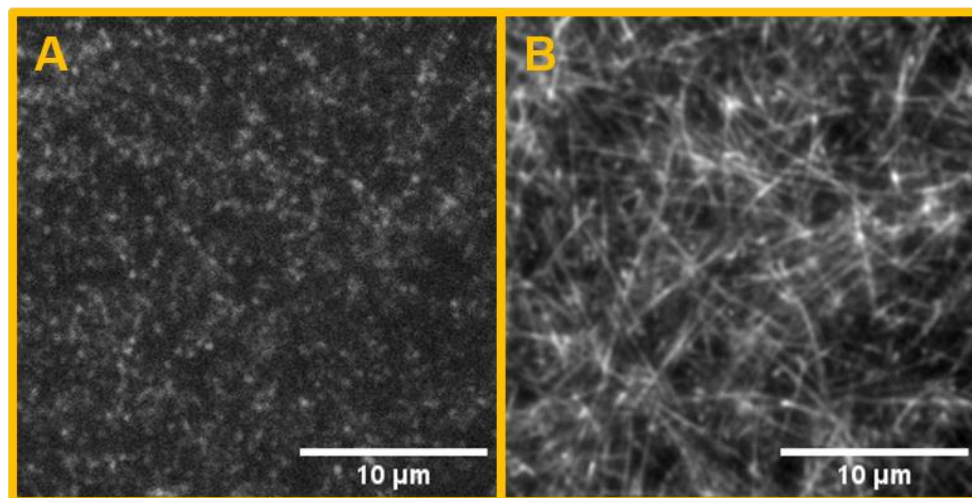


Figure 3.8. Single-frame and average projection of 1 μM ZnPcTS@Gel. (A) A single frame from the raw video captured at a ZnPcTS concentration of 1 μM . (B) Average projection of a full video over 600 frames. Imaging details: laser 642 nm, emission filter LP 650 nm.

Whilst gel morphology is largely homogenous across the samples analysed at a 10 μM ZnPcTS concentration, there exist areas (mostly towards the edge of the sample wells) that exhibit a reduced density of gel fibres. In these areas, labelled as ‘low-density’ areas, gel fibres tend to twist to a greater extent, which contrasts with the ‘high-density’ areas where gel fibres are typically straight. Fluorophore movement is also seen through the fibres in the low-density areas. A phenomenon not observed in the high-density area of fibres is the apparent movement of the fibres themselves. This movement is characterised as the swaying of the fibre parallel to its position. This side-to-side movement results in the fibres appearing wider in the average and maximum projections. More significant movement is observed more rarely with whole fibres repositioning themselves over the course of several frames (Fig. 3.9).

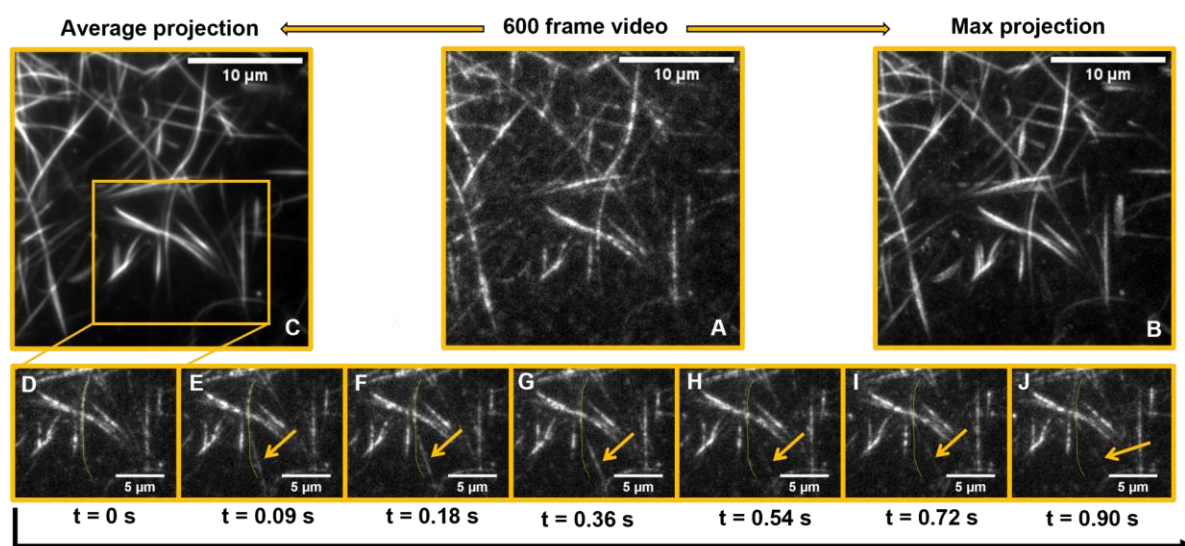


Figure 3.9. Single-frame, average projection, and max projection of low-density area of $10\ \mu\text{M}$ **ZnPcTS@Gel** along with representation of fibre movement. (A) A single frame from a raw video captured at a **ZnPcTS** concentration of $10\ \mu\text{M}$ which is intended to represent the 600-frame video. (B) Maximum projection of the 600-frame video. (C) Average projection of the 600-frame video. (D-J) Images show displacement of fibre from its original position as a function of time. The yellow line is drawn as a reference to the starting position of the fibre. In less than a second, the fibre moves slightly (tracked by arrow) to the right before its lower section moves out of the focal plane in a movement resembling a whipping motion. Imaging details: laser 642 nm, emission filter LP 650, Laser Power 100%.

3.2.2. Low loading fluorophore dynamics

Lowering further the **ZnPcTS** concentration to $0.1\ \mu\text{M}$ results in an average image gel morphology when extending the duration of the acquired videos albeit not to the same level of detail as the $1\ \mu\text{M}$ or $10\ \mu\text{M}$ **ZnPcTS** gels (Fig. 3.10). Clearly, the decreased number of **ZnPcTS** fluorophores in the $0.1\ \mu\text{M}$ sample cannot travel through enough of the fibre structure to reveal its true morphology. SEM confirmed, however, that the external xerogel morphology is very similar between gels containing $10\ \mu\text{M}$, $1\ \mu\text{M}$ and $0.1\ \mu\text{M}$ **ZnPcTS** (Fig. 3.4). Powder X-ray diffraction (PXRD) analysis of xerogels containing fluorophore concentrations $10\ \mu\text{M}$ and $0.1\ \mu\text{M}$ also show an indistinguishable gel structure (Fig. 3.11).

0.1 μM ZnPcTS@Gel

Frame from video

Average Image

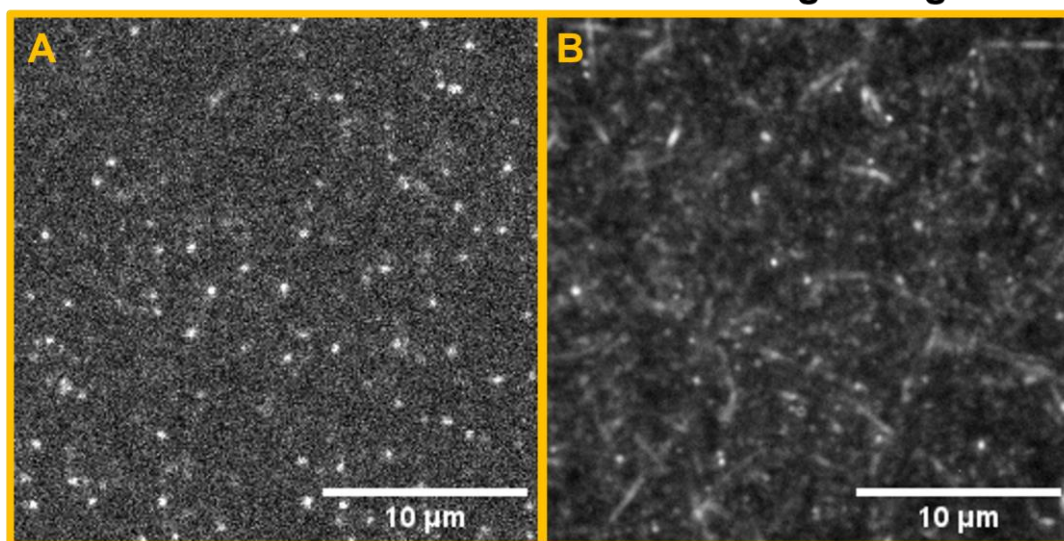


Figure 3.10. TIRF micrographs of a ZnPcTS@Gel sample containing a ZnPcTS concentration of 0.1 μM . (A) TIRF micrograph of a single frame (of 600) where individual fluorophores can be clearly observed though fibre morphology not easily discerned. (B) TIRF micrograph of the average projection over the 600 frames referenced in A shows very little detail of the gel morphology. All images taken with 642 nm laser and LP filter at 650 nm. Laser power 100%.

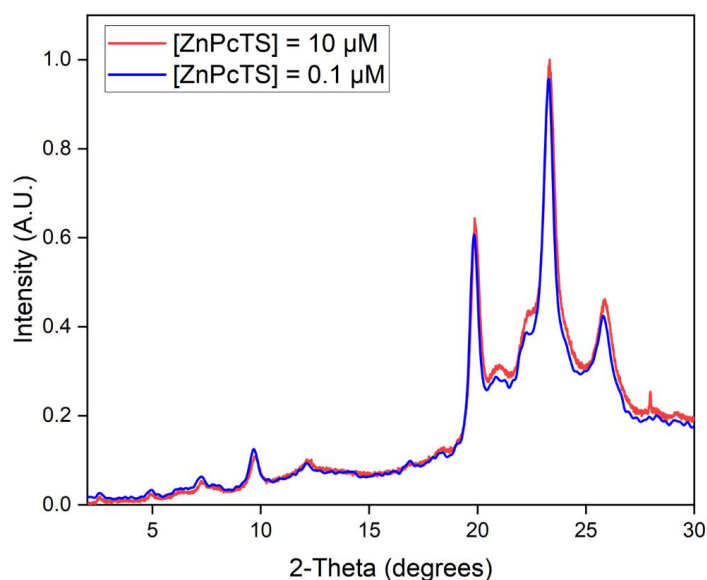


Figure 3.11. Powder X-ray diffractograms of ZnPcTS@Gel xerogels containing a fluorophore loading of 10 μM (red line) and 0.1 μM (blue line).

To obtain the optimal view of fibre morphology at a concentration of $0.1 \mu\text{M}$ **ZnPcTS**, extended videos (3000 frames) were acquired. **Figure 3.12(A-C)** show the gradual building up of the TIRF image (average projection) of a $0.1 \mu\text{M}$ **ZnPcTS** gel over the course of 3000 frames. This gradual building up of the image over time suggests that the fluorophores are confined to small sections of any individual fibre, and that they tend not to move between fibres at least on the timescale of these experiments (54 s). This observation could be indicative of fluorophores being located between the lamellae that form the fibres rather than on the fibre surface. In the latter case, fluorophore movement between fibres would be expected by desorption and re-adsorption. Also, importantly, there is no net movement of the fluorophores away from the region where they are encapsulated and the movement is robust, meaning it continues apparently the same throughout the measurements, unlike our previous work concerning a carboxylated fluorophore.²⁹ This observation is further evidence of the non-disruptive electrostatic interaction between the sulfonate and imidazolium groups in these composite gels.

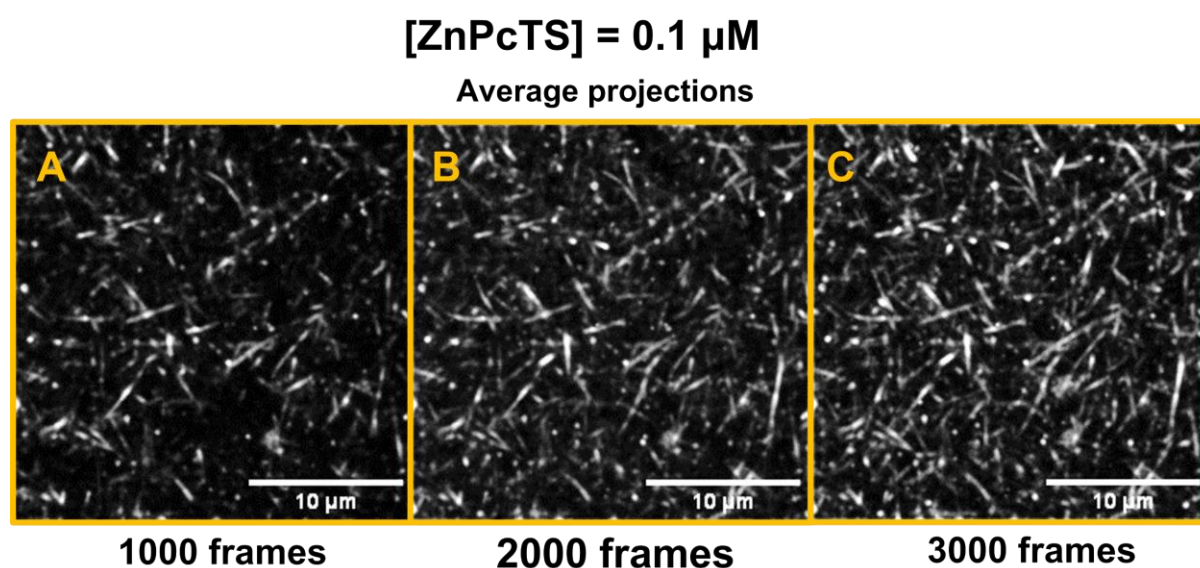


Figure 3.12. (A-C) Average projections of gel containing $0.1 \mu\text{M}$ **ZnPcTS** show morphology being ‘built up’ by fluorophore diffusion along fibres. All images taken with 642 nm laser and LP filter at 650 nm. Laser power 100%.

Fluorophore dynamics can be characterized by tracking the z-axis intensity as a function of time for a given region of interest (ROI) along a gel fibre shown in **Fig. 3.13A**. **Figure 3.13(B-C)** display these z-profile plots where clear maxima can be seen which correspond to a fluorophore residing in the given ROI. In frames where the z-axis intensity is considerably higher than the background, it can be assumed that a fluorophore is residing in

the ROI and that the ROI is therefore in an ‘on state’. Conversely, a ROI being in the ‘off state’ for a specific frame means that z-axis intensity is close to background levels and a fluorophore is not residing in the ROI. On/off plots are useful tools for analysing the movement characteristics of fluorophores in this system. The principle of microscopic reversibility is exemplified in some on/off plots, in that fluorophores do not travel in any particular direction, other than being confined to the one-dimensional scaffold of the gel fibre. This non-preference for directional movement (beyond the constrained path provided by the scaffold) leads to instances where a fluorophore remains within a ROI for an extended period of time (**Fig. 3.14**). To achieve a robust analysis, however, it is desirable to measure the speed of individual fluorophores, whose overlapping behaviour cannot be analysed quantitatively with on/off plots, using particle tracking.

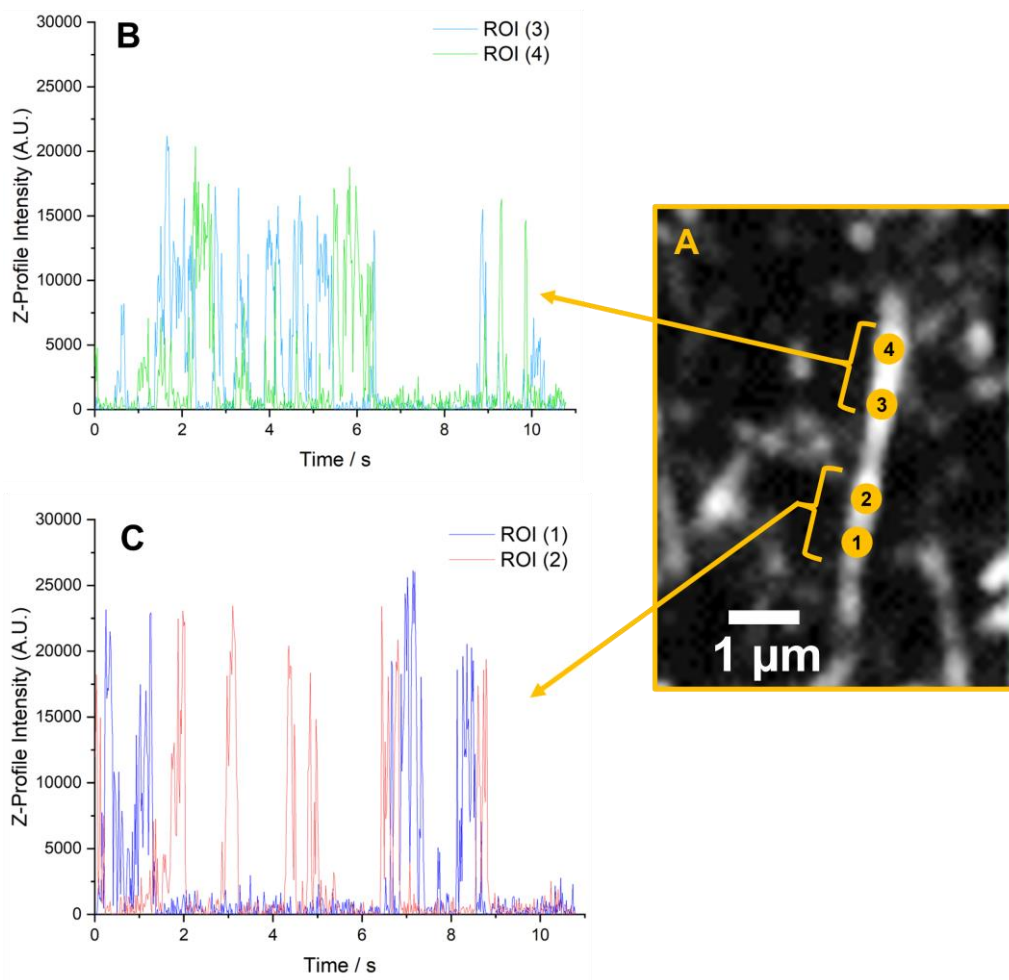


Figure 3.13. (A) A magnified average projection showing four ROI's in a fibre. (B-C) Z-profile intensity versus time plots for the four ROI's show maxima corresponding to a fluorophore being present in the given ROI in A. All images laser wavelength of 642 nm, observation with 650 nm LP filter.

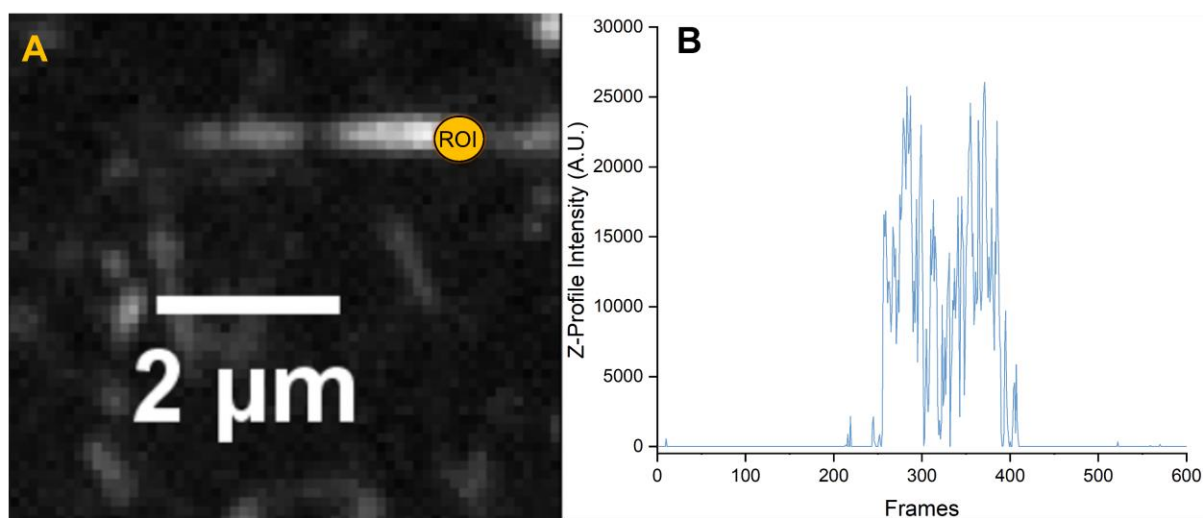


Figure 3.14. TIRF micrograph containing a ROI and subsequent z-profile intensity plot. (A) TIRF micrograph of an average projection of a 600-frame video of **ZnPcTS@Gel** with a [**ZnPcTS**] of 0.1 μM . A ROI was placed over a section of a fibre. Laser wavelength of 642 nm, observation with 650 nm LP filter. (B) Z-profile intensity plot over 600 frames indicates a fluorophore resided in the ROI for ~ 150 frames (~ 2.7 s).

3.2.3. Light and acid-controlled speed/encapsulation modulation

In the case of the 0.1 μM **ZnPcTS@Gel**, individual fluorophore movement is clear enough that particle tracking algorithms may be used. A versatile tool for single particle tracking is TrackMate, an ImageJ plugin.³¹ Particle tracking was performed using the Linear Assignment Problem (LAP) tracker along with the Difference of Gaussians (DoG) detector. The LAP tracker creates track segments on a frame-by-frame basis, linking particles between frames whilst the DoG detector is one of several options available on the Trackmate plugin and is optimal for objects of pixel size 5 – 10 pixels. Typically, several thousand instantaneous velocity measurements were taken from the tracks produced. These tracks appeared as straight or slightly curved lines, suggesting fluorophore trajectories were along single fibres and that the fluorophores are present inside rather than on top of the fibres because significant directional deviation between fibres would be observed in the case of the latter. The mean values of the velocity measurements were then calculated to yield average instantaneous velocities.

It was reasoned that if photothermal events give rise to molecular movement, varying the laser power of the excitation light source (and consequently the irradiance) may influence the rate of fluorophore movement. Varying the level of laser power does not alter the energy of incoming photons (with the excitation wavelength being kept at a constant 642 nm), but simply increases the light flux. A greater number of fluorophore excitations conceivably would result

in a greater extent of local heating, leading to increased rate of traveller diffusion. Laser powers were raised from 30% of the maximum power to 100% in increments of 10%. Typically, a 600 frame movie was collected of a 25.6 x 25.6 μm area of the gel sample at each laser power, upon which particle tracking analysis was conducted after denoising of the video.

Calculating mean instantaneous velocities (MIV's) for each laser power revealed that traveller diffusion rate increases linearly with increasing laser power (**Fig. 3.15A**). These measurements imply that under no light irradiation, **ZnPcTS** is mobile despite the lack of photothermal heating; room temperature thermal energy is sufficient to move the phthalocyanine along the fibres. This mobility is likely a consequence of the relatively weak electrostatic interactions between the **ZnPcTS** travellers and gelator, with photothermal heating during irradiation providing extra energy for the rate of traveller diffusion. **Figure 3.15B** displays the straight tracks (referenced to in a previous paragraph) of the mobile fluorophores, indicating fluorophore diffusion is occurring along the lengths of fibres.

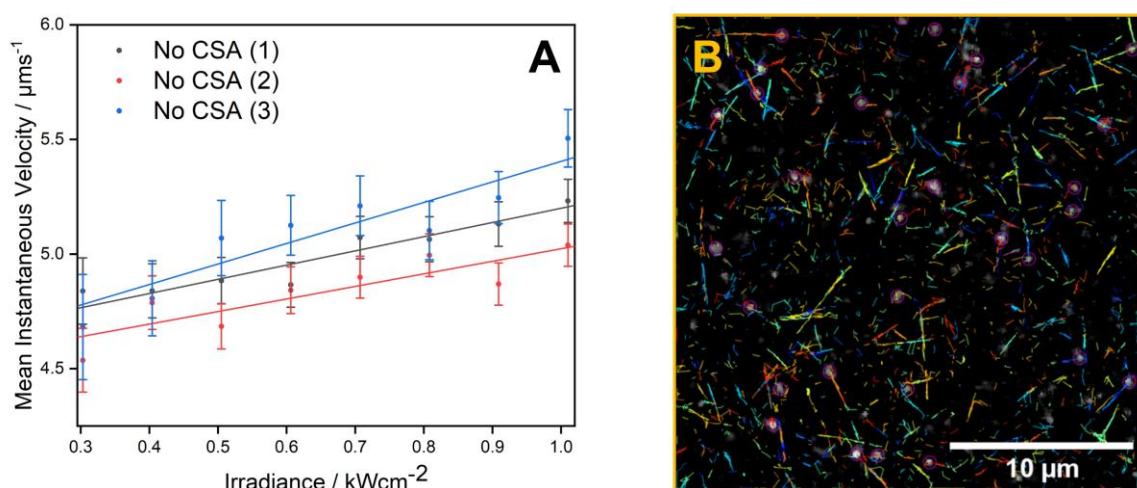


Figure 3.15. *Quantitative analysis of fluorophore movement with particle tracks. (A) Plot of Mean Instantaneous Velocity (MIV) against irradiance for several areas of 0.1 μM ZnPcTS@Gel samples. (B) Recorded tracks from a video of 0.1 μM ZnPcTS. Track colours do not refer to any parameter and are for distinguishing between tracks.*

The chemistry of the medium can also be used to modulate fluorophore velocity, so the addition of acids into the gel system was explored. The introduction of camphorsulfonic acid (**CSA**) into 0.1 μM **ZnPcTS@Gel** (to a final concentration of 1.2 mM) was made in the aqueous solution containing the **ZnPcTS** before gel formation. **CSA** is a sterically hindered acid ($\text{pK}_a \sim 1.2$ in water), that would be incorporated into the gel fibres by displacing bromide ions

between gel lamellae because of its hydrophobic character. Gel formation and its subsequent macroscopic appearance did not appear altered macroscopically by the presence of CSA and as characterized by SEM (Fig. 3.16), though rheological analysis indicates the presence of structural differences (Fig. 3.17).

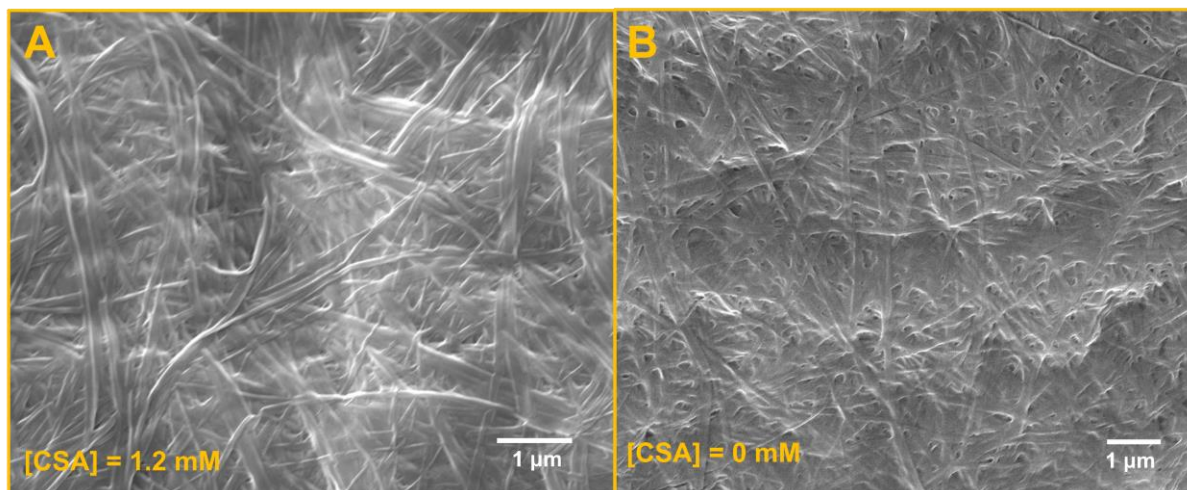


Figure 3.16. (A) SEM image showing fibre morphology of ZnPcTS@Gel xerogel with [ZnPcTS] of $0.1 \mu\text{M}$ and [CSA] of 1.2 mM . (B) SEM image showing fibre morphology of ZnPcTS@Gel xerogel with [ZnPcTS] of $0.1 \mu\text{M}$ and no CSA.

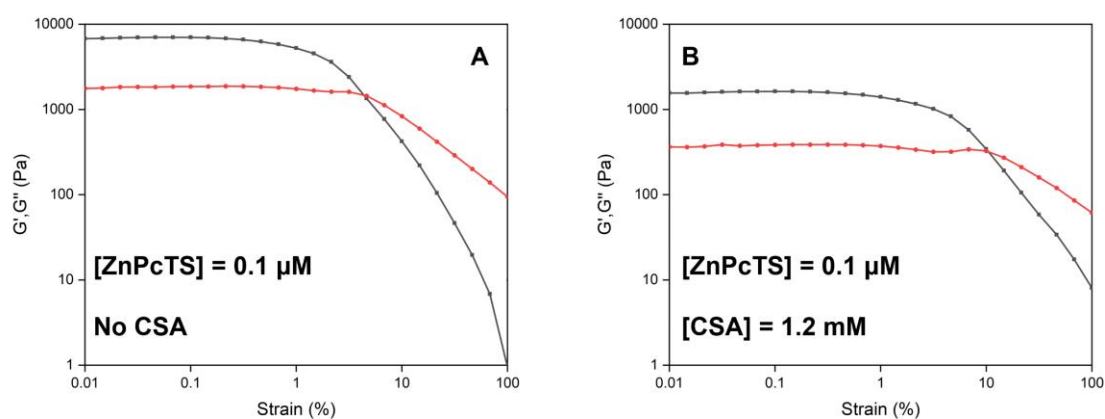


Figure 3.17. Shear stress profiles showing storage (G' , black curve) and loss (G'' , red curve) moduli obtained of ZnPcTS@Gel at with $[1.2\text{Br}] = 12 \text{ mM}$ in water-ethanol ratio 1:1 with varying CSA concentrations. (A) [ZnPcTS] = $0.1 \mu\text{M}$, no CSA. (B) [ZnPcTS] = $0.1 \mu\text{M}$, [CSA] = 1.2 mM .

In the three control samples containing no CSA (shown in Fig. 3.15A), at maximum irradiance (1.01 kWcm^{-2}), the MIV was measured to be $5.23 \pm 0.09 \mu\text{ms}^{-1}$, $5.50 \pm 0.13 \mu\text{ms}^{-1}$, and $5.04 \pm 0.09 \mu\text{ms}^{-1}$. As laser power was lowered, the rate of decrease of MIV in these samples (assuming a linear relationship based on the data acquired) was calculated to be

$0.62 \pm 0.17 \mu\text{ms}^{-1}\text{kW}^{-1}\text{cm}^2$, $0.55 \pm 0.16 \mu\text{ms}^{-1}\text{kW}^{-1}\text{cm}^2$, and $0.90 \pm 0.23 \mu\text{ms}^{-1}\text{kW}^{-1}\text{cm}^2$, respectively. MIV at zero irradiance was estimated by extrapolating a linear fit to the data points collected and noting the y-intercept for this fit. Zero irradiance MIV's for the three control samples were $4.58 \pm 0.12 \mu\text{ms}^{-1}$, $4.48 \pm 0.12 \mu\text{ms}^{-1}$, and $4.51 \pm 0.18 \mu\text{ms}^{-1}$, respectively. These slope values along with the extrapolated MIV values at zero irradiance indicate that delivering an irradiance of 1 kWcm^{-2} to the sample raises the average speed of the fluorophores by approximately 15%.

Imaging the **CSA**-containing gel under identical TIRF conditions to the samples previously shown, traveller movement was once again observed. Particle tracking analysis of the video TIRF micrographs reveals a greater traveller velocity in comparison with the gel containing no **CSA** (**Fig. 3.18A**). MIV values calculated for the four **CSA** samples at maximum irradiance (1.01 kWcm^{-2}) were $8.24 \pm 0.14 \mu\text{ms}^{-1}$, $8.42 \pm 0.14 \mu\text{ms}^{-1}$, $7.75 \pm 0.12 \mu\text{ms}^{-1}$ and $7.86 \pm 0.13 \mu\text{ms}^{-1}$, respectively. These MIV values are an average of 61% greater than in the sample containing no **CSA**, indicating a significant effect on the interaction between the traveller and the path brought about by its presence. At maximum irradiance, two samples of $0.1 \mu\text{M ZnPcTS@Gel}$ containing **CSA** were shown to exhibit slightly higher MIV values than two others outside the margin of error. Inhomogeneities within the supramolecular structure of the gel (for example, the number of bilayers in the particular fibre or the precise packing within them) likely contribute to the varying MIV values measured for separate areas of the same macroscopic gel sample. Local **ZnPcTS** concentration differences and solvent composition variations could also influence fluorophore movement. Zero irradiance (dark) MIV values of the **CSA** samples are significantly higher than the control samples, with values of were $6.25 \pm 0.17 \mu\text{ms}^{-1}$, $6.33 \pm 0.18 \mu\text{ms}^{-1}$, $6.61 \pm 0.16 \mu\text{ms}^{-1}$, and $6.60 \pm 0.17 \mu\text{ms}^{-1}$, respectively. Another significant deviation of the **CSA** samples from the controls was in their greater measured change in mean velocity with laser power. Note that the two **CSA** samples with higher calculated MIV at maximum irradiance exhibit significantly steeper slopes ($1.77 \pm 0.23 \mu\text{ms}^{-1}\text{kW}^{-1}\text{cm}^2$ and, $1.86 \pm 0.24 \mu\text{ms}^{-1}\text{kW}^{-1}\text{cm}^2$) than the two others ($1.19 \pm 0.22 \mu\text{ms}^{-1}\text{kW}^{-1}\text{cm}^2$ and $1.23 \pm 0.23 \mu\text{ms}^{-1}\text{kW}^{-1}\text{cm}^2$). Again, these differences are likely a result of local variations in structure and/or composition of the gel material. **Figure 3.18B** displays the straight tracks of the mobile fluorophores, indicating fluorophore diffusion is occurring along the lengths of fibres.

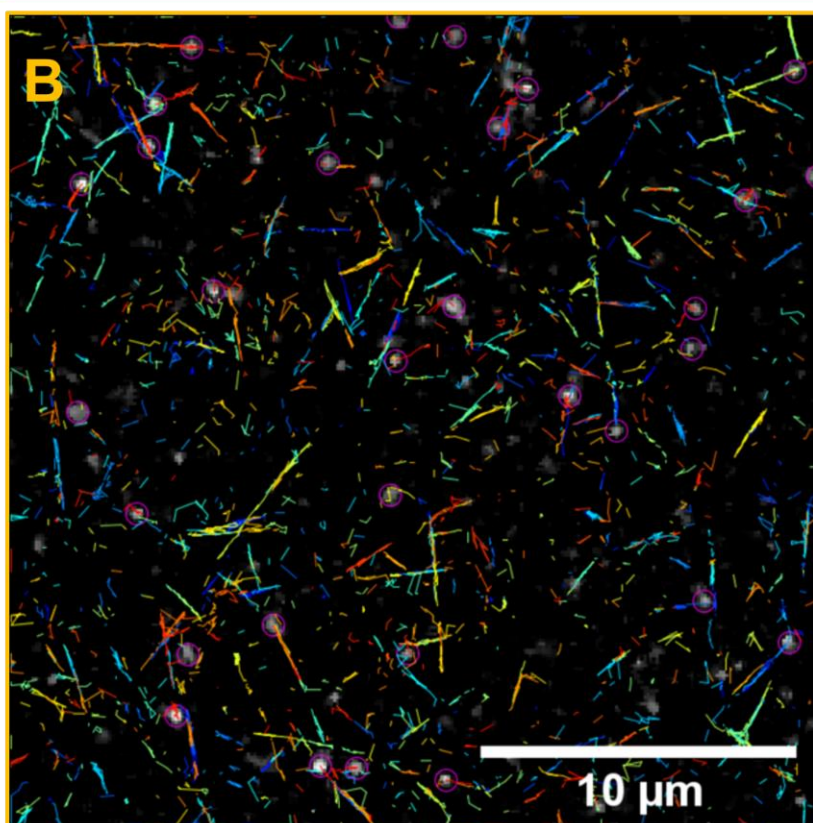
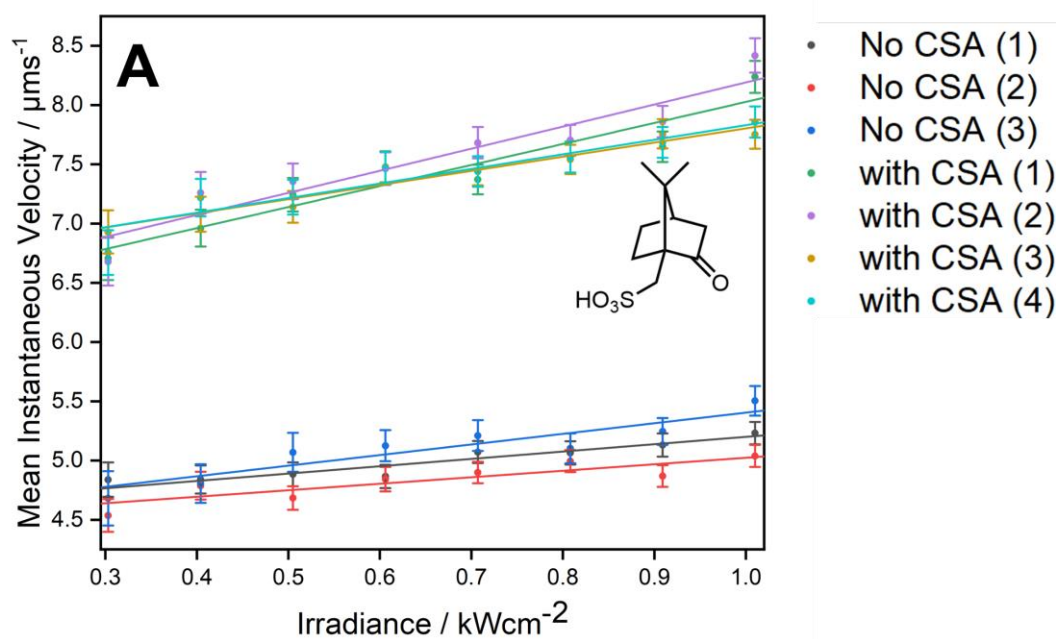


Figure 3.18. (A) Plot of MIV against irradiance for several areas of $0.1 \mu\text{M}$ ZnPcTS@Gel samples with and without CSA (1.2 mM, structure included). (B) Recorded tracks from a video of $0.1 \mu\text{M}$ ZnPcTS@Gel containing no CSA. Track colours do not refer to any parameter and are for distinguishing between tracks.

The greater average rate of traveller diffusion observed in the **CSA** samples could be attributed to two complementary factors. The **CSA** encapsulated into gel fibres generates a different chemical environment to the pure bromide gelator. This structural change, as identified in the rheological measurements and powder X-ray diffraction experiments (**Fig. 3.17**, **Fig. 3.19**), weakens the electrostatic interactions between **ZnPcTS** and gelator, promoting the elevated velocity under irradiation. Weakening of the electrostatic interactions could also have resulted in the fluorophores being more susceptible to the photothermal heating brought about by irradiation, which would therefore account for the steeper slopes measured for the **CSA** samples with respect to the control samples.

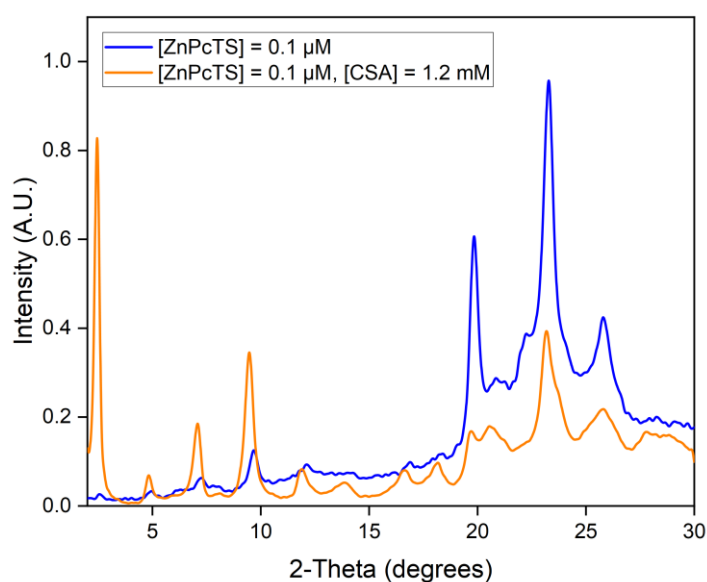


Figure 3.19. Powder X-ray diffractograms of **ZnPcTS@Gel** xerogels containing a fluorophore loading of $0.1 \mu\text{M}$ (blue line) and containing a fluorophore loading of $0.1 \mu\text{M}$ with **CSA** (1.2 mM) (orange line).

In addition to MIV analysis, standard mean square displacement (MSD) analysis (that quantifies the deviation from an original position over a period of time) was also performed. This analysis results in a diffusion coefficient (D) which can be used to compare diffusion rates between systems. Along with the quantification of movement, MSD can also explain the manner in which diffusion occurs, whether it be directed, Brownian, or confined.^{22,32,33} The MSD analysis (**Fig. 3.20A**) yielded plots that confirmed that diffusion was confined in the case of **ZnPcTS@Gel** both with and without **CSA**, validating the observation of fluorophore diffusion along fibres. A significant increase in **ZnPcTS** D values was observed between no-**CSA** and **CSA** containing **ZnPcTS@Gel** gels with a $\sim 90\%$ increase between the former

and the latter ($0.22 \pm 0.02 \mu\text{m}^2\text{s}^{-1}$ to $0.41 \pm 0.03 \mu\text{m}^2\text{s}^{-1}$) under an irradiance of 1.01 kWcm^{-2} , corroborating the MIV analysis (**Fig. 3.20B**). A decrease in D is seen with the lowering of irradiance with both the CSA/No-CSA systems. The zero irradiance D values for both systems are non-zero, also supporting the MIV analysis.

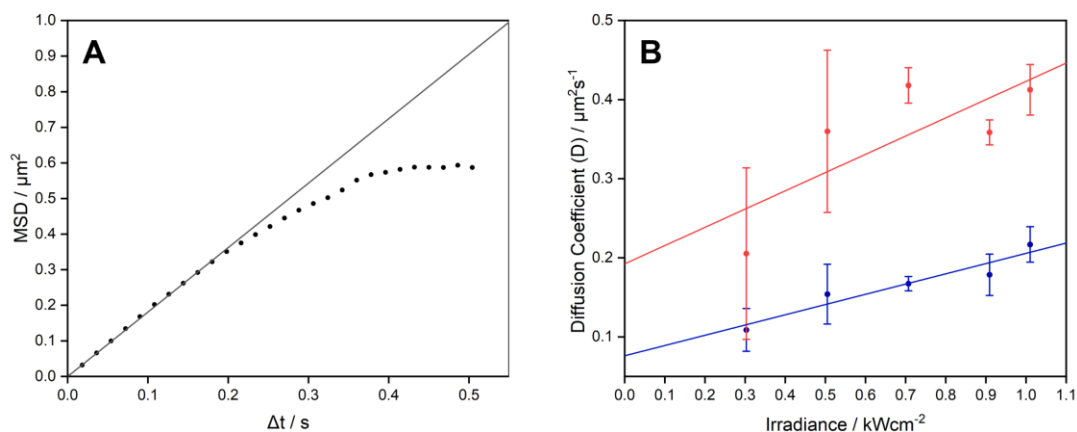


Figure 3.20. (A) MSD plot for **ZnPcTS** within a **ZnPcTS@Gel** system containing 1.2 mM CSA displaying confined diffusion. (B) Plot of calculated diffusion coefficients for **ZnPcTS** as part of the gel system containing 1.2 mM CSA (red) and containing no **CSA** (blue) over a range of irradiances.

To test the effect of sulfonate protonation on the traveller movement, an analogous gel system containing $0.1 \mu\text{M ZnPcTS@Gel}$ along with 4-toluene sulfonic acid (**PTSA**, 1.2 mM) was also prepared. Again, gel formation occurred no differently to those discussed previously and SEM characterisation of the xerogel reveals a fibre morphology indistinguishable from those previously discussed (**Fig. 3.21**), though rheological analysis and PXRD indicate the presence of microscopic structural differences brought about relatively high loading of **PTSA** relative to the fluorophore (**Fig. 3.22**, **Fig. 3.23**).

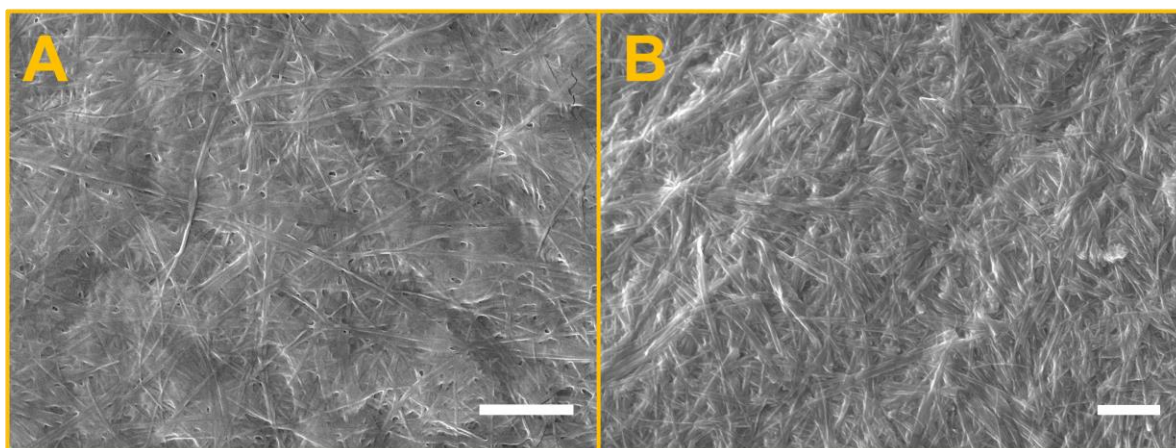


Figure 3.21. (A) SEM image showing fibre morphology of **ZnPcTS@Gel** xerogel with $[ZnPcTS]$ of $0.1 \mu\text{M}$ and $[PTSA]$ of 1.2 mM . (B) SEM image showing fibre morphology of **ZnPcTS@Gel** xerogel with $[ZnPcTS]$ of $0.1 \mu\text{M}$ and no **PTSA**. Scale bars correspond to $2 \mu\text{m}$.

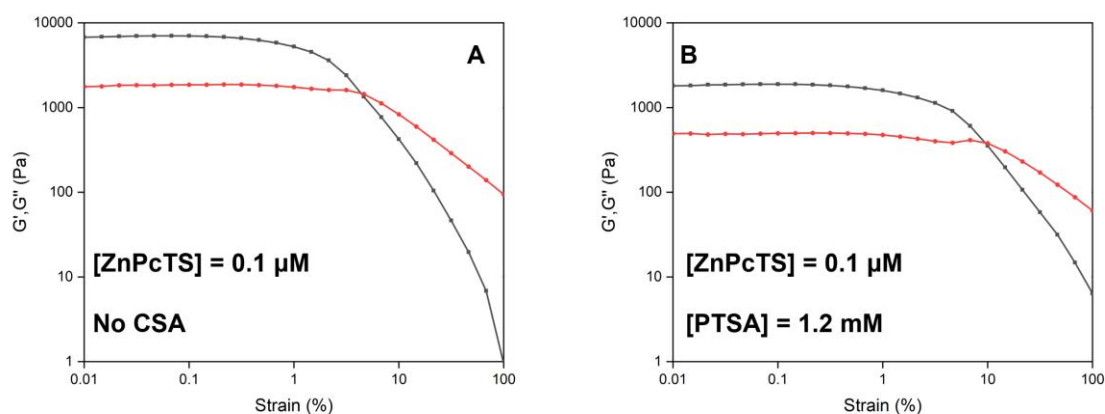


Figure 3.22. Shear stress profiles showing storage (G' , black curve) and loss (G'' , red curve) moduli obtained of **ZnPcTS@Gel** at 12 mM (**1.2Br** concentration) in water-ethanol ratio $1:1$ with varying **ZnPcTS** and **PTSA** concentrations. (A) $[ZnPcTS] = 0.1 \mu\text{M}$, no **PTSA**. (B) $[ZnPcTS] = 0.1 \mu\text{M}$, $[PTSA] = 1.2 \text{ mM}$.

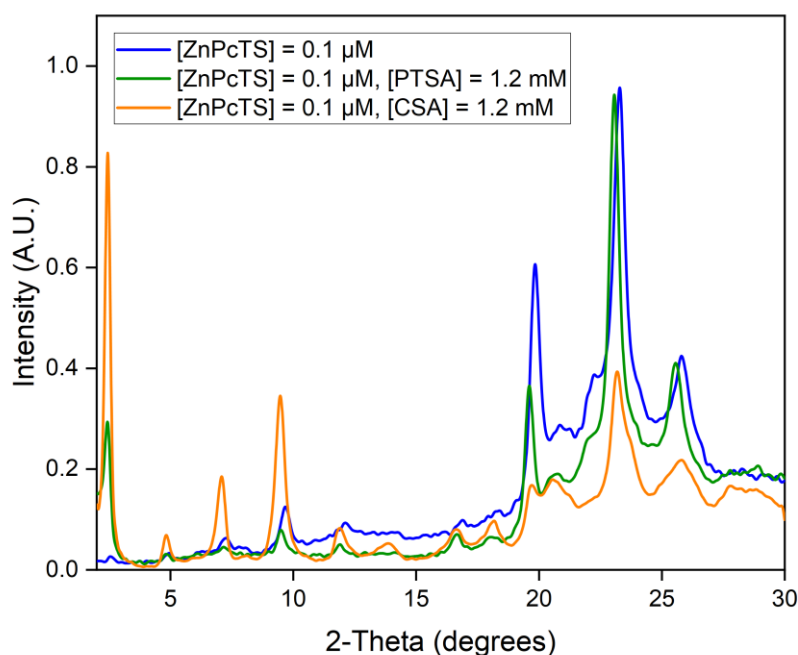
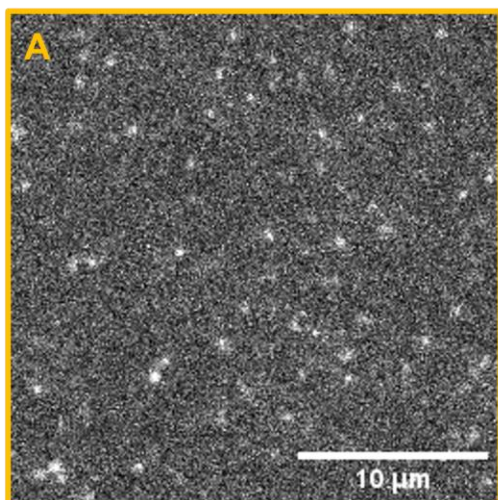


Figure 3.23. Powder X-ray diffractograms of **ZnPcTS@Gel** xerogels containing a fluorophore loading of 0.1 μM with no added **PTSA** or **CSA** (blue line), 0.1 μM with 1.2 mM **PTSA** (green line), and 0.1 μM with 1.2 mM **CSA** (orange line).

As analysed in the TIRF microscope, the movement dynamics were greatly changed compared with both the gels with and without added **CSA**. Rather than directional movement of fluorophores through straight fibres, fluorophores look to exhibit ‘random walk’ motion, presumably in the interstitial liquid outside of the fibres. The excess of **PTSA** ($\text{p}K_{\text{a}} = -2.8$) protonates the sulfonate groups of the **ZnPcTS** ($\text{p}K_{\text{a}} = \sim -2$) to an extent.³⁴ The lack of an electrostatic driving force for encapsulation of the traveller within gel fibres means it stays in the liquid component of the gel. The average projection (**Fig. 3.24**) therefore does not display fibres as before, but only single spots of high intensity, possibly owing to some fluorophores sticking to points on gel fibres. MSD analysis on these non-confined fluorophores still resulted in MSD plots that displayed confined diffusion (**Fig. 3.25**). Despite their presence in the interstitial liquid between fibres, the MSD plots suggest that the fibres in the vicinity of **ZnPcTS** provide a barrier to pure Brownian diffusion. Despite the confined nature of the diffusion, the D value obtained at 1.01 kWcm^{-2} is an order of magnitude greater than that of **ZnPcTS** in the presence of **CSA** ($10.2 \pm 0.2 \mu\text{m}^2\text{s}^{-1}$ **PTSA** to $0.41 \pm 0.03 \mu\text{m}^2\text{s}^{-1}$ **CSA**).

0.1 μM ZnPcTS@Gel w 1.2mM PTSA

Frame from video



Average projection

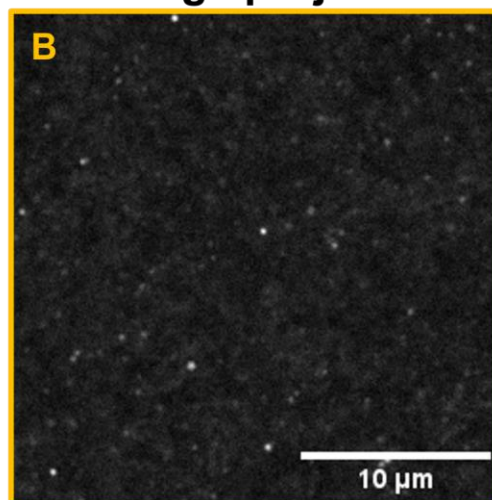


Figure 3.24. TIRF micrographs of a **ZnPcTS@Gel** sample containing a **ZnPcTS** concentration of 0.1 μM and **PTSA** concentration of 1.2 mM. (A) TIRF micrograph of a single frame (of 600) where individual fluorophores can be observed and fibre morphology not discernible. (B) TIRF micrograph of the average projection over the 600 frames referenced in A highlights no fibre morphology as the fluorophores are not confined to the fibres. All images taken with 642 nm laser and LP filter at 650 nm. Laser power 100%.

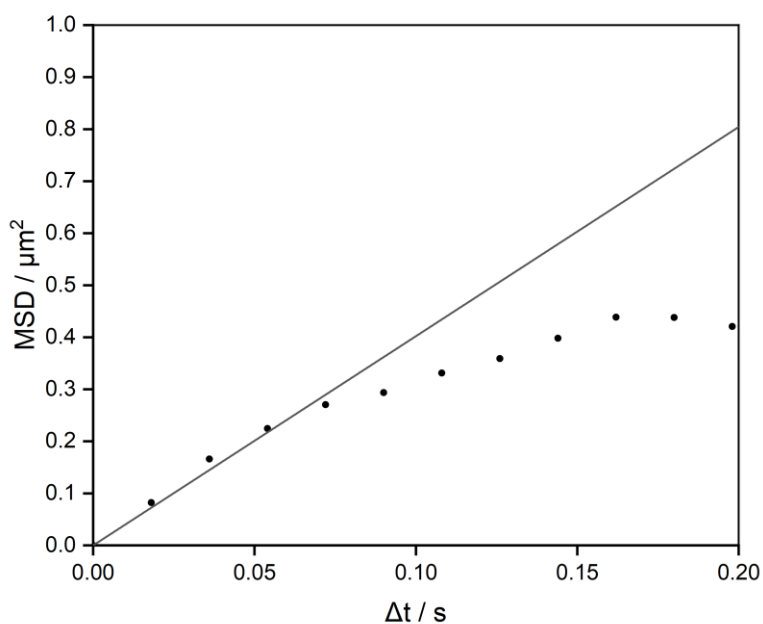


Figure 3.25. MSD plot for unencapsulated **ZnPcTS** within a **ZnPcTS@Gel** system containing 1.2 mM **PTSA** displaying confined diffusion.

Therefore, addition of **PTSA** gives the opportunity to monitor the effect of gradually increasing protonation state upon fluorophore movement and encapsulation. Gel samples containing 2, 4, 8, and 16 eq. of **PTSA** with respect to **ZnPcTS** were prepared; no deviation from normal gel formation was observed macroscopically and as characterized by SEM. When these gel samples were analysed using TIRF microscopy, the fluorophores are mostly encapsulated within gel fibres (**Fig. 3.26B**), even at 16 eq. **PTSA**. The presence of apparently solvent-incorporated fluorophores is seen but not to the same extent as within gels containing 1.2 mM **PTSA**. The movement dynamics in these samples were measured in an identical fashion to that described above. **Figure 3.26A** shows the relationship between **PTSA** concentration within the gel and mean instantaneous velocity at various laser powers corresponding to different irradiance levels. From 0 to 8 eq. of **PTSA**, the mean speed of fluorophores gradually increases. This effect is presumably a consequence of the increased protonation state and lower anionic character of the phthalocyanine resulting in weaker electrostatic attraction between the fluorophores and the gelator path. However, moving to a **PTSA** concentration of 16 eq., the mean speed of the fluorophores decreases. We interpret this effect as **PTSA** replacing the bromide anions in the gel fibres and providing a physical obstacle to fluorophore movement. MSD analysis resulted in a similar trend to that seen in **Fig. 3.26A** (**Fig. 3.27**). A doubling of [**PTSA**] from 4 equivalents to 8 equivalents resulted in a $\sim 60\%$ increase in D ($0.26 \pm 0.01 \mu\text{m}^2\text{s}^{-1}$ to $0.41 \pm 0.03 \mu\text{m}^2\text{s}^{-1}$). The same decrease in D from 8 eq. to 16 eq. of **PTSA** is also seen, matching the MIV analysis.

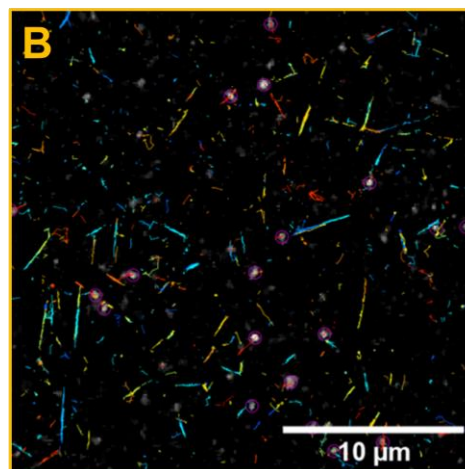
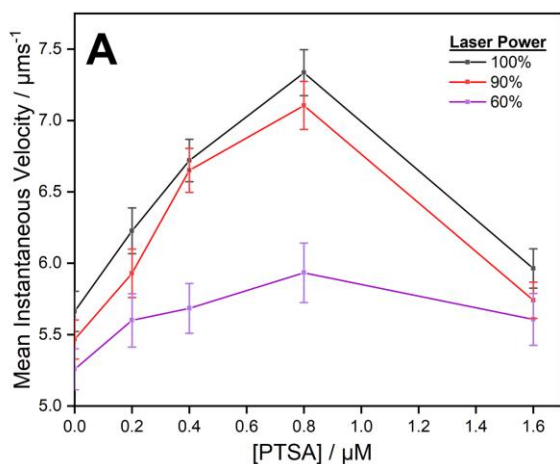


Figure 3.26. (A) A plot of MIV at different laser powers (100% = 1.01 kWcm^{-2}) versus *PTSA* concentration where an increase in [*PTSA*] results in increased rate of fluorophore movement up until gel containing 1.6 eq. *PTSA*. (B) Recorded tracks from a video of $0.1 \mu\text{M}$ *ZnPcTS* 1.6 eq. of *PTSA* where some unencapsulated tracks can be seen. Colours do not refer to any parameter and are for distinguishing between tracks.

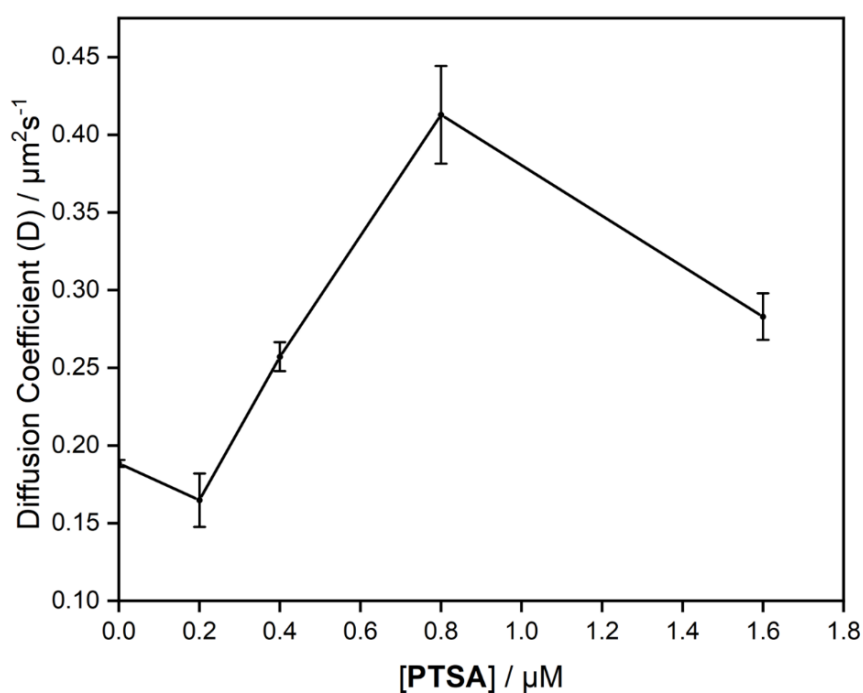


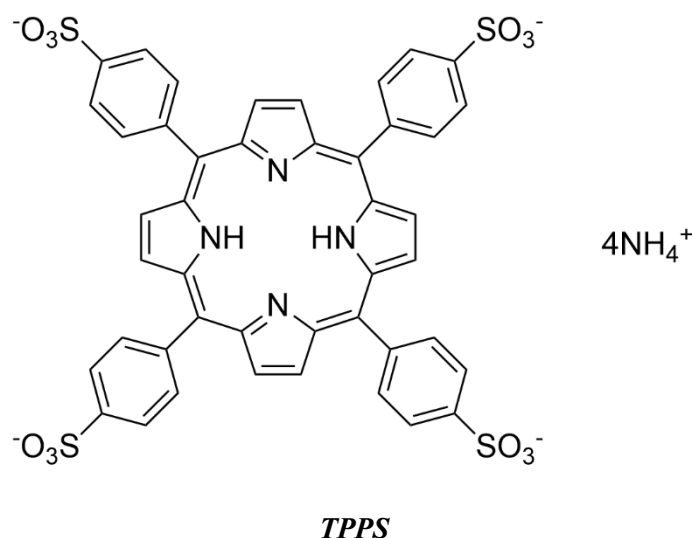
Figure 3.27. Plot of calculated diffusion coefficients for *ZnPcTS* as part of the gel system containing almost equimolar amounts (with respect to *ZnPcTS*) of *PTSA*.

The solvent system chosen for the gel has a critical effect on the fluorophore behaviour in the material. In the samples analysed here, the 1:1 water-ethanol ratio has been discussed. The TIRF microscopy of gels prepared at 6:4 and 7:3 water-ethanol ratios resulted in a significant amount of unencapsulated **ZnPcTS**.

Overall, the imidazolium gels containing **ZnPcTS** fluorophores in varying concentrations reveal full encapsulation within gel fibres, but the included molecules are dynamic even in the absence of light irradiation. The rate of movement of these molecules is controlled by the irradiance acting on the system, and by the presence of molecules that can influence their ionisation. This control of molecular diffusion in a confined pathway is a step towards artificial movement along robust fibres, as the system described here has essentially no degradation over the timescale of the experiments.

3.3. 5,10,15,20-(Tetra-4-sulfonatophenyl)porphyrin (TPPS)

The observation of free diffusion of single **ZnPcTS** molecules shown in the previous work when compared with the stationary carboxylated porphyrin can be attributed to weaker electrostatic interactions between the cationic gelator and sulfonate groups on the periphery of the phthalocyanine compared with those of the carboxylate groups and the gelator.²⁹ To investigate this further, a sulfonated porphyrin 5,10,15,20-(tetra-4-sulfonatophenyl)porphyrin (**TPPS**) was incorporated into the same **1.2Br** gel system.



TPPS is a water-soluble fluorophore that has been studied in relation to its potential as a PDT photosensitizer though photoinactivation of bacteria using this compound has produced largely poor results.³⁵⁻³⁷ As a porphyrin, the photophysical properties are different compared phthalocyanines in general and **ZnPcTS** specifically (**Fig. 3.28**). In both aqueous solution and

in 1:1 water-ethanol, the Soret band of **TPPS** is the major absorption maximum at ~ 405 nm, with Q-bands of decreasing intensity between ~ 450 nm to 600 nm. Unlike in the case of **ZnPcTS**, the absorption maximum of **TPPS** is diminished in 1:1 water-ethanol compared with in water (**Fig. 3.28**). Whilst the fluorescence emission intensity of **TPPS** is not considerably diminished in water compared to 1:1 water-ethanol, the emission profile does differ in that an additional peak is present in the water sample (**Fig. 3.29**). This extra peak is potentially indicative of increased aggregation in the solely aqueous environment. As with **ZnPcTS**, incorporation of the **TPPS** fluorophore into the **1.2Br** gel led to a significant decrease in fluorescence intensity, though the emission peaks remained in the same positions as those of **TPPS** in 1:1 water-ethanol.

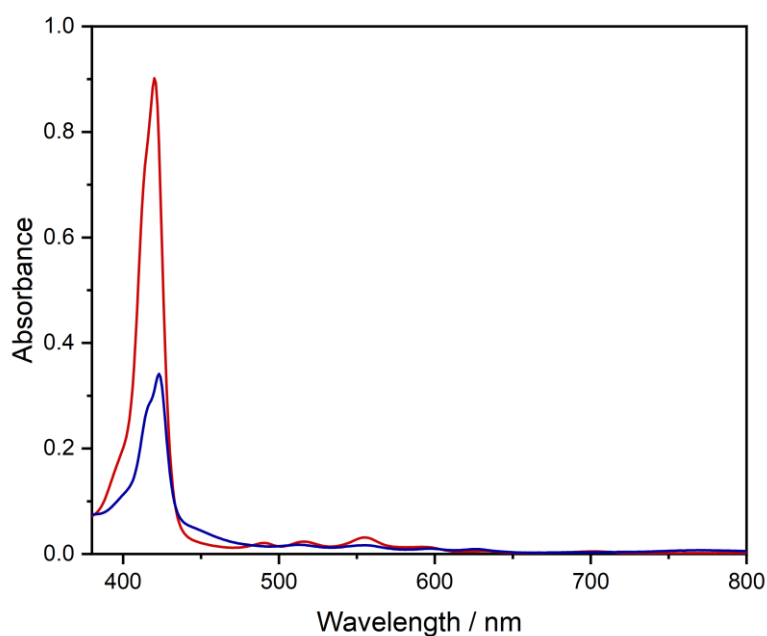


Figure 3.28. Absorption spectra of **TPPS** in water (red) and in 1:1 water-ethanol (blue) both at a concentration of $20 \mu\text{M}$.

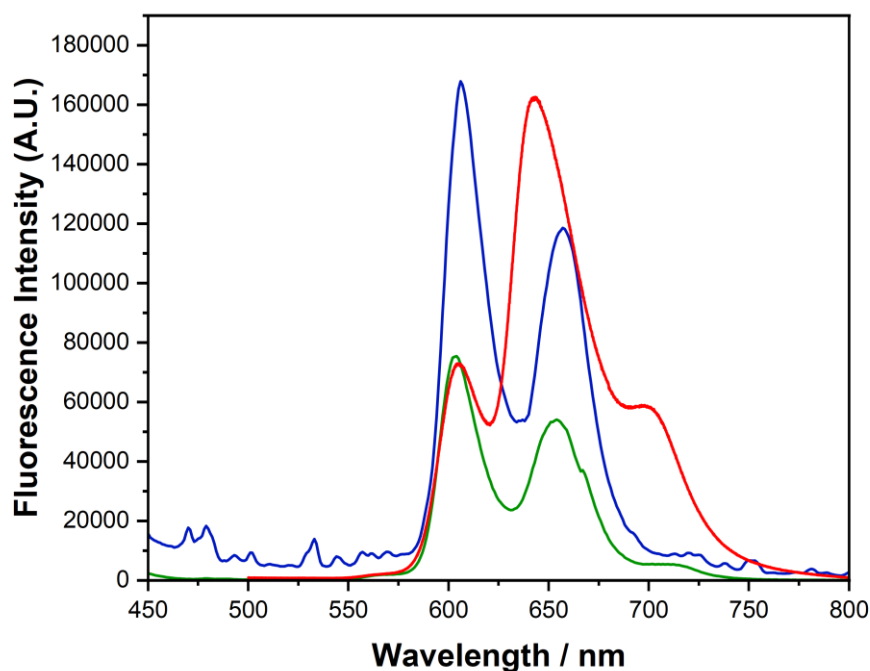


Figure 3.29. Fluorescence emission spectra of *TPPS* in water (red) at a *TPPS* concentration of $10\ \mu\text{M}$, in 1:1 water-ethanol (blue) with a *TPPS* concentration of $10\ \mu\text{M}$, and in a **1.2Br** gel (green) with a *TPPS* concentration of $100\ \mu\text{M}$. $\lambda_{\text{exc}} = 420\ \text{nm}$ for these fluorescence measurements.

3.3.1. Fibre morphology and fluorophore dynamics

Curiously, irradiation with a 405 nm laser did not result in any considerable fluorescence signal from the **TPPS@Gel** sample used in the TIRF study. The photophysical studies on **TPPS** shown in the previous figures indicate that the main absorption peak (Soret band) is significant and results in a substantial fluorescence signal that should be captured by the EMCCD camera utilized in conjunction with the TIRF microscope. Further to this, excitation at 642 nm does indeed result in measurable fluorescence which can be used to image the **TPPS@Gel** fibres. Whilst the Q-band of **TPPS** does exhibit a small peak at $\sim 640\ \text{nm}$, it was expected that the 405 nm excitation would result in a much stronger signal. As imaging with excitation at 642 nm did lead to adequate signal-to-noise ratio and resolution, the 642 nm irradiation was carried out for the duration of these experiments with **TPPS**.

1.2Br gel morphology is only marginally altered in the presence of $10\ \mu\text{M}$ **TPPS** when compared with $10\ \mu\text{M}$ **ZnPcTS**. **Figure 3.30** shows a comparison of the two gel systems and the morphology they possess. In the case of **ZnPcTS@Gel**, fibres are all relatively straight in areas of high fibre density. However, fibres in the **TPPS@Gel** system seem to be more

disturbed. This disruption of morphology could be a consequence of the relatively high laser power used to irradiate the porphyrin fluorophores and subsequent photothermal heating. Fluorescence intensity arising from between the fibres seem to indicate that **TPPS** is not fully encapsulated within the gel fibres to the same extent as **ZnPcTS**.

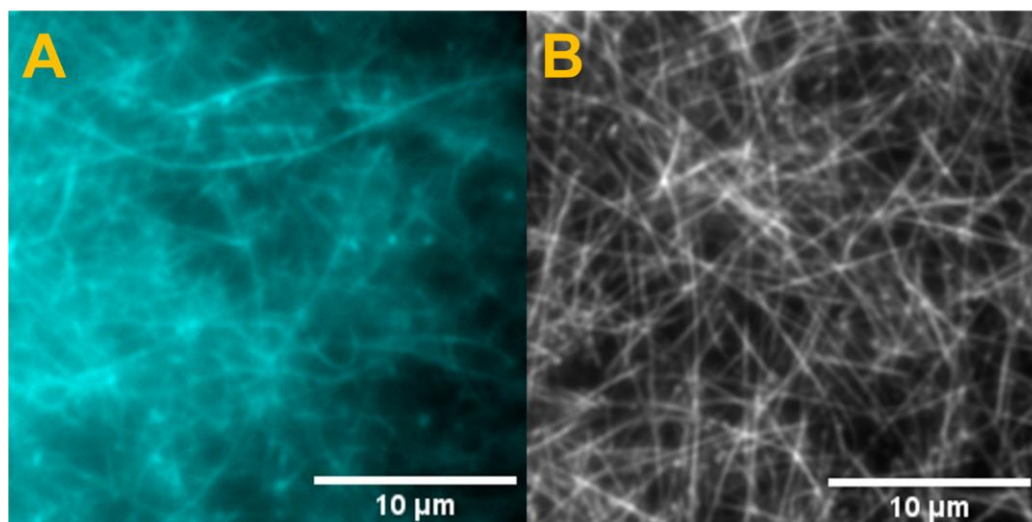


Figure 3.30. Comparison of TIRF micrographs of **TPPS@Gel** and **ZnPcTS@Gel**. (A) **TPPS@Gel**, $[TPPS] = 10 \mu\text{M}$. (B) **ZnPcTS@Gel**, $[ZnPcTS] = 10 \mu\text{M}$. All images taken with 642 nm laser and LP filter at 650 nm. Laser power 100%.

It was not possible to conclude from these videos whether fluorophore movement was occurring as the low signal-to-noise ratio meant that any flickering that characterized fluorophore movement in the **ZnPcTS@Gel** system was not discernible from the background noise. In addition to the low signal-to-noise ratio, photobleaching of **TPPS** took place over the course of the recorded videos which presented itself as a decrease in average fluorescence intensity over time (**Fig. 3.31**).

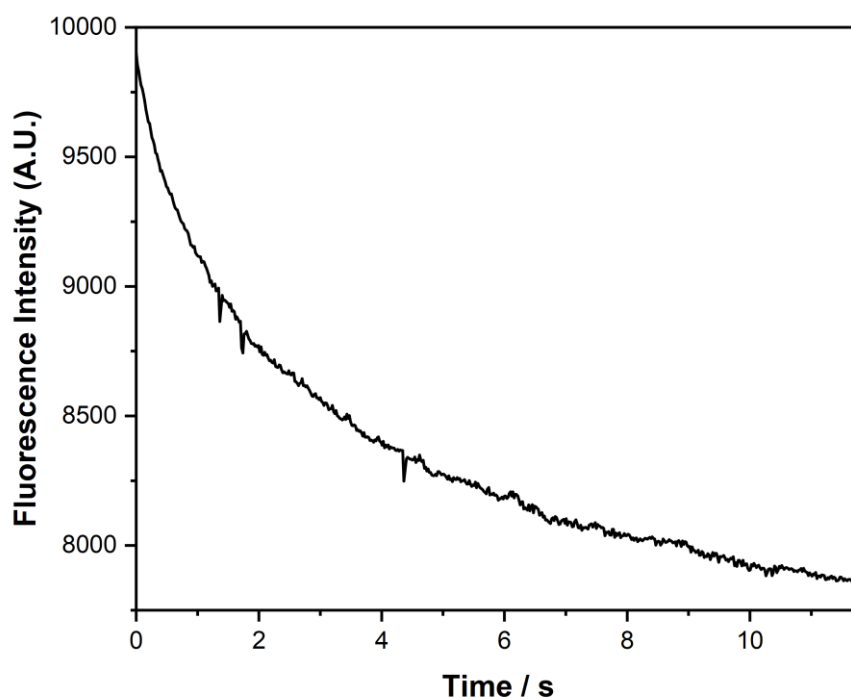


Figure 3.31. Fluorescence intensity photobleaching of **TPPS** when irradiated with 642 nm laser light over the course of ~ 10 s.

Reducing the **TPPS** concentration to 0.1 μM resulted in the loss of visibility of the gel fibres in the raw video much like in the case of 0.1 μM **ZnPcTS@Gel**. Unlike the **ZnPcTS@Gel** system, there was no diffusion of the **TPPS** fluorophores within the gel fibres. Though some unencapsulated **TPPS** fluorophores exhibited Brownian diffusion between gel fibres, most of the **TPPS** molecules imaged remained stationary presumably upon or within the gel fibres with occasional photo-blinking. **Figure 3.32** displays both the average and maximum projection of a 600-frame video. This lack of movement suggests that fluorophore diffusion cannot be explained solely by the electrostatic interactions between ionic groups on the periphery of the fluorophore and the cationic gelator as it would be expected that **TPPS** should act largely the same as **ZnPcTS**.

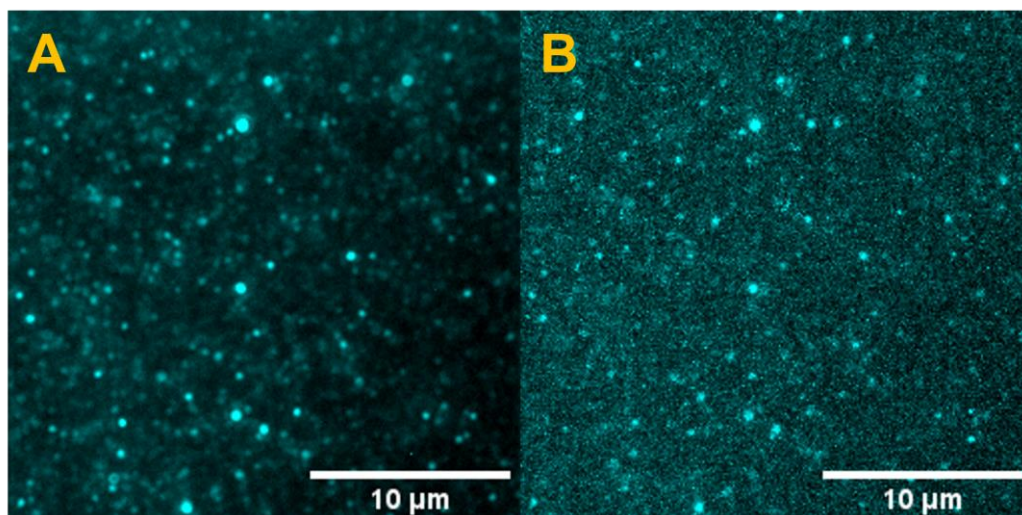
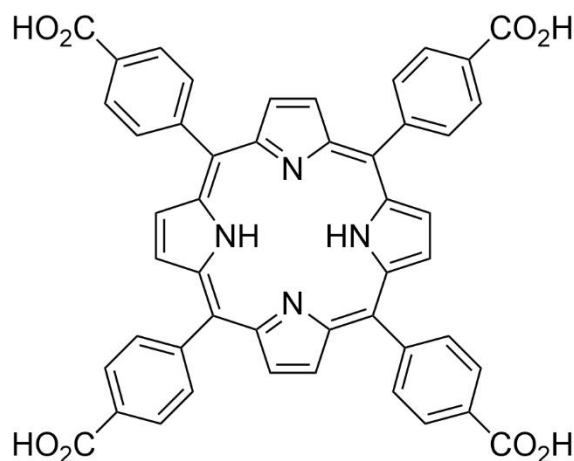


Figure 3.32. Comparison of TIRF micrographs of *TPPS@Gel* average and maximum projections. (A) Average projection of *TPPS@Gel* video, $[TPPS] = 0.1 \mu\text{M}$. (B) Maximum projection of *TPPS@Gel* video, $[TPPS] = 0.1 \mu\text{M}$. All images taken with 642 nm laser and LP filter at 650 nm. Laser power 50%.

3.4. Mixed system (TCPP and ZnPcTS)

The compound 5,10,15,20-tetrakis(4-carboxyphenyl)porphyrin (**TCPP**) is a tetracarboxylated porphyrin that has been studied as an incorporated fluorophore in **1.2Br** gel systems.^{26,29} As a carboxylate when deprotonated by base in solution, it differs from the previous two studied fluorophores.



TCPP

It was shown by Samperi *et al.* that **TCPP** exhibits no dynamics within gel fibres without the presence of an azobenzene (**Azo**) molecular switch. In the study, fluorophore movement was promoted by the photoisomerisation of a water-soluble azobenzene derivative. Upon irradiation of the **TCPP@Azo@Gel** with 405 nm light, *cis-trans* isomerisation of **Azo** results

in a structural deformation of the gel fibres which allows for **TCPP** movement. **TCPP** movement occurs when irradiating with various excitation wavelengths, though movement is more pronounced at 405 nm owing to the overlap of both the **TCPP** and **Azo** absorption bands. As it has been shown that **ZnPcTS** is able to diffuse through gel fibres without the need for a molecular switch such as **Azo**. Combining both **ZnPcTS** and **TCPP** may provide the impetus for **TCPP** to diffuse without a molecular switch.

Initial measurements focused on **ZnPcTS@TCPP@Gel** systems with both fluorophores at a concentration of 60 μM . This concentration was chosen to gain a view of the overall fibre morphology. When irradiating the system at 642 nm (so as to excite **ZnPcTS**), it is immediately clear that the resolution is much lower than in the case of **ZnPcTS**. This could either be a consequence of **TCPP** quenching **ZnPcTS** fluorescence or incomplete encapsulation of fluorophores into the fibres, meaning fluorescence arising from fluorophores present in the interstitial liquid between fibres is clouding the view of those encapsulated. **Figure 3.33** shows an average projection of a 600-frame video collected of **ZnPcTS@TCPP@Gel** with a fluorophore concentration of 60 μM . It is apparent that fibre morphology looks to be altered by the presence of **TCPP**. In addition, randomly positioned blobs of fluorescence intensity are present, which may correspond to aggregates of **ZnPcTS**.

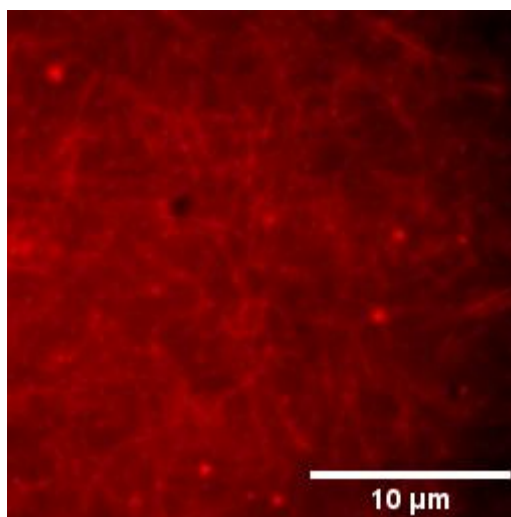


Figure 3.33. Average projection TIRF micrograph of **ZnPcTS@TCPP@Gel** [**ZnPcTS**] = 60 μM , [**TCPP**] = 60 μM . Image taken with 642 nm laser and LP filter at 650 nm. Laser power 50%.

When exciting at 405 nm (and intermittently at 642 nm between frames), **TCPP** fluorescence is obtained. It was hypothesized that providing the **ZnPcTS** with irradiation between frames whilst irradiating **TCPP** continuously may promote movement of the latter. **Figure 3.34A** is

solely **ZnPcTS**, whilst **3.34B** shows the fluorescence arising mainly from **TCPP**, as it is possible that the tail end of the Soret band of **ZnPcTS** is excited at this wavelength.

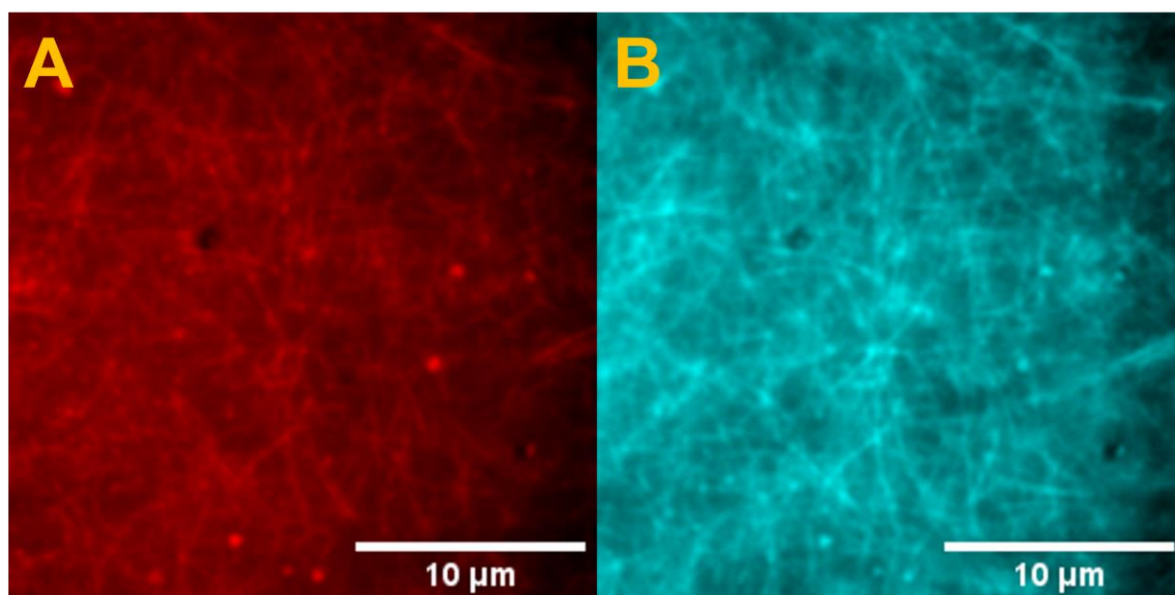
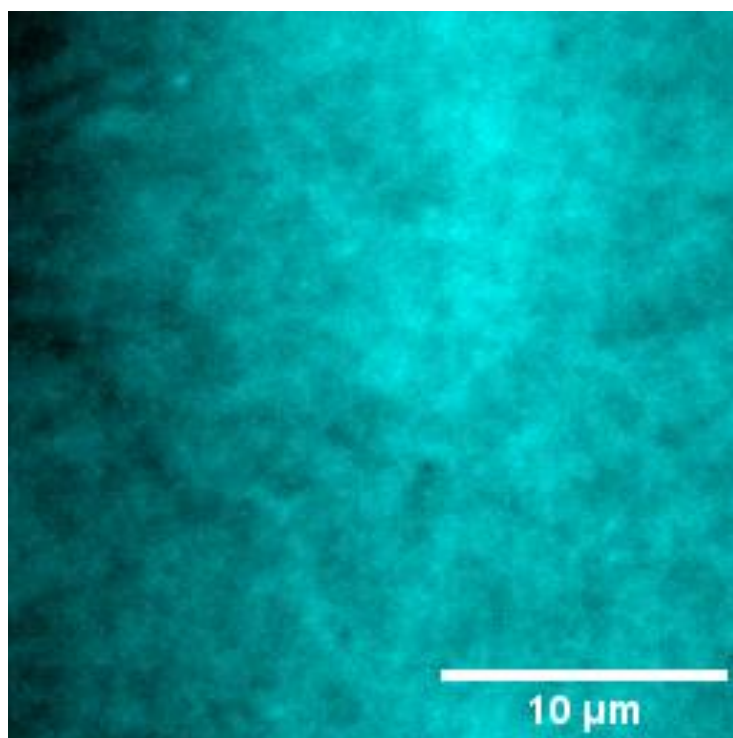


Figure 3.34. (A) Average projection TIRF micrograph of **ZnPcTS@TCPP@Gel**, $[\text{ZnPcTS}] = 60 \mu\text{M}$, $[\text{TCPP}] = 60 \mu\text{M}$, image taken with 642 nm laser and LP filter at 650 nm. Laser power 50%. (B) Average projection TIRF micrograph of **ZnPcTS@TCPP@Gel**, $[\text{ZnPcTS}] = 60 \mu\text{M}$, $[\text{TCPP}] = 60 \mu\text{M}$, image taken with 405 nm laser and LP filter at 650 nm, laser power 5%, intermittent 642 nm pulse between frames.

Gel morphology in each of the projections in **Fig. 3.34** is aligned, meaning that **TCPP** and **ZnPcTS** occupy the same fibres. **TCPP** movement is still not observed with irradiation at 405 nm and 642 nm intermittent pulses, meaning that **ZnPcTS** has little-to-no effect on the behaviour of **TCPP** within the gel fibres.

At a fluorophore (**ZnPcTS** and **TCPP**) concentration of $0.1 \mu\text{M}$, irradiation with the 405 nm laser results does not allow for any visualisation of fluorophores or fibres with just a cloudy haze seen at multiple laser powers (**Fig. 3.35**).



*Figure 3.35. Average projection TIRF micrograph of **ZnPcTS@TCPP@Gel**, $[ZnPcTS] = 0.1 \mu M$, $[TCPP] = 0.1 \mu M$, image taken with 405 nm laser and LP filter at 650 nm. Laser power 50%.*

When imaging **ZnPcTS** with a 642 nm laser, it is observed that the directional movement of the fluorophores is similar to that seen in the **ZnPcTS@Gel** system. However, the number of individual directional fluorophore movements is considerably reduced. In addition to this, many **ZnPcTS** fluorophores are unencapsulated and diffuse freely in the interstitial liquid, which may explain the poor resolution of fibres in the 60 μM fluorophore samples. MIV measurements (**Fig. 3.36**) conducted upon the **ZnPcTS** diffusion in the 0.1 μM **ZnPcTS/TCPP** samples show an average speed which is considerably higher than the gel sample containing only **ZnPcTS**. This increase in MIV of **ZnPcTS** in the presence of **TCPP** is likely a consequence of the high number of unencapsulated **ZnPcTS** fluorophores, which diffuse more quickly throughout the interstitial liquid.

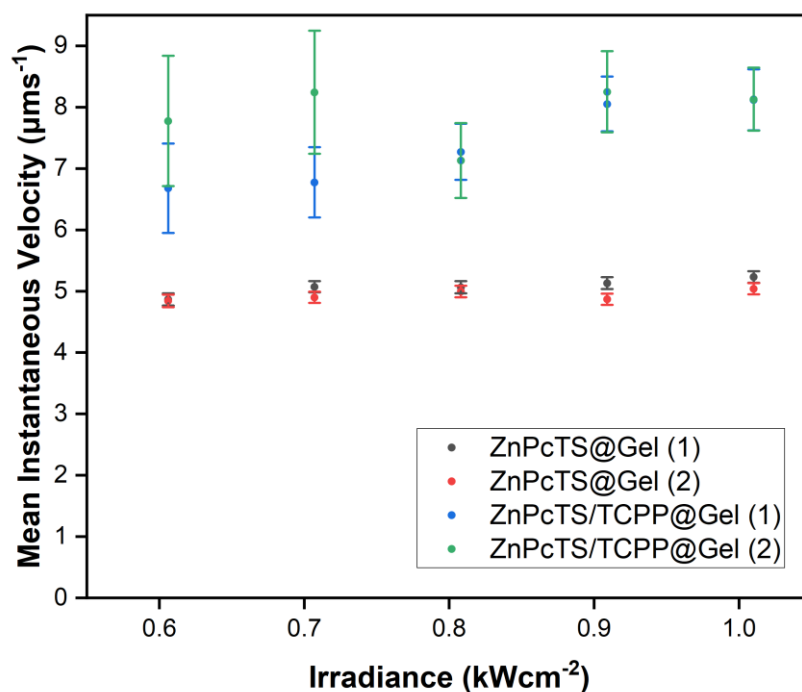
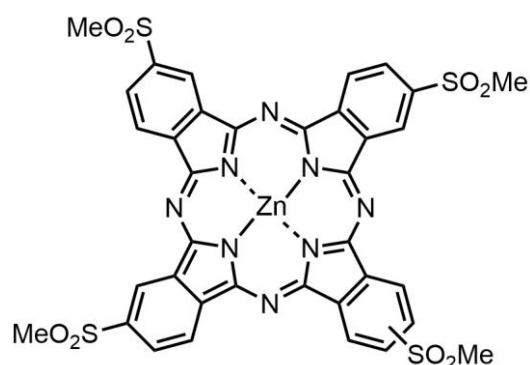


Figure 3.36. Plot of MIV against irradiance for two areas of $0.1 \mu\text{M}$ **ZnPcTS@TCPP@Gel** (green and blue) and **ZnPcTS@Gel** (black and red).

3.5. Zinc(II) phthalocyanine tetrasulfonatomethyl (**ZnPcSO₂Me**)

The compound zinc(II) tetrasulfonatomethyl phthalocyanine (**ZnPcSO₂Me**) is a fluorescent compound similar in structure to **ZnPcTS** though possessing four sulfonatomethyl groups instead of sulfonic acid groups as in the case of **ZnPcTS**. This compound therefore provides a unique opportunity to investigate the electrostatic interactions between the peripheral groups of the phthalocyanine fluorophores and the cationic supramolecular gelator network. As a neutral compound, **ZnPcSO₂Me** would still be expected to be at least partially incorporated into the gel fibres, though the lack of ionic character should result similar diffusion behaviour to that seen with **ZnPcTS**.



ZnPcSO₂Me

As a non-water soluble compound and unlike **ZnPcTS**, **ZnPcSO₂Me** had to be solvated in the ethanolic phase containing **1.2Br** prior to gel preparation. Macroscopically, gel formation was not observably altered by this change. The absorption profile of **ZnPcSO₂Me** indicated that most of the fluorophore was encapsulated within the gel fibres (**Fig. 3.37**). In 1:1 water-ethanol solution, the absorption spectrum of **ZnPcSO₂Me** suggests a considerable degree of aggregation brought about by the interaction of hydrophobic phthalocyanine with the partially aqueous environment. In the **1.2Br** gel, however, the absorption profile of **ZnPcSO₂Me** appears significantly non-aggregated.

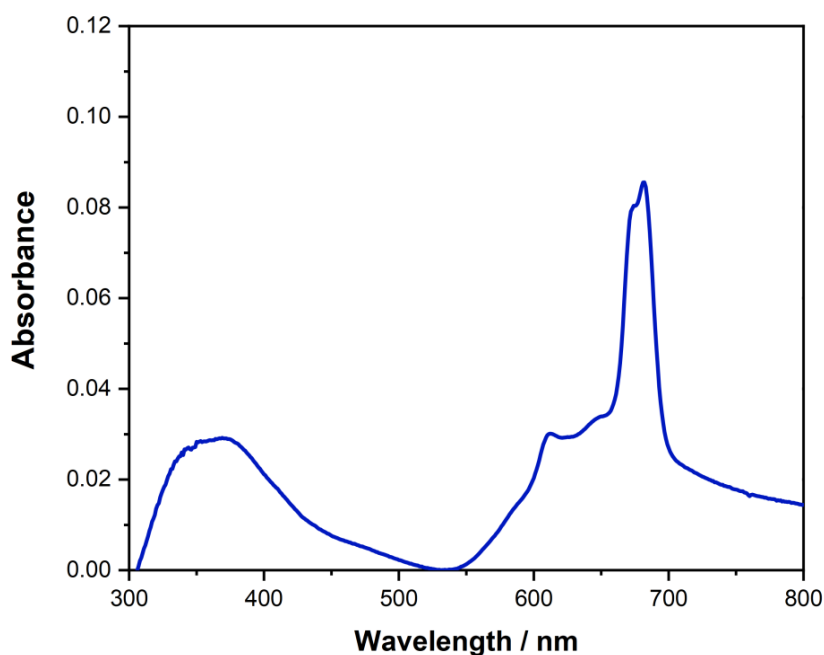


Figure 3.37. UV-Visible absorption spectrum of **ZnPcSO₂Me@Gel** with $[\text{ZnPcSO}_2\text{Me}] = 100 \mu\text{M}$.

Under imaging with a 642 nm laser, **ZnPcSO₂Me** fluorophores can be seen to be largely confined to the gel fibres as with **ZnPcTS** (**Fig. 3.38**). The signal-to-noise ratio in this system appears lower than that of **ZnPcTS@Gel**, which could be a consequence of some unencapsulated **ZnPcSO₂Me** fluorophores residing in the interstitial liquid between gel fibres. Notably, there is fluorophore diffusion occurring along fibre pathways. This finding supports the claim that the electrostatic interaction between fluorophore and the cationic gelator molecules that constitute the fibres is responsible for fluorophore diffusion.

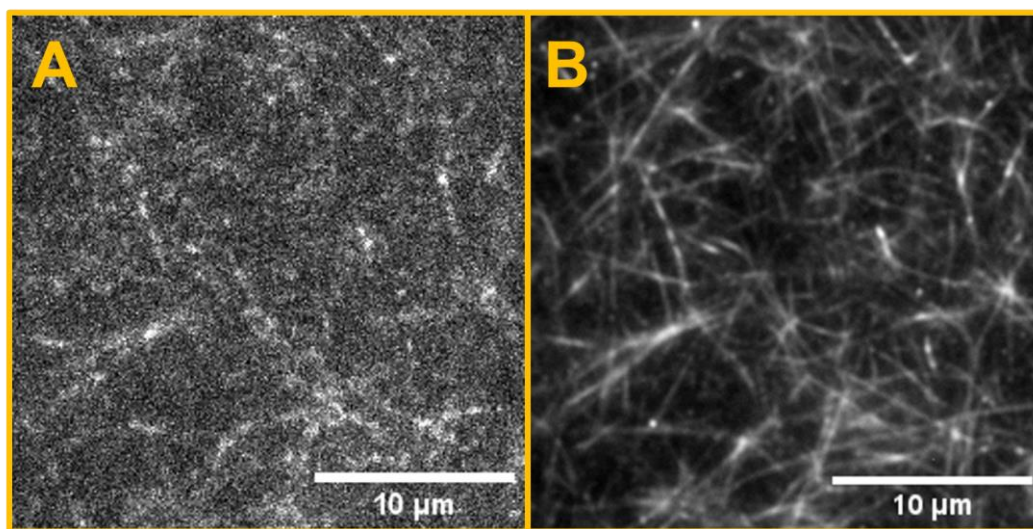


Figure 3.38. TIRF micrographs of a **ZnPcSO₂Me@Gel** sample containing a **ZnPcSO₂Me** concentration of 0.1 µM. (A) TIRF micrograph of a single frame (of 600) where some individual fluorophores can be observed, and fibre morphology is discernible. (B) TIRF micrograph of the average projection over the 600 frames referenced in A highlights the gel fibre morphology. All images taken with 642 nm laser and LP filter at 650 nm. Laser power 100%.

Despite being only at a concentration of 0.1 µM, individual **ZnPcSO₂Me** fluorophores are not discernible enough for movement to be quantifiable through single particle tracking. It is possible for the fluorophore movement to be represented as an ‘on/off’ plot as seen in **Fig. 3.39**. Like with **ZnPcTS**, along particular fibres, specific regions of interest fluctuate with fluorescence intensity as fluorophores move in and out.

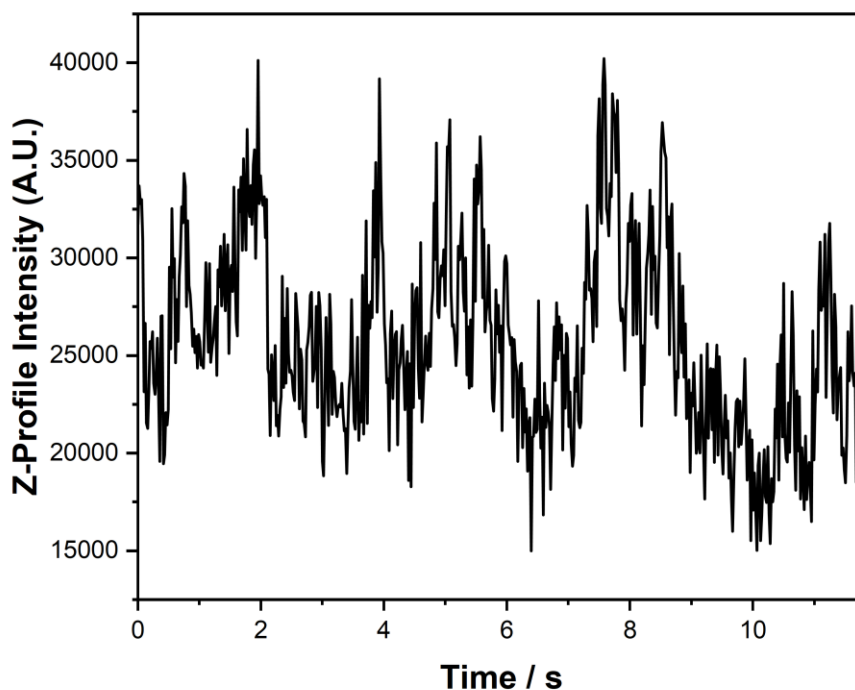


Figure 3.39. Z-profile intensity plot over 600 frames (11.82 s) shows fluorescence intensity fluctuations which represents ZnPcSO_2Me fluorophore movement within the 1.2Br gel.

3.6. Conclusion

ZnPcTS has been found, through TIRF microscopy, to diffuse through the fibres of a hydrated 1.2Br gel. At a ZnPcTS concentration of $10\ \mu\text{M}$, diffusion is observable by eye and average projections gathered over several hundred video frames shows gel morphology. When the ZnPcTS concentration is lowered to $0.1\ \mu\text{M}$, individual fluorophore molecule diffusion can be observed. This individual fluorophore motion allowed for the quantification of such movement using both MIV and MSD analysis. Through analysis of MSD curves, it was found that the diffusion observed was confined in nature. Both MIV and MSD analysis a linear relationship between the irradiance experienced by the sample and the resulting speed of fluorophores. The introduction of the bulky acid CSA at a concentration of $1.2\ \text{mM}$ into the gel system resulted in an approximately twofold increase in both the MIV and diffusion coefficient compared to the control without CSA , at almost any irradiance value. The addition of PTSA at a concentration of $1.2\ \text{mM}$ into the gel system resulted in ZnPcTS not being taken up into the gel fibres and were diffusing in the interstitial liquid between them. When the PTSA concentration was reduced to roughly equimolar values relative to ZnPcTS , the fluorophores were largely present in gel fibres though some expelled fluorophores were seen. Increasing

PTSA concentration gradually increased **ZnPcTS** speed through the weakening of electrostatic interactions between the sulfonate anions of the fluorophore and the cationic heads of the lamellae as a result of protonation.

When a sulfonated porphyrin (**TPPS**) was incorporated into the gel system at a concentration of 10 μM , gel morphology could be observed and differed from that seen in the **ZnPcTS@Gel** system. Fluorescence arising from between fibres indicated that **TPPS** was not entirely taken up by the gel fibres. Significant photobleaching of **TPPS** in the gel was also observed.

When a mixed system containing **ZnPcTS** and the tetracarboxylated porphyrin **TCPP** was analysed using TIRF microscopy, the signal-to-noise seen for the emission arising from 642 nm excitation was lower than in the case of **ZnPcTS** alone. This decrease in signal was either a result of fluorescence quenching by **TCPP** or by noise being caused by unencapsulated fluorophores between gel fibres. Stationary spots corresponding to **ZnPcTS/TCPP** aggregates were also observed. Excitation at 405 nm and 642 nm laser light resulting in emission from the same fibres, meaning that **ZnPcTS** and **TCPP** occupied the same fibres. When fluorophore concentration was dropped for diffusion analysis, 405 nm irradiation resulted in a haze where no individual fluorophores or fibres could be seen. 642 nm irradiation did allow for **ZnPcTS** diffusion analysis, and it was found that their average speed was higher in the presence of **TCPP** than without. This speed increase could be a consequence of interactions between the porphyrin and phthalocyanine, or a result of unencapsulated **ZnPcTS**.

A sulfonatomethyl phthalocyanine (**ZnPcSO₂Me**), when incorporated into the imidazolium gel, showed a gel morphology that differed from that of **ZnPcTS@Gel**. Diffusion of this fluorophore was also observed though could not be quantified. The z-profile plot over a fibre region of interest displayed this movement, with regular peaks and troughs referring to the movement of **ZnPcSO₂Me** fluorophores.

In summary, this chapter provides an opportunity to study confined diffusion at the microscale, allowing us to gain insights into the local environment of gel fibres and the impact of added molecules on their properties. Additionally, it serves as a valuable means to investigate the behaviour of fluorophores and how their dynamics can be influenced by the presence of additional species such as acids.

3.7. Experimental

3.7.1. General procedures

Solvents and reagents used in this study were of an analytical grade. Zinc(II) phthalocyanine tetrasulfonic acid was purchased from PorphChem. The gels described in this study were mostly prepared at a 1:1 water-ethanol ratio (though 6:4 and 7:3 water-ethanol ratio control samples were used once) though always with a final **1.2Br** gelator concentration of 12 mM. For experiments with **ZnPcTS/TPPS/TCPP** fluorophores, a 2.4 mM stock solution of the fluorophore in Milli-Q water (either with or without 4 equivalents of NaOH) was prepared and subsequently diluted in a glass vial to achieve the desired concentration of fluorophore in the final gel. TIRF samples were prepared by mixing the diluted fluorophore solution with an equal volume of an ethanolic 24 mM **1.2Br** gelator solution. Rapid and thorough mixing of the ethanolic and aqueous solutions was carried out to ensure homogeneity before transferring the gelating mixture into a compartment well of the sample holder which was then left undisturbed at room temperature to allow gel formation. A small amount of Blu Tak was fitted over the top of the well to limit ethanol evaporation. For solid-state fluorescence and absorption measurements, the gelating mixture (still in the micropipette) was quickly transferred to a cuvette of path length 1 mm. For FTIR measurements, gels were formed in the glass vials and were then dried overnight under vacuum desiccation to form xerogels. The gelation time of the gels prepared in this study were always below one minute, and gel formation was deemed to have occurred when no flow was exhibited during a vial-inversion test.

Fluorescence imaging was performed on a Zeiss Elyra PS1 super resolution microscope equipped with Zen 2012 acquisition and processing software, fitted with an alpha Plan-Apochromat 100×/1.46 Oil DIC M27 Elyra objective lens operating in TIRF (Total internal reflection fluorescence), using either a 642 nm (150 mW at 100% LP) or 405 nm (4.3 mW / cm²) laser and emission filters LP 650 nm for **ZnPcTS**, **TPPS**, and **TCPP**. A droplet of 30 °C oil (Zeiss, Immersol™ 518F/30°) was cast on the objective before imaging. The TIRF angle used was 68°. Automatic focusing was always adopted to keep constant the desired focal plane during the acquisition. Image acquisition was performed in the TIRF modality. Videos recorded in TIRF were generally acquired with an EM-CCD (Andor EM-CCD camera iXon Du 897) with 200 gain and 18 ms exposure time per frame over 600 frames. For visualisation purposes, 600 images of the recording were collapsed into single image (Z project in Fiji) using either average or maximum intensity projections. Maximum projections displayed all maximum intensity values (signals from single molecules) cumulatively, therefore resulting in

an image revealing the fibres scaffolds along which the fluorophores diffused. Average projections calculated the average intensity for each pixel, and therefore results in a view of the morphology with a significant amount of noise removed. Samples were prepared directly into CELLview™ Microscopic Slides with Glass Bottoms by Greiner Bio-One GmbH that have a 10 well compartmentalisation block allowing to form the gel in situ and perform the imaging directly without any further sample manipulation. Image processing was carried out with Fiji image analysis software. Particle tracking was carried out on the videos of the 0.1 μM **Fluorophore@Gel** samples using the TrackMate (v6.0.3) plugin within Fiji. Denoising of the raw videos was achieved by the consecutive subtracting of the average projection. A median filter was then applied to the videos before particle tracking analysis to further limit the noise. This denoising process shown in **Fig. 3.40**. The built-in DoG detector was used to identify spots corresponding to fluorophores, whilst the LAP tracker was employed to track the individual fluorophores. The instantaneous velocity measurements produced for each video, typically numbering in the thousands, were averaged to yield a mean instantaneous velocity for each video collected. MSD analysis was carried out through the ‘msdanalyzer’ toolkit on MATLAB developed by Tinevez *et al.*

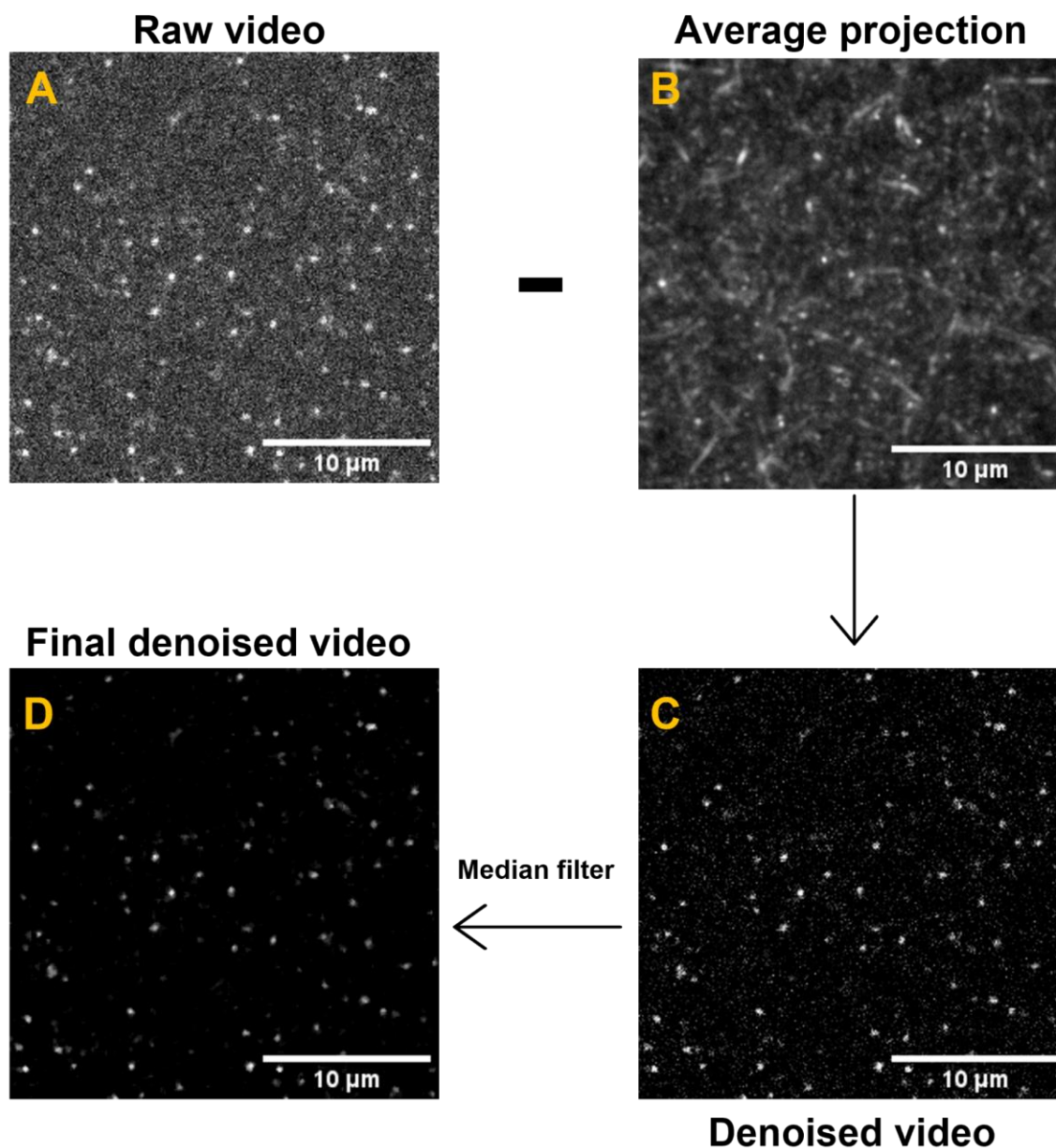


Figure 3.40. Process for denoising raw videos. (A) TIRF micrograph of a single frame from the raw video captured at a **ZnPcTS** concentration of $0.1 \mu\text{M}$ which is intended to represent the 600 frame video. (B) First average projection of the video represented by A. (C) Result of the subtraction of the average projection from each frame of the video, with subsequent lowered noise level. Steps A-B repeated two further times. (D) Result of applying a median filter (radius 1 micron) to the denoised video represented by C, which further reduces level of noise. Imaging details: laser 642 nm, emission filter LP 650 nm, laser power 100%.

UV-Visible extinction spectroscopy was performed using a Cary 5000 UV-Visible spectrophotometer (Agilent). Fluorescence spectroscopy and absolute fluorescence quantum yield measurements were carried out on a FLS 980 spectrometer (Edinburgh Instruments)

equipped with a front face sample holder or integrating sphere. The fluorescence and fluorescence quantum yield measurements were carried out using quartz cuvette of path length 1 mm and 10 mm, respectively.

Powder X-ray diffraction patterns were acquired with a PANalytical MPD X-ray powder diffractometer in Bragg–Brentano geometry, using Cu K α radiation (K α 1 = 1.540560 Å and K α 2 = 1.544390 Å) with a voltage and current of 40 kV and 40 mA, respectively. Each sample was prepared from 1.5 mL of gel and was dried under reduced pressure for three days to obtain the xerogel. The powder was collected and placed on a brass sample holder for data acquisition over the 2 θ range between 2 and 30°, with a step size of 0.013°. Rheological measurements were taken using an Anton Paar Physica MCR 301 rheometer. Infra-red spectra were recorded on a Bruker Tensor 27 instrument equipped with a Pike GladiATR attachment with a diamond crystal.

3.8. References

1. N. L. Thompson, T. P. Burghardt, D. Axelrod, *Biophys. J.*, 1981, 33, 435 – 454.
2. D. Axelrod, N. L. Thompson, T. P. Burghardt, *J. Microsc.*, 1983, 129, 19 – 28.
3. J. W. Lichtman, J. Conchello, *Nat. Methods*, 2005, 2, 910 – 919.
4. M. Oheim, A. Salomon, A. Weissman, M. Brunstein, U. Becherer, *Biophys. J.*, 117, 795 – 809.
5. J. R. Magana, B. Gumi-Audenís, R. P. Tas, L. Gascoigne, D. L. Atkins, I. K. Voets, *Chem. Eur. J.*, 2020, 26, 15330 – 15336.
6. R. Xue, C. Ge, K. Richardson, A. Palmer, M. Viapiano, J. L. Lannutti, *ACS Appl. Mater. Interfaces*, 2015, 7, 8606 – 8614.
7. Y. Fan, H. Sheen, Z. Chen, Y. Liu, K. Tsai, K. Wu, *Microfluid. Nanofluidics*, 2015, 19, 85 – 94.
8. M. Rose, N. Hirmiz, J. M. Moran-Mirabal, C. Fradin, *Membr. J.*, 2015, 5, 702 – 721.
9. R. Walder, D. K. Schwartz, *Soft Matter*, 2011, 7, 7616 – 7622.
10. N. Ruthardt, D. C. Lamb, C. Bräuchle, *Mol. Ther.*, 2011, 19, 1199 – 1211.
11. B. Roux, T. Allen, S. Bernèche, W. Im, *Q. Rev. Biophys.*, 2004, 37, 15 – 103.
12. S. S. Stojilkovic, J. Tabak, R. Bertram, *Endocr. Rev.*, 2010, 31, 845 – 915.
13. Y. Zhong, J. Wang, W. Liu, Y. Zhu, *Mol. Med. Rep.*, 2013, 8, 311 – 319.
14. R. Drummond, C. Huang, P. S. Grant, S. R. Duncan, *J. Power Sources*, 2019, 433, 126579.
15. A. C. Forse, J. M. Griffin, C. Merlet, J. Carretero-Gonzalez, A. O. Raji, N. M. Trease, C. P. Grey, *Nat. Energy*, 2017, 2, 16216.

16. E. Bi, H. Chen, F. Xie, Y. Wu, W. Chen, Y. Su, A. Islam, M. Grätzel, X. Yang, L. Han, *Nat. Commun.*, 2017, 8, 15330.
17. P. Benedek, O. K. Forslund, E. Nocerino, N. Yazdani, N. Matsubara, Y. Sassa, F. Jurányi, M. Medarde, M. Telling, M. Månsson, V. Wood, *ACS Appl. Mater. Interfaces*, 2020, 12, 16243 – 16249.
18. R. Rossi, B. E. Logan, *J. Chem. Eng.*, 2021, 422, 130150.
19. R. Rossi, G. Baek, P. E. Saikaly, B. E. Logan, *ACS Sustainable Chem. Eng.*, 2021, 9, 2946 – 2954.
20. Y. Guo, J. Bae, Z. Fang, P. Li, F. Zhao, G. Yu, *Chem. Rev.*, 2020, 120, 7642 – 7707.
21. B. J. Morgan, *Philos. Trans. Royal Soc. A*, 2021, 379, 20190451.
22. M. F. Serag, M. Abadi, S. Habuchi, *Nat. Commun.*, 2014, 5, 5123.
23. A. Robson, K. Burrage, M. C. Leake, *Philos. Trans. Royal Soc. B*, 2013, 386, 20120029.
24. R. L. Benoit, D. Boulet, M. Fréchet, *Can. J. Chem.*, 1988, 66, 12.
25. M. Samperi, L. Pérez-García, D. B. Amabilino, *Chem. Sci.*, 2019, 10, 10256 – 10266.
26. M. Samperi, David Limón, D. B. Amabilino, L. Pérez-García, *Cell Rep.*, 2020, 1, 100030.
27. M. Rodrigues, A. C. Calpena, D. B. Amabilino, M. L. Garduño-Ramírez, L. Pérez-García, *J. Mater. Chem. B*, 2014, 2, 5419 – 5429.
28. K. N. Fish, *Curr. Protoc. Cytom.*, 2022, 2, e517.
29. M. Samperi, B. Bdiri, C. D. Sleet, R. Markus, A. R. Mallia, L. Pérez-García, D. B. Amabilino, *Nat. Chem.*, 2021, 13, 1200 – 1206.
30. S. Marullo, F. D'Anna, M. Cascino, R. Noto, *J. Org. Chem.*, 2013, 78, 10203 – 10208.
31. J. Tinevez, N. Perry, J. Schindelin, G. M. Hoopes, G. D. Reynolds, E. Laplantine, S. Y. Bednarek, S. L. Shorte, K. W. Eliceiri, *Methods*, 2017, 115, 80 – 90.
32. P. Burgos, Z. Zhang, R. Golestanian, G. J. Leggett, M. Geoghegan, *ACS Nano*, 2009, 3, 3235 – 3243.
33. M. F. Serag, S. Habuchi, *Nat. Commun.*, 2017, 8, 15675.
34. J. P. Guthrie, *Can. J. Chem.*, 1978, 56, 17.
35. S. Nistorescu, A. Udrea, M. A. Badea, I. Lungu, M. Boni, T. Tozar, F. Dumitrache, V. Maraloiu, R. G. Popescu, C. Fleaca, E. Andronescu, A. Dinischiotu, A. Staicu, M. Balas, *Pharmaceutics*, 2021, 13, 2130.
36. D. A. Caminos, E. N. Durantini, *Biochem. Mol. Bio. Educ.*, 2007, 35, 64 – 69.
37. H. Kato, K. Komagoe, T. Inoue, K. Masuda, T. Katsu, *Photochem. Photobiol.*, 2018, 17, 954 – 963.

Chapter 4

**Synthesis of galactose glycopolymers and
preparation of gel-polymer hybrid
materials containing photosensitizer**

4.1. Background

As discussed in the introduction, polymers, which encompass two main types of polymerisations, step-growth (SG) and chain-growth (CG), are ubiquitous in the research surrounding hydrogels and soft materials more generally. Recent advances in synthesis techniques have facilitated the production of highly specialized and functional polymers.^{1,2}

SG polymerisation is a fundamental process where monomers with multiple reactive sites come together to create polymers (**Fig. 4.1**). As these monomers react, they form bonds, either by condensation or addition reactions. Understanding SG polymerisation is crucial for customising polymer properties and developing advanced materials, making it a prominent subject in polymer chemistry and materials research.³⁻⁵

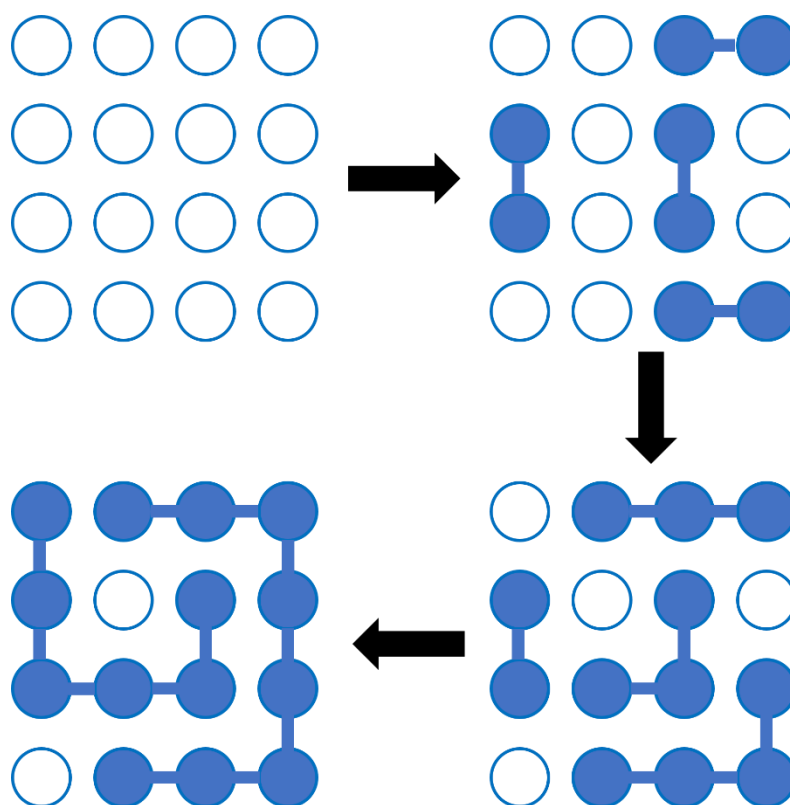
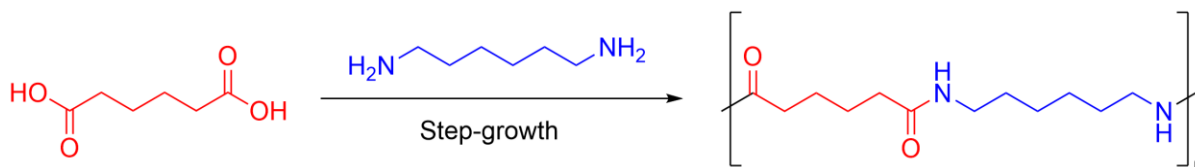


Figure 4.1. General representation of SG polymerisation.

A famous example of a polymer prepared using SG polymerisations is Nylon 66 (**Scheme 4.1**), which is produced through condensation of hexamethylenediamine with adipic acid.



Scheme 4.1. Reaction for the step-growth polymerisation of Nylon 66 through the condensation of hexamethylenediamine with adipic acid.

SG can also be carried out with starting reagents which possess three or more functionalisation sites and can be used to form branched and crosslinked structures, a technique that has been utilized for preparing various types of materials including coatings, network polymers, and hydrogels.⁴⁻⁶

CG polymerisations, on the other hand, often employ radical initiators to begin the growth of polymer chains. Mechanistically, CG polymerisation differs from SG polymerisation as the former displays a somewhat linear increase in chain length over time whereas the latter only forms the long chains towards the very end of the reaction. Also, there are specific initiation and termination steps which need to occur for polymerisation to be complete.⁷ Within CG polymerisation techniques, there are several different classes which possess their own advantages and drawbacks. Free-radical polymerisation is a CG technique whereby an activated radical initiator (often itself activated thermally or through photolysis) attacks a monomer, which then goes on to attack another monomer creating a propagating polymer chain (Fig. 4.2).

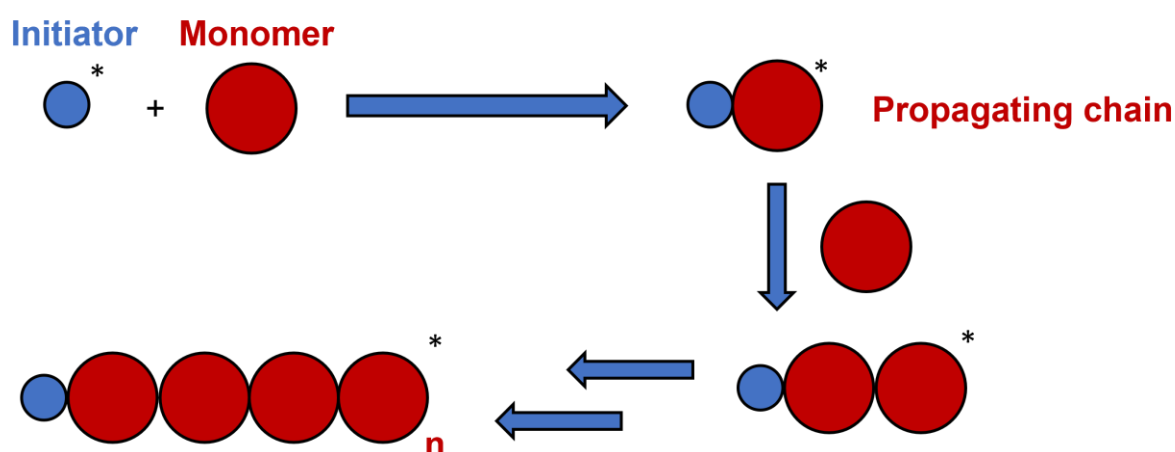


Figure 4.2. General representation of CG polymerisation.

In radical polymerisation, initiators are activated through dissociation of the molecule by an external stimulus. Ideally, radical initiators should be stable at room temperature and ambient conditions though be quick to dissociate given the intended stimulus. An example of a

commonly used initiator is the azo compound azobisisobutyronitrile (AIBN) shown in **Fig. 4.3**. When exposed to temperatures above 40 °C, the molecule decomposes forming nitrogen gas and two cyanoprop-2-yl radicals which can begin the process of polymerisation.

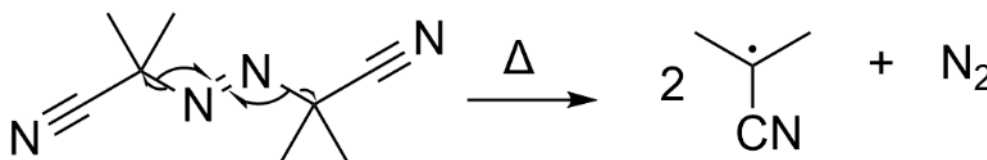


Figure 4.3. Under thermal activation, the radical initiator AIBN dissociates resulting in the formation of nitrogen gas and two cyanoprop-2-yl radicals.

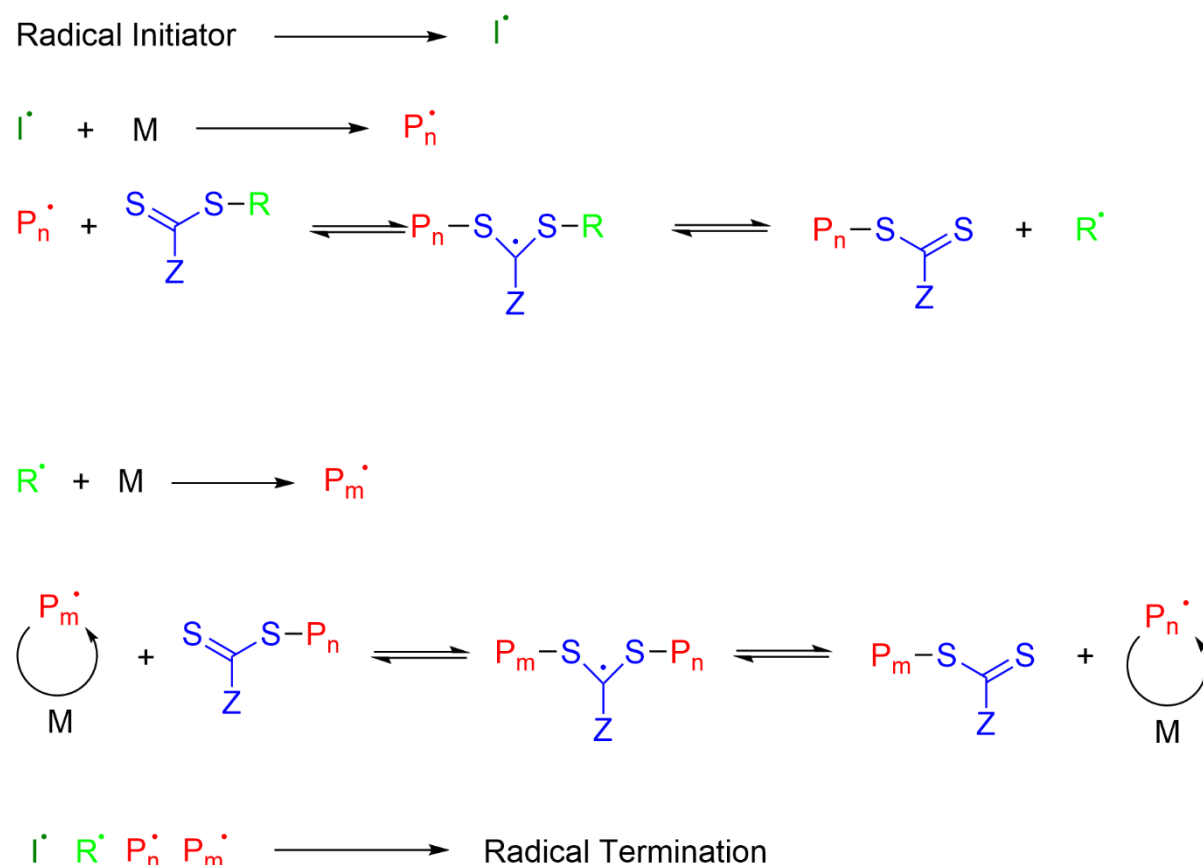
Once the initiator is converted to an active radical, the propagation process occurs. During propagation, the activate initiator groups attack the monomer leaving an active centre now upon the monomer. This activated monomer is then able to attack other monomer units, resulting in a propagating chain. Finally, chain termination occurs whereby the active site of one monomer reacts with that of another forming a covalent bond resulting in a completed polymer chain.

Within CG polymerisations, more generally, are further class of polymerisations known as reversible-deactivation radical polymerisations (RDRP's). Often described as 'living' or 'controlled' polymerisations, RDRP's are versatile techniques that can be used on a wide array of monomers. Atom-transfer radical polymerisation (ATRP) is an example of an RDRP which utilizes transition metal catalysts to form carbon-carbon bonds. Such transition metal catalysts are often copper based containing a functionalized ligand. ATRP has been used to form branched copolymers which, upon modulation of reaction conditions, can form different of gels.⁸ Nitroxide-mediated radical polymerisation (NMP) is another type of RDRP which uses nitroxide initiators and shows promise for the preparation of a broad range of supramolecular architectures.⁹

Reversible addition-fragmentation chain-transfer (RAFT) polymerisation is further class of RDRP which makes use of a chain-transfer agent (CTA) to govern the propagation of the polymer chains. Discovered towards the turning of the 21st century, RAFT allows for the formation of polymers with reliable molecular weights, robust end-group functionality, and low mass dispersity.¹⁰

Mechanistically, RAFT polymerisation differs to the approach taken with ATRP and NMP where the persistent radical effect is relied upon and no radical initiator is required.¹¹ RAFT polymerisation makes use of degenerative transfer, where a source of radicals from an initiator

is required.¹² As mentioned, the presence of a CTA is required for the polymerisation to occur. RAFT CTAs typically possess a thiocarbonylthio group which can react with a radical species.¹³ CTA's containing various attached groups can be used to modulate reactivity and can also contain groups that can be functionalized post-polymerisation. The general mechanism for RAFT polymerisation is shown in **Scheme 4.2**.



Scheme 4.2. Mechanism for RAFT polymerisation. Image adapted from Ref. 6 with permission from the ACS Publications.

The first step as seen in **Scheme 4.2A** is radical initiation which can be carried out depending on the activation requirement of the specific initiator to form radical \mathbf{I}^{\bullet} . Step **B** involves the propagation of radical chains caused the reaction of \mathbf{I}^{\bullet} with the monomer \mathbf{M} to form the propagating polymeric radical \mathbf{P}_n^{\bullet} , which enters an equilibrium between active and dormant species *via* the CTA as seen in step **C-E**. Step **D** is the re-initiation of the monomer by the leaving group radical from the CTA, \mathbf{R}^{\bullet} , to form the propagating chain \mathbf{P}_m^{\bullet} . \mathbf{P}_m^{\bullet} then enters the main RAFT equilibrium in step **E**. Here, the existing radicals (and, consequently, possibilities for polymer chain expansion) are distributed across all species that have not undergone termination. Ideally, these radicals are evenly distributed, ensuring that chains have uniform

growth opportunities and a narrow polydispersity. Finally, termination occurs between the radical species still left in the reaction shown in step F.

In practice, RAFT polymerisation is largely conducted upon monomers containing vinyl groups which provide the backbone for the final polymer. Within this class of vinyl compounds, the vinyl groups themselves are often conjugated (**Fig. 4.4**) to other double bonds, to an aromatic ring (as in the case of styrene), or to a carbonyl groups (in the cases of acrylates or acrylamides).^{14,15} This conjugation renders the monomer more reactive towards polymerisation, though less reactive vinyl compounds are able to undergo RAFT polymerisation.

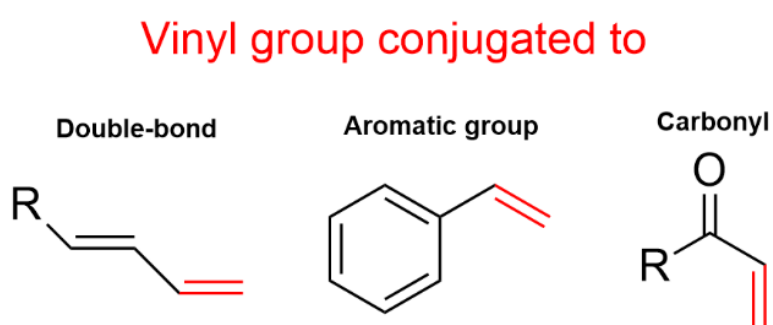


Figure 4.4. Vinyl groups are made more reactive by conjugation to either double bonds, aromatic groups, or carbonyl groups.

Glycopolymers are synthetic polymers containing pendant sugar groups as the repeating unit. They have found myriad uses in different applications ranging from being employed as biomaterials for biomedical applications to acting as sensors.^{16,17} In addition, the preparation of nanomaterials such as unimolecular carriers and nanoparticles has been shown by use of certain glycopolymers.^{18,19} In practice, glycopolymers can be prepared through the polymerisation of monomers containing sugar groups or by post-polymerisation functionalisation using sugar-based reagents. When synthesized through RAFT polymerisation, it is the former approach of polymerising sugar-based monomers that is often chosen, as it allows for homogenous distribution of sugar units throughout each polymer chain.²⁰

Hydrogels can also be accessed through the preparation of glycopolymers.²¹ A hydrogel prepared by Deng *et al.* used collagen and a galactopyranose-based glycopolymer and has shown promise for corneal applications.²² It was also shown that incorporation of the glycopolymer enhanced the tensile strength and stability of the composite gel compared with

that of the collagen gel control sample. A lactobionate-based glycopolymer hydrogel was prepared by coupling a boronic acid to the diol present in the lactobionate.²³ This glycopolymer system exhibited high insulin loading into its porous structure along with sensitivity to glucose, rendering the hydrogel an attractive system for controlled insulin delivery.

In this chapter, the synthesis of galactose glycopolymers will be described along with their incorporation within the 1,3-bis[(3-octadecyl-1-imidazolium)methyl]benzene di-bromide gel (**1.2Br@Gel**) system to produce a low molecular weight (LMW) gelator-glycopolymer hybrid system. Being a partially anionic species, it is anticipated that the targeted galactose glycopolymer might interact with the cationic groups on the gel, potentially disrupting the system. Given its nature as a multicomponent system, co-assembly is conceivable and could contribute to enhanced rheological properties, along with alterations to the behaviour of encapsulated fluorophores with respect to the work carried out in the previous chapters. The synthesis of the CTA used in the polymerisation will also be discussed. This novel hybrid gel material will then be characterized and analysed using a range of techniques.

4.2. Glycopolymer and chain-transfer agent synthesis

4.2.1. CTA synthesis (sodium 3-[(1-oxo-1-prop-2-yn-1-ylamino-propan-2-yl-thio)carbonothioyl]thio} propane-1-sulfonate)

RAFT polymerisation requires a CTA to control the final molecular weight and polydispersity when free-radical mechanism is employed. The chosen CTA must possess a reactive group which can be easily broken by a monomer radical. This group is typically a thiocarbonylthio-type moiety, which are present in dithioesters, dithiocarbamates, and trithiocarbonates.^{10,24,25} The choice of CTA is dependent upon the reaction conditions and crucially upon the choice of monomer. Trithiocarbonate CTAs are commonly used as a result of their relatively high stability to hydrolysis, high transfer constants (measure of the extent to which the CTA can control rates of propagation/transfer) and synthetic accessibility. Given the monomers and final polymers are water soluble, the target CTA should contain an ionic group to confer aqueous solubility. The chosen CTA was therefore sodium 3-[(1-oxo-1-prop-2-yn-1-ylamino-propan-2-yl-thio)carbonothioyl]thio} propane-1-sulfonate (**CTA1**) (**Fig. 4.5**). **CTA1** possesses the core trithiocarbonate group at the centre of the molecule along with an anionic sulfonate group at one end, and propargyl group at the other. The presence of this propargyl group allowed for potential post-polymerisation functionalisation through click chemistry. Fluorescent moieties have been attached to such polymers using this approach.²⁶

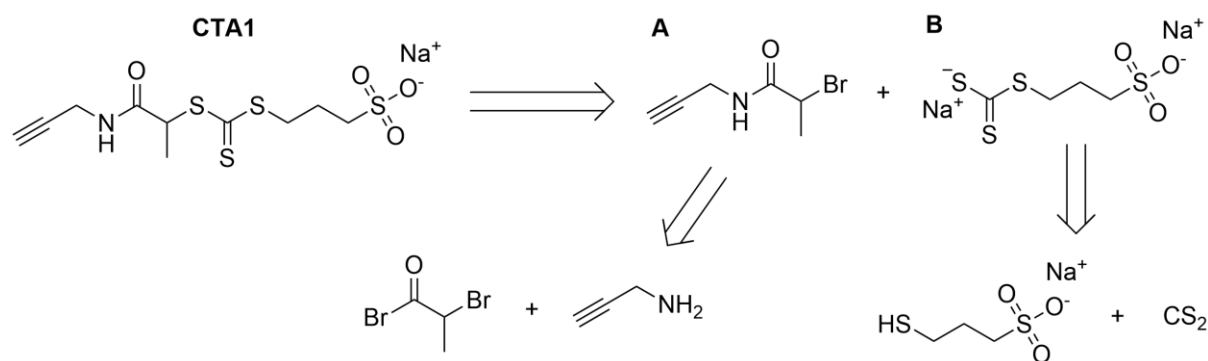


Figure 4.5. Scheme of the retrosynthesis of **CTA1** to compounds **A** and **B**. The retrosynthesis of these precursor compounds (**A** and **B**) to commercially available starting reagents are also shown.

Figure 4.5 also shows a retrosynthetic scheme whereby the **CTA1** product is formed through the reaction of 2-bromo-*N*-(prop-2-yn-1-yl)propanamide (**Fig. 4.5A**) with sodium 3-(dithiocarboxylatothio)propyl sulfonate (**Fig. 4.5B**). As **A** and **B** are not commercially available, these compounds must be synthesized as shown from the further retrosynthesis in **Fig. 4.5**.

The synthesis of 2-bromo-*N*-(prop-2-yn-1-yl)propanamide (**A**) was carried out through the reaction of 2-bromopropionyl bromide with propargylamine in THF. After stirring at room temperature for 2 hours, an acidic workup was carried out upon the crude mixture before being purified by column chromatography. The final product **A** was obtained in 60% yield. Sodium 3-(dithiocarboxylatothio)propyl sulfonate was synthesized through the reaction of sodium 3-mercaptopropyl sulfonate with carbon disulfide in methanol under basic conditions. In the presence of NaOH, the thiol group is deprotonated, allowing it to attack into the carbon disulfide resulting in a trithiocarbonate compound. Early attempts of this reaction led to low conversions of around 40 – 50%. The solubility of sodium 3-mercaptopropyl sulfonate in methanol is relatively low owing to its sulfonate group, so in later attempts this starting material was milled in a pestle and mortar beforehand to aid solubilisation. Also, sonication was employed to maximise the amount of sodium 3-mercaptopropyl sulfonate in solution and the duration of this sonication was lengthened in response to the initial poor conversions. In addition to these considerations, considerable degassing of the methanol solvent was carried out by injecting a steady stream of argon gas for around one hour in order to limit the amount of oxygen in the solvent which could affect the reaction. With these considerations in place, conversion was only improved by ~ 10% over 24 hours. The duration of reaction was then increased to 48 hours. This increase in reaction duration led to a conversion of > 90%. It is clear from the conversion seen that the further 24 hours of reaction time was necessary to reach

completion. The yellow solid obtained from the reaction was washed with diethyl ether to remove impurities and was characterized as the product **B** obtained in 75% yield.

The final reaction to form **CTA1** required the reaction of product **A** and **B** in acetone. The poor solubility of the **B** dianion in acetone necessitated the use of 15-crown-5, which forms a complex with the sodium cations and increases the solubility of **B**. Upon reaction completion and workup, a significant amount of crown ether co-eluted along with the product. Precipitation of the product in diethyl ether removed a considerable amount of the co-eluted crown ether, though trace amounts remained which could not be removed using this method. To remove the trace crown ether from the product, Amberlite sodium ion exchange resin was used. This resin consists of beads containing a polymer matrix with sodium cations on its exterior. When mixed with crown ether and product in water, the crown ether is preferentially bound to these beads which can be simply filtered out of the mix. After stirring with this resin in water, the product was filtered and attempted to be freeze-dried. Issues with freeze-dryer equipment rendered the technique unviable, and the water removed instead by vacuum distillation. Removing the water using vacuum distillation required relatively elevated temperatures and contributed to **CTA1** product degradation observable using ^1H nuclear magnetic resonance (NMR) spectroscopy (**Fig. 4.6**). In addition, multiple Amberlite mixings were required to remove the majority of the crown ether, exacerbating the degradation. ^1H NMR spectroscopy suggests the degradation was likely hydrolysis of the trithiocarbonate group. This degradation required a second column chromatography purification step to remove the hydrolysed product, with the degradation resulting in a significant diminishing of yield.

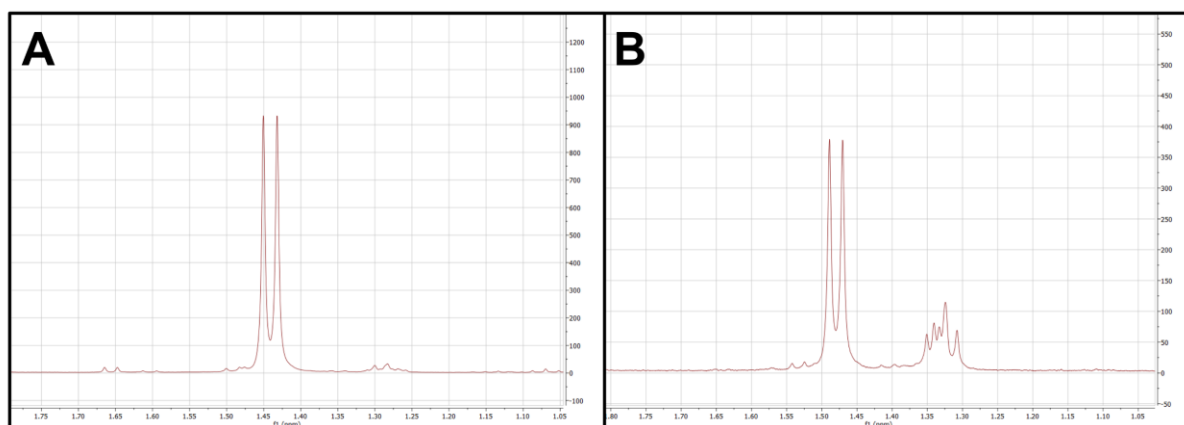


Figure 4.6. ^1H NMR of the methyl group present on *CTA1*. (A) Subsection of the ^1H NMR spectrum of *CTA1* after the first flash column purification where the impurity peak at ~ 1.28 ppm is minor compared with the product methyl group doublet at 1.48 ppm. (B) Subsection of the ^1H NMR spectrum of *CTA1* after several Amberlite washings and subsequent rotary evaporations where the degradation product peak at ~ 1.38 ppm can be seen to have grown significantly.

4.2.2. Galactose monomer synthesis (β -D-galactopyranosyloxyethyl acrylamide)

Galactose is a monosaccharide sugar that is often found in nature combined with other sugars, as in the case of lactose, which consists of a glucose unit combined with a galactose unit.²⁷ Galactose more generally can exist in four isomeric forms (**Fig. 4.7**), with these isomers being based on the pyranose (six-membered ring) or furanose (five-membered ring) varieties.

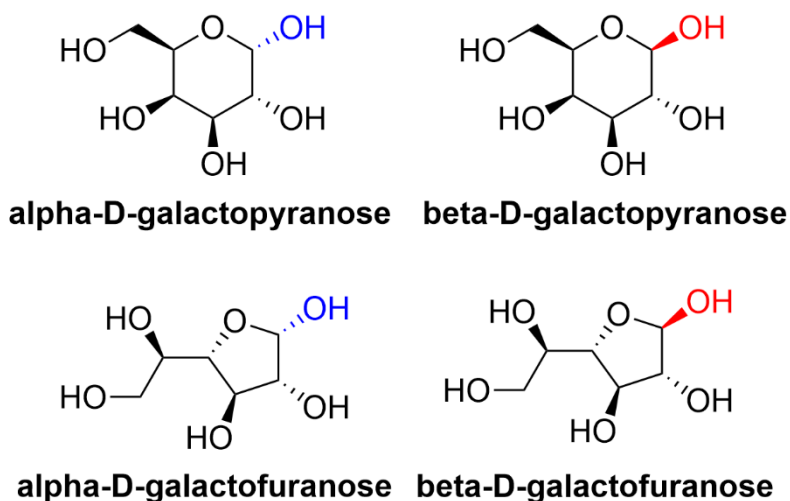


Figure 4.7. Structures of the 6-membered (top) and 5-membered (bottom) isomers of galactose along with the two anomers alpha (left) and beta (right).

To build a suitable galactose-based monomer for RAFT polymerisation, a group must be incorporated which would become the backbone of the final polymer. Acrylamide derivatives

are commonly utilized in RAFT polymerisations.²⁸⁻³¹ As discussed, conjugation of the vinyl group to a carbonyl group as is the case in acrylamide renders the vinyl group reactive towards polymerisation. The synthetic scheme for the preparation of **GalMon** is shown in **Fig. 4.8**.

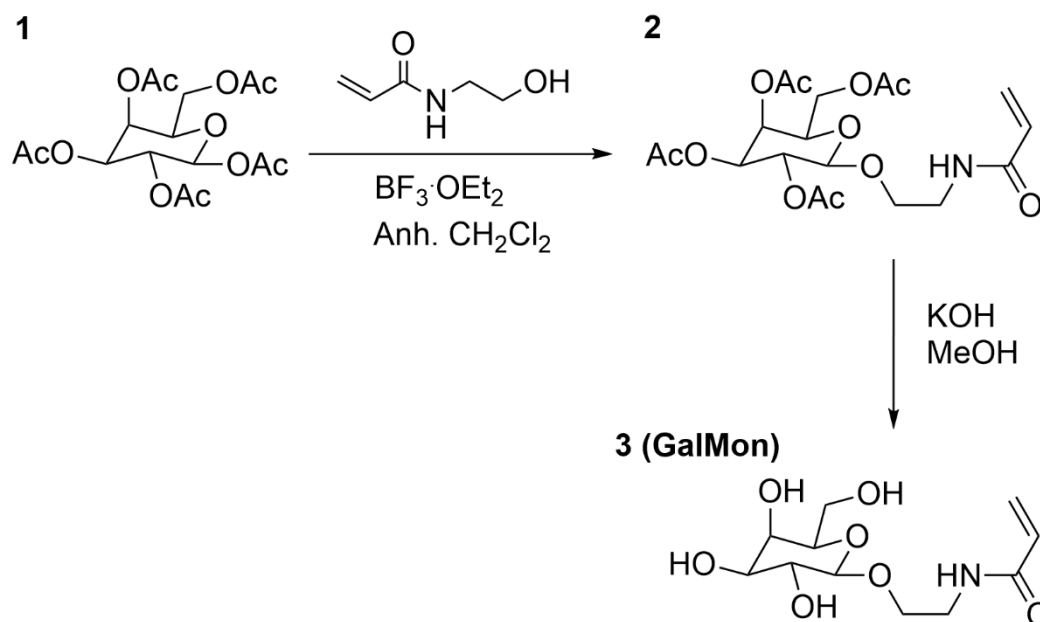


Figure 4.8. β -D-Galactopyranose pentaacetate (**1**) undergoes the Lewis acid-promoted glycosylation with *N*-hydroxyethyl acrylamide to form intermediate **2** followed by the hydrolysis of the acetate groups to form the final monomer **3 (GalMon)**.

The pentaacetate starting material (β -D-galactopyranose pentaacetate) was required for the glycosylation step, as the peracetylated derivative acts as an accessible glycosyl donor allowing the acrylamide group to be easily attached.³² After the Lewis acid-promoted glycosylation reaction to form intermediate **2** and subsequent purification through flash chromatography, a hydrolysis step was carried out on **2** by use of KOH in methanol to yield the final monomer **3 (GalMon)**.

4.2.3. Glycopolymer synthesis

Three different glycopolymers based on the **GalMon** monomer were chosen for further study for their incorporation into **1.2Br@Gels (Fig. 4.9)**. These three glycopolymers were prepared with differing molecular weights, so as to provide some insight into how the final weight of the polymer could influence polymer-gel properties. Molecular weight can be tuned in RAFT polymerisation by altering the ratio of CTA to monomer, and this approach was used to achieve the three different molecular weights. In addition, the weights of the prepared polymers would be over a wide range to magnify any morphological change brought about by greater molecular weight.

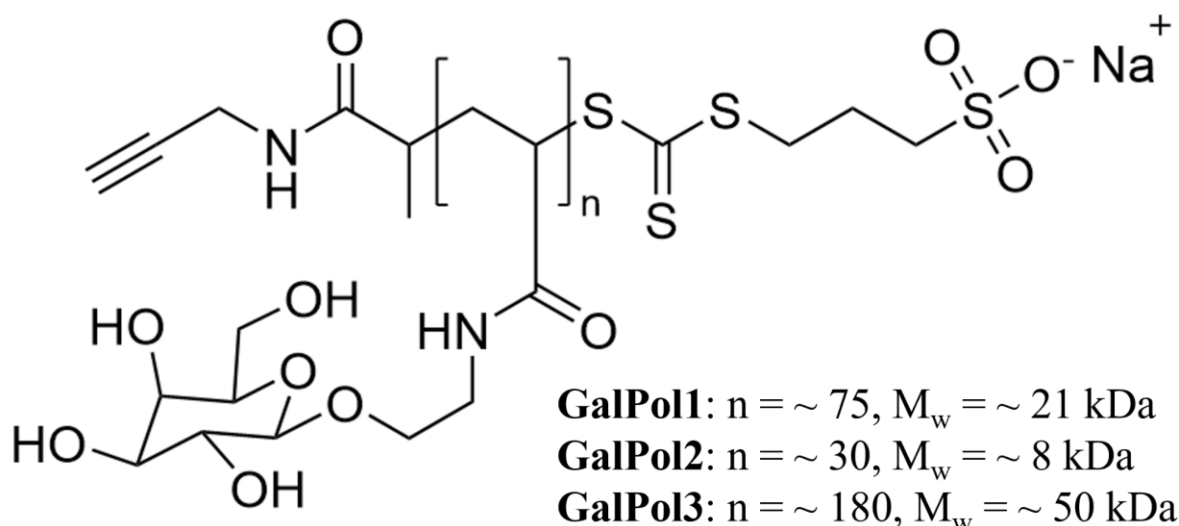


Figure 4.9. Molecular structure of the **GalPol** polymer with the n corresponding to the degree of polymerisation. Three polymers were targeted with M_w values ranging from ~ 8 kDa to ~ 50 kDa.

The polymerisation itself was tracked using ^1H NMR spectroscopy, with aliquots of polymerisation mixture taken at hourly intervals. The NMR spectra exhibited a significant decrease in the intensity of the vinyl peaks, indicating the successful conversion of the monomer into the desired polymer products (**Fig. 4.10**). Furthermore, there were observable peaks at lower ppm values, which corresponded to the polymer backbone formation.

However, when attempting to determine the degree of polymerisation through NMR analysis, certain limitations were encountered. Specifically, a challenge arose due to the overlapping of a reference methyl peak present adjacent to the trithiocarbonate group with another peak in the spectrum. This overlap posed difficulties in accurately integrating the peaks and obtaining reliable quantitative data.

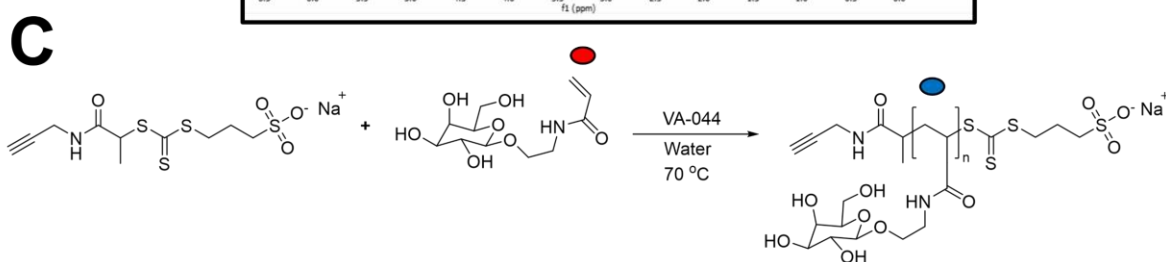
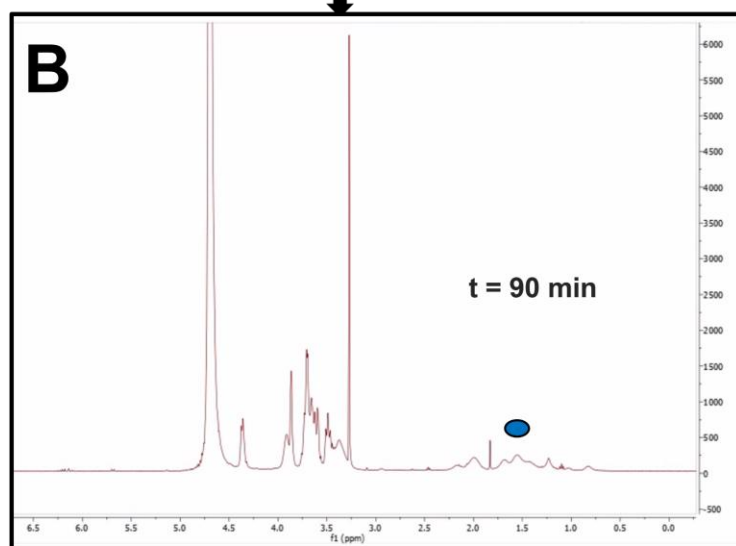
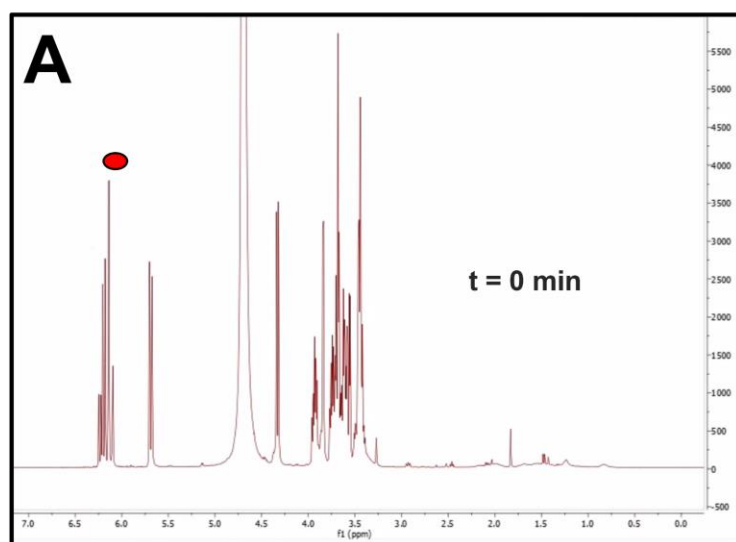


Figure 4.10. (A) ^1H NMR spectrum of the initial polymerisation mixture containing chain-transfer agent (CTA1), monomer (GalMon), and initiator (VA-044) with the vinyl proton peaks at $\sim 6.3 - 5.5$ ppm labelled with a red marker. (B) ^1H NMR spectrum of same mixture after being heated at 70°C for ~ 90 minutes showing the disappearance of the vinyl peaks and formation of peaks between $\sim 2 - 1$ ppm corresponding to the protons on the polymer backbone labelled with a blue marker. (C) Reaction scheme for the polymerisation of GalMon with the vinyl protons of GalMon and aliphatic protons of the polymer backbone labelled red and blue, respectively.

After completion of the polymerisations and subsequent workups, three waxy off-white solids were obtained. Whilst degree of polymerisation could be ascertained (for only two of the polymers) through integrating the ^1H NMR spectra, size-exclusion chromatography (SEC) was required to obtain a molecular weight distribution. SEC is a chromatographic technique whereby molecules can be separated by size, and therefore by molecular weight. SEC columns commonly consist of porous beads that enable the separation of molecules with varied sizes (or a single polymer with varying chain lengths). As the molecules pass through the column, they spend different durations within the pores, resulting in differing flow rates for disparate polymers. This flow rate difference effectively separates the molecules based on their respective sizes. The observed molecular weight values of the products differed from expectations based on the calculated reaction stoichiometries, and the corresponding chromatograms can be seen in **Fig. 4.11**.

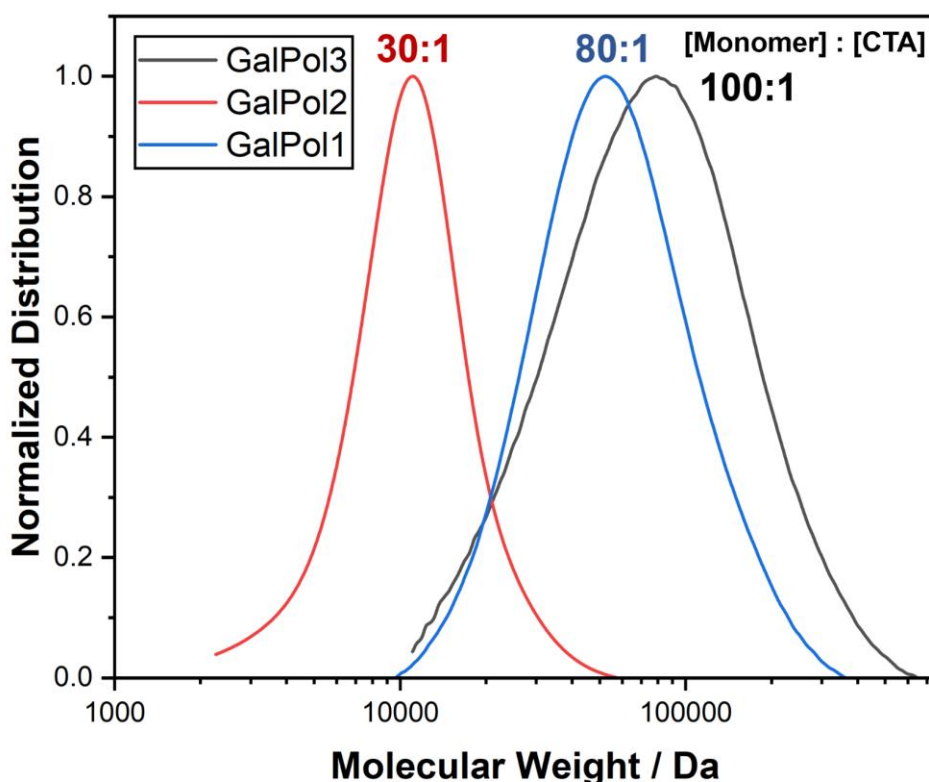


Figure 4.11. Molecular weight distribution plots for **GalPol1** (blue), **GalPol2** (red), and **GalPol3** (black), with the [monomer] : [CTA] ratios labelled above each respective peak.

However, the goal of obtaining polymers with varying molecular weights was successfully achieved. The molecular weight distributions of **GalPol1** and **GalPol3** were noticeably broad,

and not centred around values consistent with the calculations, though it is true that deviation from calculated values should be expected. It is important, however, to investigate the potential reasons behind this. One possibility is that the precise amount of monomer was not accurately measured, especially considering the challenging nature of handling the highly viscous **GalMon** material. It is possible that not all of it was included in the reaction as the monomer was solvated in a separate vial prior to addition into the reaction tube. Additionally, the amount of initiator used has been known to contribute to broad distributions, which is undesirable when aiming for narrower molecular weight distributions. When calculating potential molecular weight values for the polymers, the ratio of initiator to monomer was kept constant, though the ratio of CTA to initiator would necessarily change to achieve this. When there is an excess of initiators compared to CTA, it becomes possible for a higher rate of initiation reactions to occur, potentially leading to a greater concentration of actively growing polymer chains. This increased concentration, in turn, raises the likelihood of chain transfer and termination reactions taking place. It should be noted that the polymer with the lowest dispersity (\bar{D}) (**GalPol2**) also possessed the lowest ratio of initiator to CTA, and increasing this ratio increased the \bar{D} in the case of **GalPol1** and **GalPol3**. This trend supports the notion that initiator to CTA ratio influenced the molecular weight distributions of the polymers.

Despite the molecular weight values and distribution of the polymers not being perfect according to the calculations, they were deemed satisfactory to proceed with the next phase of the study.

4.3. Characterisation of Glycopolymer@Gel system

4.3.1. Macroscopic and SEM characterisation of Glycopolymer@Gel system

Initially, gelation tests were conducted on the systems under investigation. Additionally, multiple concentrations of the same polymer were explored to assess their impact on the properties of the materials. The determination of the exact concentration of the polymer can be challenging given the molecular weight distributions, so the monomer equivalent concentration was used as a proxy. While this approach yielded satisfactory results, there is a slight variation in charge between samples due to larger polymers containing fewer end-chain CTA units. This variation is illustrated in the example image (**Fig. 4.12**).

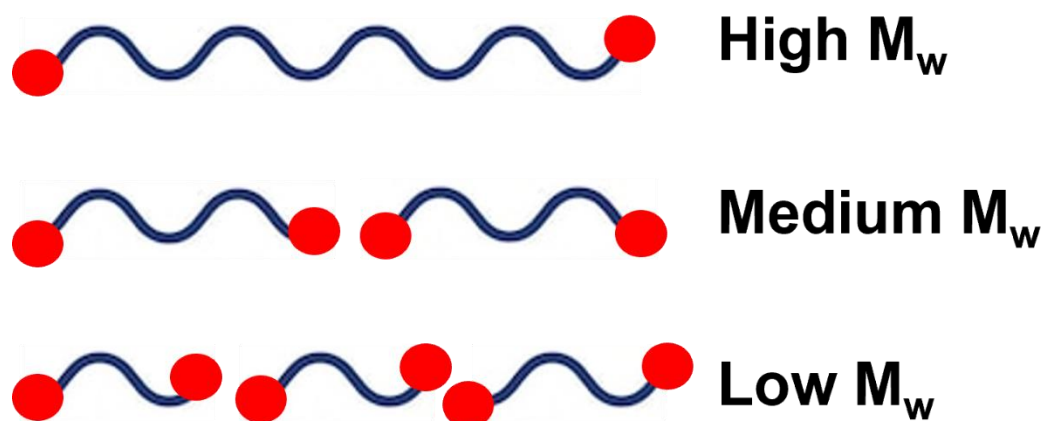


Figure 4.12. Representation of the difference between polymers of varying molecular weight distributions but the same monomer concentration. At high molecular weights, the ratio of CTA end chains (red spots) to polymer backbone (blue lines) is low and therefore the average charge on the polymer system is low. At medium molecular weights at the same monomer concentration, the same amount of polymer backbone is present but the ratio of CTA end chains to the polymer backbone is higher resulting in a greater average charge. Finally in the case of the low molecular weights at the same monomer concentration, the same amount of polymer backbone is present but the ratio of CTA end chains to polymer backbone is much higher resulting in a much greater average charge.

Gelation tests using **GalPol1** at a concentration of 1.2 mM (using monomer molecular weight, 10% with respect to **1.2Br**) were carried out using a fixed 1:1 water-ethanol ratio and gelator concentration (12 mM) and demonstrated little difference in gel formation compared to the control sample without polymer, with the gel taking approximately 25 – 30 seconds to form. Similar results were observed for the 12 mM concentration of **GalPol1** (100% with respect to **1.2Br**) sample, although slightly more turbidity was observed upon addition of the aqueous phase. However, with the 60 mM **GalPol1** sample (500% with respect to **1.2Br**), extreme turbidity was observed upon addition of the aqueous phase, and gel formation occurred within 15 seconds. This decrease in gelation time was also observed for **GalPol2** and **GalPol3** and could be caused by the polymer providing a nucleation point onto which fibres can grow, resulting in faster network formation. A study of the morphological properties of the **Glycopolymer@Gel** samples was carried out using scanning electron microscopy (SEM) to see if the differences seen in gelation time and macroscopic appearance is translated into a change in microscopic gel morphology. The SEM micrographs (**Fig. 4.13**) show a change in gel morphology with increasing polymer concentration (measured using monomer concentration). In the case of **GalPol2**, which happens to be the polymer with the lowest average molecular weight, little difference is seen in terms of morphology between

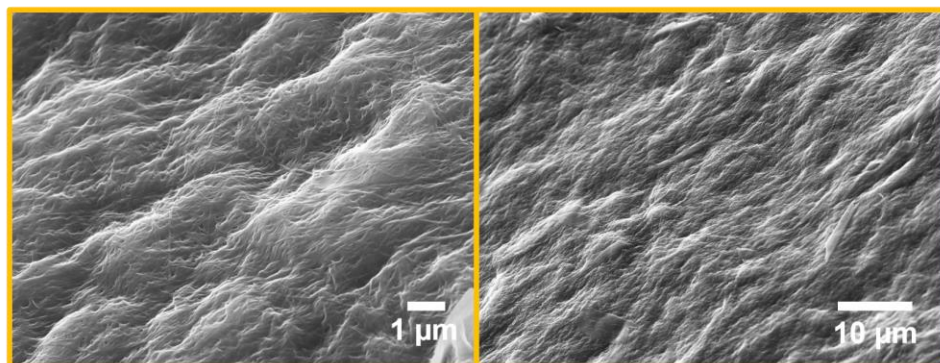
GalPol2@Gel and the control **1.2Br@Gel** at a polymer concentration of 1.2 mM. This similarity is supported by the fact that gel formation does not appear to be influenced at least at the macroscopic scale by the presence of the polymer. Long thin fibres are observed and can be seen in both low and high magnification micrographs. When the polymer concentration is increased to 12 mM (equimolar with **1.2Br**), some change is seen with fibres looking more distorted, though this interpretation is complicated by the drying artifacts (surface crumpling) seen especially in the low magnification micrograph. A significant distortion of the gel morphology is seen when the polymer concentration is increased to 60 mM, with fibres barely being visible either at low or high magnifications. It is also important to note that the gels containing varying concentrations of **GalPol1** and **GalPol3** were not characterized using SEM microscopy, and the greater molecular weight of those polymers could have an amplified effect upon the distortion of gel morphology.

[GalPol2]

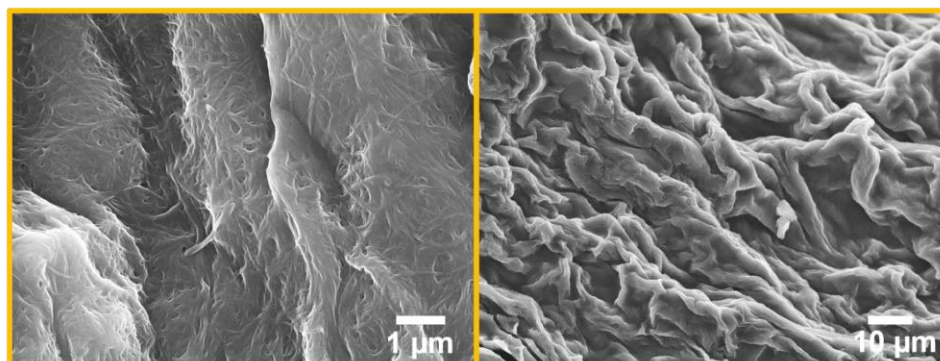
High Mag

Low Mag

1.2 mM



12 mM



60 mM

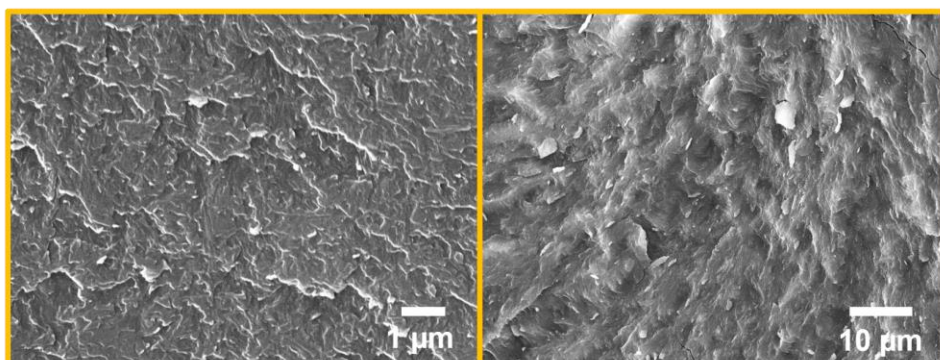


Figure 4.13. SEM micrographs of **Glycopolymer@Gel** samples collected at various (1.2 mM, 12 mM, 60 mM) polymer (**GalPol2**) concentrations (as measured by monomer concentration). [1.2Br] = 12 mM, 1:1 water-ethanol for all images.

Overall, inclusion of the prepared galactose based glycopolymers into the pristine imidazolium gels does influence gel morphology, especially at higher polymer concentrations. The effect of the inclusion of these polymers in conjunction with other added species will be further investigated here.

4.3.2. ZnPcTS@PolymerGel

In preparation for total internal reflection fluorescence (TIRF) microscopy on a **Glycopolymer@Gel** containing incorporated zinc phthalocyanine tetrasulfonic acid (**ZnPcTS**), photophysical measurements were carried out upon **ZnPcTS@GalPol2@Gel**. It

was possible that the presence of **GalPol2** could influence the aggregation properties within the gel, and therefore affect the fluorophore's behaviour as seen using the TIRF microscope. Absorption and fluorescence spectra of **ZnPcTS@GalPol2@Gel** are shown in **Fig. 4.14**. Deviation from the standard **ZnPcTS@Gel** absorption spectrum is seen at all concentrations (1.2 mM, 12 mM, 60 mM) of **GalPol2**. The Q-band is smoother in the presence of **GalPol2**, indicating that the number of aggregation states of **ZnPcTS** is lower than in the absence of the polymer. The general shape of the Q-band does, however, indicate that **ZnPcTS** is largely present in its aggregated form when incorporated into the gel as the aggregate peak at ~ 635 nm is predominant over the unaggregated ~ 675 nm peak. The absorption maximum also increases in intensity with increased **GalPol2** concentration, probably as a result of light scattering. The fluorescence behaviour of **ZnPcTS** is generally unchanged with the addition of **GalPol2**, with a single emission peak at ~ 700 nm. The intensity of these fluorescence peaks between polymer concentrations parallels that of the absorption spectra, with the higher polymer concentrations resulting in greater fluorescence emission. The fact that **ZnPcTS** retained its photophysical properties in the presence of **GalPol2** allowed for the continuation to the TIRF studies.

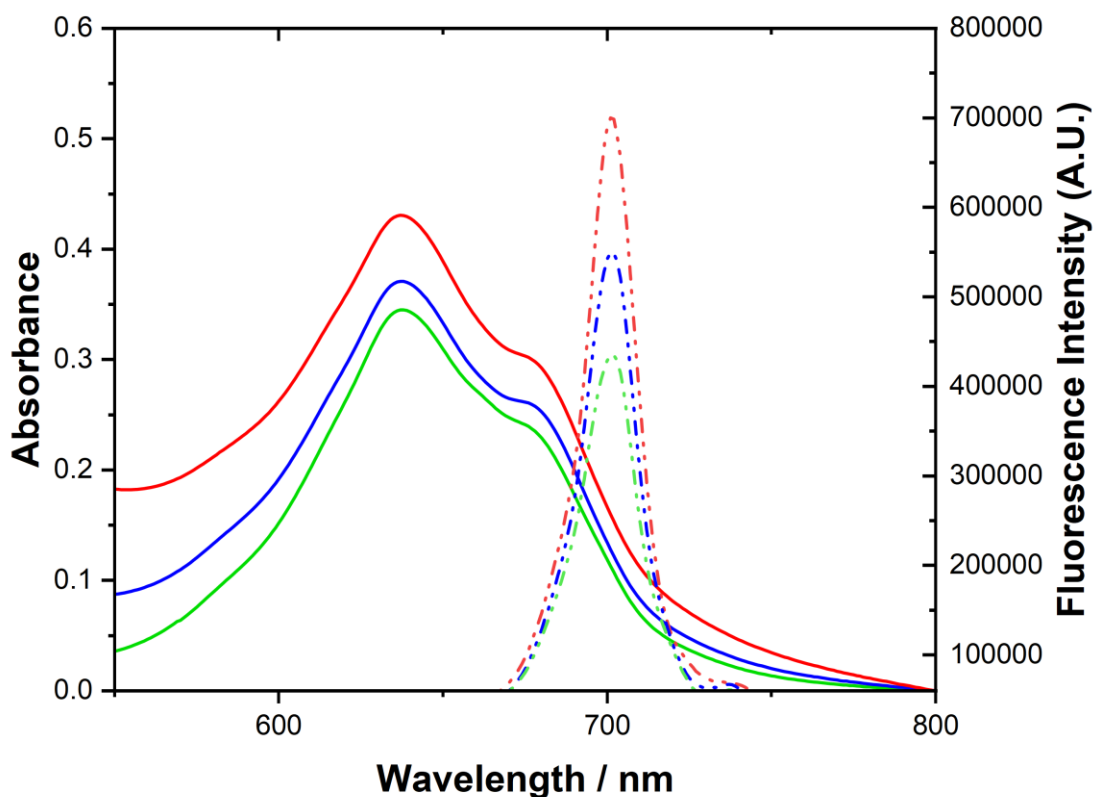


Figure 4.14. Absorption (solid line) and emission (dotted line) spectra of **ZnPcTS@GalPol2@Gel** samples, $[\text{ZnPcTS}] = 150 \mu\text{M}$, $[\text{1.2Br}] = 12 \text{ mM}$, 1:1 water ethanol. $[\text{GalPol2}] = 1.2 \text{ mM}$ (green), $[\text{GalPol2}] = 12 \text{ mM}$ (blue), $[\text{GalPol2}] = 60 \text{ mM}$ (red). $\lambda_{\text{exc}} = 630 \text{ nm}$ for all fluorescence measurements.

4.3.3. **ZnPcTS@PolymerGel TIRF study**

Similar studies to those conducted in Chapter 3 were carried out on the **1.2Br** gel containing both **ZnPcTS** as a fluorophore and containing varying concentrations of a synthesized galactose polymer. The initial study was conducted on the polymer **GalPol2**, as that **Glycopolymer@Gel** had been characterized using photophysical and morphological techniques. As with the SEM study, the monomer concentration of **GalPol2** was varied from 1.2 mM to 12 mM and 60 mM whilst the **1.2Br** and **ZnPcTS** concentration were kept the same at 12 mM and 10 μM , respectively. Similarly to the SEM study, TIRF micrographs taken of **ZnPcTS@GalPol2@Gel** with a **GalPol2** concentration of 1.2 mM showed little change from micrographs of **ZnPcTS@Gel** alone, indicating that even the hydrated state gel morphology is not significantly altered by the inclusion of 1.2 mM **GalPol2** (**Fig. 4.15**). Gel fibres are largely

straight with little curvature and the length of fibres tend to be easily identifiable over the course of the image.

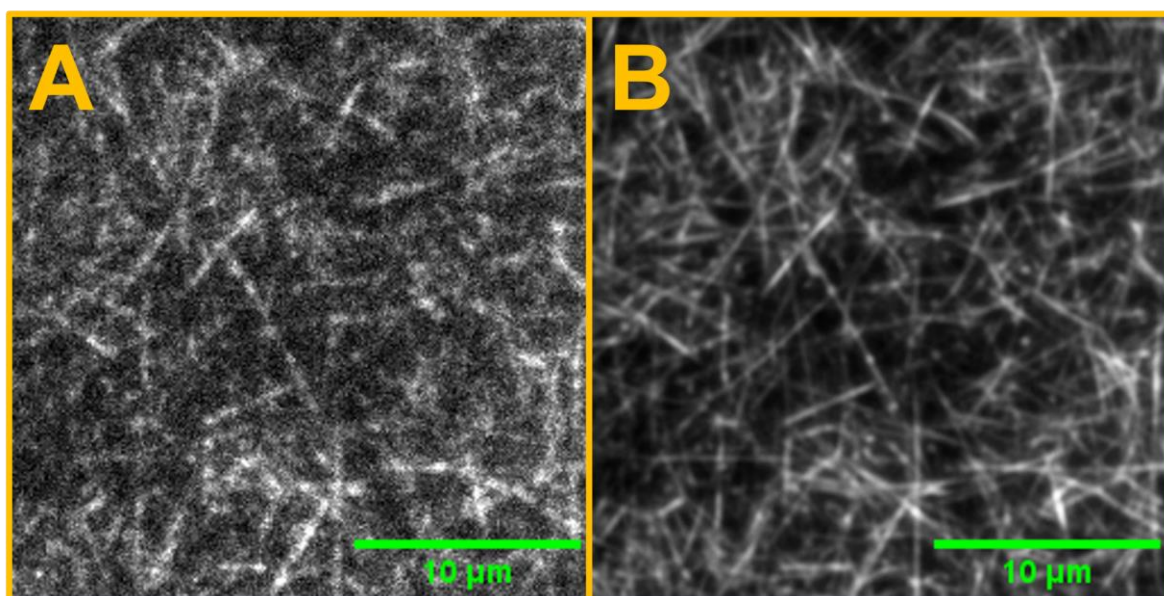


Figure 4.15. TIRF micrographs of a **ZnPcTS@GalPol2@Gel** sample containing a **ZnPcTS** concentration of $10\ \mu\text{M}$ and **GalPol2** concentration of $1.2\ \text{mM}$. (A) TIRF micrograph of a single frame (of 600) where gel fibres can be discerned. (B) TIRF micrograph of the average projection over the 600 frames referenced in A shows detail of the gel morphology. All images taken with $642\ \text{nm}$ laser and LP filter at $650\ \text{nm}$. Laser power 100%.

The fluorophore diffusion described in Chapter 3 was also observable in the **ZnPcTS@GalPol2@Gel** system and represented in **Fig. 4.16**. As the concentration of **ZnPcTS** was $10\ \mu\text{M}$ (so as to observe fibre morphology), single molecule diffusion analysis such as MSD analysis could not be carried out on these collected videos.

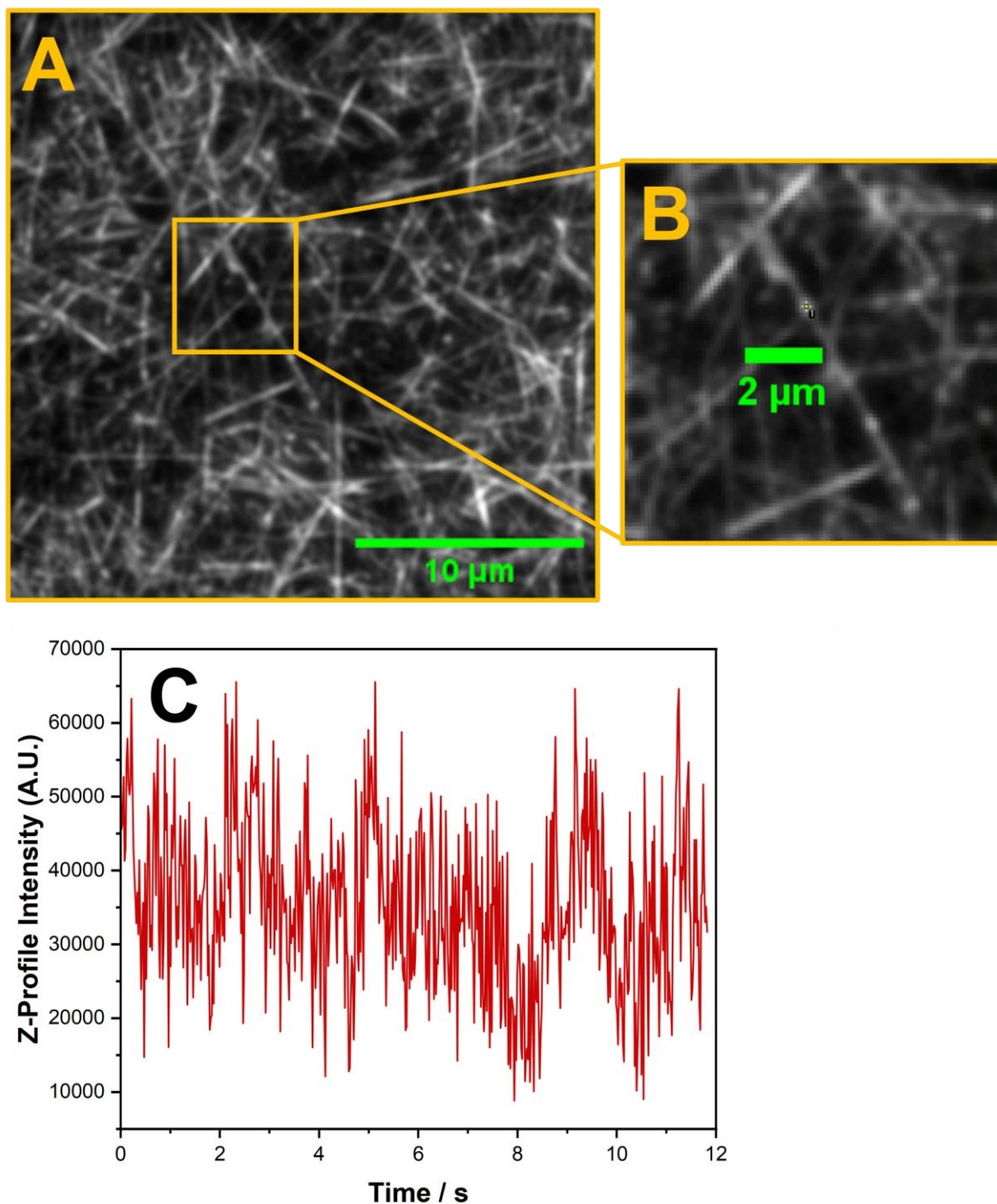


Figure 4.16. TIRF micrograph containing a ROI and subsequent z-profile intensity plot. (A) TIRF micrograph of an average projection of a 600-frame video of $\text{ZnPcTS@GalPol2@Gel}$ with a $[\text{ZnPcTS}]$ of $10 \mu\text{M}$ and a $[\text{GalPol2}]$ of 1.2 mM . A ROI was placed over a section of a fibre. Laser wavelength of 642 nm , observation with 650 nm LP filter. (B) Zoomed in selection containing the fibre and ROI with which the z-profile intensity was plotted. (C) Z-profile intensity plot over 600 frames indicated that fluorophores moved in and out of the ROI over the duration of the collected video.

As the **GalPol2** concentration was increased from 1.2 mM to 12 mM, fibre morphology began to change considerably (**Fig. 4.17**), though fluorophore movement was still observed as before. Whilst long and straight fibres are still observable on both the raw video and average projection, the majority of fibres appear fragmented and relatively short. The appearance of these apparently broken fibres could be a mixture of a morphological change brought about by polymer addition, or by fluorophores not being able to diffuse freely through the fibres. If the added **GalPol2** was providing an obstacle to diffusion, only certain sections of each fibre would be fluorescently ‘labelled’ over the course of the TIRF videos, resulting in the observed fragmented fibre structure. However, given that SEM analysis does show considerable morphological change upon the addition of 12 mM **GalPol2**, it is likely that morphology is also contributing to this effect.

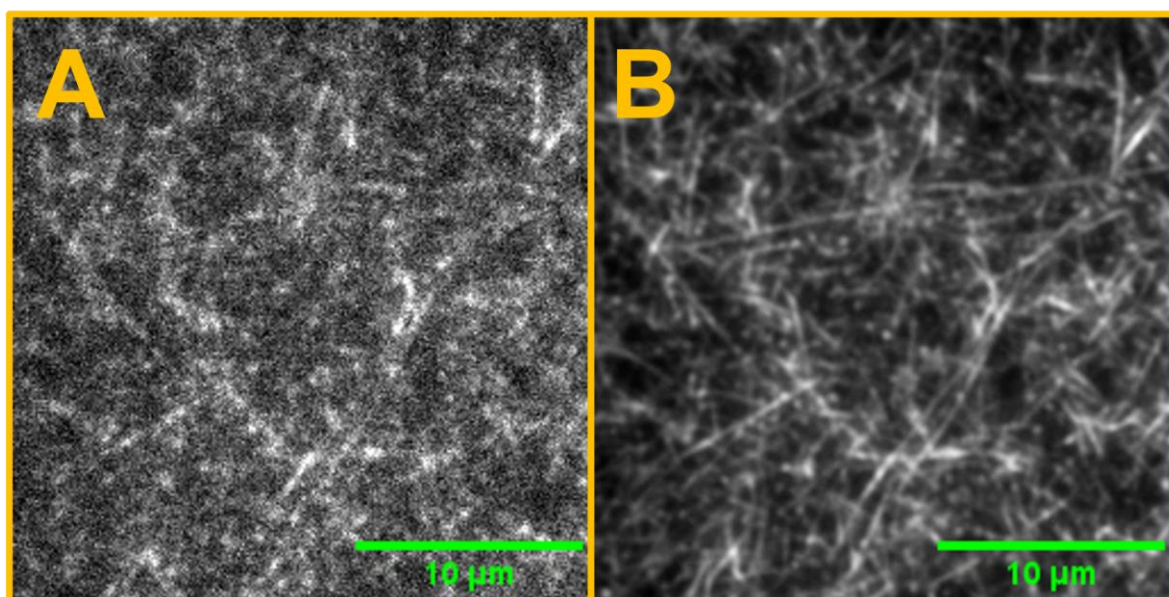


Figure 4.17. TIRF micrographs of a **ZnPcTS@GalPol2@Gel** sample containing a **ZnPcTS** concentration of 10 μM and **GalPol2** concentration of 12 mM. (A) TIRF micrograph of a single frame (of 600) where gel fibres can be discerned. (B) TIRF micrograph of the average projection over the 600 frames referenced in A shows detail of the gel morphology. All images taken with 642 nm laser and LP filter at 650 nm. Laser power 100%.

Increasing the **GalPol2** concentration to 60 mM had a similarly noticeable effect on the apparent morphology of the gel fibres observed in the average projection TIRF micrographs (**Fig. 4.18**). No fibres can be discerned in the raw video, though the **ZnPcTS** fluorophore motion is still observed. When examining **GalPol2@Gel** through SEM at a polymer concentration of 60 mM, noticeable deformations in the fibre structure were observed, reaching

an extent to where individual fibres became indistinguishable. This strongly suggests that the high concentration of **GalPol2** hampers the formation of the gel morphology typically observed in pristine **1.2Br** gel samples and samples containing lower concentrations of **GalPol2**.

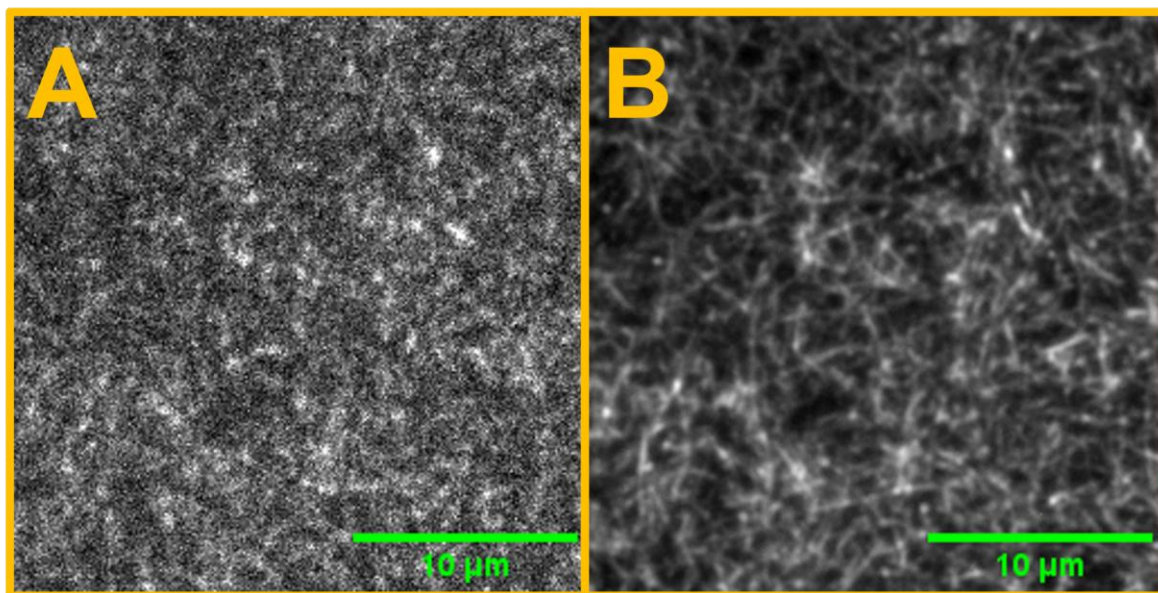


Figure 4.18. TIRF micrographs of a **ZnPcTS@GalPol2@Gel** sample containing a **ZnPcTS** concentration of $10\ \mu\text{M}$ and **GalPol2** concentration of $60\ \text{mM}$. (A) TIRF micrograph of a single frame (of 600) where gel fibres cannot be identified. (B) TIRF micrograph of the average projection over the 600 frames referenced in A shows some detail of the gel morphology. All images taken with $642\ \text{nm}$ laser and LP filter at $650\ \text{nm}$. Laser power 100%.

Another noticeable difference between gel samples containing glycopolymer and those that do not is the change in intensity of the fluorescence signal arising from irradiation with the $642\ \text{nm}$ excitation light. It was found that even with the inclusion of $12\ \text{mM}$ **GalPol2**, fluorescence signal dropped by around a factor of 4 (**Fig. 4.19**). When **GalPol2** concentration was increased to $60\ \text{mM}$, a further marginal decrease in fluorescence signal was also observed. This decrease in fluorescence signal could be caused by heightened aggregation caused by the polymer, though the UV-Visible absorption spectra do not suggest a substantial change in aggregation state. It is also possible, however, that a greater percentage of **ZnPcTS** is present in the interstitial space solubilised by the polymer.

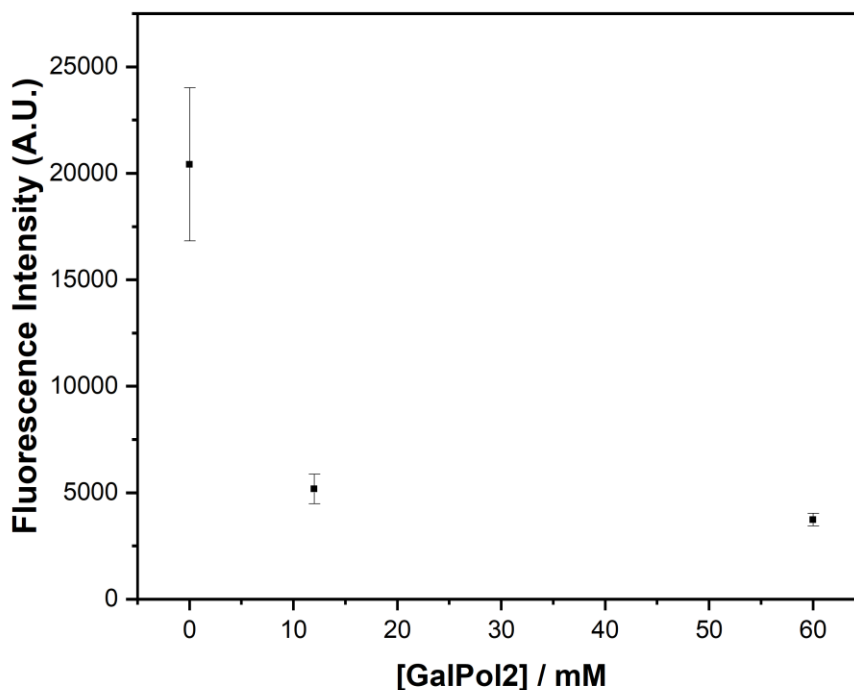


Figure 4.19. Plot of fluorescence signal arising from the average projection of **ZnPcTS@GalPol2@Gel** at a [**ZnPcTS**] concentration of 10 μ M against the concentration of incorporated **GalPol2**.

Considering the significant impact of glycopolymer concentration on gel morphology, it is worthwhile to explore the potential influence on the diffusion of fluorophores. In Chapter 3, it was determined that fluorophore diffusion predominantly takes place within the fibres rather than along their surfaces. This conclusion was drawn based on the observation that if fluorophores were located on the outer surface of the fibres, it would be more likely for their transfer to occur between fibres in non-parallel orientations. Considering that the majority of the computed fluorophore trajectories were straight (accounting for the curvature of individual fibres), it can be inferred that observed fluorophore diffusion primarily occurs through the fibres. It is likely that the glycopolymers would reside on the outside of fibres, meaning any influence of fluorophore diffusion would be indirect through the modification of fibres.

GalPol3 was chosen for these experiments due to its broader molecular weight distribution, which is expected to have a more significant impact on fluorophore diffusion. This choice enables the possibility of detecting larger effects through MSD analysis. Again, the concentration of **GalPol3** was increased stepwise from 0 mM to 12 mM to 60 mM (by monomer concentration). Unlike with the experiments on TIRF fibre morphology, the **ZnPcTS**

concentration was kept at a constant 0.1 μM to compare with the previous diffusion analysis without glycopolymers.

Figure 4.20 displays a frame from raw video and an average projection over 600 frames of **GalPol3@ZnPcTS@Gel** with a **GalPol3** concentration of 12 mM. **ZnPcTS** diffusion occurs in an apparently identical fashion in the presence of glycopolymer to without. An increase in the number of fluorophores that remain still in a given location for an extended period is observed relative to that seen without glycopolymer, which is likely a consequence of morphological disruption brought about by the presence of **GalPol3**. For fluorophore speed analysis, laser power was kept at a constant 100% and **GalPol3** concentration was varied.

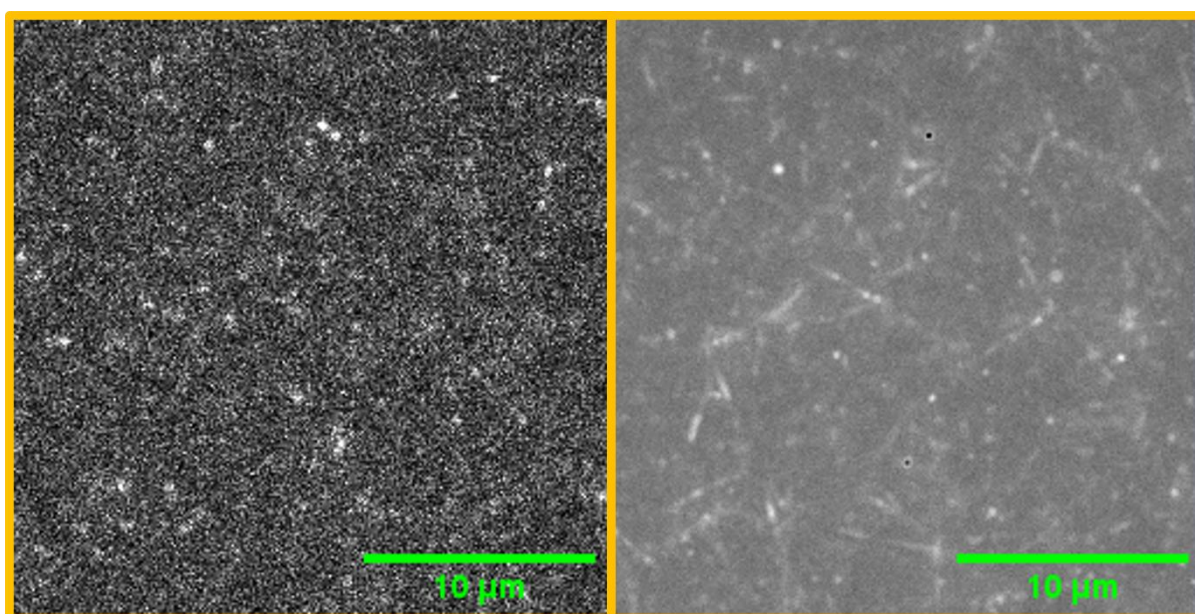


Figure 4.20. TIRF micrographs of a **ZnPcTS@GalPol3@Gel** sample containing a **ZnPcTS** concentration of 0.1 μM and **GalPol3** concentration of 12 mM. (A) TIRF micrograph of a single frame (of 600) where gel fibres can be discerned. (B) TIRF micrograph of the average projection over the 600 frames referenced in A shows detail of the gel morphology. All images taken with 642 nm laser and LP filter at 650 nm. Laser power 100%.

Analysis on the fluorophore motion showed a measured increase in MIV with increasing **GalPol3** concentration (**Fig. 4.21**). When **GalPol3** was not present, MIV was calculated to be around $5.26 \pm 0.23 \mu\text{m s}^{-1}$. Increasing the **GalPol3** concentration to 12 mM has a noticeable effect on the speed of the fluorophores with a rise to $6.74 \pm 0.39 \mu\text{m s}^{-1}$. Increasing **GalPol3** concentration further to 60 mM increases the MIV to $7.61 \pm 0.25 \mu\text{m s}^{-1}$. This data shows a clear trend to higher MIV values with increasing **GalPol3** concentration. This could be in part a consequence of the distortion of fibres by the glycopolymer resulting in weaker electrostatic

interactions between the cationic lamellae units and anionic sulfonate groups. Another possibility is a direct interaction between the glycopolymer units and the phthalocyanine sulfonate groups. Such an interaction could explain the fluorescence intensity decrease with increasing glycopolymer concentration, with excitation being dissipated through heat through aggregation rather than fluorescence emission. Despite this, no fluorescence intensity decrease was observed in the previous study with **ZnPcTS@Gel** containing camphorsulfonic acid (CSA). The enhancement of fluorophore speed in the presence of glycopolymer could therefore be attributed to an alternative mechanism of interaction between the glycopolymer and fluorophore, distinct from the fibre structural changes induced by CSA observed in the previous chapter.

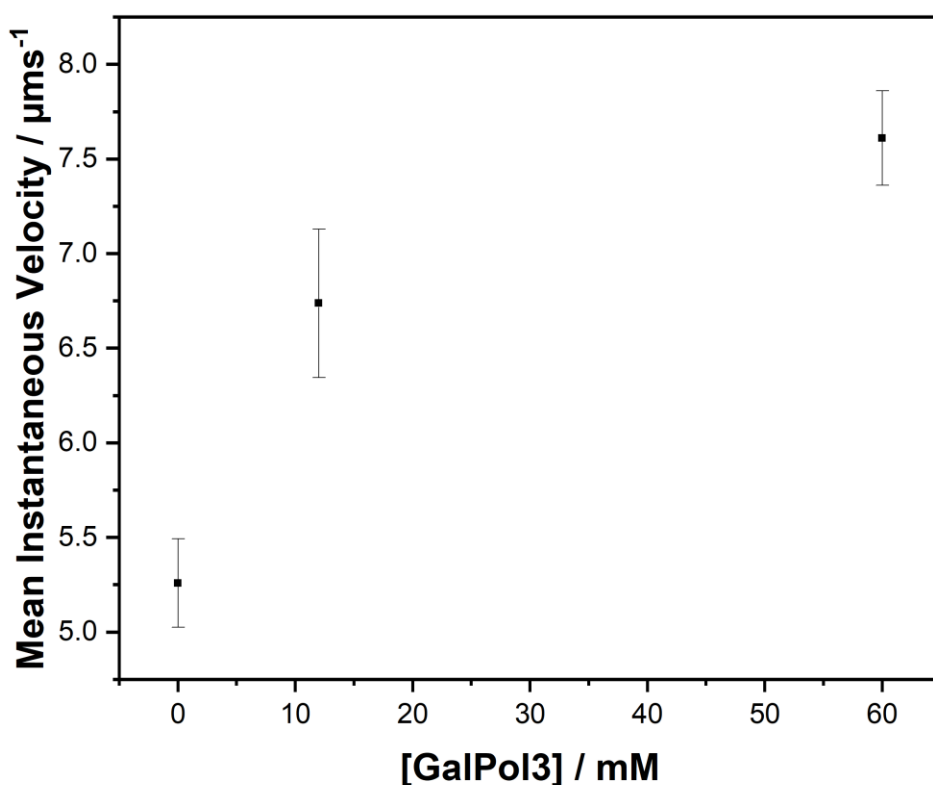


Figure 4.21. Quantitative analysis of fluorophore movement with particle tracks. Plot of MIV against [GalPol3] for several areas of a **ZnPcTS@GalPol3@Gel** sample, [ZnPcTS] = 0.1 μM .

4.4. Conclusion

Three galactose based glycopolymers were synthesized with differing molecular weights. The precursors for these polymerisations were also synthesized including the CTA. Whilst two of the glycopolymers prepared had a larger dispersity than would be expected given RAFT

conditions, it was possible to investigate the influence of these glycopolymers on the physical properties of a **1.2Br** imidazolium gel as well as how incorporated fluorophore behaviour could be affected by the presence of such polymers. It was found that the inclusion of each of the prepared glycopolymers does not have a significant effect upon the macroscopic properties of the gel, at least at the polymer concentrations used in this study. Gelation time was shortened to approximately 15 seconds at a glycopolymer concentration of 60 mM. At the microscale, fibre morphology was shown to be distorted heavily at glycopolymer concentrations of 60 mM, though some fibre disruption could be seen at 12 mM as observed through conventional SEM imaging. Whilst not having a significant effect on the photophysical properties of **ZnPcTS** as measured using UV-Visible absorption and fluorescence spectroscopy, TIRF imaging showed a similar disruption in hydrated fibre morphology. A decrease in **ZnPcTS** fluorescence intensity in the presence of glycopolymer was also found, hinting at potential interactions between fluorophore and polymer. Along with this, the speed of **ZnPcTS** fluorophores as measured using MIV analysis was shown to increase with increasing glycopolymer concentration. Overall, this study highlights how the macroscopic and microscopic properties of a supramolecular gel can be influenced by the presence of a polymeric additive.

4.5. Experimental

4.5.1. General procedures

The gels described in this chapter were prepared at a 1:1 water-ethanol ratio always with a final **1.2Br** gelator concentration of 12 mM. For experiments with **ZnPcTS** fluorophores, a 2.4 mM stock solution of the fluorophore in Milli-Q water was prepared and subsequently diluted in a glass vial to achieve the desired concentration of fluorophore in the final gel. TIRF samples were prepared by mixing the diluted fluorophore solution with an equal volume of an ethanolic 24 mM **1.2Br** gelator solution. Rapid and thorough mixing of the ethanolic and aqueous solutions was carried out to ensure homogeneity before transferring the gelating mixture into a compartment well of the sample holder which was then left undisturbed at room temperature to allow gel formation. A small amount of Blu Tak was fitted over the top of the well to limit ethanol evaporation. For solid-state fluorescence and absorption measurements, the gelating mixture (still in the micropipette) was quickly transferred to a cuvette of path length 1 mm. For SEM measurements, gels were formed in the glass vials and were then dried overnight under vacuum desiccation to form xerogels. SEM images were acquired with a JEOL 7100F FEG-SEM system on samples cast on aluminium stubs, dried under vacuum and coated with a 5 nm thick layer of iridium. Image acquisition was performed using a working distance of 6

mm and 10 kV accelerating voltage. The gelation time of the gels prepared in this study were always below one minute (though times varied with glycopolymer concentration), and gel formation was deemed to have occurred when no flow was exhibited during a vial-inversion test.

Fluorescence imaging was performed on a Zeiss Elyra PS1 super resolution microscope equipped with Zen 2012 acquisition and processing software, fitted with an alpha Plan-Apochromat 100×/1.46 Oil DIC M27 Elyra objective lens operating in TIRF (Total internal reflection fluorescence), using a 642 nm (150 mW at 100% LP) laser and emission filters LP 650 nm for **ZnPcTS**. A droplet of 30 °C oil (Zeiss, Immersol™ 518F/30°) was cast on the objective before imaging. The TIRF angle used was 68°. Automatic focusing was always adopted to keep constant the desired focal plane during the acquisition. Image acquisition was performed in the TIRF modality. Videos recorded in TIRF were generally acquired with an EM-CCD (Andor EM-CCD camera iXon Du 897) with 200 gain and 18 ms exposure time per frame over 600 frames. For visualisation purposes, 600 images of the recording were collapsed into single image (Z project in Fiji) using either average or maximum intensity projections. Maximum projections displayed all maximum intensity values (signals from single molecules) cumulatively, therefore resulting in an image revealing the fibres scaffolds along which the fluorophores diffused. Average projections calculated the average intensity for each pixel, and therefore results in a view of the morphology with a significant amount of noise removed. Samples were prepared directly into CELLview™ Microscopic Slides with Glass Bottoms by Greiner Bio-One GmbH that have a 10-well compartmentalisation block allowing to form the gel *in situ* and perform the imaging directly without any further sample manipulation. Image processing was carried out with Fiji image analysis software. Particle tracking was carried out on the videos of the 0.1 μM **ZnPcTS@Glycopolymer@Gel** samples using the TrackMate (v6.0.3) plugin within Fiji. Denoising of the raw videos was achieved by the consecutive subtracting of the average projection. A median filter was then applied to the videos before particle tracking analysis to further limit the noise. The built-in difference of gaussians (DoG) detector was used to identify spots corresponding to fluorophores, whilst the linear assignment problem (LAP) tracker was employed to track the individual fluorophores. The instantaneous velocity measurements produced for each video, typically numbering in the thousands, were averaged to yield a mean instantaneous velocity for each video collected.

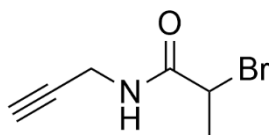
UV-Visible extinction spectroscopy was performed using a Cary 5000 UV-Visible spectrophotometer (Agilent). Fluorescence spectroscopy and absolute fluorescence quantum

yield measurements were carried out on a FLS 980 spectrometer (Edinburgh Instruments) equipped with a front face sample holder or integrating sphere. The fluorescence and fluorescence quantum yield measurements were carried out using quartz cuvette of path length 1 mm and 10 mm, respectively.

4.5.2. Synthetic procedures

Solvents and reagents used in this study were of an analytical grade. Zinc(II) phthalocyanine tetrasulfonic acid was purchased from PorphyChem. Mass Spectra were obtained using Bruker Compass MicroTOF, using electron spray ionisation (ESI). Chromatography purifications were performed using Sigma-Aldrich Silica Gel (pore size 60Å, particle size 40 – 63 µm) and thin-layer chromatography was carried out on E. Merck silica gel plates irradiated using 365 nm UV light. NMR spectra were acquired on a Bruker AV400 spectrometer and NMR spectra were recorded at room temperature. All chemical shifts are reported in δ parts per million (ppm), using the solvent residual signal as an internal standard and the coupling constant values (J) are reported in Hertz (Hz). The following abbreviations are used for signal multiplicities: s, singlet; d, doublet; t, triplet; m, multiplet; and b, broad.

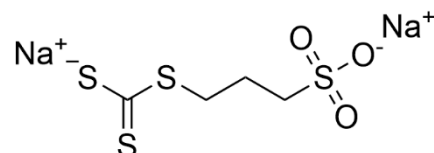
2-Bromo-*N*-(prop-2-yn-1-yl)propenamide



Bromopropionyl bromide (8.62 g, 39.93 mmol) was dissolved in THF (50 mL) and cooled to 0 °C. Propargylamine (2.00 g, 36.31 mmol) and Et₃N (5.51 g, 54.45 mmol) were added to THF (50 mL) in separate flask. Propargylamine/Et₃N solution were added dropwise to the 0 °C bromopropionyl bromide solution under stirring and a beige suspension was yielded. After 1 h, water (100 mL) added to flask to yield a clear orange solution. The mixture was separated with Et₂O and washed with H₂SO₄ solution (0.2 M) twice and washed with DI water once. The solvent was removed *in vacuo* to yield a crude brown oil. The oil was purified by column chromatography (Silica gel 60 Å, particle size 35–70 µm, gradient elution from 100% petroleum ether to 100% Et₂O) to yield an off-white solid characterized as 2-bromo-*N*-(prop-2-yn-1-yl)propenamide (4.14 g, 60%). ¹H NMR (400 MHz, CDCl₃) δ /ppm 6.57 (m, 1H, CONH), 4.43 (q, $J = 7.1$ Hz, 1H, CHCH₃), 4.10 (dd, $J = 7.1$ Hz, $J = 2.6$ Hz, 2H, CH₂N), 2.30 (t, $J = 2.6$ Hz, 1H, HC≡C-), 1.91 (d, $J = 7.1$ Hz, 3H, CHCH₃). ¹³C NMR (101 MHz, CDCl₃)

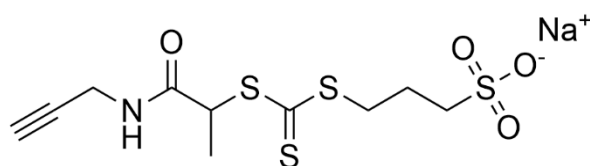
δ /ppm 168.9 (CONH), 78.7 (HC \equiv C), 72.2 (HC \equiv C), 44.6 (CHBr), 30.0 (CH₂), 23.1 (CH₃). IR ν max ATR/cm⁻¹: 3279, 3066, 2129, 1643, 1539, 1190.

Sodium 3-(dithiocarboxylatothio)propyl sulfonate



Sodium 3-mercaptopropionate (4.00 g, 22.45 mmol) was finely ground in pestle and mortar before being added to methanol (50 mL). NaOH (0.94 g, 23.57 mmol) was dissolved in a separate flask of methanol (20 mL) and added dropwise to the methanolic sodium 3-mercaptopropionate suspension. The mixture was sonicated for 30 min before degassing at room temperature for further 1 h. Carbon disulfide (5.39 mL, 89.78 mmol) was added dropwise to the degassed mixture at 0 °C which turned the mixture bright yellow. The mixture was stirred at room temperature under inert atmosphere for 48 h. The mixture was then poured into diethyl ether (200 mL) to yield a yellow solid after filtration which was then washed with further diethyl ether and the resulting yellow solid was characterized as sodium 3-(dithiocarboxylatothio)propyl sulfonate (3.84 g, 75%). ¹H NMR (400 MHz, D₂O) δ /ppm 3.25 (t, J = 7.3 Hz, 2H, ⁻O₃SCH₂), 2.95 (m, 2H, C(S)SCH₂), 2.06 (m, 2H, CH₂CH₂CH₂). ¹³C NMR (101 MHz, D₂O) δ /ppm 49.9 (⁻O₃SCH₂), 39.5 (C(S)SCH₂), 23.4 (CH₂CH₂CH₂). IR ν max ATR/cm⁻¹: 3400, 1634, 1446, 1397, 1188, 1045, 1017, 990, 841, 735.

Sodium 3-([(1-oxo-1-prop-2-yn-1-ylamino)propan-2-yl-thio]carbonothioyl)thio}propane-1-sulfonate (CTA1)

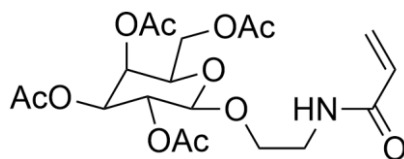


Sodium 3-(dithiocarboxylatothio)propyl sulfonate (1.78 g, 6.09 mmol) was added to acetone (40 mL) before the addition of 15-crown-5 (2.46 g, 11.18 mmol) to the mixture. 2-Bromo-*N*-(prop-2-yn-1-yl)propanamide (0.97 g, 5.08 mmol) was dissolved in separate flask of acetone and this was added dropwise to the previous acetone mixture cooled to 0 °C. The mixture was left stirring at room temperature for 18 h. The solvent was removed *in vacuo* and the residue was purified by flash chromatography (Silica gel 60 Å, particle size 35–70 μm, gradient elution from 100% ethyl acetate to 100% methanol) to yield the product containing

co-eluted

15-crown-5. 15-Crown-5 was removed by precipitation of product in diethyl ether. Trace amounts of 15-crown-5 was further removed by repeated product washings with Amberlite™ IR-120(Na) ion exchange resin in water. The product was then purified further to remove hydrolysis products using flash chromatography (Silica gel 60 Å, particle size 35–70 µm, 20% methanol in ethyl acetate) to yield a yellow solid characterized as **CTA1** (0.26 g, 15 %). ¹H NMR (400 MHz, D₂O) δ/ppm 4.58 (m, 1H, SCHCH₃), 3.90 (d, *J* = 2.5 Hz, 2H, NHCH₂), 3.47 (t, *J* = 7.2 Hz, 2H, O₃SCH₂), 2.93 (m, 2H, C(S)SCH₂), 2.52 (t, *J* = 2.5 Hz, 1H, C≡CH), 2.03 – 2.12 (m, 2H, CH₂), 1.48 (d, *J* = 7.4 Hz, 3H, CH₃). ¹³C NMR (101 MHz, D₂O) δ/ppm 223.4 (C(S)S), 173.7 (CONH), 79.9 (C≡CH), 72.1 (C≡CH), 49.6 (SCHCH₃), 49.3 (C(S)SCH₂), 35.1 (O₃SCH₂), 29.2 (NHCH₂), 23.2 (CH₃), 15.6 (CH₂CH₂CH₂). IR ν max ATR/cm⁻¹: 3464, 3407, 3265, 1641, 1539, 1446, 1215, 1170, 1055, 827. ESI-TOF mass spectrometry: expected *m/z* [M-H]⁻ 339.9811, found 339.9814.

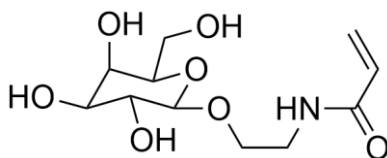
Precursor 2,3,4,6-tetra-O-acetyl-β-D-galactopyranosyloxyethyl acrylamide (GalMonPre)



β-D-galactose pentaacetate (50.37 g, 128.9 mmol) was dissolved in dry dichloromethane (100 mL) and *N*-hydroxyethyl acrylamide (22.4 g, 196 mmol) was added under stirring. The mixture was then cooled to 0 °C and boron trifluoride dietherate (27.4 g, 194 mmol) was added dropwise. Upon addition of all the boron trifluoride dietherate, the mixture was stirred at room temperature. The reaction progress was tracked by movement of anomeric carbon peak in the ¹³C NMR spectra. After 6 days, starting material anomeric carbon (~ 92 ppm) was completely diminished and product peak (~ 100 ppm) indicated reaction completion. Triethylamine (Et₃N) (21.6 g, 213 mmol) was added to dichloromethane (50 mL) and the mixture was cooled to 0 °C. The crude reaction mixture was added dropwise to this Et₃N solution before all being added into an aqueous NaHCO₃ (65 g, 778 mmol) solution. The organic phase was washed twice with NaHCO₃, three times with deionised water before being dried over magnesium sulfate. The organic solvent was removed *in vacuo* to yield a crude brown oil. Flash chromatography (Silica gel 60 Å, particle size 35–70 µm, 20% ethyl acetate in diethyl ether) was carried out on multiple batches of crude product to yield a crystalline solid characterized as **GalMonPre** (23.5 g, 41%). ¹H NMR (400 MHz, DMSO-*d*₆) δ/ppm 8.12 (t, *J*

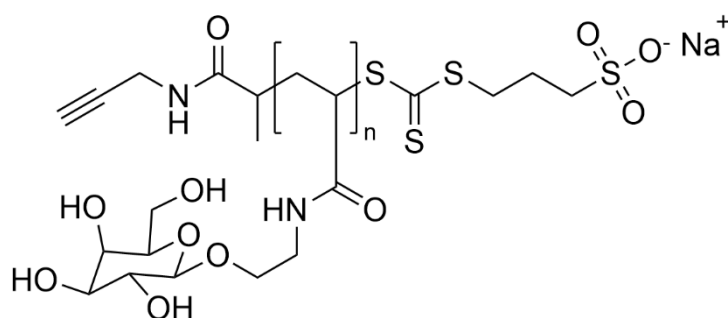
= 5.6 Hz, 1H, *NH*), 6.23 (dd, $J = 17.2$ Hz, $J = 10.2$ Hz, 1H, $CH=CH_2$), 6.08 (dd, $J = 17.1$ Hz, $J = 2.3$ Hz, 1H, $CH=CHH$), 5.58 (dd, $J = 10.1$ Hz, $J = 2.3$ Hz, 1H, $CH=CHH$), 5.59 – 5.23 (m, 1H, CH), 5.16 (dd, $J = 10.4$ Hz, $J = 3.6$ Hz, 1H, CH), 4.94 (dd, $J = 10.4$ Hz, $J = 8.0$ Hz, 1H, CH), 4.73 (d, $J = 8.0$ Hz, 1H, CH (anomeric)), 4.24 – 4.16 (m, 1H, CH), 4.09 – 3.99 (m, 2H, CH_2OCOCH_3), 3.78 – 3.56 (m, 2H, $COCH_2CH_2NH$), 3.33 – 3.22 (m, 2H, $COCH_2CH_2NH$), 2.11 (s, 3H, CH_3), 2.00 (s, 3H, CH_3), 1.98 (s, 3H, CH_3), 1.91 (s, 3H, CH_3). ^{13}C NMR (101 MHz, DMSO- d_6) δ /ppm 170.8 ($C(O)CH_3$), 170.4 ($C(O)CH_3$), 170.0 ($C(O)CH_3$), 169.6 ($C(O)CH_3$), 165.2 (NHCO), 132.1 ($CH=CH_2$), 125.6 ($CH=CH_2$), 100.5 (CH (anomeric)), 70.8 ($CHCH_2OAc$), 70.4 ($CHOAc$), 69.0 ($CHOAc$), 68.1 ($CHOAc$), 67.8 (CH_2CH_2NH), 61.8 ($CHCH_2OAc$), 39.1 (CH_2NH), 21.2 (CH_3), 20.9 (CH_3), 20.9 (CH_3). IR ν max ATR/ cm^{-1} : 3256, 1743, 1645, 1612, 1548, 1364, 1214.

β -D-galactopyranosyloxyethyl acrylamide (GalMon)



KOH (0.056 g, 1.0 mmol) was dissolved in methanol (50 mL). **GalMonPre** (4.45 g, 10.0 mmol) was added to this basic solution and stirred at room temperature for 20 h. The mixture was then passed through a pad of silica pre-packed with methanol (Silica gel 60 Å, particle size 35–70 μ m, 100% methanol) to yield a viscous oil characterized as β -D-galactopyranosyloxyethyl acrylamide (2.09 g, 92%). 1H NMR (400 MHz, DMSO- d_6) δ /ppm 8.10 (t, $J = 5.7$ Hz, 1H, *NH*), 6.25 (dd, $J = 17.1$ Hz, $J = 10.1$ Hz, 1H, $CH=CH_2$), 6.09 (dd, $J = 17.1$ Hz, $J = 2.3$ Hz, 1H, $CH=CHH$), 5.59 (dd, $J = 10.1$ Hz, $J = 2.3$ Hz, 1H, $CH=CHH$), 4.86 (s, 1H, *OH*), 4.74 (s, $J = 1$ Hz, *OH*), 4.61 (t, $J = 5.7$ Hz, 1H, *OH*), 4.38 (d, $J = 4.5$ Hz, 1H, CH (anomeric)), 4.14 – 4.06 (m, 1H, *OH*), 3.81 – 3.71 (m, 1H, $CHOH$), 3.56 – 3.46 (m, 1H, $CHOH$), 3.39 – 3.17 (m, 8H, OCH_2CH_2NH , $CHOH$, $CHOH$, CH_2OH). ^{13}C NMR (101 MHz, DMSO- d_6) δ /ppm 165.1 (NHCO), 132.2 ($CH=CH_2$), 125.7 ($CH=CH_2$), 104.2 (CH (anomeric)), 75.8 ($CHCH_2OH$), 73.8 ($CHOH$), 71.0 ($CHOH$), 68.6 ($CHOH$), 68.2 (CH_2CH_2NH), 61.0 ($CHCH_2OH$). IR ν max ATR/ cm^{-1} : 3294, 2886, 1655, 1620, 1547, 1411, 1039.

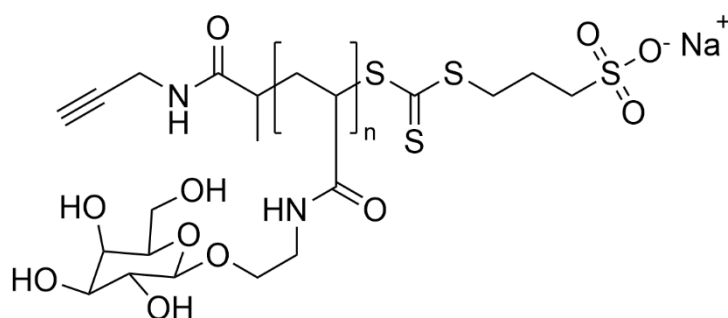
GalPol1 Glycopolymer



β -D-galactopyranosyloxyethyl acrylamide (GalMon, 208 mg, 0.751 mmol), sodium 3-[[[(1-oxo-1-prop-2-yn-1-ylamino-propan-2-yl-thio)carbonothioyl]thio}propane-1-sulfonate) **CTA1** (3.2 mg, 0.0094 mmol) and VA-044 (0.243 mg, 0.751 μ mol, from stock solution) were dissolved in 429 μ L of DI water in a glass tube equipped with a magnetic bar. The tube was sealed with a rubber septum, cooled in an ice bath, and degassed by nitrogen bubbling over 45 min. The polymerisation was started by placing the tube in an oil bath set at 70 °C and was left to proceed for 1 h under stirring. The conversion was monitored by ¹H NMR analysis of aliquots withdrawn from the reaction mixture every 1 h. The reaction was stopped at a monomer conversion of at least 90% by opening the tube to the air. The solution was diluted with water and then transferred into a dialysis bag with a molecular weight cut-off (MWCO) of 3 kDa. The polymer was dialysed against DI water for 3 days with frequent water changes and then the water was removed *in vacuo* to yield a waxy off-white solid **GalPol1**.

Conversion: 95%; Mn,_{th} = 21.3 kDa; Mn,_{SEC} = 63.4 kDa; Đ: 1.53.

GalPol2 Glycopolymer

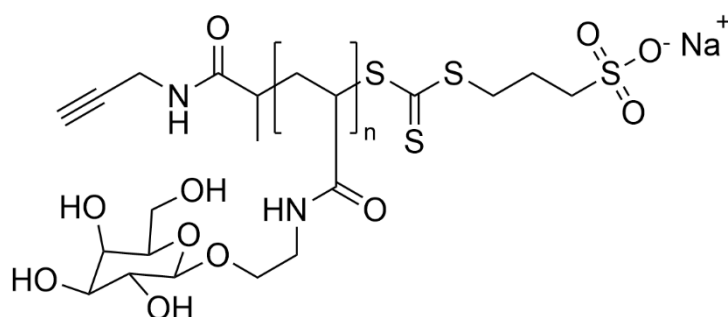


β -D-galactopyranosyloxyethyl acrylamide (GalMon, 354 mg, 1.28 mmol), sodium 3-[[[(1-oxo-1-prop-2-yn-1-ylamino-propan-2-yl-thio)carbonothioyl]thio}propane-1-sulfonate) **CTA1** (14.5 mg, 0.043 mmol) and VA-044 (0.41 mg, 1.28 μ mol, from stock solution) were dissolved in 730 μ L of DI water in a glass tube equipped with a magnetic bar. The tube was

sealed with a rubber septum, cooled in an ice bath, and degassed by nitrogen bubbling over 45 min. The polymerisation was started by placing the tube in an oil bath set at 70 °C and was left to proceed for 1 h under stirring. The conversion was monitored by ^1H NMR analysis of aliquots withdrawn from the reaction mixture every 1 h. The reaction was stopped at a monomer conversion of at least 90% by opening the tube to the air. The solution was diluted with water and then transferred into a dialysis bag with a molecular weight cut-off (MWCO) of 3 kDa. The polymer was dialysed against DI water for 3 days with frequent water changes and then the water was removed *in vacuo* to yield a waxy off-white solid **GalPol2**.

Conversion: 95%; $M_{n,\text{th}} = 7.8$ kDa; $M_{n,\text{SEC}} = 11.6$ kDa; Đ : 1.28.

GalPol3 Glycopolymer



β -D-galactopyranosyloxyethyl acrylamide (GalMon, 573 mg, 2.07 mmol), sodium 3-[(1-oxo-1-prop-2-yn-1-ylamino-propan-2-yl-thio)carbonothioyl]thio}propane-1-sulfonate), **CTA1** (3.55 mg, 0.0104 mmol) and VA-044 (0.67 mg, 2.08 μmol , from stock solution) were dissolved in 1182 μL of DI water in a glass tube equipped with a magnetic bar. The tube was sealed with a rubber septum, cooled in an ice bath, and degassed by nitrogen bubbling over 45 min. The polymerisation was started by placing the tube in an oil bath set at 70 °C and was left to proceed for 1 h under stirring. The conversion was monitored by ^1H NMR analysis of aliquots withdrawn from the reaction mixture every 1 h. The reaction was stopped at a monomer conversion of at least 90% by opening the tube to the air. The solution was diluted with water and then transferred into a dialysis bag with a molecular weight cut-off (MWCO) of 3 kDa. The polymer was dialysed against DI water for 3 days with frequent water changes and then the water was removed *in vacuo* to yield a waxy off-white solid **GalPol3**.

Conversion: 95%; $M_{n,\text{th}} = 50.0$ kDa; $M_{n,\text{SEC}} = 80.2$ kDa; Đ : 1.9.

4.6. References

1. D. Lu, X. Zou, C. Li, *High Perform. Polym.*, 2022, 35, 439 – 468.
2. S. T. Knox, N. J. Warren, *React. Chem. Eng.*, 2020, 5, 405 – 423.
3. O. Z. Durham, D. A. Shipp, *Polym. Rev.*, 2020, 61, 54 – 79.
4. Y. Gao, K. Peng, S. Mitragotri, *Adv. Mater.*, 2021, 33, 2006362.
5. B. A. J. Noordover, A. Heise, P. Malanowski, D. Senatore, M. Mak, L. Molhoek, R. Duchateau, C. E. Koning, R. A. T. M. van Benthem, *Prog. Org. Coat.*, 2009, 65, 187 – 196.
6. L. Tan, B. Tan, *Chem. Soc. Rev.*, 2017, 46, 3322 – 3356.
7. K. Matyjaszewski, M. Möller, *Polymer Science: A Comprehensive Reference*, Elsevier Science, Amsterdam, 2012.
8. H. Gao, K. Matyjaszewski, *Prog. Polym. Sci.*, 2009, 34, 317 – 350.
9. H. R. Lamontagne, B. H. Lessard, *ACS Appl. Polym. Mater.*, 2020, 2, 5327 – 5344.
10. J. Chiefari, Y. K. Chong, F. Ercole, J. Krstina, J. Jeffery, T. P. T. Le, R. T. A. Mayadunne, G. F. Meijs, C. L. Moad, G. Moad, E. Rizzardo, S. H. Thang, *Macromolecules*, 1998, 31, 5559 – 5562.
11. H. Fischer, *Chem. Rev.*, 2001, 101, 3581 – 3610.
12. A. Goto, T. Fukuda, *Prog. Polym. Sci.*, 2004, 29, 329 – 385.
13. S. Perrier, *Macromolecules*, 2017, 50, 7433 – 7447.
14. D. Gunaydin, P. Grysan, D. F. Schmidt, R. Dieden, M. Weydert, A. S. Shaplov, *New J. Chem.*, 2022, 46, 15321 – 15333.
15. R. Hoogenboom, U. S. Schubert, W. Van Camp, F. E. Du Prez, *Macromolecules*, 2005, 38, 7653 – 7659.
16. C. Kalirajan, A. Dukle, A. J. Nathaneal, T. Oh, G. Manivasagam, *Polymers*, 2021, 13, 3015.
17. R. Jelinek, S. Kolusheva, *Chem. Rev.*, 2004, 104, 5987 – 6016.
18. J. Madeira do O, R. Foralosso, G. Yilmaz, F. Mastrotto, P. J. S. King, R. M. Xerri, Y. He, C. F. van der Walle, F. Fernandez-Trillo, C. A. Laughton, I. Styliari, S. Stolnik, G. Mantovani, *Nanoscale*, 2019, 11, 21155-21166.
19. J. E. Petch, P. Gurnani, G. Yilmaz, F. Mastrotto, C. Alexander, S. Heeb, M. Cámara, G. Mantovani, *ACS Appl. Mater. Interfaces*, 2021, 13, 19230 – 19243.

20. S. G. Spain, M. I. Gibson, N. R. Cameron, *J. Polym. Sci., Part A: Polym. Chem.*, 2007, 45, 2059 – 2072.
21. M. R. Thalji, A. A. Ibrahim, K. F. Chong, A. V. Soldatov, G. A. M. Ali, *Top. Curr. Chem.*, 2022, 380, 45.
22. C. Deng, F. Li, J. M. Hackett, S. H. Chaudhry, F. N. Toll, B. Toye, W. Hodge, M. Griffith, *Acta Biomater.*, 2010, 6, 187 – 194.
23. B. Cai, Y. Luo, Q. Guo, X. Zhang, Z. Wu, *Carbohydr. Res.*, 2017, 445, 32 – 39.
24. D. Wang, T. Li, *Acc. Chem. Res.*, 2023, 56, 462 – 474.
25. H. Xue, D. Li, H. Cai, X. Sun, W. Wan, *Macromolecules*, 2023, 56, 1898 – 1906.
26. D. Boffoli, F. Bellato, G. Avancini, P. Gurnani, G. Yilmaz, M. Romero, S. Robertson, F. Moret, F. Sandrelli, P. Caliceti, S. Salmaso, M. Cámara, G. Mantovani, F. Mastrotto, *Drug Deliv. Transl. Res.*, 2022, 12, 1788 – 1810.
27. N. Sasaoka, H. Imamura, A. Kakizuka, *iScience*, 2018, 19, 211 – 221.
28. H. Mori, M. Matsuyama, K. Sutoh, T. Endo, *Macromolecules*, 2006, 39, 4351 – 4360.
29. U. C. Palmiero, A. Chovancová, D. Cuccato, G. Storti, I. Lacík, D. Moscatelli, *Polymer*, 2016, 98, 156 – 164.
30. A. J. Convertine, B. S. Lokitz, A. B. Lowe, C. W. Scales, L. J. Myrick, C. L. McCormick, *Macromol. Rapid Commun.*, 2005, 26, 791 – 795.
31. R. W. Lewis, R. A. Evans, N. Malic, K. Saito, N. R. Cameron, *Polym. Chem.*, 2018, 9, 60 – 68.
32. J. Khamsi, R. A. Ashmus, N. S. Schocker, K. Michael, *Carbohydr. Res.*, 2012, 357, 147 – 150.

Chapter 5

**Confocal imaging of fluorophore-
containing imidazolium hydrogels**

5.1. Background

Confocal microscopy is a type of fluorescence microscopy offering increased contrast and resolution when compared to conventional epifluorescence microscopy techniques. This increased contrast and resolution is achieved by employing a spatial pinhole to remove out-of-focus light.¹ Confocal microscopy, therefore, allows the imaging of a specific focal plane within a sample, along with the potential for three-dimensional imaging with the collation of these individual layers (Z-stack). The general set-up for a confocal microscope can be seen in Fig. 5.1.

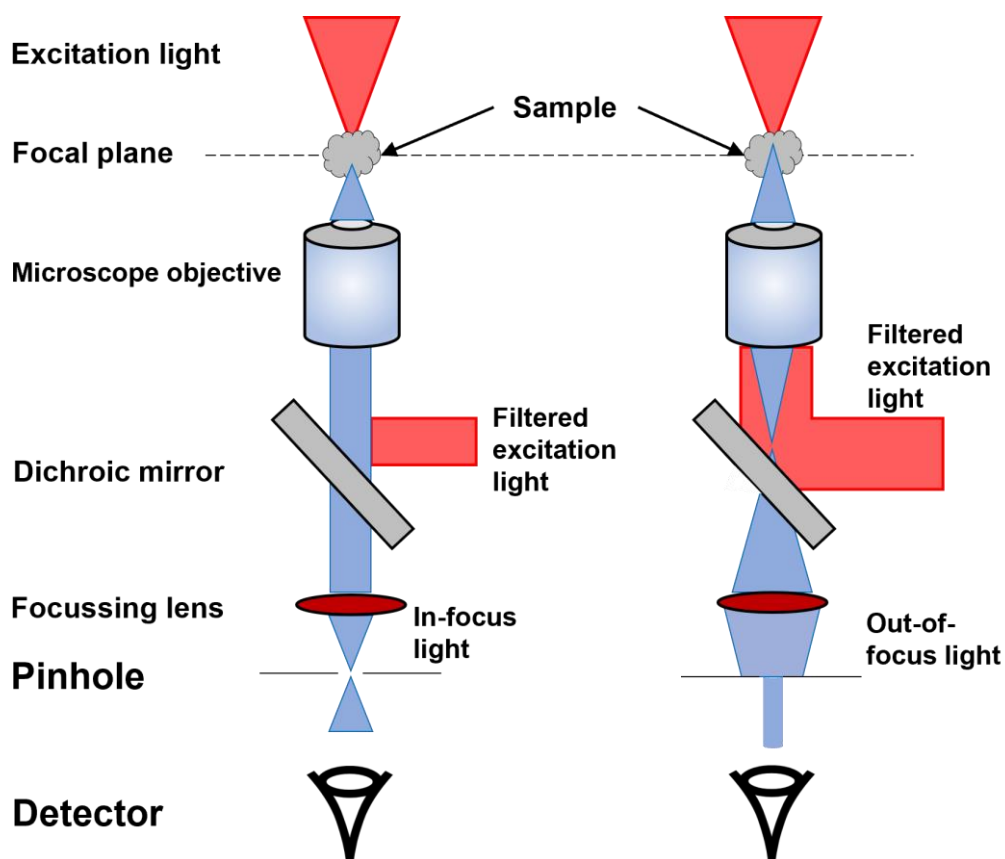


Figure 5.1. A confocal microscope irradiates a sample with excitation light which then passes through an objective. In-focus light passes through the pinhole (left) whilst out-of-focus light (right) is largely prevented from passing through the pinhole. The detector therefore picks up only in-focus light leading to greater contrast and resolution.

Whilst there are several methods to carry out horizontal scanning using a confocal microscope, the most prevalent is the approach used by confocal laser scanning microscopes (CLSMs). CLSMs use a series of mirrors to direct a laser linearly across the x- and y- axes of the samples to build up a micrograph. CLSM finds much of its use in the bioimaging of cells.² Bioimaging involves staining cells with various fluorescent compounds, including a wide range of staining

fluorophores developed for diverse purposes. The compound 4',6-diamidino-2-phenylindole (DAPI) is a commonly used fluorophore that binds strongly to DNA, rendering it an effective nuclear staining agent.³

Despite its numerous advantages in fluorescence imaging, confocal microscopy is not commonly used in materials analysis. The ability of CLSM to gain cross-sectional information of certain samples grants a non-destructive view into the internal properties of a given material, which conventional scanning electron microscopy (SEM) or atomic force microscopy (AFM) techniques cannot achieve. The relatively simple sample preparation is also an important consideration when comparing to types of electron microscopy or AFM, with the latter techniques generally requiring dry samples that potentially require further preparation steps involving coating or embedding into a matrix. On the other hand, material samples that are to be analysed through CLSM need to either possess an inherent fluorescent moiety or have an added fluorescent additive for imaging. Whilst an extra preparation step is not terminal to the use of CLSM for materials analysis, it is vital to understand how any fluorescent additive may influence the structure of a given material. This consideration indicates that CLSM is most powerful when used in conjunction with higher-resolution techniques such as SEM and AFM (which are not restricted by the Abbe limit), which together can result in a more robust and reliable view of a material's properties.

Confocal microscopy is particularly well-suited for imaging supramolecular hydrogels because it allows for a detailed examination of their internal morphology, which is often more critical than surface characteristics. An early example of hydrogel characterisation through confocal microscopy was carried out on a supramolecular hydrogel formed through the self-assembly of glycosylated amino acid gelators.⁴ In this context, a nitrobenzoxadiazole fluorophore was introduced into the gel, preferentially binding to the hydrophobic domains of the supramolecular structure and enabling the visualisation of contrasts between hydrophilic and hydrophobic regions (**Fig. 5.2**).

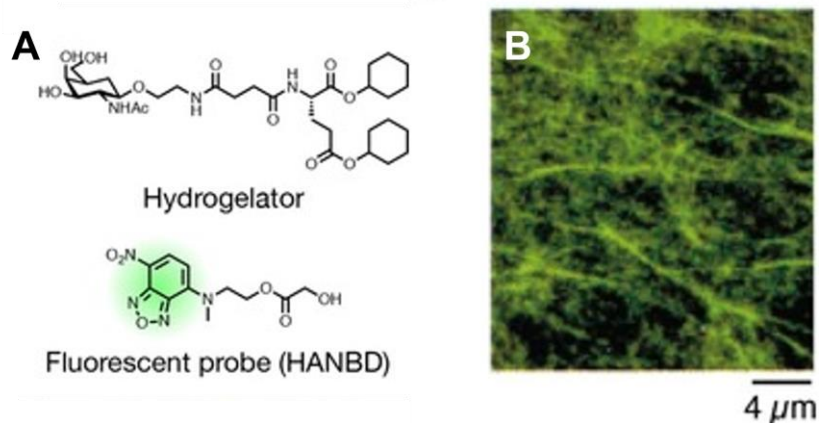


Figure 5.2. (A) A glycosylated amino acid hydrogelator self-assembles into a supramolecular hydrogel into which a nitrobenzoxadiazole fluorescent probe was inserted. (B) CLSM micrograph of the hydrogel with green fluorescence arising from the probe. Image adapted from Ref. 5 with permission from Wiley.

Recent studies, exemplified by the work of Onogi *et al.*, explore the self-sorting behaviour of a composite hydrogel using confocal microscopy.⁶ Here, the formation of a supramolecular structure (through the heating/cooling method) was tracked *in situ* with confocal microscopy. The study observed and tracked the formation of fibres resulting from the interaction between a peptide and an amphiphilic phosphate hydrogelator, along with the use of two specific fluorescent staining compounds (**Fig. 5.3**). Additionally, a cross-sectional view was obtained, enabling the visualisation of a three-dimensional network.

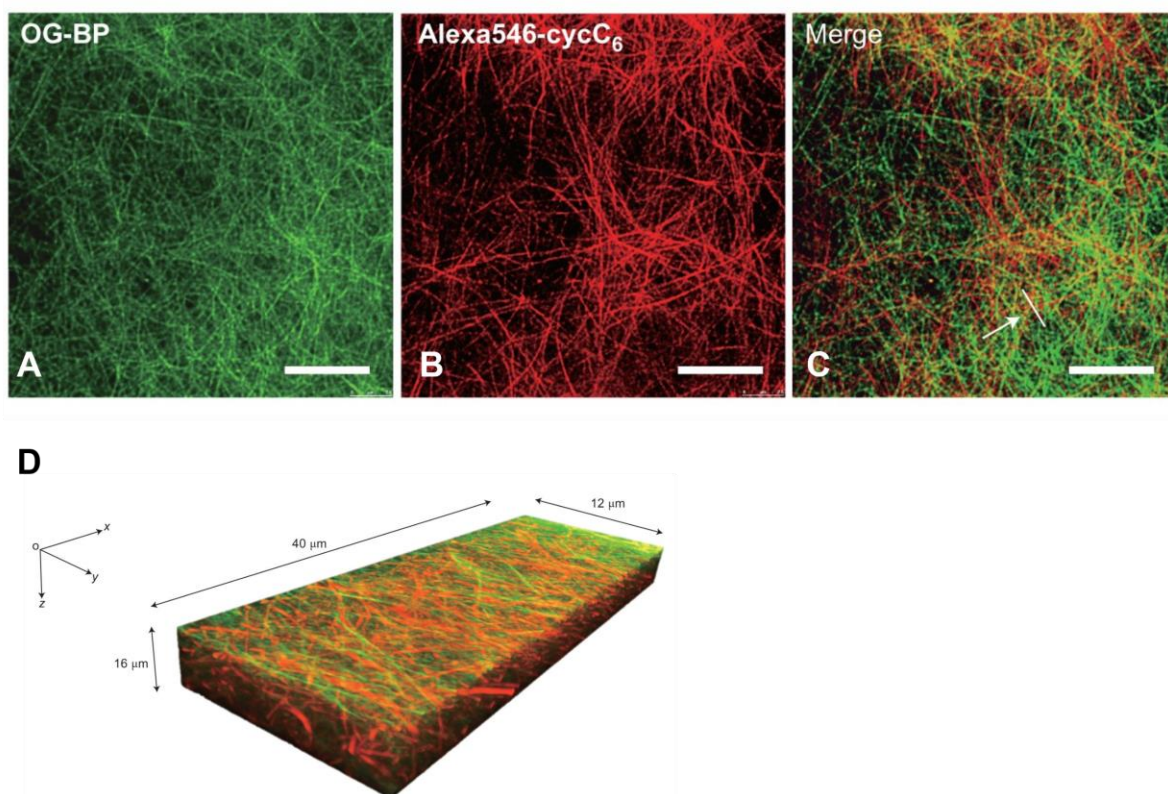


Figure 5.3. CLSM micrographs of a four-component hydrogel mixture. (A) Micrograph of stained peptide gelator fibres. (B) Micrograph of stained amphiphilic phosphate gelator fibres. (C) Micrograph of the merging of the channels of A and B reveals the full fibre morphology. (D) Z-stack of micrographs seen in C. Scale bars correspond to 5 μm . Image adapted from Ref. 6 with permission from Springer Nature.

In another example of CLSM hydrogel imaging, Kotlarchyk *et al.* employed laser tweezers and confocal reflection microscopy to visualize fibrin hydrogels. They successfully integrated microrheology and imaging to establish a method for investigating the relationship between mechanical characteristics and microenvironmental factors.⁷ CLSM has also found application in characterising multiresponsive dynamic hydrogels and measuring hydrogel elasticity.⁸⁻¹⁰

The objective of this project was to image bis-imidazolium hydrogels containing fluorescent compounds using CLSM and establish correlations between these micrographs and those obtained using total internal reflection fluorescence (TIRF) microscopy. Various fluorophores would be employed to emphasise the gel morphology and potentially investigate the specific behaviour of individual fluorophores within gel fibres.

5.2. Zinc(II) phthalocyanine tetrasulfonic acid (ZnPcTS) and 5,10,15,20-(Tetra-4-sulfonatophenyl)porphyrin

Imaging with the confocal microscope involved placing a portion of a pre-formed gel sample onto a glass coverslip. In certain experiments, a second glass slide was used to compress the gel sample, facilitating the imaging of relatively weak fluorophores. Imaging was first carried out on a sample of 1,3-bis[(3-octadecyl-1-imidazolium)methyl]benzene di-bromide gelator gel containing zinc phthalocyanine tetrasulfonic acid (**ZnPcTS@Gel**). This material was previously studied using TIRF microscopy (Chapter 3), where gel morphology was analysed along with fluorophore dynamics at low fluorophore loading (0.1 μM). To conduct CLSM measurements, a minimum **ZnPcTS** loading of 150 μM was necessary for viable imaging. As compressing the gel between two glass slides was necessary for imaging, many parts of the gel were broken (**Fig. 5.4**). This can be most clearly seen in **Fig. 5.4B**, where two sections of a gel are separated by ~ 25 microns with fibres in between. Images containing broken areas of the gel (**Figs 5.4B,D**) enable the visualisation of individual fibres, while the resolution does not permit this in images of a homogeneous gel area (**Figs 5.4A,C**).

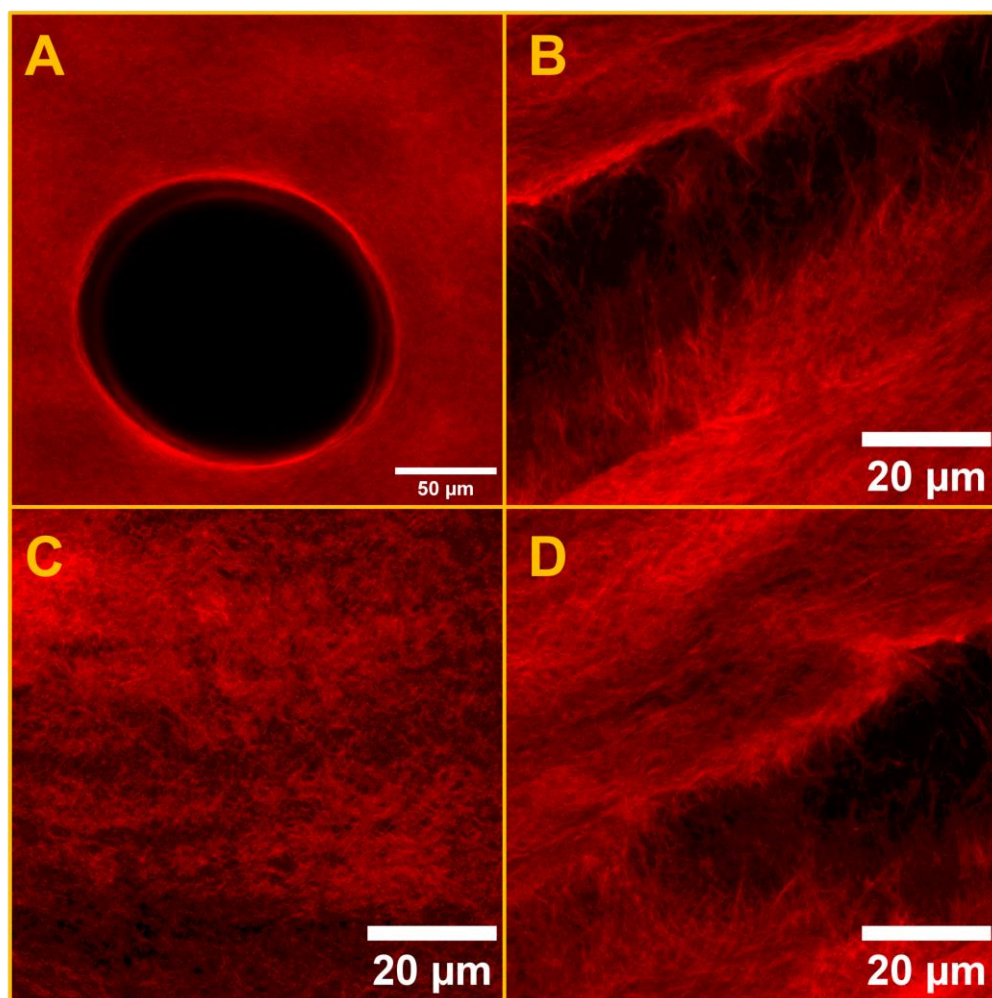


Figure 5.4. Snapshots of **ZnPcTS@Gel** at various scales. (A) Snapshot of a bubble present in a **ZnPcTS@Gel** sample. (B) Snapshot of an area where the **ZnPcTS@Gel** has been pulled apart when compressed. (C) Snapshot of an unbroken area of **ZnPcTS@Gel**. (D) Snapshot of a partially broken area of **ZnPcTS@Gel**. Imaging details: laser 650 nm, emission LP filter 650 nm, laser power 100%.

Increasing the **ZnPcTS** loading still further did not yield an appreciable increase to the resolution of images acquired and lowering the concentration to the point of being able to image single molecules was not viable. Gels containing 5,10,15,20-(tetra-4-sulfonatophenyl)porphyrin tetraammonium (**TPPS**) (**Fig. 5.5**) were then prepared for CLSM analysis. **TPPS** has a higher fluorescence quantum yield than **ZnPcTS**, so it was conceivable that higher-resolution images could be obtained. Structurally, **TPPS** is similar to **ZnPcTS**, with four peripheral sulfonate units and their subsequent interactions with the positively charged heads of the **1.2Br** gelator allowing potentially for movement along gel fibres as seen with TIRF microscopy of **ZnPcTS@Gel** samples.

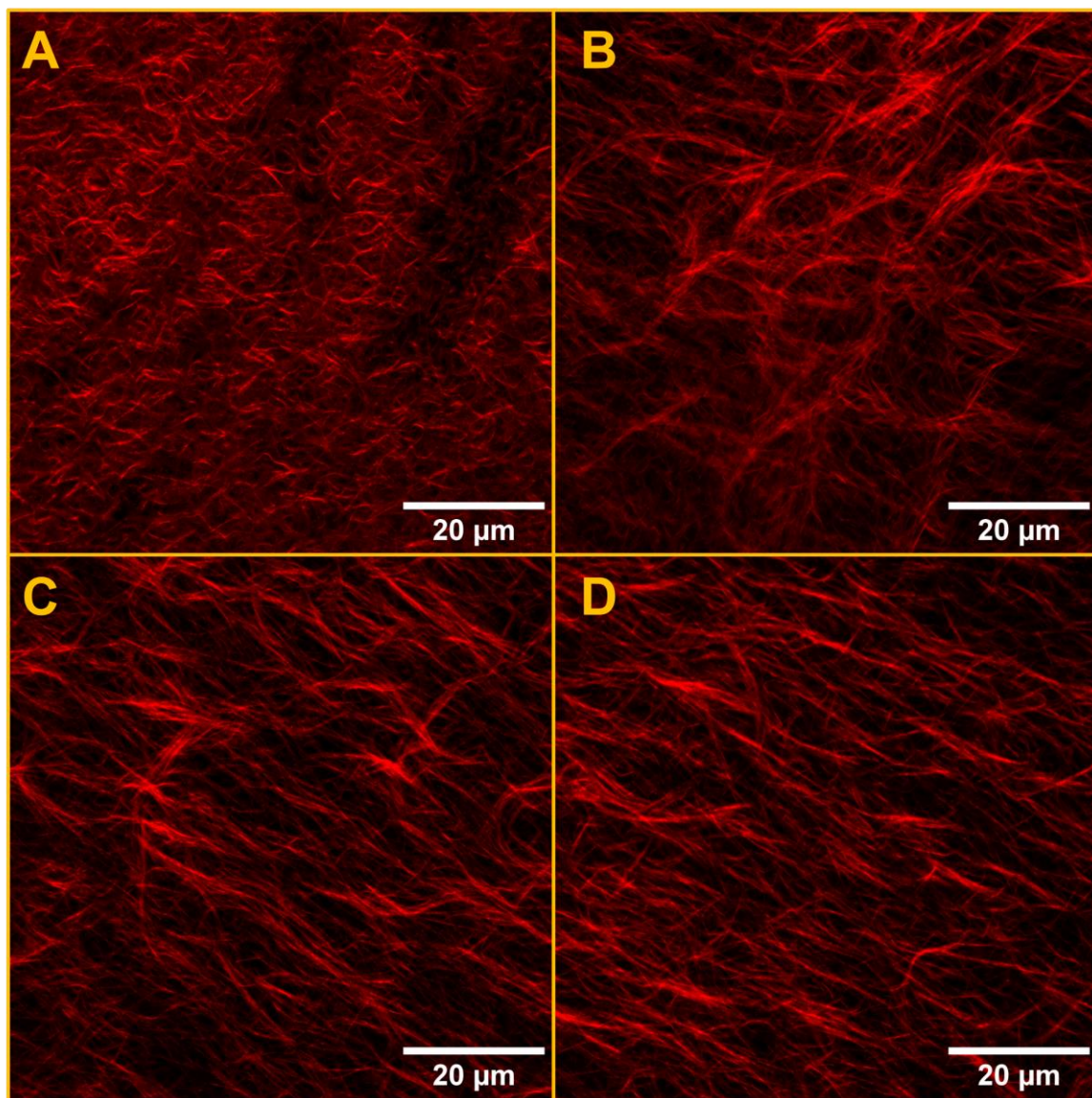


Figure 5.5. Snapshots of *TPPS@Gel*. (A) Structure of *TPPS*. (B-E) Snapshots of *TPPS@Gel* displaying more resolved fibre morphology than *ZnPcTS@Gel*. [*TPPS*] = 150 μ M. Imaging details: laser 405 nm, emission LP filter 650 nm, laser power 100%

TPPS@Gel with the same fluorophore concentration as **ZnPcTS@Gel** (150 μ M) (**Fig. 5.5**) displayed fibres that were much more resolved than the latter. This increase in resolution can be attributed to more intense fluorescence of **TPPS**. Despite requiring the compression of the gel between glass slides, fibres could be seen throughout the sample rather than exclusively in areas of gel breakage. **TPPS@Gel** exhibited clustering of fibre density around specific areas. Fibres also tend to curve and twist in random directions in a manner that matches previous SEM and TIRF imaging of a porphyrin encapsulated within this gel system. Fibre width could not be accurately measured as the measured fluorescence are made up of individual airy disks that correspond to a distribution.

As with **ZnPcTS@Gel**, it was not possible to observe any potential fluorophore movement in the **TPPS@Gel** sample. When **TPPS@Gel** was studied under TIRF conditions (Chapter 3), no fluorophore diffusion could be observed. Again, single molecule imaging proved unviable as the lowering of **TPPS** concentration resulted in very low signal-to-noise.

5.3. DPP@Gels

Whilst gel morphology was observable using both **ZnPcTS** and **TPPS**, an increase in resolution was required to effectively image the gels. Whilst **ZnPcTS** and **TPPS** are both fluorescent enough to image, porphyrins and phthalocyanines generally have relatively low quantum yields compared with commercial fluorophores. A class of synthetic fluorophores of major recent interest are derivatives of diketopyrrolopyrrole (DPP), a heterocyclic dilactam-based dye (**Fig. 5.6**).

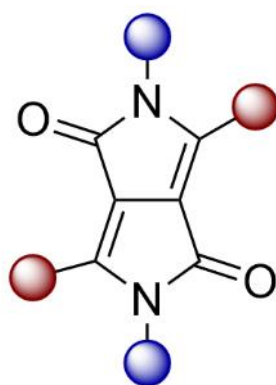


Figure 5.6. The core of a DPP is 2,5-dihydropyrrolo[3,4-*c*]pyrrole-1,4-dione, which can be functionalized either on the lactam nitrogens (blue) or the 3 and 6 positions of the core (red).

Accidentally discovered in the 1970's, DPPs are versatile dyes that are easily functionalized.¹² Functionalisation of the DPP core with aromatic units such as pyridyl, phenyl, or thiophene units results in significant π -conjugation between the electron rich (aromatic) and electron poor (DPP core) sections of the molecule. The physical and chemical properties of DPPs can be modulated through functionalisation and this has rendered them attractive for optoelectronic applications.¹³⁻¹⁵ The high fluorescence quantum yield and photostability of DPPs also makes them reliable for use in bioimaging.¹⁶

Though the preparation of hydrogels formed through the self-assembly of DPPs containing gelator moieties has been demonstrated, no research as of yet has concerned the use of DPPs for investigating hydrogel morphology using fluorescence microscopy.¹⁷ DPPs are therefore an attractive fluorescent probe to use in the bis-imidazolium gel system under investigation here.

5.3.1. PyranDPP

An *N*-hexyl DPP containing ether linked phenyltetrahydropyran groups (**PyranDPP**) was chosen as the first DPP fluorophore candidate. Whilst the previous fluorophores (**ZnPcTS** and **TPPS**) were at least partially anionic within the imidazolium gel, which is an important contributor to encapsulation, **PyranDPP** is neutral compound and though encapsulation of neutral compounds in this imidazolium gel has been demonstrated, it was unknown whether encapsulation and fluorescence in gel fibres viable.¹⁸ Gel preparation was carried out with **PyranDPP** in the ethanolic phase along with **1.2Br**, and gel formation occurred within twenty seconds. **Fig. 5.7** displays both the absorption and fluorescence emission spectra of **PyranDPP** in solution and **PyranDPP@Gel**, respectively.

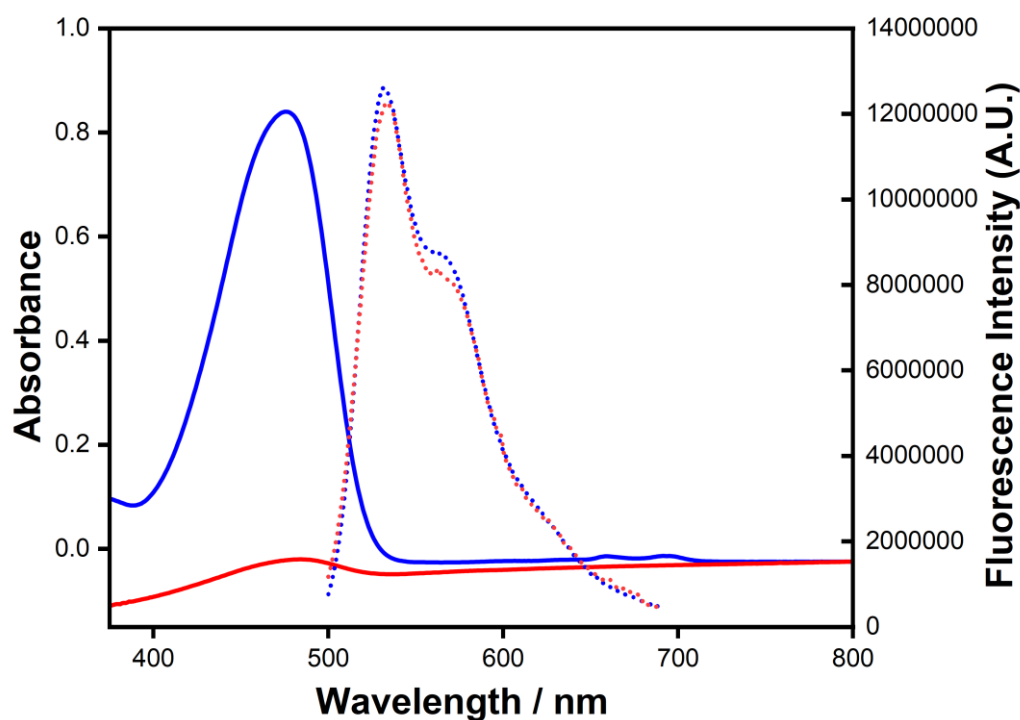


Figure 5.7. Plot displaying the absorption spectrum of **PyranDPP** in 1:1 water-ethanol solution, $[\text{PyranDPP}] = 100 \mu\text{M}$ (blue solid line), absorption spectrum of **PyranDPP@Gel**, $[\text{PyranDPP}] = 200 \mu\text{M}$ (red solid line), fluorescence emission spectrum of **PyranDPP** in 1:1 water-ethanol, $[\text{PyranDPP}] = 100 \mu\text{M}$ (blue dotted line), and fluorescence emission spectrum of **PyranDPP@Gel**, $[\text{PyranDPP}] = 200 \mu\text{M}$ (red dotted line). $\lambda_{\text{exc}} = 480 \text{ nm}$ for both fluorescence emission measurements.

As with **ZnPcTS**, incorporation of **PyranDPP** into **1.2Br** gels alters the magnitude of the absorption peak at 478 nm, though the position of this peak is unchanged by the gel. The shape

of the absorption profile matches those of six-membered DPPs more generally.^{19,20} Likewise to the absorption, there is no difference in the position or shape of the fluorescence emission maxima between the **PyranDPP** in solution or in the gel with the emission maximum falling at 532 nm with a shoulder at 568 nm.

It is immediately apparent that the resolution and signal-to-noise acquired using **PyranDPP** qualitatively far exceeds that of **ZnPcTS** and **TPPS** (**Fig. 5.8**). Additionally, compression of the gel between glass slides was not necessary to yield its effective imaging. This allowed for the gel's visualisation without significant disturbance to both its macrostructure and microstructure. Though little difference can be observed between the compressed and non-compressed gel images, repeating cyclical local domains can be seen in the non-compressed sample (**Fig. 5.8B,C**). Fluorescent spots corresponding to **PyranDPP** aggregates could also be observed at random points along gel fibres. These spots tended to grow over the course of imaging and could be a result of solvent evaporation with the water-ethanol ratio increasing and the non-water soluble **PyranDPP** precipitating.

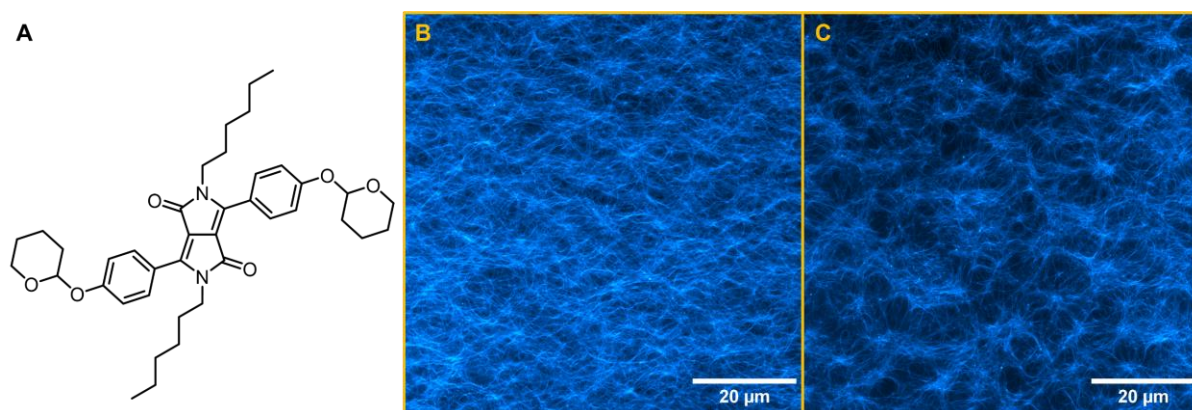


Figure 5.8. Snapshots of **PyranDPP@Gel**, $[\text{PyranDPP}] = 100 \mu\text{M}$. (A) Structure of **PyranDPP**. (B) Snapshot of the gel morphology of a compressed sample of **PyranDPP@Gel**. (C) Snapshot of the gel morphology of an uncompressed sample of **PyranDPP@Gel**. Imaging details: laser 488 nm, emission range 500-700 nm, laser power 55%.

To further investigate the encapsulation behaviour of the gel system, a gel containing both **TPPS** and **PyranDPP** was prepared. Dual-fluorophore gel systems have been shown to self-sort into separate fibre structures, although in this study there is only one supramolecular component.⁶ As before, gel formation occurred after around 20 seconds.

As the fluorescence quantum yield of **TPPS** is lower than that of **PyranDPP**, the fluorescence signal from the latter dominates the micrographs and only a faint signal can be seen of **TPPS**.

There was no separation of **PyranDPP** and **TPPS** into separate fibre domains, with the fluorophores largely occupying the same fibres.

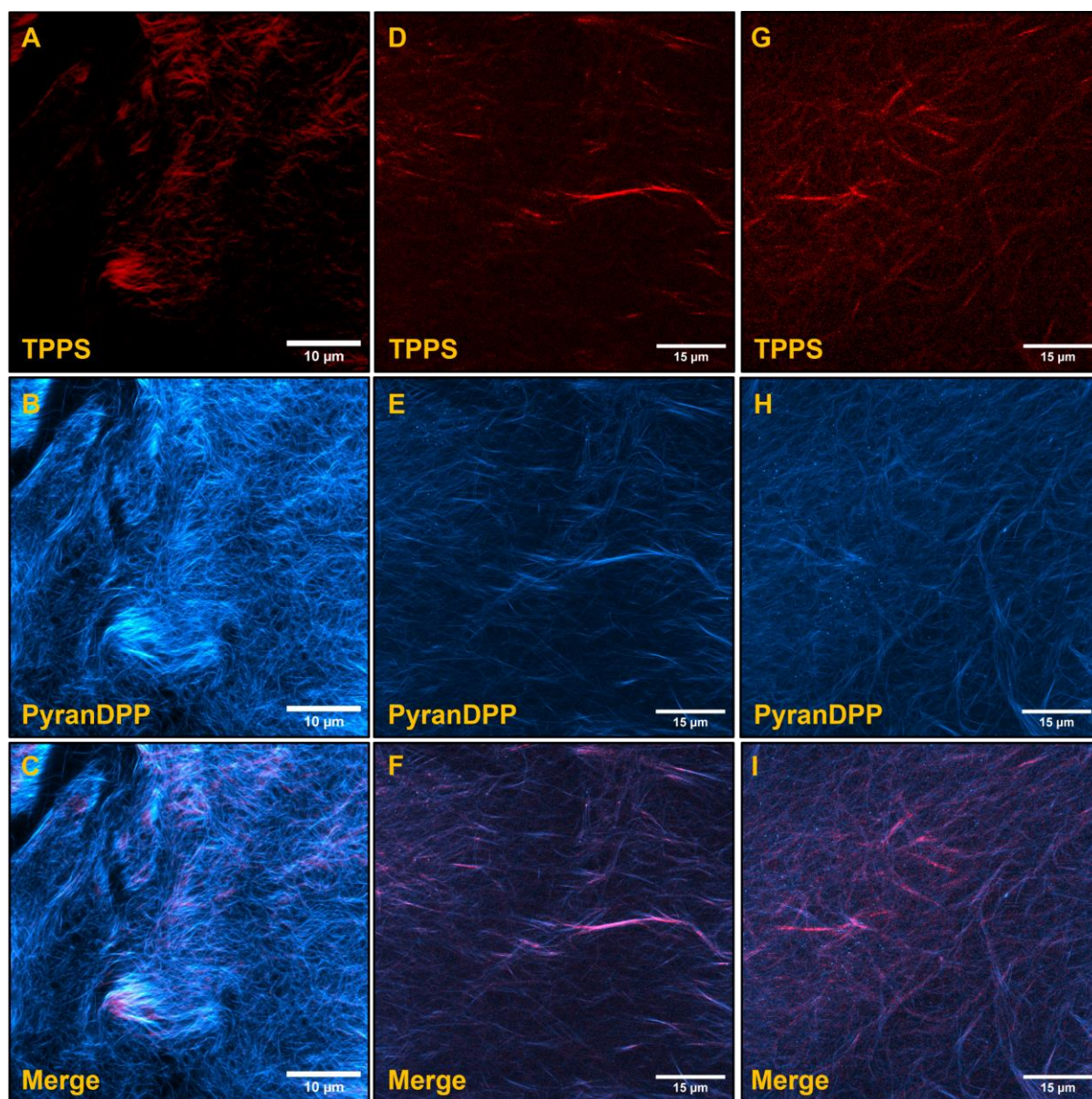
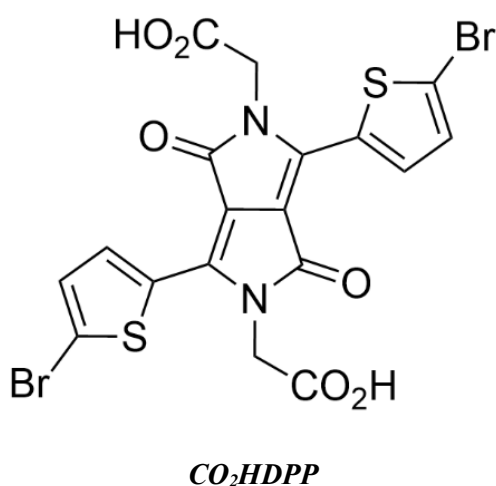


Figure 5.9. CLSM micrographs of *PyranDPP@TPPS@Gel* [*PyranDPP*] = 100 μ M, [*TPPS*] = 100 μ M. (A-C) One area of *PyranDPP@TPPS@Gel* showing the individual fluorescence signal from *TPPS* and *PyranDPP* individually, along with a merged channel micrograph. (D-F) A second area of *PyranDPP@TPPS@Gel* showing the individual fluorescence signal from *TPPS* and *PyranDPP* individually, along with a merged channel micrograph. (G-I) A final area of *PyranDPP@TPPS@Gel* showing the individual fluorescence signal from *TPPS* and *PyranDPP* individually, along with a merged channel micrograph. Imaging details: [*PyranDPP*] : laser 488 nm, emission range 500-700 nm, laser power 30%. [*TPPS*] : laser 405 nm, emission LP filter 650 nm, laser power 100%.

Figure 5.9A,C shows one area towards the bottom of the sample where **PyranDPP** and **TPPS** resides largely in the same fibres. The same can be seen in micrographs (**D-F**), with a specific fibre to the right of centre in **F** clearly showing the presence of both fluorophores. However, micrographs **G-I** do show **TPPS** signal arising along lines that do not correspond fully to fibres in the **PyranDPP** micrograph in **H**.

5.3.2. CO₂HDPP

With a reliable method for gel imaging using CLSM being developed, the DPP fluorophore library was extended by incorporating a water-soluble derivative into the **1.2Br** gel system. **CO₂HDPP** is a DPP functionalized on the dilactam nitrogens with carboxylic acid groups. These groups render the compound soluble in aqueous media. In addition, the DPP core is functionalized with thiophene groups which alter the conjugation and subsequently change the position of the absorption and fluorescence emission maxima with respect to **PyranDPP** as can be seen in **Fig. 5.10**, meaning 560 nm excitation light was chosen to be used instead of 488 nm.



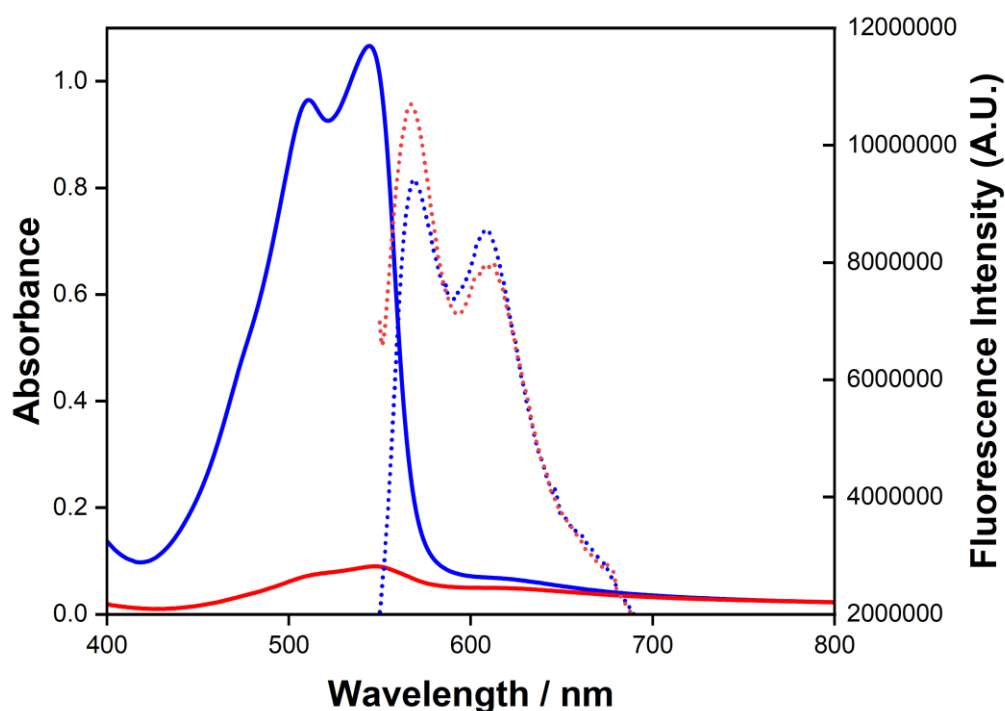


Figure 5.10. Plot displaying the absorption spectrum of **CO₂HDPP** in 1:1 water-ethanol solution, $[CO_2HDPP] = 100 \mu M$ (blue solid line), absorption spectrum of **CO₂HDPP@Gel**, $[CO_2HDPP] = 200 \mu M$ (red solid line), fluorescence emission spectrum of **CO₂HDPP** in 1:1 water-ethanol, $[CO_2HDPP] = 100 \mu M$ (blue dotted line), and fluorescence emission spectrum of **CO₂HDPP@Gel**, $[CO_2HDPP] = 200 \mu M$ (red dotted line). $\lambda_{exc} = 530 \text{ nm}$ for both fluorescence emission measurements.

As with **PyranDPP**, **CO₂HDPP** yielded significantly improved resolution compared with the porphyrin and phthalocyanine fluorophores. **Figure 5.11** shows CLSM micrographs displaying **1.2Br** gel fibres containing **CO₂HDPP**, which closely resemble those containing **PyranDPP**. By altering the microscope focus, different focal planes could be accessed. This manipulation of focus allowed for the imaging of both the bulk morphology and the fibre morphology at the position where the gel samples is in contact with the glass coverslip. It can be seen that fibre morphology in the bulk of the gel is more continuous and homogenous than that in contact with the coverslip. Additionally, the fibre density diminishes near the interface between the gel and the coverslip.

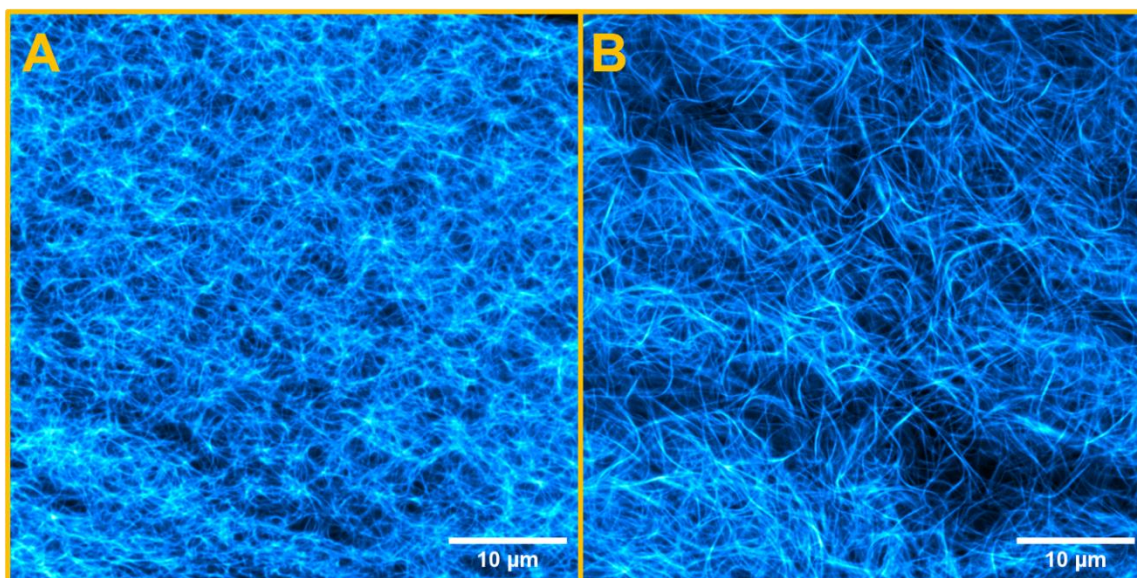


Figure 5.11. CLSM micrographs of $\text{CO}_2\text{HDPP@Gel}$, $[\text{CO}_2\text{HDPP}] = 100 \mu\text{M}$. (A) Micrograph of the bulk fibre morphology of $\text{CO}_2\text{HDPP@Gel}$. (B) Micrograph of the fibre morphology of $\text{CO}_2\text{HDPP@Gel}$ where the gel sample is in contact with the glass coverslip. Imaging details: laser 560 nm, emission range 565 – 700 nm, laser power 30%.

There was significant photobleaching of CO_2HDPP over the course of these experiments, an example of which can be seen in **Fig. 5.12**. The photobleaching led to a deterioration of resolution over the duration of laser irradiation. After an area of sample was irradiated for 10 minutes, the z-profile intensity decreased by $\sim 60\%$.

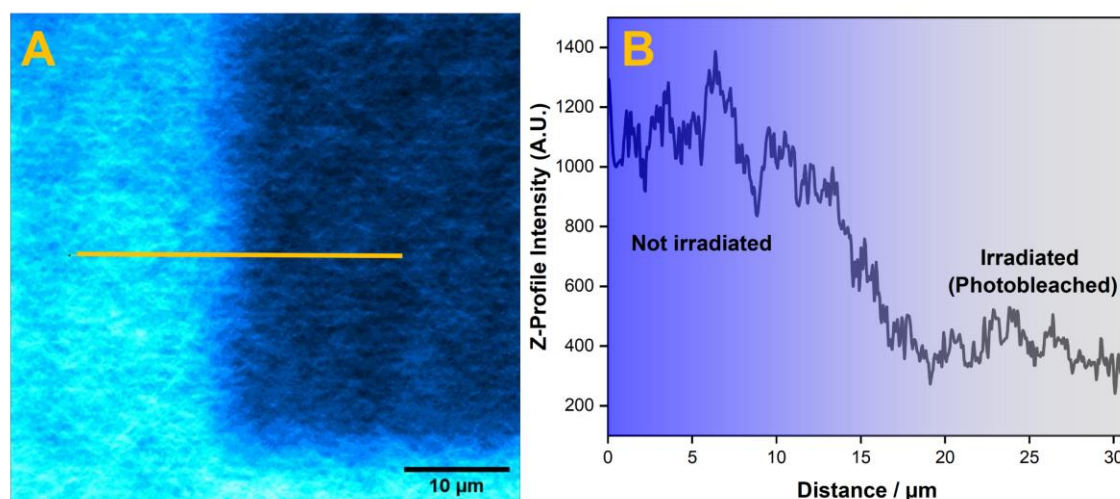


Figure 5.12. (A) Micrograph of $\text{CO}_2\text{HDPP@Gel}$ containing areas of high intensity (left) not touched by laser irradiation and low intensity (right) which was subjected to 10 minutes of continuous irradiation of 560 nm light. (B) Intensity profile of the yellow line in A shows a sharp decrease in the area irradiated with 560 nm light for 10 minutes. Imaging details: laser 560 nm, emission range 565 – 700 nm, laser power 100%.

In spite of the photobleaching issue, **CO₂HDPP** remained an appealing choice for exploring the three-dimensional fibrous structure through z-stack experiments. In contrast to **PyranDPP**, **CO₂HDPP** does not exhibit the aggregates that result in spots in the micrographs. Initial z-stack experiments were carried out within the bulk of the material where fibre density was high. This high fibre density made it difficult to visualize individual fibres in the 3D stack (**Fig. 5.13**). Z-stacks were also collected from images located near the gel-coverslip interface. Here, the fibre density was slightly lower meaning that individual fibres could be better resolved. As seen in **Fig. 5.13B**, the gel morphology at the gel-coverslip interface consists of loosely adhered fibres followed by the bulk of the sample which is better represented by **Fig. 5.13A**.

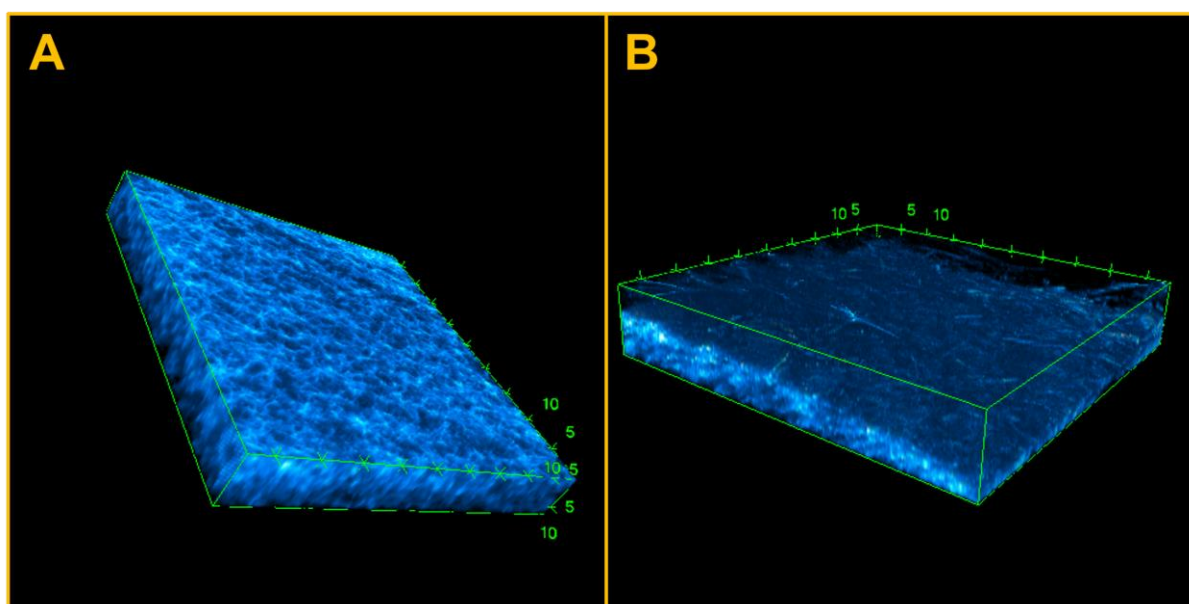
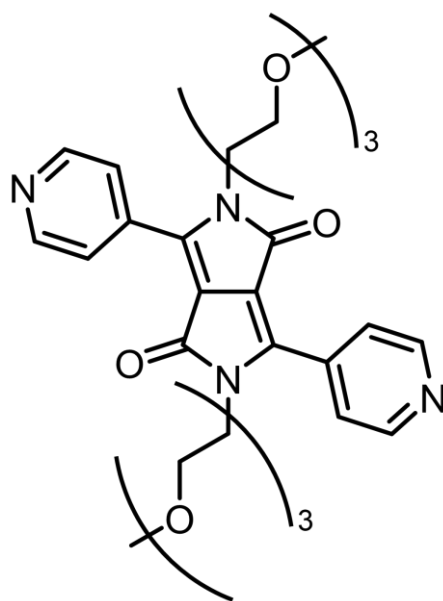


Figure 5.13. (A) Three-dimensional view of a z-stack of x-y slice images collected of **CO₂HDPP@Gel** in an area of high fibre density. (B) Three-dimensional view of a z-stack of x-y slice images collected of **CO₂HDPP@Gel** in an area of low fibre density near the gel-coverslip interface. Units of boundary boxes are μm . Imaging details: laser 560 nm, emission range 565 – 700 nm, laser power 30%.

5.3.3. Pyridine/PyridiniumDPPs

Further non-ionic water-soluble DPPs were also incorporated into this gel system. **PEG3DPP** is a DPP functionalized on the dilactam nitrogens with a polyethylene glycol chain possessing three such units. Pyridine groups are also present on the core of the DPP.



PEG3DPP

As with **PyranDPP** and **CO₂HDPP**, the absorption profile of **PEG3DPP** is largely unchanged with incorporation into the **1.2Br** gel compared to its shape in 1:1 water-ethanol solution (**Fig. 5.14**). **PEG3DPP** possesses an absorption maximum of ~ 467 nm in 1:1 water-ethanol and ~ 476 nm in **PEG3DPP@Gel**, with a significantly decreased magnitude in the case of the latter. There is a considerable difference in the fluorescence profile of **PEG3DPP** in 1:1 water-ethanol solution and in the **1.2Br** gel. Although both fluorescence profiles display a maximum at ~ 545 nm, **PEG3DPP@Gel** possesses a shoulder at ~ 578 nm which is not present in the case of **PEG3DPP** in 1:1 water-ethanol. This shoulder could be evidence of excimer emission brought about by aggregation within the **1.2Br** gel system.

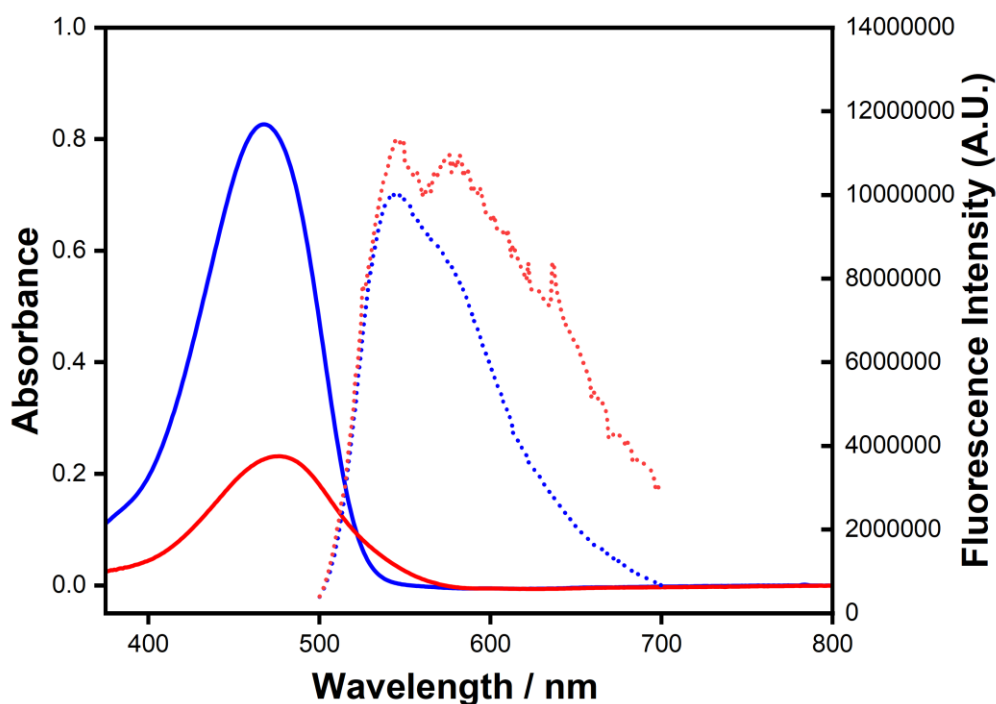


Figure 5.14. Plot displaying the absorption spectrum of **PEG3DPP** in 1:1 water-ethanol solution, $[PEG3DPP] = 50 \mu M$ (blue solid line), absorption spectrum of **PEG3DPP@Gel**, $[PEG3DPP] = 200 \mu M$ (red solid line), fluorescence emission spectrum of **PEG3DPP** in 1:1 water-ethanol, $[PEG3DPP] = 50 \mu M$ (blue dotted line), and fluorescence emission spectrum of **PEG3DPP@Gel**, $[PEG3DPP] = 200 \mu M$ (red dotted line). $\lambda_{exc} = 480 \text{ nm}$ for both fluorescence emission measurements.

CLSM imaging of **PEG3DPP@Gel** revealed an unexpected phenomenon. Rather than the gel fibres encapsulating the **PEG3DPP** fluorophores and showing little fluorescence from the interstitial liquid, the fluorescence signal originated solely from the interstitial liquid. As a result, the fibres appeared as dark silhouettes against a bright background (**Fig. 5.15**). This lack of encapsulation preference was hypothesised to be a consequence of the hydrophilicity of the fluorophore.

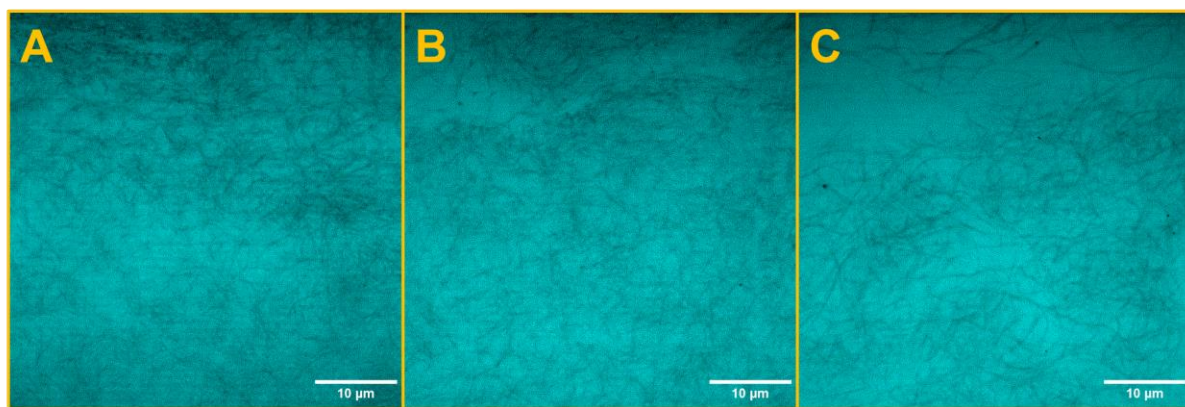


Figure 5.15. (A-C) CLSM micrographs of *PEG3DPP@Gel*, $[PEG3DPP] = 150 \mu M$, where fluorophores are not encapsulated by fibres and therefore fibres appear as silhouettes against the fluorescent background. Imaging details: laser 488 nm, emission range 500-700 nm, laser power 30%.

After roughly 5 minutes, however, the bright background dissipated, and the fibre silhouettes seemed to gain fluorescence intensity (**Fig. 5.16**). This change indicated the movement of fluorophores from the interstitial liquid into the fibres. Between 4 to 8 minutes, the background fluorescence mostly disappeared, and the fluorescence intensity within the fibres began to dominate. Concurrently, the gel sample underwent positional changes over time. This movement resulted from the gel sample shrinking as the solvent evaporated during the experiment. Consequently, it appears as though the fibres themselves are in motion. In reality, the focal plane remains constant, and the fibres move within it as the gel contracts due to shrinking. This shrinking process makes it impossible to track an individual fibre silhouette encapsulating fluorophores over time, and only an ensemble view of migration can be obtained.

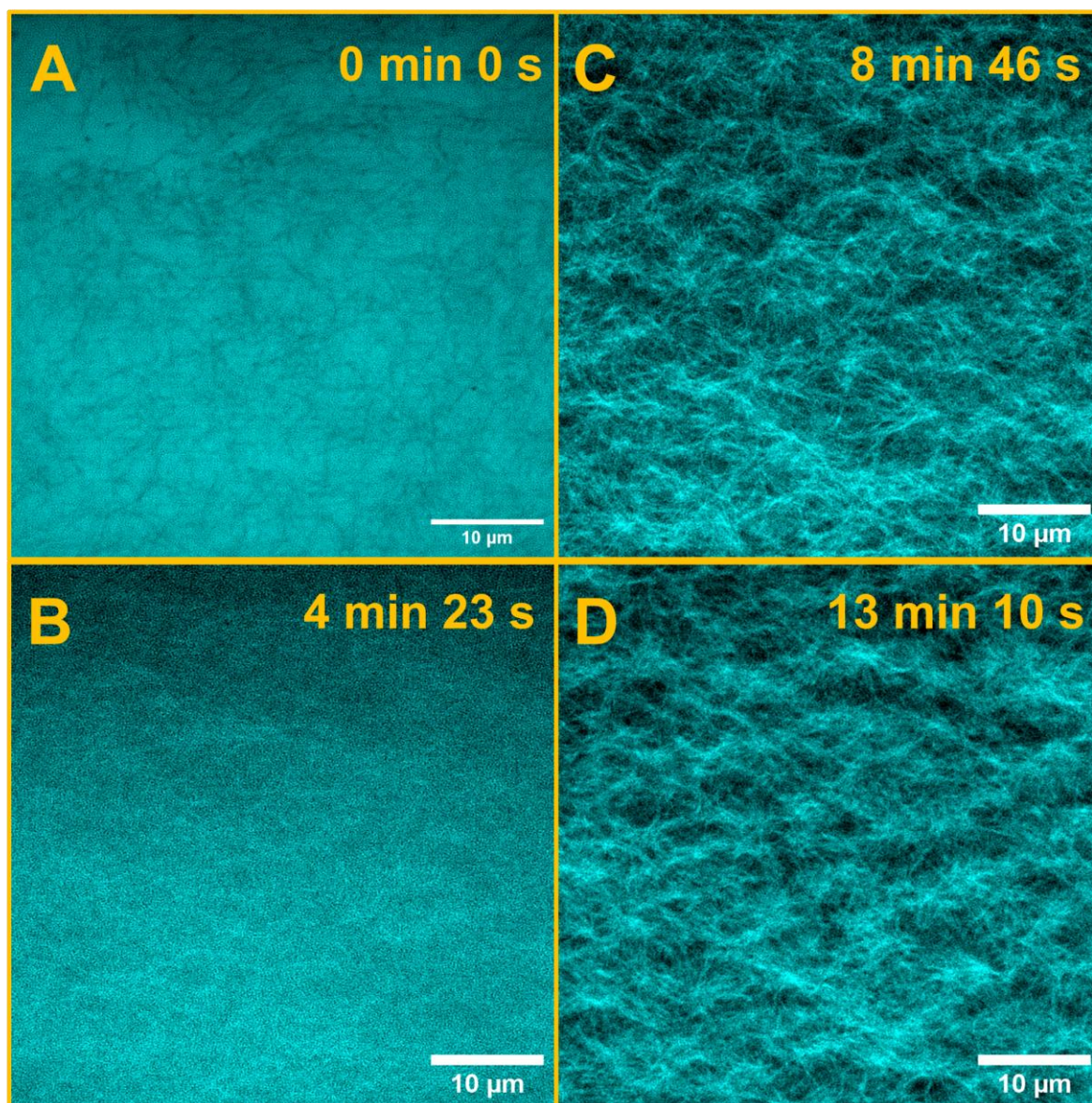


Figure 5.16. CLSM micrographs of *PEG3DPP@Gel*, $[PEG3DPP] = 150 \mu M$, showing the migration of *PEG3DPP* into *1.2Br* fibres. (A) Micrograph of *PEG3DPP@Gel* showing fibre silhouettes at $t = 0$ s. (B) Micrograph of *PEG3DPP@Gel* showing the initial migration of *PEG3DPP* into fibres, with some fluorescence signal still in the interstitial areas at $t = 4$ min 23 s. (C) Micrograph of *PEG3DPP@Gel* showing the significant migration of *PEG3DPP* into fibres, with little fluorescence signal still in the interstitial areas at $t = 8$ min 46 s. (D) Micrograph of *PEG3DPP@Gel* showing the completion of *PEG3DPP* migration into fibres, with little-to-no fluorescence signal still in the interstitial areas at $t = 13$ min 10 s. Imaging details : laser 488 nm, emission range 500-700 nm, laser power 30%.

It was hypothesized that the evaporation of solvent (water and ethanol) over the course of the imaging process contributed to the migration of the DPP fluorophores into the gel fibres. To test this hypothesis, a control experiment was carried out where another glass plate was gently

placed over the top of the gel sample. This glass plate would limit the extent to which the solvent was removed. Over the course of 15 minutes, both the **PEG3DPP** migration and the shrinking of the gel sample were not observed, with the same black fibre silhouettes remaining relatively stationary over the timeframe of the movie (**Fig. 5.17**).

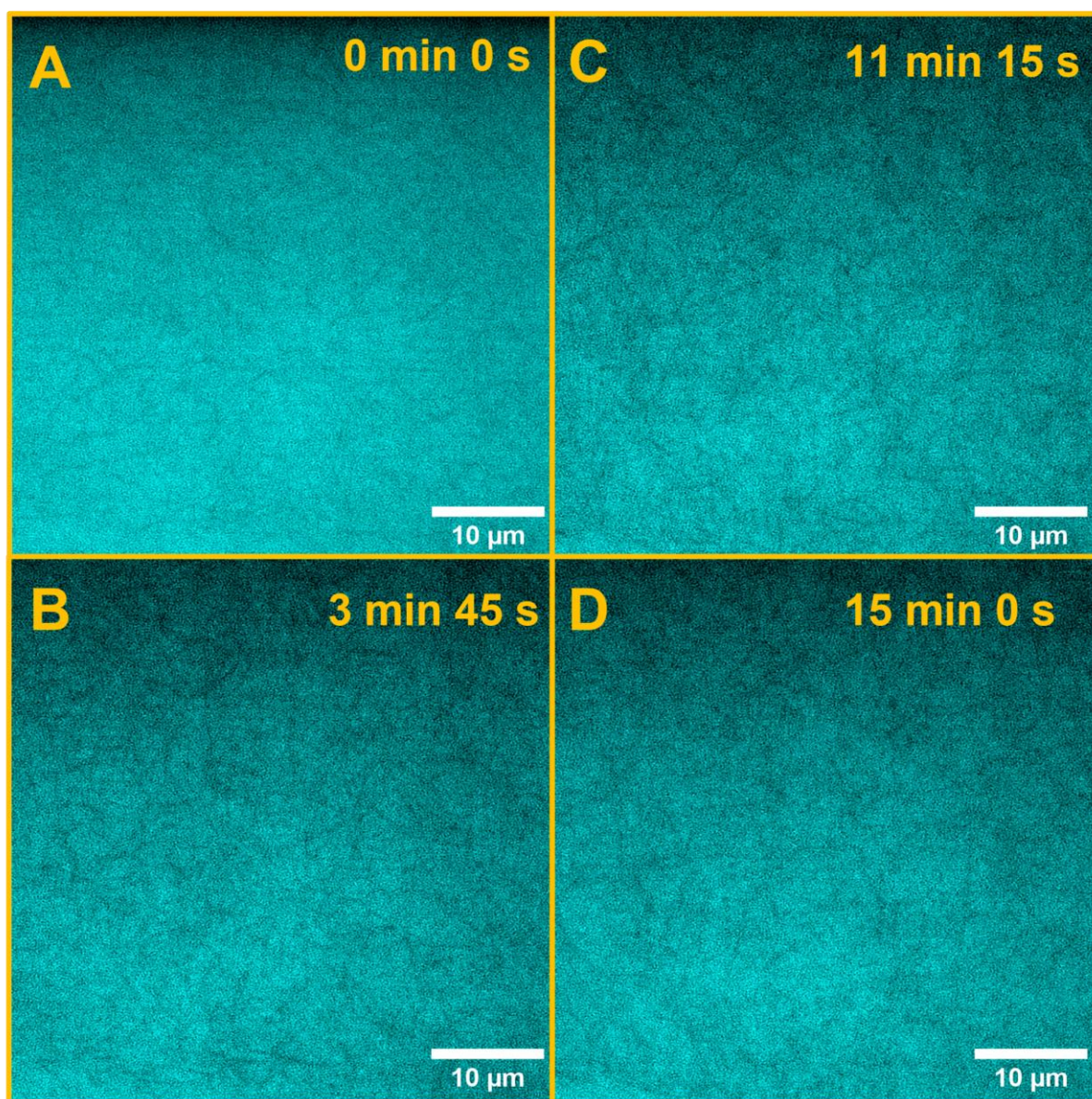
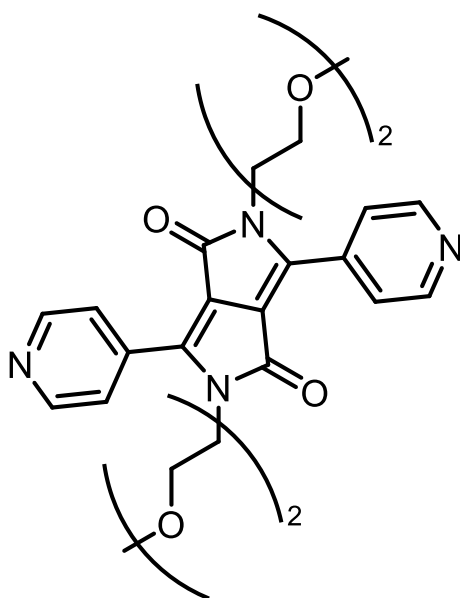


Figure 5.17. CLSM micrographs of **PEG3DPP@Gel** with a glass plate preventing solvent evaporation, $[PEG3DPP] = 150 \mu M$, showing no migration of **PEG3DPP** into **1.2Br** fibres. (A) Micrograph of **PEG3DPP@Gel** showing fibre silhouettes at $t = 0$ s. (B) Micrograph of **PEG3DPP@Gel** showing no migration of **PEG3DPP** into fibres at $t = 3$ min 45 s. (C) Micrograph of **PEG3DPP@Gel** showing still no migration of **PEG3DPP** into fibres, with a slight photobleaching of fluorescence at $t = 11$ min 15 s. (D) Micrograph of **PEG3DPP@Gel** showing no migration of **PEG3DPP** into fibres with further photobleaching of fluorescence at $t = 15$ min 0 s. Imaging details : laser 488 nm, emission range 500-700 nm, laser power 30%.

It was not immediately clear what was causing the fluorophore both not to be encapsulated nor why solvent evaporation promoted their encapsulation during imaging. As a more hydrophilic compound than the previous DPPs which were effectively encapsulated upon gel formation, **PEG3DPP** may have preferred to reside in the interstitial liquid. Evaporation of the ethanol component of the solvent system would occur faster than that of water, meaning the solvent environment around the fibres would contain an increasing proportion of water over time. As mentioned, this increase in solvent hydrophilicity should have the opposite effect of causing the **PEG3DPP** to remain in the interstitial liquid upon ethanol evaporation.

To test this hydrophilicity hypothesis further, a DPP identical to **PEG3DPP** but possessing a polyethylene glycol chain length of 2 instead of 3 (**PEG2DPP**) was imaged as part of the **1.2Br** gel. **PEG2DPP** should be marginally less hydrophilic than **PEG3DPP**, which may influence its encapsulation behaviour.



PEG2DPP

As with all of the previous DPPs studied here, the absorption profile of **PEG2DPP** is largely unchanged with incorporation into the **1.2Br** gel compared to its shape in 1:1 water-ethanol solution (**Fig. 5.18**). **PEG2DPP** possesses an absorption maximum of ~ 467 nm in 1:1 water-ethanol and ~ 471 nm in **PEG2DPP@Gel**, with a significantly decreased magnitude in the case of the latter. Unlike in the case of **PEG3DPP**, the fluorescence profile is also largely unchanged between the gel and solution phase, with a fluorescence emission maximum at ~ 547 nm.

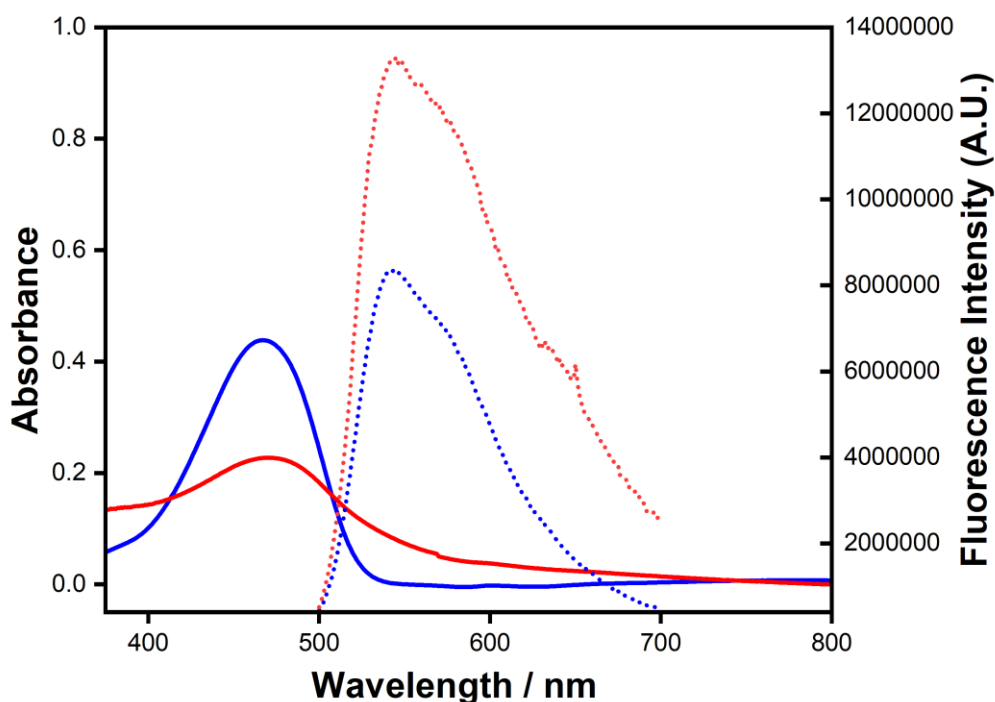


Figure 5.18. Plot displaying the absorption spectrum of **PEG2DPP** in 1:1 water-ethanol solution, $[PEG2DPP] = 50 \mu M$ (blue solid line), absorption spectrum of **PEG2DPP@Gel**, $[PEG2DPP] = 200 \mu M$ (red solid line), fluorescence emission spectrum of **PEG2DPP** in 1:1 water-ethanol, $[PEG2DPP] = 50 \mu M$ (blue dotted line), and fluorescence emission spectrum of **PEG2DPP@Gel**, $[PEG2DPP] = 200 \mu M$ (red dotted line). $\lambda_{exc} = 480 \text{ nm}$ for both fluorescence emission measurements.

CLSM imaging of **PEG2DPP@Gel** displayed fluorophore behaviour similar to that seen in **PEG3DPP@Gel**. Fibre silhouettes are more clearly seen with **PEG2DPP@Gel**, indicating that there is greater preference for the fluorophore to reside in the interstitial liquid (**Fig. 5.19**). However, a significant increase in the time taken for encapsulation to finally occur upon solvent evaporation with **PEG2DPP** requiring ~ 20 minutes for encapsulation to occur whereas **PEG3DPP** encapsulation occurred after only 4-6 minutes. This increase in encapsulation time suggests that hydrophilicity is not the main factor influencing encapsulation during confocal imaging.

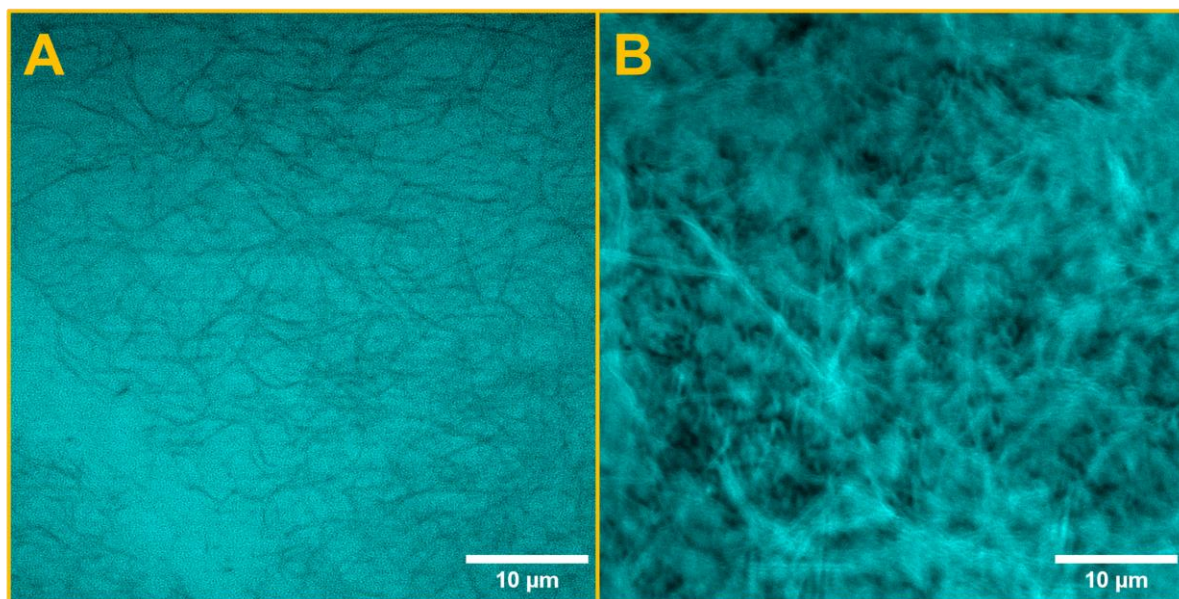
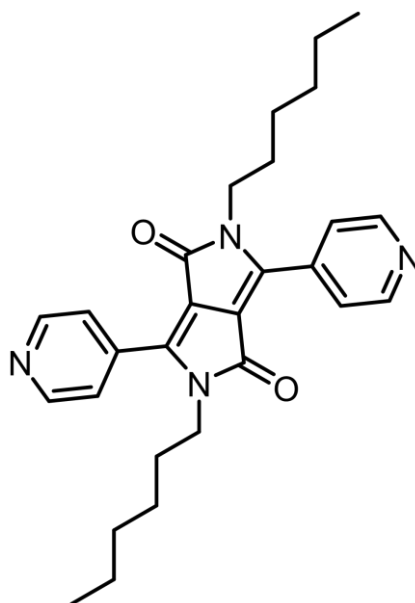


Figure 5.19. CLSM micrographs of *PEG2DPP@Gel*, [*PEG2DPP*] = 150 μ M, showing the migration of *PEG2DPP* into **1.2Br** fibres. (A) Micrograph of *PEG2DPP@Gel* showing fibre silhouettes at $t = 0$ s. (B) Micrograph of *PEG2DPP@Gel* showing the completion of *PEG2DPP* migration into fibres. Imaging details : laser 488 nm, emission range 500-700 nm, laser power 30%.

As it became clear that the PEG groups may not have been the main contributing factor to the migration behaviour observed in the previous DPPs, a DPP containing the core pyridine groups as before but with hexyl groups on the dilactam nitrogens was chosen to be studied as part of the **1.2Br** gel. **PyrHexDPP** provides a method of testing whether the PEG groups were required for the DPP migration, or if the pyridine groups were involved.



PyrHexDPP

As with the previous pyridine-flanked DPPs, the absorption and fluorescence profiles of **PyrHexDPP** are not greatly changed with incorporation into the **1.2Br** gel compared with the solution phase (**Fig. 5.20**). The absorption maximum of **PyrHexDPP** is located at ~ 473 nm in both 1:1 water-ethanol and in the **1.2Br** gel. The fluorescence emission maxima lie at ~ 548 nm and ~ 550 nm for **PyrHexDPP** in 1:1 water-ethanol and in **1.2Br** gel, respectively.

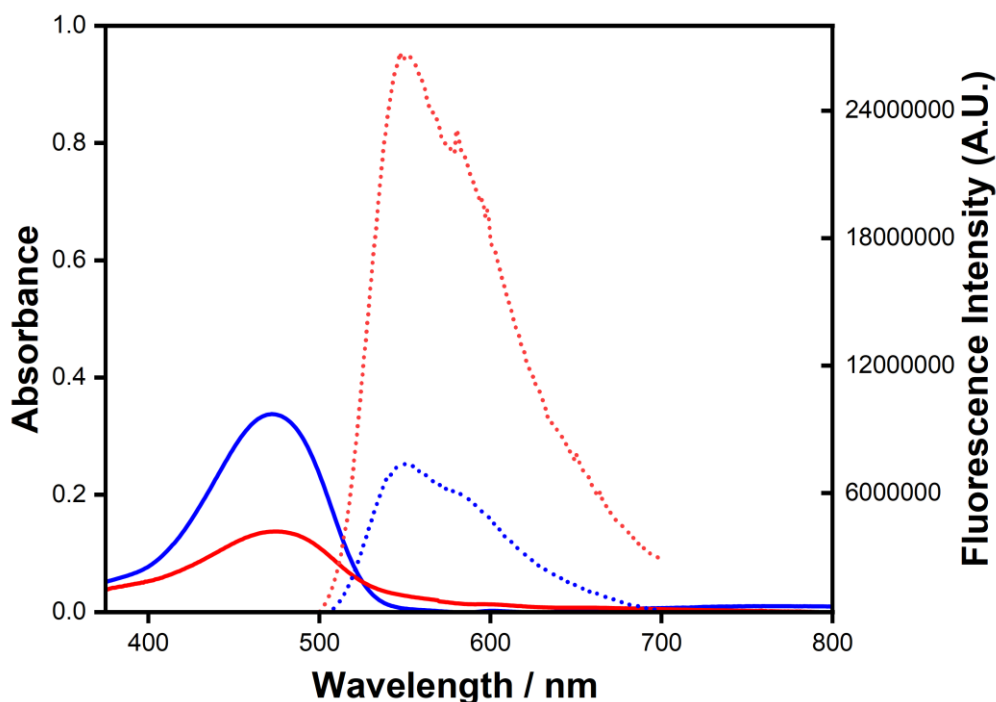


Figure 5.20. Plot displaying the absorption spectrum of **PyrHexDPP** in 1:1 water-ethanol solution, $[\text{PyrHexDPP}] = 50 \mu\text{M}$ (blue solid line), absorption spectrum of **PyrHexDPP@Gel**, $[\text{PyrHexDPP}] = 200 \mu\text{M}$ (red solid line), fluorescence emission spectrum of **PyrHexDPP** in 1:1 water-ethanol, $[\text{PyrHexDPP}] = 50 \mu\text{M}$ (blue dotted line), and fluorescence emission spectrum of **PyrHexDPP@Gel**, $[\text{PyrHexDPP}] = 200 \mu\text{M}$ (red dotted line). $\lambda_{\text{exc}} = 480$ nm for both fluorescence emission measurements.

As with **PEG2DPP** and **PEG3DPP**, **PyrHexDPP** was initially located in the interstitial liquid between fibres when imaged using CLSM, as indicated by the presence of black fibre silhouettes (**Fig. 5.21**). Upon solvent evaporation, **PyrHexDPP** began to migrate into the fibres, with the process taking roughly 7-10 minutes to occur. The fact that this DPP migration phenomenon occurred without the presence of the PEG units strongly indicates the pyridine groups on the core of the molecule is contributing to the effect.

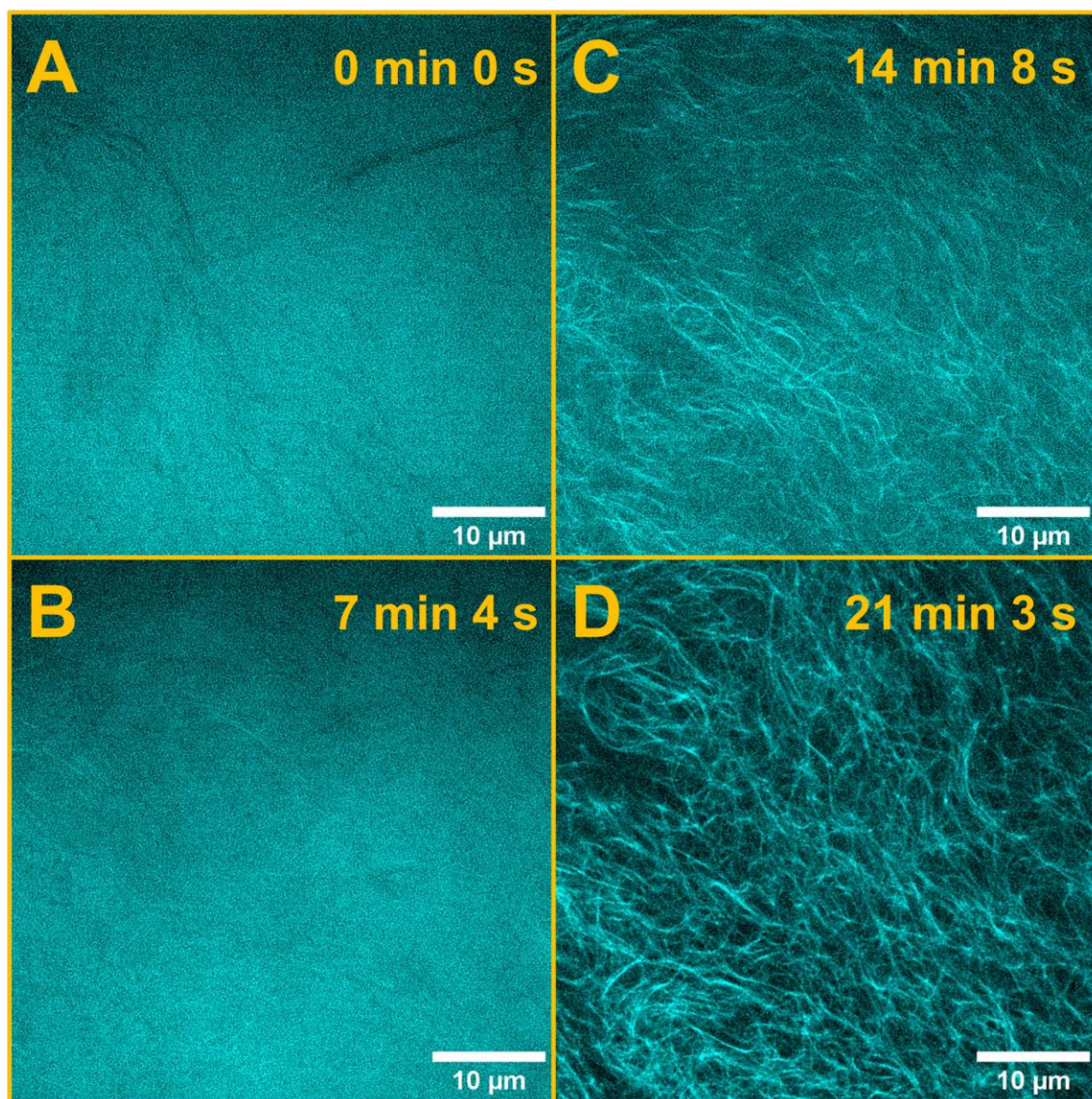


Figure 5.21. CLSM micrographs of *PyrHexDPP@Gel*, $[PyrHexDPP] = 150 \mu M$, showing the migration of *PyrHexDPP* into **1.2Br** fibres. (A) Micrograph of *PyrHexDPP@Gel* showing fibre silhouettes at $t = 0$ s. (B) Micrograph of *PyrHexDPP@Gel* showing the initial migration of *PyrHexDPP* into fibres, with some fluorescence signal still in the interstitial areas at $t = 7$ min 4 s. (C) Micrograph of *PyrHexDPP@Gel* showing the significant migration of *PyrHexDPP* into fibres, with little fluorescence signal still in the interstitial areas at $t = 14$ min 8 s. (D) Micrograph of *PyrHexDPP@Gel* showing the completion of *PyrHexDPP* migration into fibres, with little-to-no fluorescence signal still in the interstitial areas at $t = 21$ min 3 s. Imaging details : laser 488 nm, emission range 500-700 nm, laser power 30%.

As it was established that the pyridine groups play a role in the migration of the **DPPs** into **1.2Br** gel fibres as a consequence of solvent evaporation, experiments regarding acid-base phenomena were designed. The basicity of the pyridyl nitrogens is heavily influenced by their

conjugation to the DPP core. Whilst free pyridine has a pK_a of ~ 5.23 in water and ~ 5.5 in THF, the pK_a of the pyridyl groups on **PyrHexDPP** is 0.22 in THF.^{21,22} This change in pK_a is expected given the conjugation to the heavily electron deficient DPP core. It is therefore unlikely that these pyridyl groups are being protonated when incorporated into the gel. However, a control experiment with **PyrHexDPP@Gel** containing an amount of base (NaOH) was carried out.

It was found that the addition of an equimolar amount of NaOH in **PyrHexDPP@Gel** does not influence the migratory behaviour of the fluorophores in the **1.2Br** (Fig. 5.22).

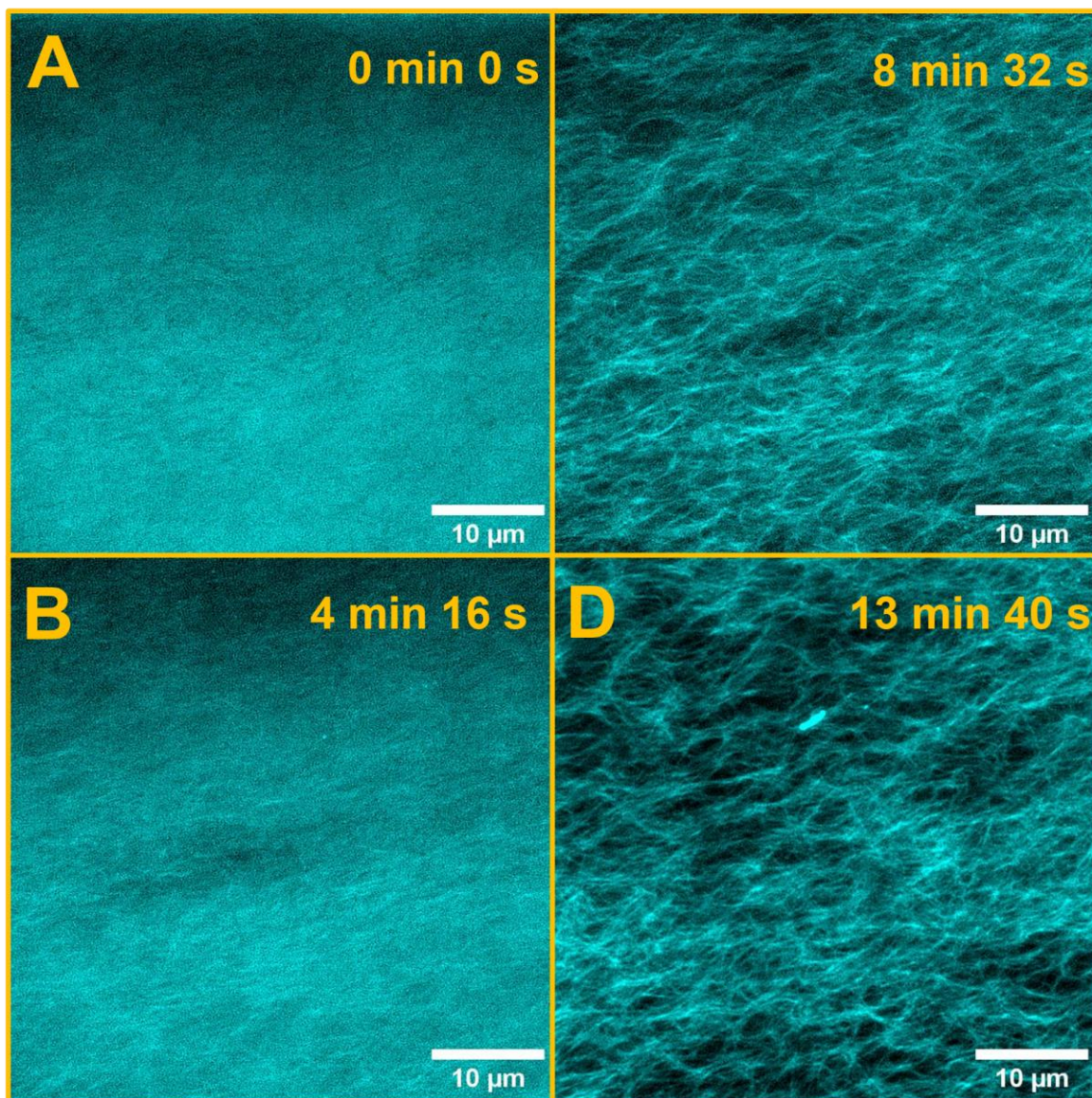
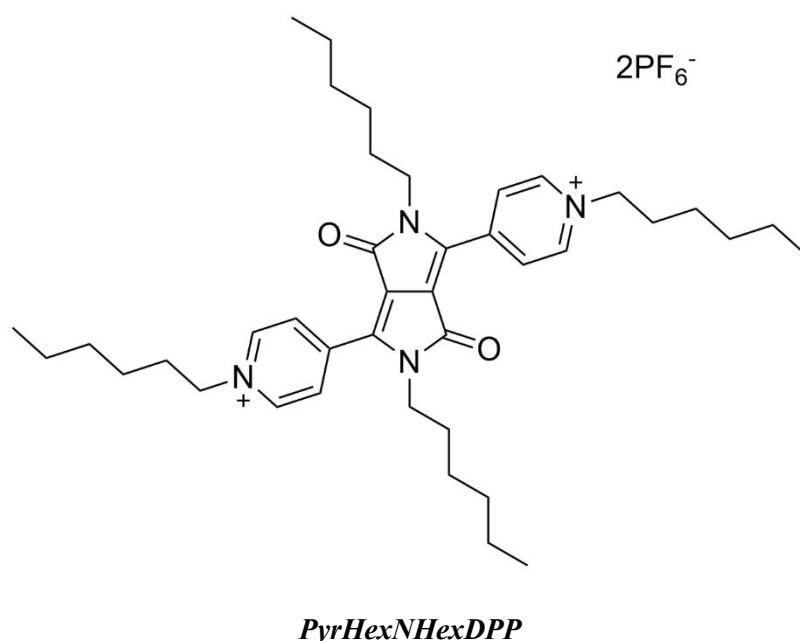


Figure 5.22. CLSM micrographs of *PyrHexDPP@NaOH@Gel*, $[PyrHexDPP] = 200 \mu M$, $[NaOH] = 200 \mu M$, showing the migration of *PyrHexDPP* into *1.2Br* fibres in the presence of NaOH. (A) Micrograph of *PyrHexDPP@NaOH@Gel* showing fibre silhouettes at $t = 0$ s. (B) Micrograph of *PyrHexDPP@NaOH@Gel* showing the initial migration of *PyrHexDPP* into fibres, with some fluorescence signal still in the interstitial areas at $t = 4$ min 16 s. (C) Micrograph of *PyrHexDPP@NaOH@Gel* showing the significant migration of *PyrHexDPP* into fibres, with little fluorescence signal still in the interstitial areas at $t = 8$ min 32 s. (D) Micrograph of *PyrHexDPP@NaOH@Gel* showing the completion of *PyrHexDPP* migration into fibres, with little-to-no fluorescence signal still in the interstitial areas at $t = 13$ min 40 s. Imaging details : laser 488 nm, emission range 500-700 nm, laser power 30%.

To purposely protonate the pyridine groups present on **PyrHexDPP**, a considerably strong acid such as trifluoroacetic acid (TFA) would be required owing to the low pK_a of the pyridine nitrogens when attached to the DPP core. Gelation tests of **PyrHexDPP@Gel** were carried out again with differing amounts of TFA present. However, at both a TFA concentration of 200 μM and 20 μM , gel formation was not able to occur. TFA was likely providing an obstacle to **1.2Br** self-assembly, and as a result only gelator precipitation occurred.

Rather than protonation, another route towards a pyridinium-flanked DPP was required. **PyrHexNHexDPP** is a DPP compound related to **PyrHexDPP** in that the lactam nitrogens are still alkylated, but instead of pyridine groups flanking the DPP core, alkylated pyridinium groups are present. As a doubly cationic species, it was unlikely that a strong enough driving force for **PyrHexNHexDPP** to be encapsulated by the also cationic **1.2Br** would be present. Another consideration is the position taken up by the anionic hexafluorophosphate counterions. PF_6^- anions have an ionic radius of 254 pm, slightly larger than that of bromide's 196 pm.^{23,24} Therefore, distortion of fibres brought on by this size increase of anion residing between the lamellae should be considered.



The absorption profile of **PyrHexNHexDPP** in 1:1 water-ethanol solution is markedly dissimilar to most of the DPPs studied in this work in that two major absorption bands are present at both 574 nm and 692 nm, respectively (**Fig. 5.23**). These peaks are likely caused by aggregates, as **PyrHexNHexDPP** possesses a single absorption maximum at around 475 nm in DMSO.²² A small absorption maximum at around 475 nm is seen in the absorption spectrum of **PyrHexNHexDPP** in 1:1 water-ethanol but is small in magnitude indicating low abundance

of disaggregated DPP in this solvent system. The fluorescence emission maximum from **PyrHexNHexDPP** falls at ~ 622 nm in both 1:1 water-ethanol and when encapsulated in the **1.2Br** gel.

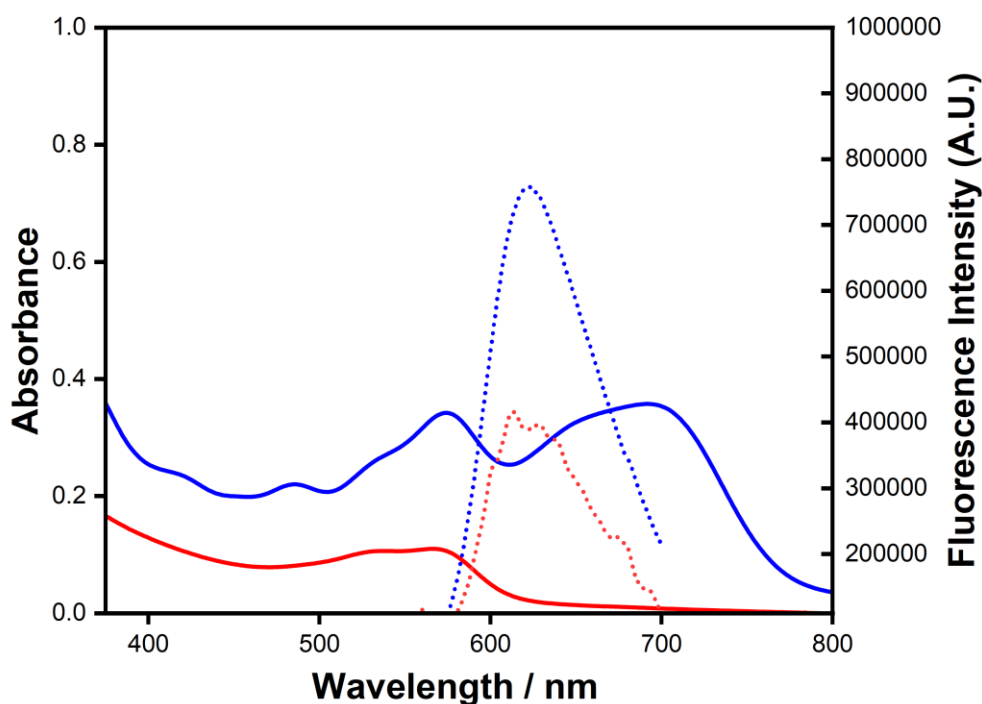


Figure 5.23. Plot displaying the absorption spectrum of **PyrHexNHexDPP** in 1:1 water-ethanol solution, $[\text{PyrHexNHexDPP}] = 200 \mu\text{M}$ (blue solid line), absorption spectrum of **PyrHexNHexDPP@Gel**, $[\text{PyrHexNHexDPP}] = 300 \mu\text{M}$ (red solid line), fluorescence emission spectrum of **PyrHexNHexDPP** in 1:1 water-ethanol, $[\text{PyrHexNHexDPP}] = 300 \mu\text{M}$ (blue dotted line), and fluorescence emission spectrum of **PyrHexNHexDPP@Gel**, $[\text{PyrHexNHexDPP}] = 200 \mu\text{M}$ (red dotted line). $\lambda_{\text{exc}} = 545 \text{ nm}$ for both fluorescence emission measurements.

Despite the fluorescence characteristics of **PyrHexNHexDPP** being alike to those DPPs that displayed migratory behaviour into the gel fibres, such behaviour from this DPP was not observed (**Fig. 5.24**). Notably, no fibre morphology was observable indicating that **PyrHexNHexDPP** was not encapsulated within the gel fibres. However, upon allowing solvent evaporation, no migratory behaviour is observed. This is to be expected as there would be a lack of preference for the cationic DPP to enter the cationic gel fibres. An average projection micrograph of the **PyrHexNHexDPP** video shows individual fluorophores that are not mobile nor adhere to any linear shapes resembling fibres.

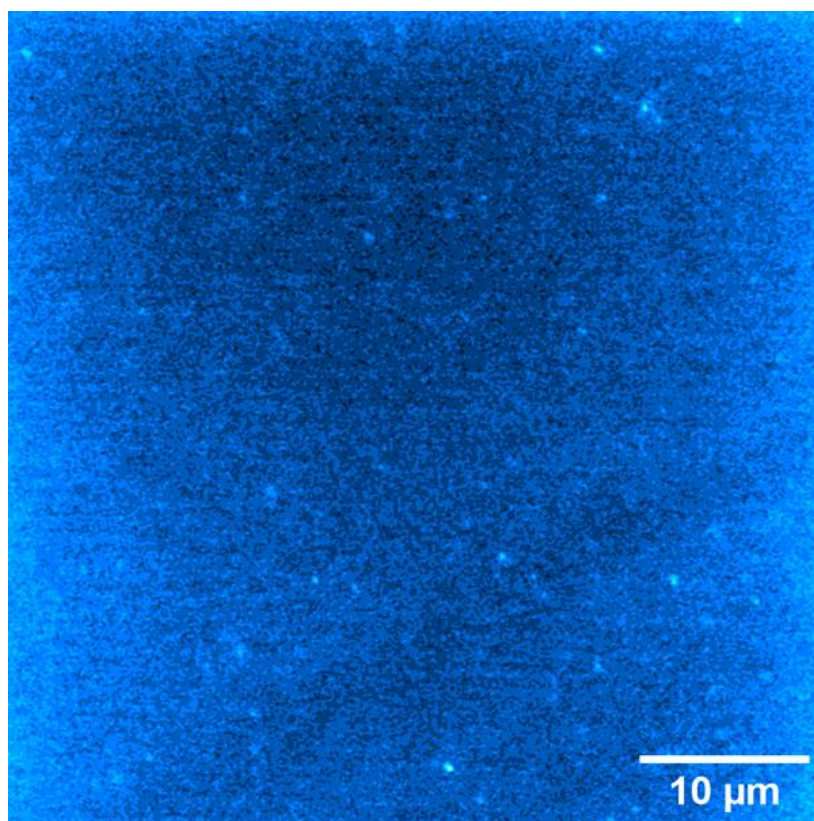


Figure 5.24. CLSM micrograph of PyrHexNHexDPP@Gel, [PyrHexNHexDPP] = 200 μ M, showing no migration of PyrHexNHexDPP into 1.2Br fibres. Imaging details: laser 560 nm, emission range 565 – 700 nm, laser power 30%.

5.4. Conclusion

In summary, CLSM was employed to image **1.2Br** gel morphology through the use of fluorescent compounds which ‘light up’ the gel fibres under excitation. It was found that gel imaging was heavily dependent on the fluorophore used, with **ZnPcTS** and **TPPS** not providing an optimally detailed view of such morphology. In addition, sample preparation either through the compression of gel between glass plates or simply situating the gel sample upon a glass coverslip influenced the gel morphology as measured with CLSM. DPP fluorophores were utilized to more effectively image gel morphology, with the greater fluorescence providing significantly increased signal-to-noise and apparent resolution. Fluorophore dynamics were also observed with the migration of certain DPPs into gel fibres in which before solvent evaporation were excluded from the fibres. It was discovered that solvent evaporation played a significant role in this phenomenon, as did the pyridine groups which flanked the DPPs which exhibited this migratory behaviour though the exact reason for this behaviour remains unclear. Overall, this work has presented a facile route to the direct imaging of hydrated gel morphology in extensive detail.

5.5. Experimental

CLSM imaging was carried out on a Zeiss LSM 900 with AiryScan 2 on an Observer platform system running Zen Black software. The scanning was in unidirectional sequential line mode with sixteen times averaging to reduce noise. Images were analysed with ImageJ. Objectives used during this study were: Fluar 5x (N.A. = 0.25), resolution 1.33 μm , total magnification 50X, brightfield condenser. Plan Apochromat 20x (N.A. = 0.8) (DICII), resolution 0.42 μm , total magnification 200X. LD Plan-Neofluar 40x (N.A. = 0.6) (Ph2 DICII), resolution 0.56 μm , total magnification 400X. C-Apochromat 63x (N.A. = 1.2W) (Water DICII), resolution 0.28 μm , total magnification 630X. EC Plan-Neofluar 100x (N.A. = 1.3 Oil) (DIC), resolution 0.26 μm , total magnification 1000X.

5.5.1. General procedures

To prepare a gel sample incorporating a water-soluble fluorophore, an aqueous fluorophore solution of the desired concentration was prepared from a 2.4 mM stock solution and was transferred and mixed with an equal volume of an ethanolic **1.2Br** solution (24 mM) in a glass vial. In the case of a non-water-soluble fluorophore, an ethanolic solution containing both **1.2Br** solution (24 mM) and the fluorophore at the desired concentration must first be prepared. An equal volume of water was then added to this and mixed, allowing for gel formation after less than a minute. The final fluorophore concentration in the gels was varied from 50 μM to 150 μM depending on the relative fluorescence of each fluorophore. The final **1.2Br** gelator concentration was always 12 mM. Turbidity was observed upon mixing aqueous and ethanolic solutions, and gelation generally occurred in less than one minute (as judged by vial inversion) to give the gel materials containing the chosen fluorophore.

For imaging of compressed samples, a sample of gel around the size of the end of a spatula was placed upon a circular glass coverslip in a holder. A plastic O-ring was placed on the glass coverslip around the sample and another circular glass plate was placed on top of this. The holder was then screwed which compressed the gel between the two glass plates to form a thin section of gel. This sample was then viewed under the Zeiss LSM 900 in Brightfield mode, before focusing on a bubble or other feature of gel under the Fluar 5x objective, the Plan Apochromat 20x objective was then used to focus further on the chosen feature. When focused on the sample feature, the 63x/100x immersion objectives were coated with oil/water-oil and focused until some fibre morphology could be seen. From here, a suitable excitation laser and filters were activated and focusing continued until sample morphology could be seen in confocal Airyscan mode. For imaging of uncompressed samples, the same procedure as above

was followed but the gel sample placed upon the glass coverslip was not compressed with a further glass plate.

5.6. References

1. *Handbook of Biological Confocal Microscopy*, J. B. Pawley, Springer New York, New York, 2, 1995.
2. S. W. Paddock, *Mol. Biotechnol.*, 2000, 16, 127 – 149.
3. J. Kapuscinski, *Biochem. Histochem.*, 1995, 70, 220 – 233.
4. S. Kiyonaka, K. Sugiyasu, S. Shinkai, I. Hamachi, *J. Am. Chem. Soc.*, 2002, 124, 10954 – 10955.
5. R. Kubota, K. Nakamura, S. Torigoe, I. Hamachi, *ChemistryOpen*, 2020, 9, 67 – 79.
6. S. Onogi, H. Shigemitsu, T. Yoshii, T. Tanida, M. Ikeda, R. Kubota, I. Hamachi, *Nat. Chem.*, 2016, 8, 743 – 752.
7. M. A. Kotlarchyk, E. L. Botvinick, A. J. Putnam, *J. Condens. Matter Phys.*, 2010, 22, 194121.
8. M. E. Harmon, W. Schrof, C. W. Frank, *Polymer*, 2003, 44, 6927 – 6936.
9. B. R. Nelson, B. E. Kirkpatrick, C. E. Miksch, M. D. Davidson, N. P. Skillin, G. K. Hach, A. Khang, S. N. Hummel, B. D. Fairbanks, J. A. Burdick, C. N. Bowman, K. S. Anseth, *Adv. Mater.*, 2023, 2211209.
10. D. Lee, M. M. Rahman, Y. Zhou, S. Ryu, *Langmuir*, 2015, 31, 9684 – 9693.
11. M. Samperi, D. Limón, D. B. Amabilino, L. Pérez-García, *Cell Rep.*, 2020, 1, 100030.
12. D. G. Farnum, G. Mehta, G. G. I. Moore, F. P. Siegal, *Tetrahedron Lett.*, 1974, 15, 2549 – 2552.
13. D. Molina, M. J. Álvaro-Martinsa, Á. Sastre-Santos, *J. Mater. Chem. C*, 2021, 9, 16078 – 16109.
14. C. B. Nielsen, M. Turbiez, I. McCulloch, *Adv. Mater.*, 2013, 25, 1859 – 1880.
15. Y. Patil, T. Jadhav, B. Dhokale, R. Misra, *EurJOC*, 2015, 2016, 733 – 738.
16. W. Li, L. Wang, H. Tang, D. Cao, *Dyes Pigm.*, 2019, 162, 934 – 950.
17. E. R. Draper, B. Dietrich, D. J. Adams, *Chem. Commun.*, 2017, 53, 1864 – 1867.
18. M. Rodrigues, A. C. Calpena, D. B. Amabilino, M. L. Garduño-Ramírez, L. Pérez-García, *J. Mater. Chem. B*, 2014, 2, 5419 – 5429.
19. S. Luňák Jr., M. Vala, J. Vyňuchal, I. Ouzzane, P. Horáková, P. Možíšková, Z. Eliáš, M. Weiter, *Dyes Pigm.*, 2011, 91, 269 – 278.

20. M. Vala, M. Weiter, J. Vyňuchal, P. Toman, S. Luňák Jr, *J. Fluoresc.*, 2008, 18, 1181 – 1186.
21. S. Tshepelevitsh, A. Kütt, M. Lõkov, I. Kaljurand, J. Saame, A. Heering, P. G. Plieger, R. Vianello, I. Leito, *Eur. J. Org. Chem.*, 2019, 2019, 6733 – 6887.
22. J. Humphreys, F. Malagrecá, P. Hume, W. Lewis, E. S. Davies, S. P. Argent, D. B. Amabilino, *Dyes Pigm.*, 2022, 197, 109836.
23. N. Q. Khuyen, Z. Zondaka, M. Harjo, J. Torop, T. Tamm, R. Kiefer, *Polymers*, 2019, 11, 849.
24. R. D. Shannon, *Acta Crystallogr. A*, 1976, 32, 751 – 767.

Chapter 6

**Cryo-SEM analysis of fluorophore-
containing imidazolium hydrogels**

6.1. Background

Scanning electron microscopy (SEM) is a type of electron microscopy in which imaging is usually performed by scanning a focused beam of electrons over a sample and measuring the secondary electrons produced by the electron beam's interaction with the atoms that constitute the sample. Although significant research was carried out through the 20th century, the first commercial SEM instrument produced was the 'Stereoscan' made by the Cambridge Scientific Instrument Company in 1965.¹⁻⁴ The scheme for the set-up of a typical SEM instrument is shown in **Fig. 6.1**.

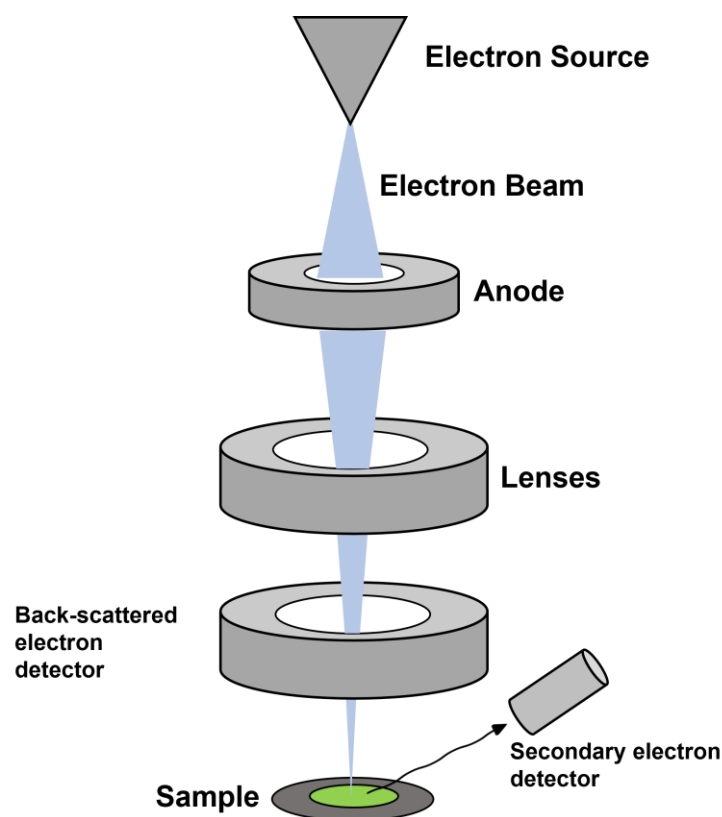


Figure 6.1. Schematic for a typical SEM instrument. An electron beam originating from the electron source is deflected onto a sample which produces backscattered and secondary electrons which are detected and used to form an image.

An electron beam is initially produced from an electron source. This electron source is often a thermionic emitter, meaning primary electrons (PEs) are liberated from a metal (usually tungsten) as a consequence of high temperature. However, many modern SEM instruments use a field emission gun (FEG) to produce an electron beam. FEGs consist of a thin (~ 100 nm) single-crystal tungsten tip spot-welded to a tungsten hairpin. When a strong negative potential

is applied, the electric field is highly concentrated within the small region of the tip. This potential results in a lowering of the work function of the tip meaning PEs can be emitted without the need for elevated temperatures. A series of anodes and lenses is then employed to deflect the beam onto the sample. Upon hitting the sample, the PEs interact with the atoms of the sample in three main ways (**Fig. 6.2**). Most commonly, beam electrons displace those in the atoms of the sample resulting in the emission of low energy secondary electrons (SEs) which are then collected in a detector. Additionally, electromagnetic radiation in the form of X-rays can be produced by the expulsion of SEs. When an inner electron is removed, an outer electron can then fill the hole created with the emission of a high energy photon. This phenomenon is the basis for energy-dispersive X-ray spectroscopy (EDS).

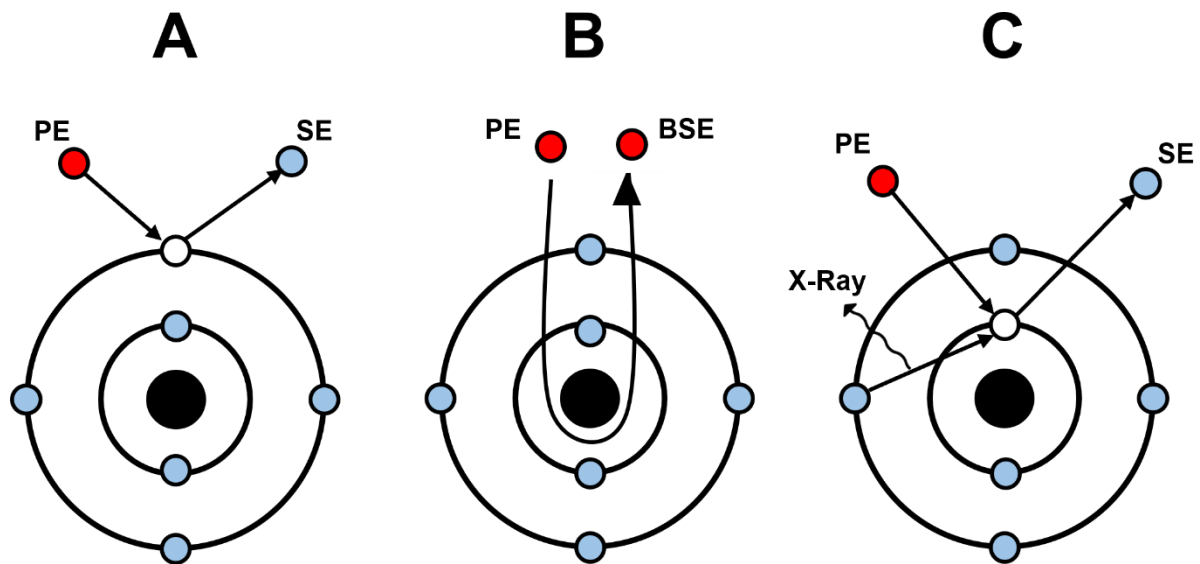


Figure 6.2. Three possible phenomena upon focusing an SEM electron beam upon a sample. (A) A high energy PE interacts with a sample atom to expel a SE. (B) A high energy PE is deflected a sample atom's nucleus resulting in the release of a high energy backscattered electron. (C) A high energy PE interacts with a sample atom to expel an inner electron to result in a SE. An outer electron then fills the inner hole and releases a photon of X-ray light.

Alternatively, the incident PEs can scatter elastically around the nuclei of the atoms of the sample that can then be detected as high energy backscattered electrons (BSEs). Atoms with heavier nuclei tend to deflect primary electrons more strongly, meaning the backscatter signal will be more intense for these heavier atoms. This effect can be exploited to detect different chemical compositions in the same sample.⁵

In the field of materials chemistry, SEM provides a relatively non-invasive method of microscale imaging. SEM also possesses versatility in terms of imaging requirements, allowing conditions to be suited to the given material. An optically active material consisting of helical nanofibres based on TiO₂ were synthesized by Che *et al.* and SEM was employed to image the material.⁶ The low dimensions of the nanofibres were such that conventional SEM imaging did not resolve the fine structure of the material, and high-resolution SEM (HRSEM) had to be employed. HRSEM modulates the energy of the incoming PEs at the point of interaction with the sample by applying a bias to the sample.⁷ By utilising this technique, the morphological properties of the nanofibres were able to be quantified. Gel materials have also been extensively studied using SEM.⁸⁻¹⁰ Pyridyl amide-based hydrogelators derived from isonicotinic acid were prepared by Kumar *et al.* and were able to form hydrogels using the heating/cooling method.¹¹ Hydrogel xerogels of different weight percentages of gelator were imaged using SEM. A three-dimensional fibrous morphology was seen with two different weight percentages. At a low weight percentage of 0.37 wt %, fibres were extended and unbroken with a considerably large distribution of fibre widths. At a weight percentage of 20 wt %, the morphology, whilst still fibrous, was significantly disturbed. Fibre width distributions are also altered by the change in weight percentage.

Cryogenic scanning electron microscopy (Cryo-SEM) is a type of SEM where a sample is cryogenically fixed (typically using liquid nitrogen) in order to image in a pseudo-hydrated state. Cryo-SEM is a powerful technique for imaging biological samples, as the drying required for conventional SEM imaging can alter the structure of such samples introducing structural artifacts. Cryo-SEM eliminates this problem and can allow a more accurate perspective on the microstructure of biological samples of interest.^{12,13}

Despite its prominence in biological imaging, Cryo-SEM has been an underutilized tool for the imaging of materials that possess a solvent phase. Hyaluronic acid-based hydrogels containing hydrogel particles were developed by Jia *et al.* and characterized using a range of analytical techniques.¹⁴ This material was cryogenically frozen using a liquid nitrogen 'slush' before being imaged using Cryo-SEM. Liquid nitrogen slushing is a technique whereby the temperature of the nitrogen is lowered by employing a vacuum. This vacuum results in the formation of some solid nitrogen resembling a slush. This lower overall temperature of the nitrogen slush results in an accelerated cooling rate. The frozen hydrogel material was then imaged under Cryo-SEM conditions. It was found that the hydrogel was made up of

interconnected porous networks containing embedded hydrogel particles. The microstructure was not analysed quantitatively.

An important complementary technique often used in conjunction with Cryo-SEM is focused ion beam (FIB) analysis. FIB-SEM refers to the use of a focused beam of gallium ions to either image or manipulate the sample surface. During sample preparation, the frozen sample is often sputtered with platinum to prevent charging. In addition to this, a portion of the sample is further coated with an organometallic layer *via* a gas injection system. This organometallic layer is to protect the sample surface during FIB milling. FIB milling cuts away a section of the sample through the organometallic layer exposing an open face of the sample. Water then sublimates from the sample surface owing to an increase in temperature revealing the microstructure underneath.

FIB has been employed to investigate the microstructure of biological samples and some battery materials.¹⁵⁻¹⁷ FIB has not, however, been utilized extensively to investigate the structure of gels. Scherman *et al.* made use of Cryo-FIB-SEM to characterize some pentapeptide hydrogels.¹⁸ The stiffness of the hydrogels was able to be modulated with changes in concentration and charge sequence (altering peptide sequence). Cryo-FIB-SEM was used to associate this stiffening with a change in fibre morphology. A decrease in gelator concentration led to a shortening of fibre lengths whilst changing the peptide sequence altered the general morphology with some variants possessing platelike assemblies and others being made up of fibrous bundles. Whilst not employing FIB, cryo-SEM was used by Kyomugasho *et al.* to visualize the microstructure of pectin gels prepared with differing cations (Zn, Fe, Ca, Mg) in combination with varying pH, pectin concentration, and cation concentration. They found that as the pH, pectin concentration, and cation concentration increased, the density of the gel network increased. When comparing pectin from citrus (more linear and less acetylated) to pectin from sugar beet (more branched and more acetylated), the citrus pectin exhibited a more tangled fibrous network.¹⁹ This study was another example of the use of cryo-SEM to visualize gels.

Given this scarcity of cryo-FIB-SEM research upon hydrogels, the imidazolium-based gels studied in this work were to be investigated using the technique. Cryo-FIB-SEM allowed the gels to be imaged closer to their native hydrated state as opposed to the xerogel form in which they have conventionally been imaged using regular SEM techniques. In addition, corroborating gel morphology as seen in its hydrated state in both confocal and total internal

reflection fluorescence TIRF microscopy was a major goal. Another aim was to compare the morphology seen using Cryo-FIB-SEM and regular SEM. Any differences in morphology could likely be a consequence of gel drying-induced artifacts.

6.2. Preliminary FIB experiments

The first step of the Cryo-FIB-SEM investigation into the imidazolium gels was to develop a method for gel cryofixation. In relation to the freezing process, there were two potential methods to apply for sample freezing. Metal mirror or ‘slam’ freezing refers to the process of punching the sample against a gold-plated copper block which has been cooled by liquid nitrogen.²⁰ Metal mirror freezing yields high cooling rates and a freezing depth of around 15 – 25 μm . Using a Leica MM80 Metal Mirror freezer apparatus, a sample of 1,3-bis[(3-octadecyl-1-imidazolium)methyl]benzene di-bromide gel (**1.2Br@Gel**) was frozen. Platinum sputtering was then carried out and the sample was ready to be manipulated and imaged. Imaging of the surface revealed a plain structure possessing no fibrous surface topography (**Fig. 6.3**).

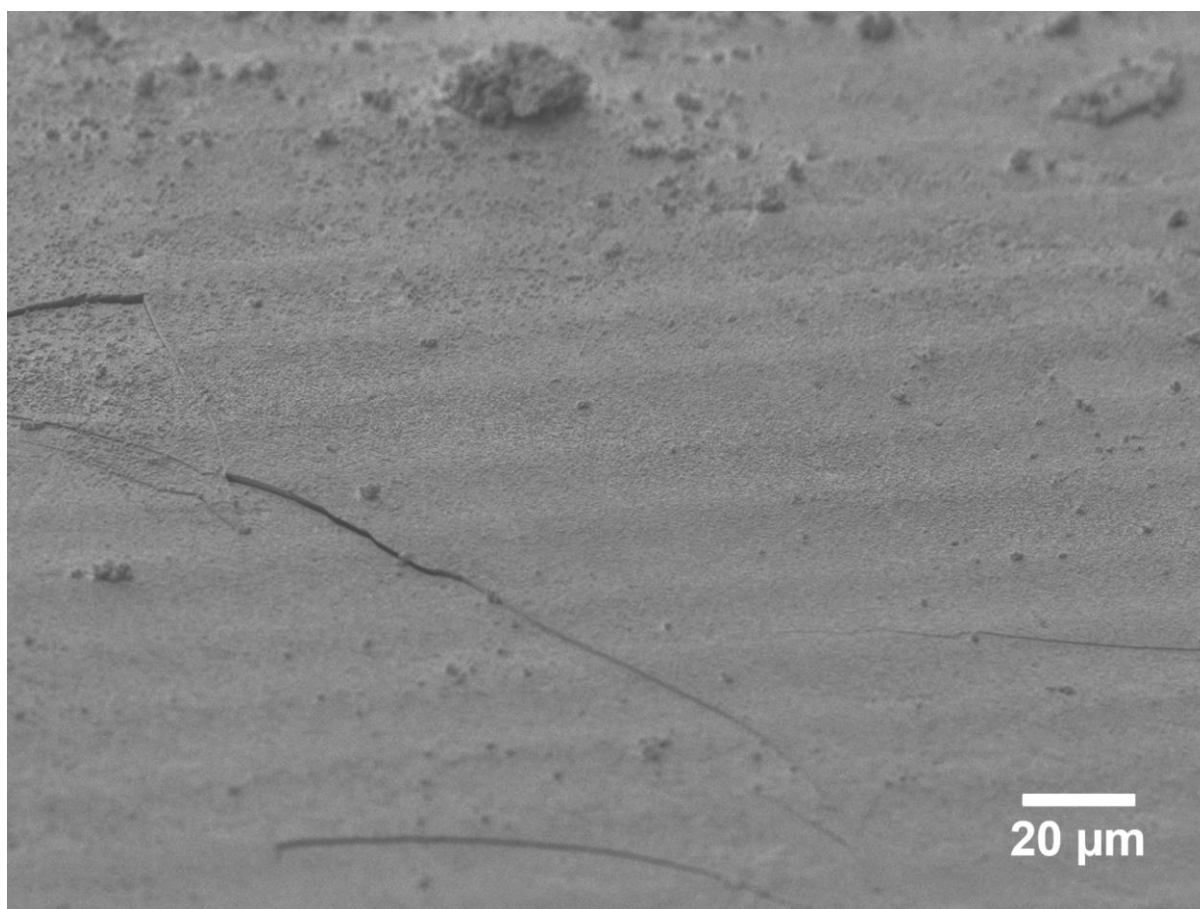


Figure 6.3. Cryo-SEM image of the surface of a **1.2Br@Gel** sample frozen by slam freezing.

The sample was then prepared for FIB milling through the sputtering of an organometallic layer onto the sample surface *via* a gas injection system. Within the area of the sample coated with an organometallic layer, three rectangular holes were milled into the surface. These holes had dimensions of around 22 μm x 20 μm and can be seen in **Fig. 6.4**.

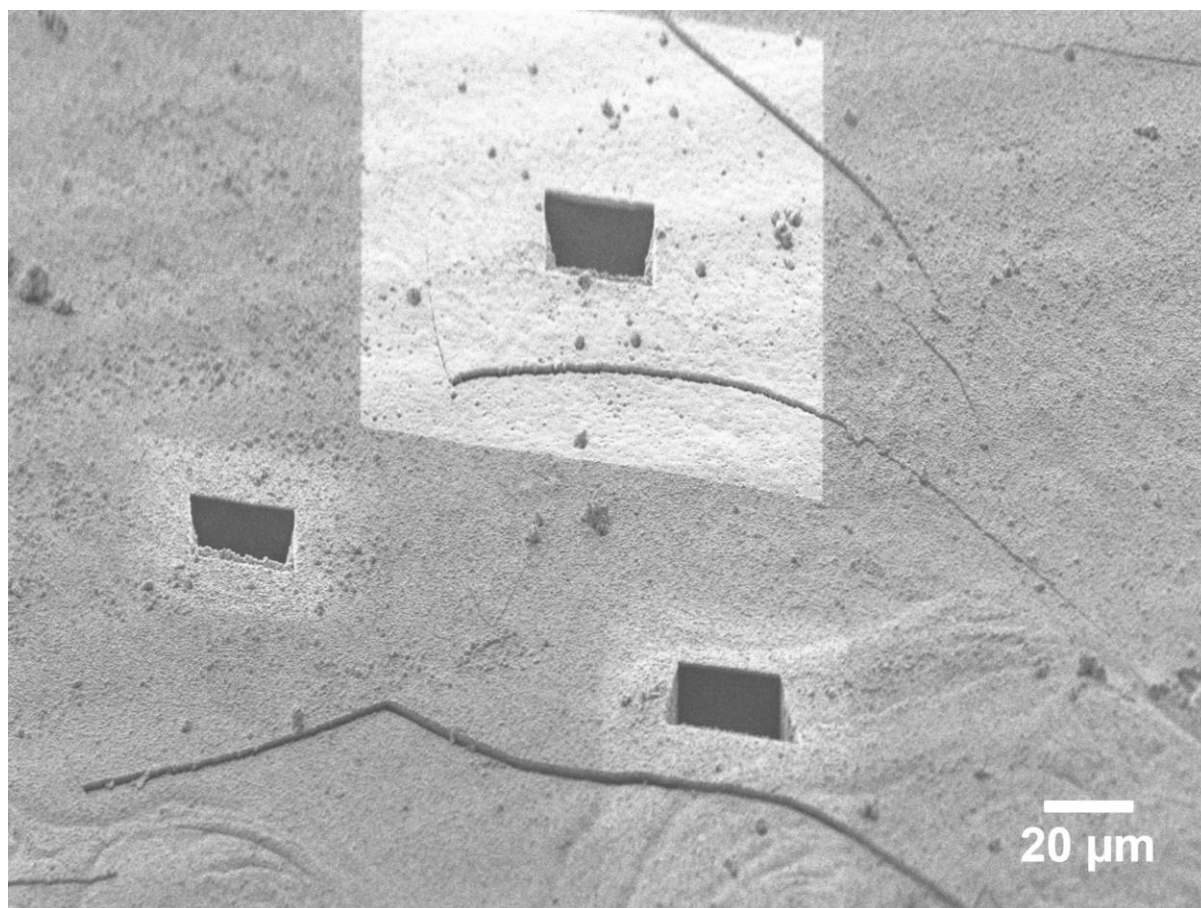


Figure 6.4. Cryo-SEM micrograph of three rectangular holes milled by FIB beam into the surface of a frozen **1.2Br@Gel** surface.

After a sublimation stage, the visible surface within the milled cavities were imaged. Initially, little physical structure can be seen with only a smooth surface visible. After several minutes of being exposed, microstructural features began to emerge. **Fig. 6.5** shows the process of the cavity surface distorting and revealing the microstructure underneath. After around 7 minutes, the face of the wall began to distort significantly. The face then detached and revealed the obvious gel morphology underneath.

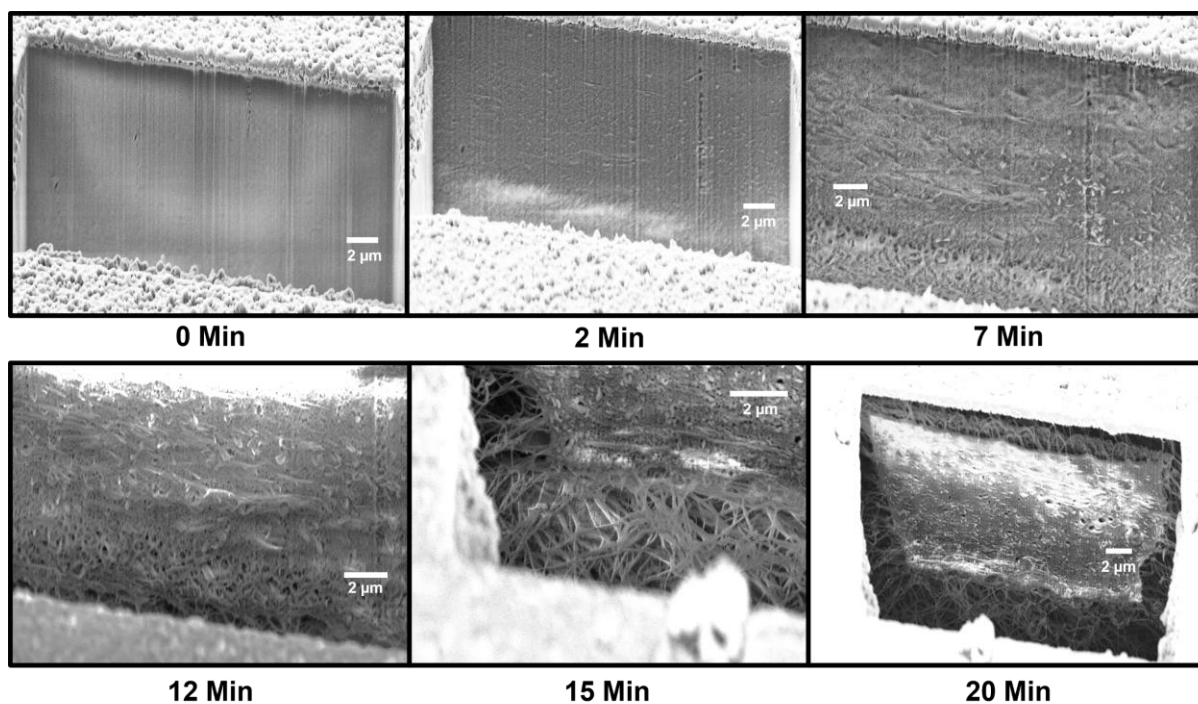


Figure 6.5. Open face of a FIB-milled cavity shows the gradual emergence of gel microstructure over time. Gel fibres become visible after ~ 7 minutes and are considerably more noticeable after ~ 15 minutes of sublimation.

Upon obtaining these promising results, a different sample preparation process was formulated. Instead of utilising the slam freezer to carry out cryofixation upon the gel samples, a simpler slush freezing method was employed. Here, a sample of gel was inserted into a cavity on a stub coated with an adhesive. The stub containing the sample was then plunged into liquid nitrogen before the formation of a nitrogen slush. This stub was then directly loaded into a preparatory chamber before being sputtered with platinum in an argon atmosphere. The sample then underwent sublimation for 45 minutes by increasing temperature from $-135\text{ }^{\circ}\text{C}$ to $-100\text{ }^{\circ}\text{C}$. The gel sample was then loaded into the main chamber to be imaged.

As with the previous sample, much of the surface showed little with respect to fibre morphology, though areas existed where a fibrous structure could be seen (**Fig. 6.6**). The presence of fibres exposed on the surface of the sample negated the need for FIB milling. This method allowed for quicker sample preparation whilst giving access to larger areas of investigable morphology as compared to the FIB milling method where the size of the area studied was limited by time taken to coat and mill.

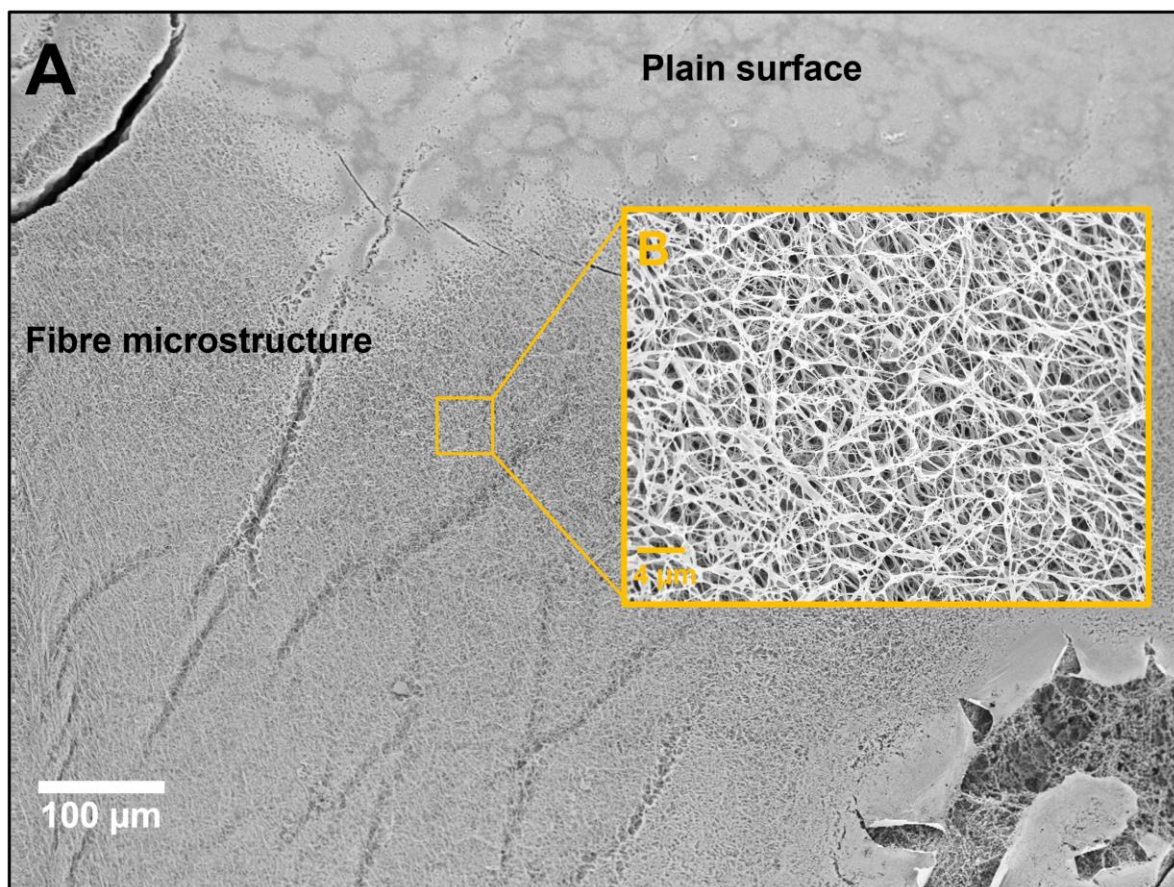


Figure 6.6. Cryo-SEM micrograph of a cryofixed **1.2Br@Gel** sample. (A) The plain surface seen at the top of the feature is predominant when imaging over the sample, though areas exist such as the lower portion which show detailed fibre morphology. (B) A magnified view of the fibre morphology.

6.3. Fibre Analysis & Drying effects / Confocal comparison

As discussed, the sample preparation process for SEM-based imaging can generally be very involved with respect to manipulation of the given sample. In biological imaging, processing of a sample to the point at which it can be imaged using such techniques has been shown to significantly influence the resulting properties of the sample.²¹ Specifically, the need for a dry sample in the high-vacuum environment present in most SEM microscopes presents issues for samples in varying areas of study.^{22,23} There has been some debate about the extent to which the images of dried sample of a gel can be truly compared with the pristine hydrated gel before drying.²⁴ On one hand, as solvent is removed through drying, the three-dimensional supramolecular network of fibres collapses to form a two-dimensional film which is then imaged using conventional SEM. This collapse itself should not necessarily directly result in artifacts. However, as solvent is removed over time, the concentration of gelator increases. It has been shown in previous work on **1.2Br** gels that concentration has an effect on the gel morphology in the dried state, so it is highly likely that the concentration increase brought

about by drying would result in more bundling and aggregation of fibres resulting in altered fibre widths.²⁵

Even in the class of LMOG gels, there is a wide variety of gelators and subsequent supramolecular architectures that can result from their self-assembly. Therefore, it is reasonable to expect that drying would have a more substantial effect upon some materials than others with respect to introducing drying artifacts. A quantitative comparison, therefore, of **1.2Br** fibre morphology both in the dried and cryofixed state could provide valuable information as to what extent drying influences such morphological properties.

A comprehensive study on the fibre widths of dried **1.2Br** gel samples was carried out by Samperi *et al.* in which an atomic force microscopy study of **1.2Br** xerogels prepared in differing water-ethanol ratios quantified the average widths of fibres.²⁶ It was found that **1.2Br** gels formed in a 1:1 water-ethanol concentration and a gelator concentration of 12 mM as used in the work presented here exhibited a fibre width distribution where 75% of fibres were between 50 and 125 nm. Despite the differences in the techniques used for measuring, a similar such distribution was also found in non-cryogenic SEM of **1.2Br** xerogels (**Fig. 6.7**). The mean fibre width of **1.2Br** fibres as measured by SEM lied at 66 ± 1.8 nm. The majority of fibres possessed widths of between 65 – 75 nm.

If the gel sample is cryogenically frozen instead of being dried during sample preparation, the three-dimensional supramolecular structure of fibres remains intact without collapsing. Indeed, significant discrepancies have been found between gel fibre widths between xerogels and native wet gels. Mears *et al.* showed that supramolecular gels prepared from dipeptide gelators exhibit considerably thicker fibres in their dried state as measured with conventional SEM when compared with the same cryogenically frozen gel samples as measured using cryogenic transmission electron microscopy (cryo-TEM) and single angle neutron spectroscopy. Aggregation of fibres was seen occasionally in cryo-TEM but was more pronounced in the dried gels, resulting in larger fibre widths.

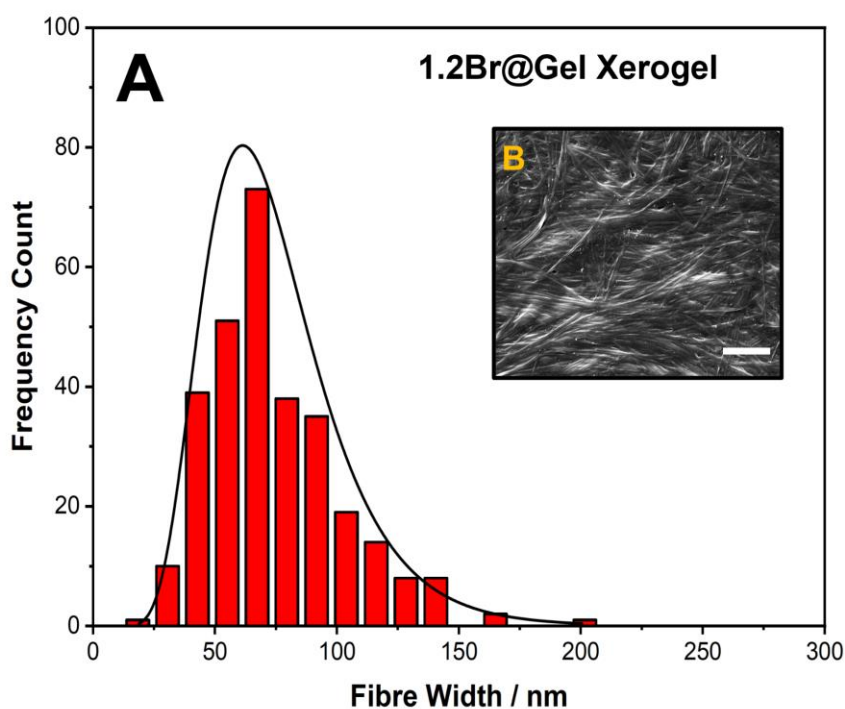


Figure 6.7. (A) Width distribution histogram of a **1.2Br@Gel** xerogel as measured through conventional SEM. (B) Conventional SEM micrograph of **1.2Br@Gel**, scale bar corresponds to 2 μm . Gel prepared in 1:1 water-ethanol and $[\mathbf{1.2Br}] = 12 \text{ mM}$.

To investigate any possible differences between fibre widths of **1.2Br@Gel** samples, measurements of the fibre widths of **1.2Br** in their frozen form were carried out. From these measurements, a distribution of gel fibre widths was found which suggested thinner fibres were a lot more prevalent in frozen gel samples than in dried gel samples (**Fig. 6.8**). In addition, a potentially multimodal distribution was found with peaks at $\sim 30 - 35 \text{ nm}$ and at $\sim 70 - 75 \text{ nm}$. This may indicate the aggregation of two single fibres into an aggregate. As the mode of the fibre widths of the dried **1.2Br** sample is $\sim 65 - 75 \text{ nm}$ with few fibres exhibiting fibre widths at around $30 - 35 \text{ nm}$, it can be concluded that aggregation of fibres is exacerbated by the supramolecular collapse which occurs upon drying.

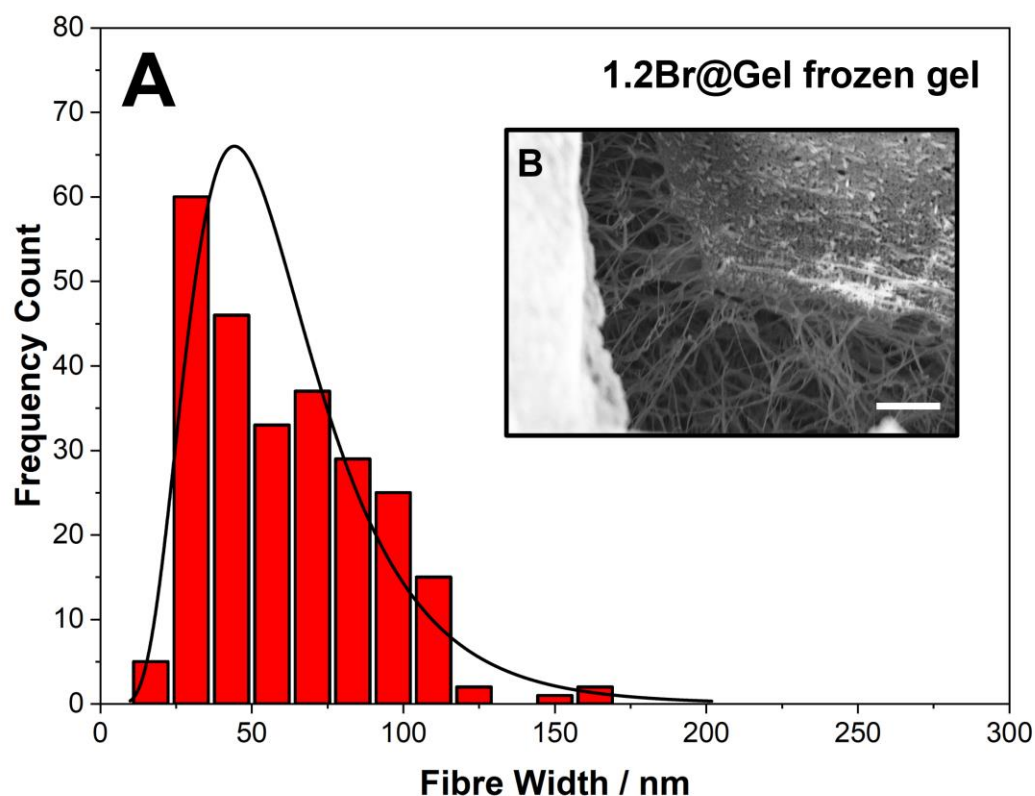


Figure 6.8. (A) Fibre width distribution histogram of a cryogenically frozen sample of **1.2Br@Gel** gel as measured through cryo-SEM. (B) Cryo-SEM micrograph of **1.2Br@Gel**, scale bar corresponds to 2 μm . Gel prepared in 1:1 water-ethanol and $[1.2\text{Br}] = 12 \text{ mM}$.

In its pristine form, there is a quantifiable difference in **1.2Br@Gel** fibre widths. The inclusion of fluorescent compounds into these gel samples for imaging purposes has shown to also influence the fibre morphology of dried gels as seen through conventional SEM. It was therefore important to investigate whether the differences seen in the pristine gel in its dried/frozen state are more or less pronounced in the presence of such incorporated fluorophores. The diketopyrrolopyrrole (DPP) derivatives studied in the previous chapter on confocal laser scanning microscopy (CLSM) provide a unique opportunity to compare the imaging of gel fibres in the dried state (conventional SEM), their close-to-native wet state (cryo-SEM), and in their truly native wet state (CLSM). **CO₂HDPP** is a water soluble DPP that was used in the imaging of **1.2Br** gels using CLSM (**Fig. 6.9**). Whilst fibre width measurements using CLSM is not possible, a view of the overall morphology as seen through CLSM can be compared qualitatively to imaging *via* cryo-SEM provided a fluorescent compound is introduced.

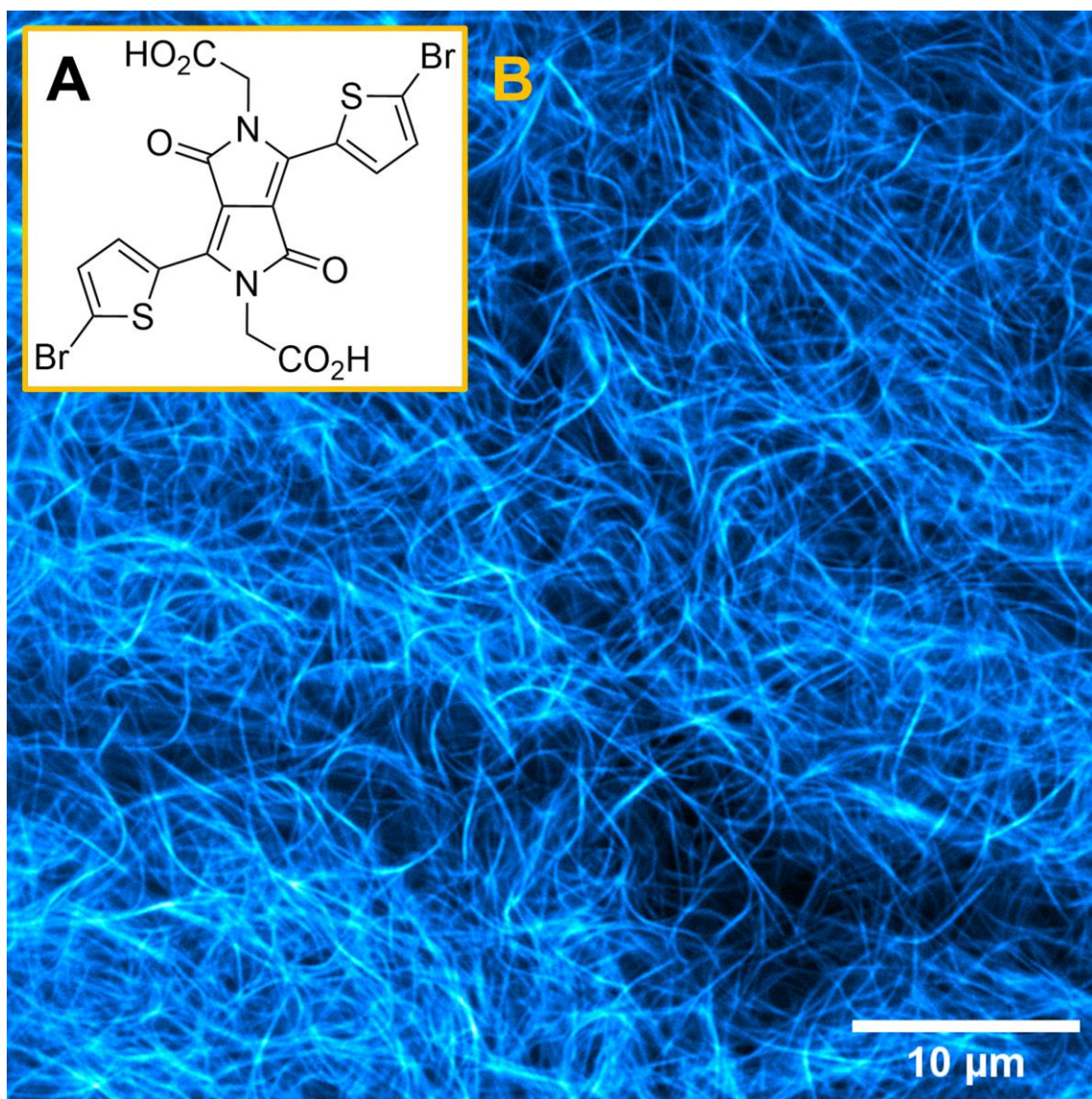


Figure 6.9. (A) Molecular structure of the water-soluble CO_2HDPP . (B) CLSM micrograph of the fibre morphology of $\text{CO}_2\text{HDPP}@Gel$ where the gel sample is in contact with the glass coverslip, $[\text{CO}_2\text{HDPP}] = 150 \mu\text{M}$. Imaging details: laser 560 nm, emission range 565 – 700 nm, laser power 30%.

CLSM imaging of $\text{CO}_2\text{HDPP}@Gel$ displayed fibres that tended to bend and exhibit curvature, both in the bulk of the gel and at the gel-glass interface. Very similar fibre morphology was seen under Cryo-SEM imaging of $\text{CO}_2\text{HDPP}@Gel$, indicating that Cryo-SEM accurately captures the gel's native wet state morphology (Fig. 6.10).

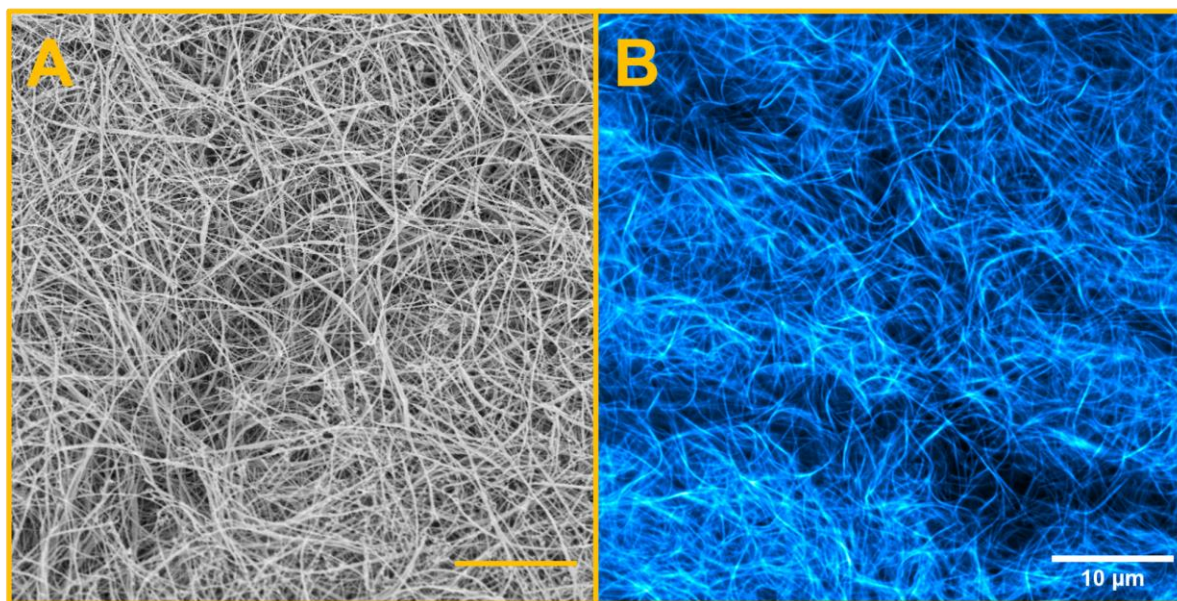


Figure 6.10. (A) Cryo-SEM micrograph of $\text{CO}_2\text{HDPP@Gel}$, $[\text{CO}_2\text{HDPP}] = 150 \mu\text{M}$, scale bar corresponds to $10 \mu\text{m}$. (B) CLSM micrograph of $\text{CO}_2\text{HDPP@Gel}$, $[\text{CO}_2\text{HDPP}] = 150 \mu\text{M}$, scale bar corresponds to $10 \mu\text{m}$. Imaging details: laser 560 nm , emission range $565 - 700 \text{ nm}$, laser power 30%.

As mentioned, the incorporation of fluorescent compounds into **1.2Br** gels can significantly alter dried gel morphology. Qualitatively, the frozen gel morphology of both **1.2Br@Gel** and **CO₂HDPP@Gel** samples are analogous to each other, with fibres curving and often bundling into larger aggregates. **CO₂HDPP@Gel**, like **1.2Br@Gel**, does show differences in its cryogenically frozen state as compared to its dried state in terms of morphology. Fibres exhibited less curvature in the dried state, and bundling is more evident (**Fig. 6.11**).

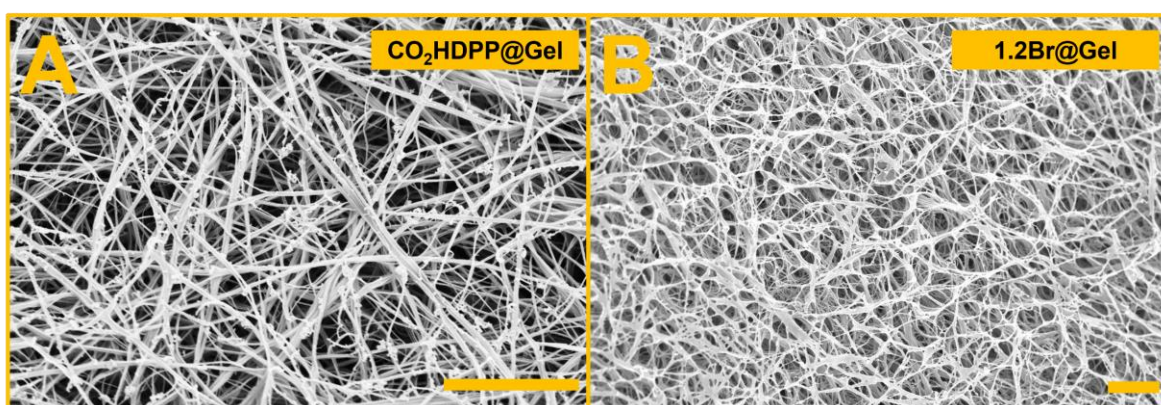


Figure 6.11. (A) Cryo-SEM micrograph of $\text{CO}_2\text{HDPP@Gel}$, $[\text{CO}_2\text{HDPP}] = 150 \mu\text{M}$, scale bar corresponds to $4 \mu\text{m}$. (B) Cryo-SEM micrograph of **1.2Br@Gel**, scale bar corresponds to $4 \mu\text{m}$.

The distribution of fibre widths in the case of $\text{CO}_2\text{HDPP@Gel}$, again like 1.2Br@Gel , differs with the gel in its frozen state compared to in its dried state. In the frozen state, $\text{CO}_2\text{HDPP@Gel}$ fibre widths are distributed with a mean value of ~ 78 nm, with most fibres possessing a width of between 55 – 74 nm (**Fig. 6.12**). This mean value is greater than the mean fibre width of 1.2Br@Gel in its frozen state, though it is to be expected that the addition of a non-trivial concentration (150 μM) of CO_2HDPP may influence this aspect of gel morphology by expelling the bromide anions between gel lamellae.

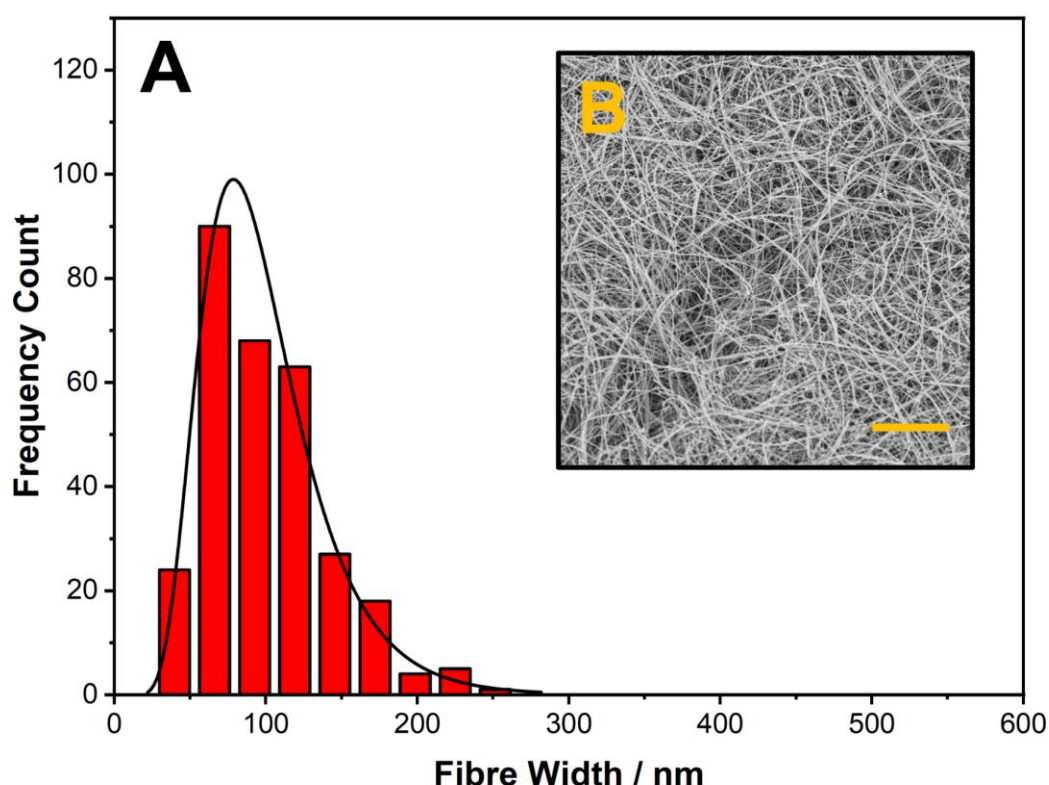


Figure 6.12. (A) Fibre width distribution histogram of a cryogenically frozen sample of $\text{CO}_2\text{HDPP@Gel}$ gel as measured through cryo-SEM. (B) Cryo-SEM micrograph of frozen $\text{CO}_2\text{HDPP@Gel}$, scale bar corresponds to 10 μm . Gel prepared in 1:1 water-ethanol and $[1.2\text{Br}] = 12$ mM, $[\text{CO}_2\text{HDPP}] = 150$ μM .

As with 1.2Br@Gel , the morphology of $\text{CO}_2\text{HDPP@Gel}$ in its dried state as measured using conventional SEM does differ from that of the frozen state. More bundling of fibres is seen, and curvature of these fibres is less pronounced. Quantitatively, the fibre width distribution is centred at ~ 98 nm, with most fibres possessing a width of between 82 – 103 nm (**Fig. 6.13**). That the dried $\text{CO}_2\text{HDPP@Gel}$ average fibre width is larger than that of the pristine dried

1.2Br@Gel is not surprising, given the already supported altering of gel morphology with the inclusion of fluorophores.

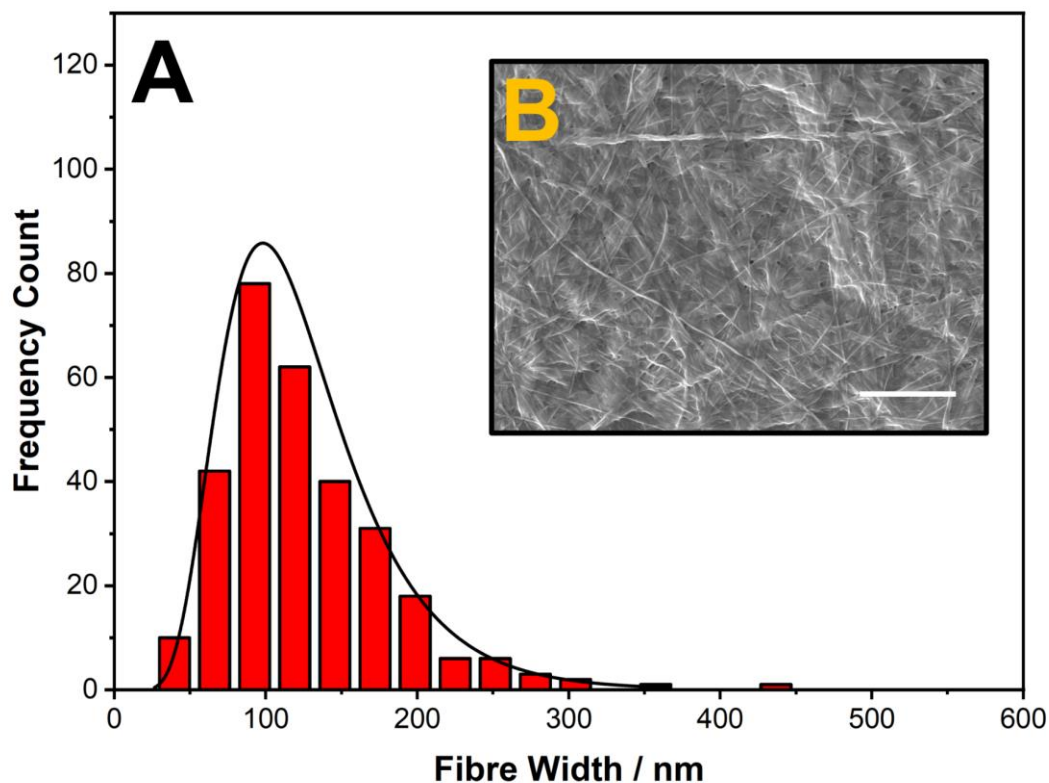


Figure 6.13. (A) Fibre width distribution histogram of a dried sample of $\text{CO}_2\text{HDPP@Gel}$ gel as measured through conventional SEM. (B) SEM micrograph of dried $\text{CO}_2\text{HDPP@Gel}$, scale bar corresponds to $10\ \mu\text{m}$. Gel prepared in 1:1 water-ethanol and $[\mathbf{1.2Br}] = 12\ \text{mM}$, $[\text{CO}_2\text{HDPP}] = 150\ \mu\text{M}$.

An unexpected result is observed when PEG3DPP@Gel is imaged using Cryo-SEM. PEG3DPP was previously incorporated into the $\mathbf{1.2Br}$ gel during the confocal studies, where the fluorophore was not immediately taken up into the fibres as previous fluorophores were. It was found that upon the evaporation of gel solvent, PEG3DPP would migrate into the gel fibres (**Fig. 6.14**). In the Cryo-SEM setup, it is probable that the gel would be cryogenically fixed before any fluorophore migration occurred.

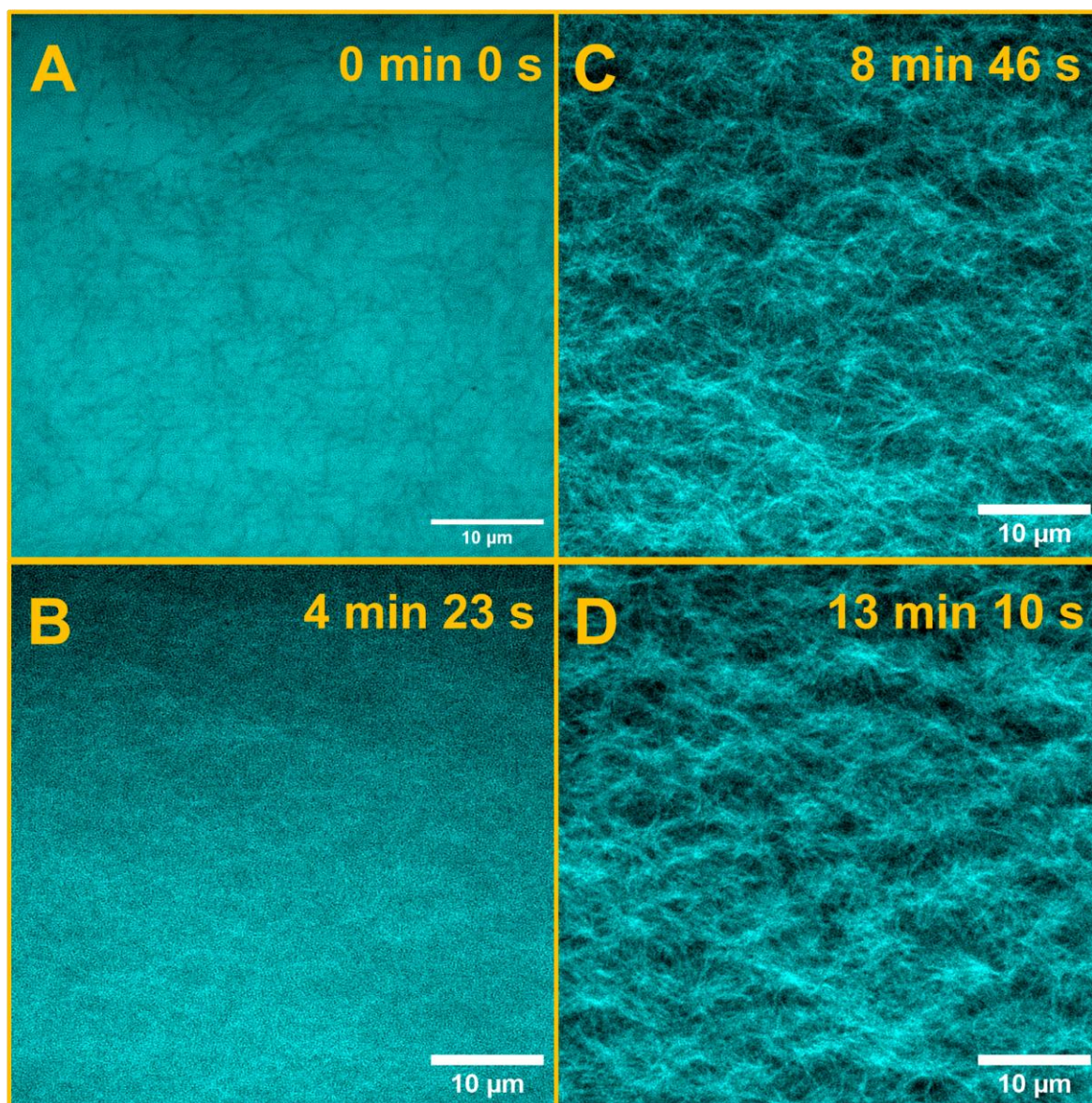


Figure 6.14. CLSM micrographs of **PEG3DPP@Gel**, $[PEG3DPP] = 150 \mu M$, showing the migration of **PEG3DPP** into **1.2Br** fibres. (A) Micrograph of **PEG3DPP@Gel** showing fibre silhouettes at $t = 0$ s. (B) Micrograph of **PEG3DPP@Gel** showing the initial migration of **PEG3DPP** into fibres, with some fluorescence signal still in the interstitial areas at $t = 4$ min 23 s. (C) Micrograph of **PEG3DPP@Gel** showing the significant migration of **PEG3DPP** into fibres, with little fluorescence signal still in the interstitial areas at $t = 8$ min 46 s. (D) Micrograph of **PEG3DPP@Gel** showing the completion of **PEG3DPP** migration into fibres, with little-to-no fluorescence signal still in the interstitial areas at $t = 13$ min 10 s. Imaging details : laser 488 nm, emission range 500-700 nm, laser power 30%. Gels prepared in 1:1 water-ethanol and $[1.2Br] = 12$ mM.

When cryogenically fixed, the apparent gel morphology of **PEG3DPP@Gel** is similar to the previous gels studied here using Cryo-SEM with fibres curving and intertwining (**Fig. 6.15**).

The fibre curvature observed in the Cryo-SEM corresponds to the apparent morphology of the silhouettes and illuminated fibres after the migration of **PEG3DPP**, as observed in the CLSM.

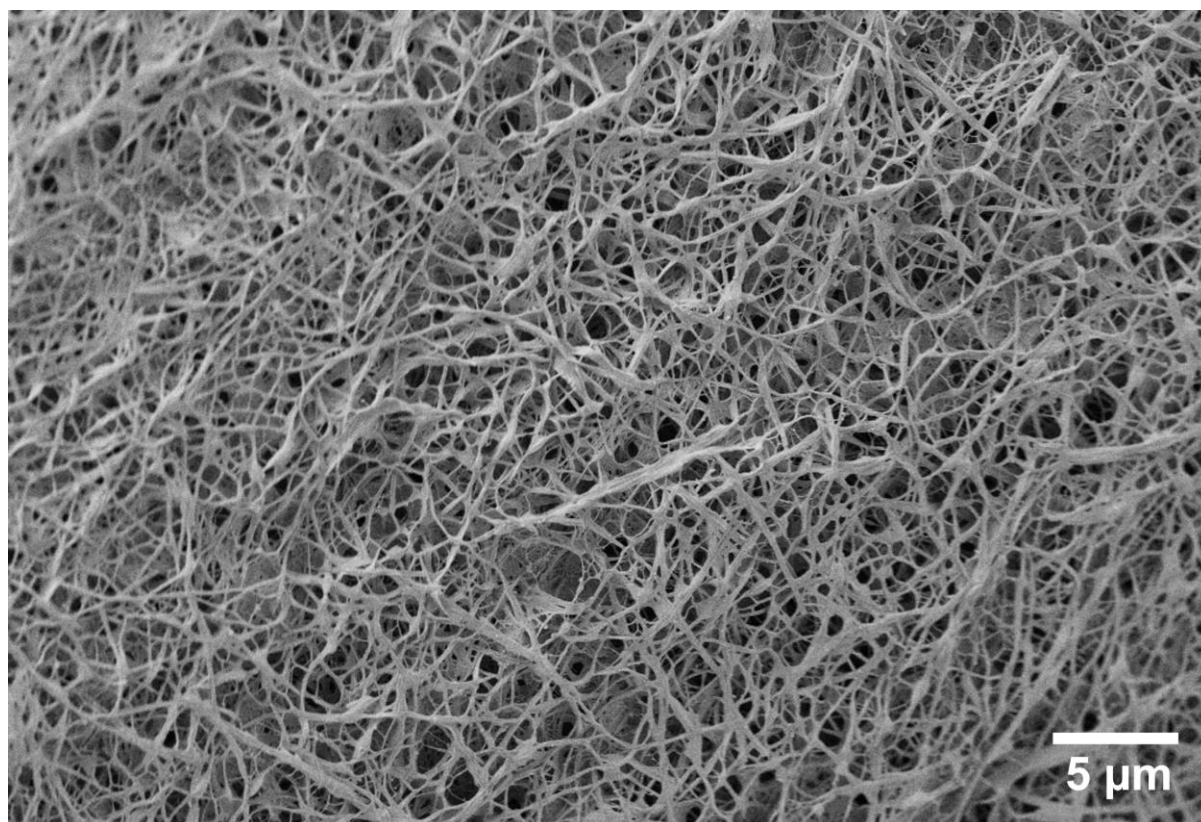


Figure 6.15. Cryo-SEM micrograph of **PEG3DPP@Gel**, $[PEG3DPP] = 150 \mu M$. Gels prepared in 1:1 water-ethanol and $[1.2Br] = 12 \text{ mM}$.

Despite these apparent similarities, fibre widths were found to be significantly thicker than those measured in **1.2Br@Gel** and **CO₂HDPP@Gel** (Fig. 6.16). Whilst the average fibre widths of the frozen **1.2Br@Gel** and **CO₂HDPP@Gel** were measured to be around 78 nm and 50 nm, respectively, the average fibre width of frozen **PEG3DPP@Gel** was measured to be 196 nm. In addition to this, the width distribution is much broader, with some fibre widths above approximately 500 nm being measured in the data collected in this study. It can be assumed that the **PEG3DPP** remains outside of the fibres under these imaging conditions, and thus presents the only sample in which a fluorophore is present in the gel but not incorporated into the fibres. It is notable that this one outlier from the trend of thinner fibres measured in the cryogenically frozen gels compared with the dried gels is the sample in which fluorophore take-up into fibres was not observed. This result indicates that the **PEG3DPP** fluorophores are influencing the fibre morphology from the interstitial area between fibres.

The observed phenomenon might be a result of the interaction between **PEG3DPP** and the **1.2Br** gelator molecules whereby the pyridyl groups of the DPP molecule interact with the mildly acidic protons on the imidazolium ring.

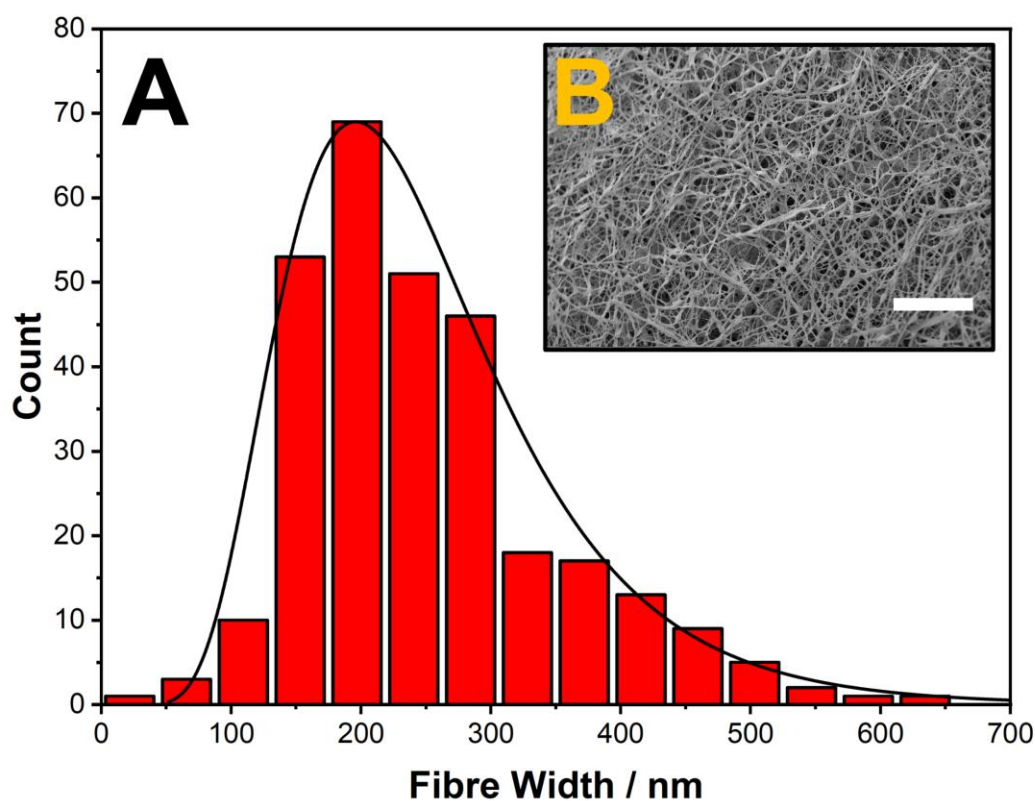


Figure 6.16. (A) Fibre width distribution histogram of a cryogenically frozen sample of **PEG3DPP@Gel** gel as measured through cryo-SEM. (B) Cryo-SEM micrograph of frozen **PEG3DPP@Gel**, scale bar corresponds to 10 μm . Gel prepared in 1:1 water-ethanol and $[1.2\text{Br}] = 12 \text{ mM}$, $[\text{PEG3DPP}] = 150 \mu\text{M}$.

The thickness of the **PEG3DPP@Gel** fibres as measured using cryo-SEM does not contrast with the measurements made on the dried gel using conventional SEM. The average fibre width of the dried **PEG3DPP@Gel** was measured to be approximately 170 nm, more than double that of the pristine **1.2Br@Gel** xerogel (**Fig. 6.17**). This sample is therefore the single example of frozen gels possessing fibres that are thicker than those measured in the dried gels.

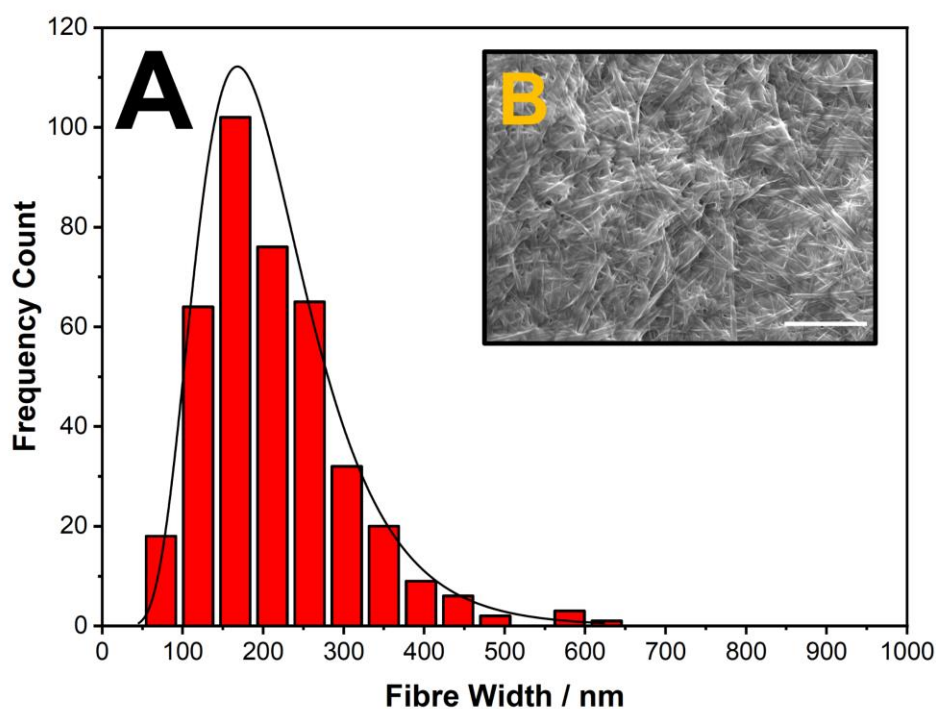


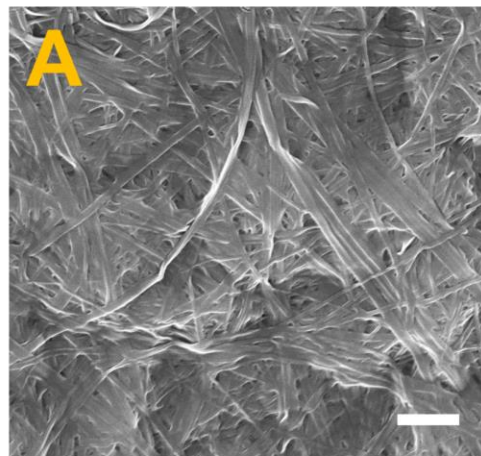
Figure 6.17. (A) Fibre width distribution histogram of a dried sample of **PEG3DPP@Gel** gel as measured through conventional SEM. (B) Conventional SEM micrograph of dried **PEG3DPP@Gel**, scale bar corresponds to 2 μm . Gel prepared in 1:1 water-ethanol and $[\mathbf{1.2Br}] = 12 \text{ mM}$, $[\mathbf{PEG3DPP}] = 150 \mu\text{M}$.

6.4. Phthalocyanine concentration investigation

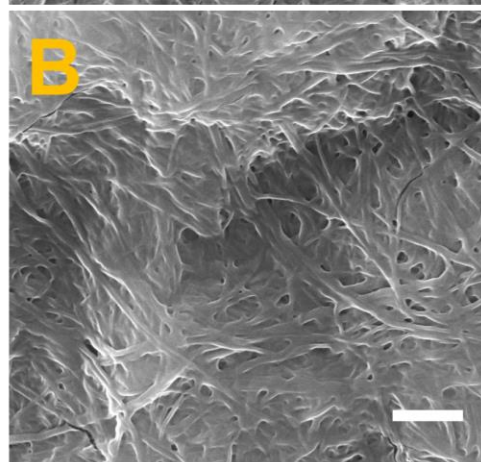
The influence of fluorophore concentration on the hydrated gel morphology of **1.2Br** gels has been reported in literature.²⁵ In the paper by Samperi *et al.*, fibre widths were found by measuring the full width at half maximum (FWHM) of an intensity cross-section over a fibre using Super-Resolution Radial Fluctuations (SRRF) microscopy. In doing this, it was found increasing fluorophore concentration gradually increased fibre width and that bundling at high concentrations still occurred in the hydrated state. Despite this, it is still not fully understood is the extent to which the concentration of the fluorophore affects the hydrated gel morphology. SRRF provided a unique method by which hydrated fibre width could be quantified, and cryo-SEM provides another solution for the same problem.

To investigate this problem further, it is important to note how dried gel morphology is influenced by fluorophore concentration. **Figure 6.18** shows the change in dried gel fibre morphology as measured with conventional SEM with increasing concentrations of zinc phthalocyanine tetrasulfonic acid (**ZnPcTS**).

[ZnPcTS] = 0 μ M



[ZnPcTS] = 100 μ M



[ZnPcTS] = 500 μ M

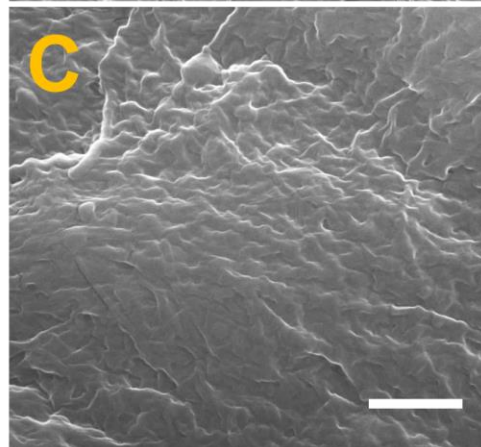


Figure 6.18. ZnPcTS@Gel SEM micrographs at multiple ZnPcTS concentrations. (A) [ZnPcTS] = 0 μ M. (B) [ZnPcTS] = 100 μ M. (C) [ZnPcTS] = 500 μ M. Gels prepared in 1:1 water-ethanol and [1.2Br] = 12 mM.

In this study, ZnPcTS concentrations of 0 μ M (control), 100 μ M, and 500 μ M were looked at using conventional SEM and cryo-SEM. As can be seen in **Fig. 6.18**, increasing ZnPcTS concentration has a significant effect upon gel morphology, with fibres becoming indistinguishable at a ZnPcTS concentration of 500 μ M. It was therefore not possible to quantify fibre lengths for the sample containing 500 μ M ZnPcTS. However, the transition from

0 to 100 μM **ZnPcTS** induced a change in the average fibre width, increasing it from approximately 70 – 80 nm in the absence of **ZnPcTS** to a width of 100 – 110 nm when 100 μM **ZnPcTS** was present. Nevertheless, even when not considering the quantifiable aspects of the micrographs, a considerable qualitative difference in morphology can be seen between the 100 μM and 500 μM **ZnPcTS** samples. **Figure 6.19** shows a comparison of the fibre width histograms of the control **1.2Br@Gel** sample and the 100 μM **ZnPcTS** sample.

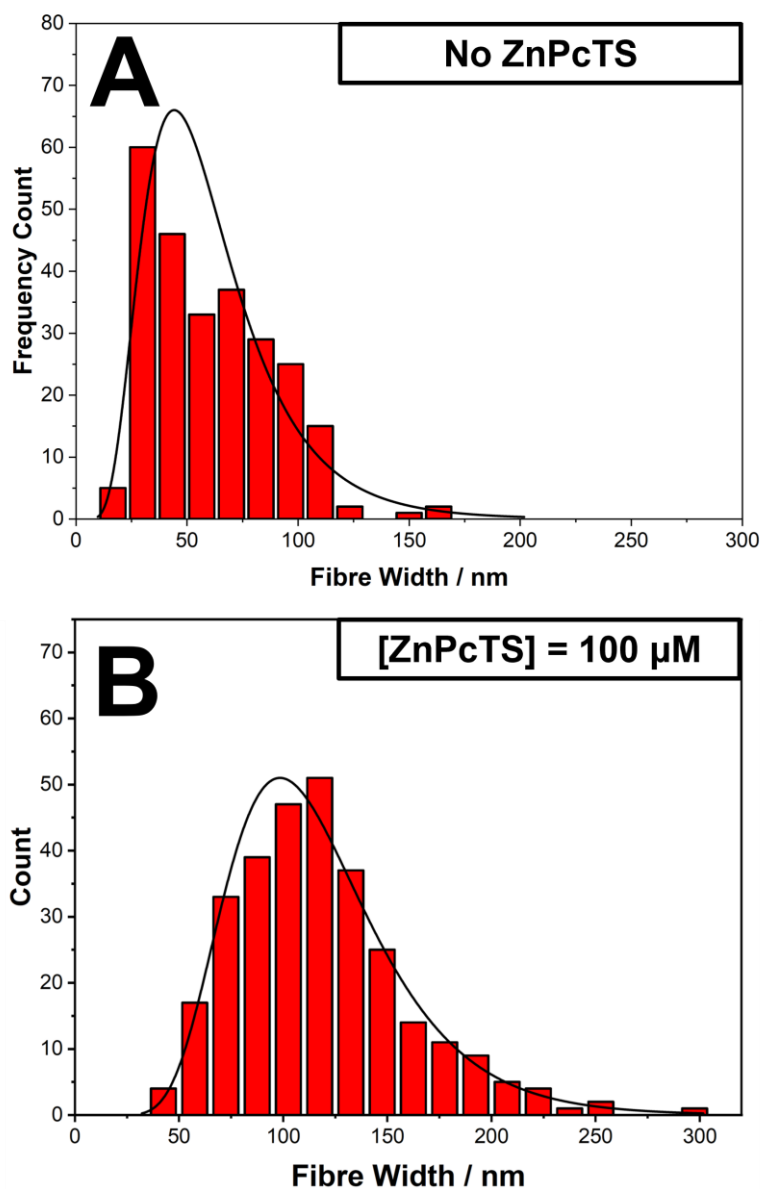


Figure 6.19. (A) Fibre width distribution histogram of a frozen sample of **1.2Br@Gel** as measured through cryo-SEM, $[\text{ZnPcTS}] = 0 \mu\text{M}$. (B) Fibre width distribution histogram of a frozen sample of **ZnPcTS@Gel** as measured through cryo-SEM, $[\text{ZnPcTS}] = 100 \mu\text{M}$. Gels prepared in 1:1 water-ethanol and $[\text{1.2Br}] = 12 \text{mM}$.

Cryo-SEM on the 0 μM **ZnPcTS** control sample was explored previously in this chapter so it will suffice to state that the average fibre width was around 45 nm, whereas in the dried gel it was found to be around 65 nm. This result indicates a natural increase in fibre widths occurs upon gel drying caused by bundling effects. Moving from 0 to 100 μM **ZnPcTS** has some effect on the general fibre morphology as seen with cryo-SEM (**Fig. 6.20**). Fibres appear to bundle more in the more concentrated sample, although the difference in apparent morphology is not as pronounced as observed in conventional SEM.

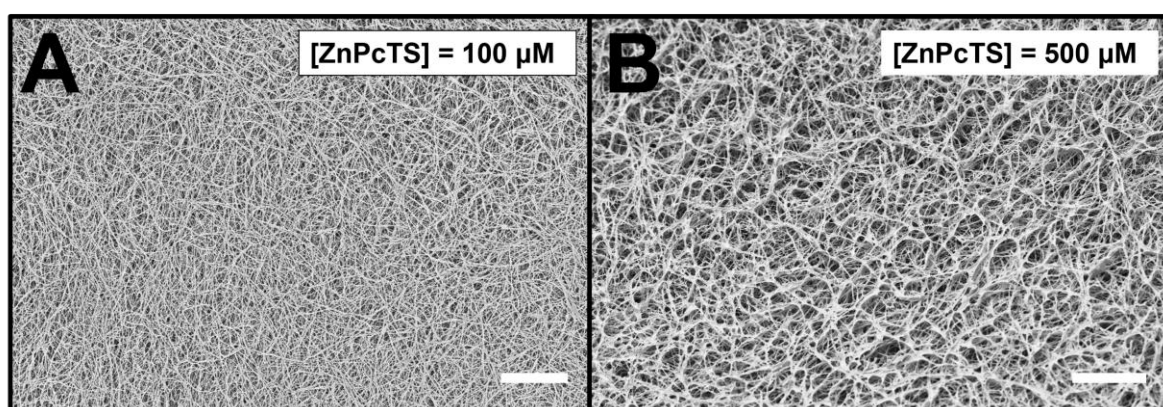


Figure 6.20. Cryo-SEM micrographs of **ZnPcTS@Gel**. (A) $[\text{ZnPcTS}] = 100 \mu\text{M}$. (B) $[\text{ZnPcTS}] = 500 \mu\text{M}$. Gels prepared in 1:1 water-ethanol and $[\text{1.2Br}] = 12 \text{ mM}$.

Although more bundling seems to be apparent in the 500 μM sample than in the 100 μM sample, average fibre thickness between the two samples is identical which can be seen in **Fig. 6.21**. Despite this, the skewness of the lognormal plot assigned to the histograms is greater in the case of the 500 μM **ZnPcTS** sample than the 100 μM sample, meaning outliers of thicker fibres are more numerable in the case of the former.

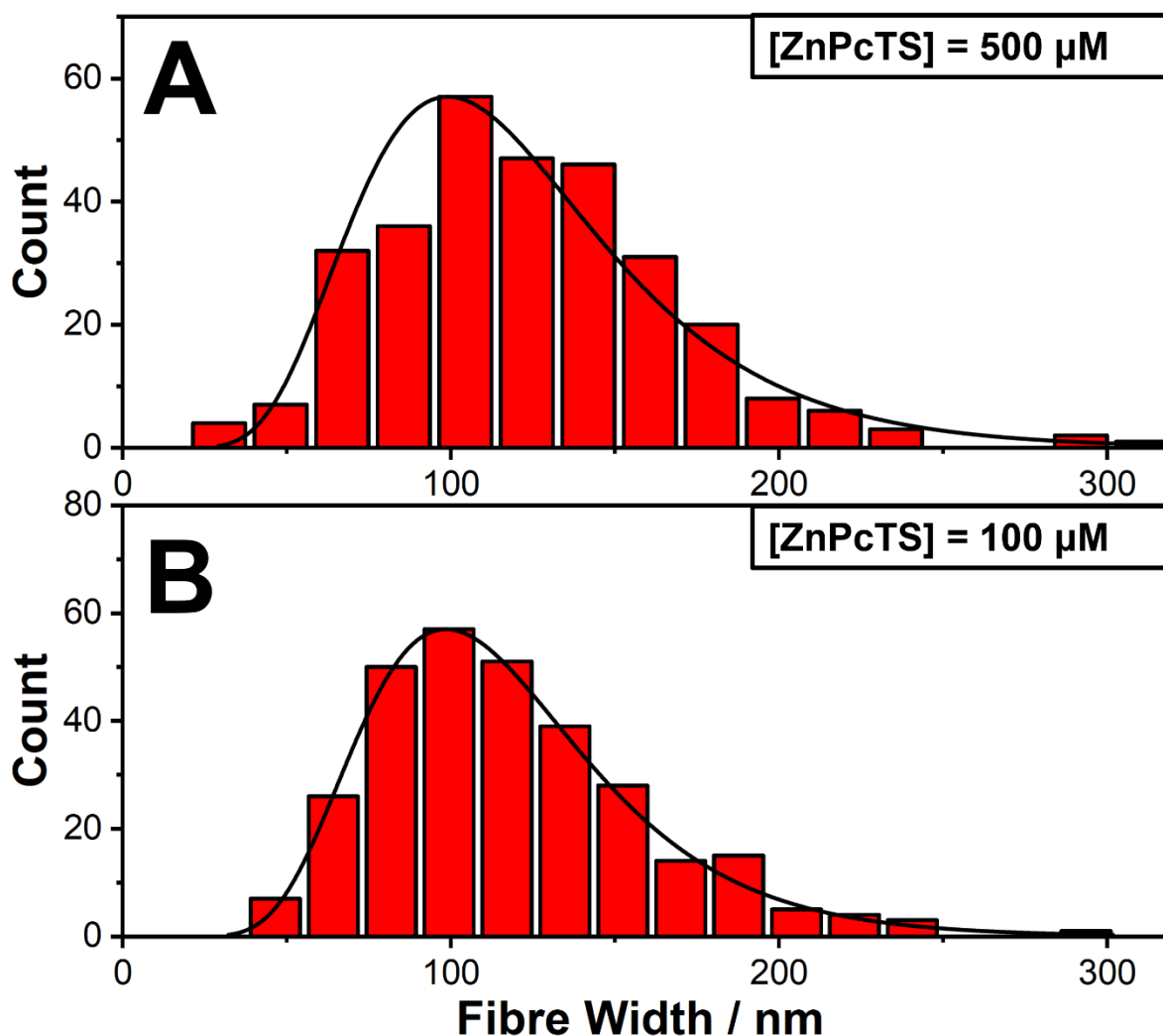


Figure 6.21. (A) Fibre width distribution histogram of a frozen sample of **ZnPcTS@Gel** as measured through cryo-SEM, $[\text{ZnPcTS}] = 100 \mu\text{M}$. (B) Fibre width distribution histogram of a frozen sample of **ZnPcTS@Gel** as measured through cryo-SEM, $[\text{ZnPcTS}] = 100 \mu\text{M}$. Gels prepared in 1:1 water-ethanol and $[\text{1.2Br}] = 12 \text{ mM}$.

This result indicates that whilst concentration does have a measurable effect upon gel fibre widths, in alignment with previous experiments, it is the drying process that contributes largely to the change in morphological properties.

6.5. Conclusion

In summary, cryo-SEM has been shown as a versatile way of imaging frozen gels. The primary objective of this chapter was to investigate the correlation between dried gel morphology and hydrated gel morphology, with a specific focus on imidazolium gels of the studied type. Initially, a method was developed to image these gels by optimising coating and sublimation conditions, resulting in satisfactory images. Subsequently, gels containing various DPP

fluorophores were imaged, and the widths of the fibres were collected and analysed using histograms for comparison. By comparing the fibre widths obtained from the conventional SEM micrographs and the dried/frozen gel samples, a comparison of their widths was made. The findings indicated that, for most tested samples, the fibre widths were smaller in the frozen samples due to reduced bundling and drying effects. However, **PEG3DPP@Gel** exhibited an exception, as the dried gel fibres were thinner than the cryogenically frozen fibres. This phenomenon was attributed to interactions between the DPP and gelator molecules during the gel formation process. Additionally, a concentration study was conducted using **ZnPcTS** as the incorporated fluorophore. It was discovered that introducing a **ZnPcTS** concentration of 100 μM to the pristine gel increased the average fibre width. However, further increasing the concentration to 500 μM did not cause any change in the measured average fibre width. This contrasts with the results observed in conventional SEM imaging of dried fibres, where an increase in **ZnPcTS** concentration from 100 μM to 500 μM resulted in significant alterations in the gel morphology, to the extent that the fibres were no longer visible. The research conducted in this chapter has illuminated the connection between guest concentrations in gel-guest systems and how the subsequent drying can impact gel morphology. This knowledge is important for understanding the properties of hydrogels in the context of their potential applications.

6.6. Experimental

6.6.1. General procedures

The gels described in this study were prepared at a 1:1 water-ethanol ratio always with a final **1.2Br** gelator concentration of 12 mM. A 2.4 mM stock solution of fluorophore was prepared (either in water or ethanol depending on solubility considerations), and subsequently diluted in a glass vial to achieve the desired fluorophore concentration. Samples containing a water-soluble fluorophore to be observed using cryo-SEM were prepared by mixing the diluted aqueous fluorophore solution with an equal volume of an ethanolic 24 mM **1.2Br** gelator solution. Samples containing a non-water-soluble fluorophore to be observed using cryo-SEM were prepared by mixing Milli-Q water with an equal volume of an ethanolic 24 mM **1.2Br** gelator solution also containing the fluorophore at the appropriate concentration. Rapid and thorough mixing of the ethanolic and aqueous solutions was carried out to ensure homogeneity. The gel was left to form before being transferred to a grooved cylindrical aluminium stub for imaging.

Cryo-FIB-SEM was carried out using a Zeiss Crossbeam 550 fitted with a Quorum 3010T cryo-stage and preparation chamber. Samples were prepared for analysis either by use of a Leica MM80 Metal Mirror freezer or by freezing in liquid nitrogen slush on grooved cylindrical aluminium stubs, using a Quorum PP3010 Prepdek slush freezer. The stubs were then secured onto the sample shuttle of the cryo-system before transfer to the preparation station at $-170\text{ }^{\circ}\text{C}$ via a liquid nitrogen slushing pot. The gels were sputtered in an argon environment using platinum for 60 s at a current of 10 mA. Once coated the shuttle was transferred to the cryo-stage in the SEM chamber and maintained at $-170\text{ }^{\circ}\text{C}$. Before cryo-FIB milling, the sample's surface underwent preparation through the application of an organometallic precursor layer dispensed from the gas injection system (GIS) of the microscope. The GIS crucible was heated to $27\text{ }^{\circ}\text{C}$, and the sample stage was adjusted to be approximately 1 to 1.5 mm below the GIS needle once inserted. The organometallic precursor layer was deposited for a duration of 10 seconds. This prepared layer was subjected to milling using a focused ion beam of gallium ions at current levels ranging from 3 nA to 0.1 nA, resulting in the creation of a cross-sectional view in the sample with an exposed, featureless surface. To observe the structure of the gels, water is removed from the surface of this face by increasing the stage temperature to $-100\text{ }^{\circ}\text{C}$ and held for a period of 30 – 60 min. During this time, water sublimates away from the gel-water interface and through topological differences, the physical structure of the hydrogel is revealed. Finally, the microstructure of the hydrogel was then imaged by SEM.

6.7. References

1. M. Knoll, *Z. Phys.*, 1935, 16, 467 – 475.
2. M. von Ardenne, *Z. Phys.*, 1938, 19, 407 – 416.
3. D. McMullan, *Proceedings of the IEE – Part II: Power Engineering*, 1953, 100, 245 – 256.
4. A. D. G. Stewart, M. A. Snelling, *Proc. 3rd European Conference Electron Microsc.*, 1965, 55 – 66.
5. J. I. Goldstein, D. E. Newbury, J. R. Michael, N. W. M. Ritchie, J. H. J. Scott, D. C. Joy, *Scanning Electron Microscopy and X-Ray Microanalysis*, Springer New York, New York, 4, 2017.
6. S. Liu, L. Han, Y. Duan, S. Asahina, O. Terasaki, Y. Cao, B. Liu, L. Ma, J. Zhang, S. Che, *Nat. Commun.*, 2012, 3, 1215.
7. L. Crouzier, A. Delvallée, S. Ducourtieux, L. Devoille, C. Tromas, N. Feltin, *Ultramicroscopy*, 2019, 207, 112847.

8. B. J. Privett, J. Youn, S. A. Hong, J. Lee, J. Han, J. H. Shin, M. H. Schoenfish, *Langmuir*, 2011, 27, 9597 – 9601.
9. W. Xue, I. W. Hamley, M. B. Huglin, *Polymer*, 2002, 43, 5181 – 5186.
10. J. Hong, H. Yang, M. Jo, H. Park, S. Choi, *Thin Solid Films*, 1997, 308 – 309, 495 – 500.
11. K. Kumar, A. Jose, P. Dastidar, A. Das, *Langmuir*, 2004, 20, 10413 – 10418.
12. C. D. Hickey, J. J. Sheehan, M. G. Wilkinson, M. A. E. Auty, *Front. Microbiol.*, 2015, 6, 99.
13. *Scanning Electron Microscopy for the Life Sciences*, H. Schatten, Cambridge University Press, Cambridge, 1, 2012.
14. A. K. Jha, R. A. Hule, T. Jiao, S. S. Teller, T. J. Clifton, R. L. Duncan, D. J. Pochan, X. Jia, *Macromolecules*, 2009, 42, 537 – 546.
15. M. Schaffer, J. Mahamid, B. D. Engel, T. Laugks, W. Baumeister, J. M. Plitzko, *J. Struct. Biol.*, 2017, 197, 73 – 82.
16. J. Z. Lee, T. A. Wynn, M. A. Schroeder, J. Alvarado, X. Wang, K. Xu, Y. S. Meng, *ACS Energy Lett.*, 2019, 4, 489 – 493.
17. H. Hao, T. Hutter, B. L. Boyce, J. Watt, P. Liu, D. Mitlin, *Chem. Rev.*, 2022, 122, 8053 – 8125.
18. D. E. Clarke, C. D. J. Parmenter, O. A. Scherman, *Angew. Chem. Int. Ed. Engl.*, 2018, 57, 7709 – 7713.
19. C. Kyomugasho, S. Christiaens, D. Van de Walle, A. M. Van Loey, K. Dewettinck, M. E. Hendrickx, *Food Hydrocoll.*, 2016, 61, 172 – 182.
20. E. L. Bearer, L. Orci, *J. Electron Microsc. Tech.*, 1986, 3, 233 – 241.
21. Y. Zhang, T. Huang, D. M. Jorgens, A. Nickerson, L. Lin, J. Pelz, J. W. Gray, C. S. López, X. Nan, *PLoS One*, 2017, 12, e0176839.
22. D. T. Osanl0o, J. Fransson, B. Bergenst0ahl, A. Millqvist-Fureby, *Dry. Technol.*, 2022, 41, 503 – 522.
23. H. Grohganz, Y. Lee, J. Rantanen, M. Yang, *Int. J. Pharm.*, 2013, 447, 224 – 230.
24. D. J. Adams, *Gels*, 2018, 4, 32.
25. M. Samperi, D. Lim0n, D. B. Amabilino, L. P0rez-García, *Cell Rep.*, 2020, 1, 100030.
26. M. Samperi, L. P0rez-García, D. B. Amabilino, *Chem. Sci.*, 2019, 10, 10256 – 10266.
27. L. L. E. Mears, E. R. Draper, A. M. Castilla, H. Su, Zhoula, B. Dietrich, M. C. Nolan, G. N. Smith, J. Dutch, S. Rogers, R. Akhtar, H. Cui, D. J. Adams, *Biomacromolecules*, 2017, 18, 3531 – 3540.

Chapter 7

Summary

7.1. Summary

Zinc phthalocyanine tetrasulfonic acid (**ZnPcTS**), a water-soluble phthalocyanine, was effectively incorporated into 1,3-bis[(3-octadecyl-1-imidazolium)methyl]benzene di-bromide (**1.2Br**) gels. This incorporation into a 1:1 water-ethanol microenvironment as part of the gel aided in reducing the aggregation of the phthalocyanine. As a result, **ZnPcTS** was able to produce more SO under irradiation with 660 nm and 635 nm laser light than the photosensitizer is usually capable of in a purely aqueous environment. The generation of SO was measured by tracking the fluorescence decay of a 9,10-anthracenedyl-bis(methylene)dimalonic acid (**ABMA**) molecular probe, with this decay rate acting as a proxy for a rate of singlet oxygen (SO) generation. When fitted to a pseudo first-order rate equation, the rate of SO generation was quantified. In addition to this, it was found that the protonation state of sulfonic acid groups present on the periphery of the isoindole units of the phthalocyanine influenced the aggregation properties and subsequently the rate of SO generation. Experiments using CsOH and NaCl confirmed that base was responsible for the increase in SO generation. Further to this, the way in which the gel was dispersed was found to be vital to the SO generation observed. Comparable results were observed for zinc tetrasulfonatomethyl phthalocyanine (**ZnPcSO₂Me**), a hydrophobic phthalocyanine. When incorporated into the **1.2Br** gel, **ZnPcSO₂Me** experienced a significant disaggregation effect compared to **ZnPcSO₂Me** in solution, which was evident through absorption spectroscopy. This reduction in aggregation resulted in a substantial enhancement in SO generation. This study highlighted how water-soluble photosensitizers prone to aggregation can be relieved of such aggregation and become effective SO generators in largely aqueous environments by the use of soft materials.

ZnPcTS was found, through total internal reflection fluorescence (TIRF) microscopy, to diffuse through the fibres of a hydrated **1.2Br** gel. At low fluorophore concentrations, individual molecular motion was observed. Analysis of this movement using mean square displacement (MSD) analysis confirmed this diffusion to be confined in nature. Mean instantaneous velocity (MIV) and MSD analysis found a linear relationship between the irradiance experienced by the sample and the resulting speed of fluorophores, with the further introduction of acids into the gel system influencing fluorophore speed and encapsulation properties. Further studies on a tetrasulfonated porphyrin (**TPPS**), a mixed system of **TCPP** and **ZnPcTS**, and a tetrasulfonatomethyl phthalocyanine (**ZnPcSO₂Me**) found differences in both fibre morphology and fluorophore behaviour. This study highlighted how electrostatic interactions between fluorophores and supramolecular architectures can lead to unexpected

behaviours on the microscale. Also notable are the ways in which such interactions could be influenced by slight changes to the system studied.

Three galactose-based glycopolymers were synthesized, each having different molecular weights. The inclusion of these glycopolymers did not have a significant impact on the macroscopic properties of the gel, at least within the polymer concentrations utilized in this investigation. However, at the microscale, the morphology of the gel fibres was noticeably distorted at various concentrations of the glycopolymers. This distortion in fibre morphology was further confirmed through TIRF imaging, which revealed similar disruptions in the hydrated fibre structure. Additionally, the presence of the glycopolymer led to a decrease in the fluorescence intensity of **ZnPcTS**, suggesting potential interactions between the fluorophore and the polymer. Interestingly, the analysis of **ZnPcTS** fluorophore speed using MIV analysis demonstrated an increase in speed with higher concentrations of the glycopolymer. This observation highlights the influence of the glycopolymer additive on the behaviour of **ZnPcTS** fluorophores. Overall, this study highlights how the presence of a polymeric additive can significantly affect both the macroscopic and microscopic properties of supramolecular gels. The distorted fibre morphology and altered fluorescence intensity and speed of **ZnPcTS** fluorophores emphasize the intricate interplay between the polymeric additive and the gel matrix. These findings contribute to our understanding of the complex interactions within gel systems and provide insights into the design and manipulation of supramolecular materials for various applications.

Confocal laser scanning microscopy (CLSM) allowed for the detailed imaging of hydrated imidazolium gels with the aid of fluorescent compounds that illuminated the gel fibres upon excitation. However, the effectiveness of gel imaging varied depending on the specific fluorophore employed, as both **ZnPcTS** and **TPPS** did not provide an optimal level of detail. Additionally, the method of sample preparation, either through compression between glass plates or placement on a glass coverslip, had an impact on the observed gel morphology as visualized by CLSM. To overcome these limitations, diketopyrrolopyrrole (DPP) fluorophores were utilized, offering improved imaging of gel morphology due to their higher fluorescence intensity, which resulted in significantly enhanced signal-to-noise ratios and apparent resolution. Interestingly, dynamics of these DPP fluorophores were also observed, with certain DPPs migrating into the gel fibres, whereas before solvent evaporation, they were excluded from the fibres. The phenomenon of fluorophore migration was found to be influenced by solvent evaporation and the presence of pyridine groups flanking the DPPs. However, the exact

underlying reasons for this behaviour remain unclear. In summary, this research provides a straightforward and effective method for directly imaging the intricate details of hydrated gel morphology. By employing CLSM with specific fluorescent compounds, this study advances our understanding of gel structures and highlights the importance of fluorophore choice and sample preparation techniques in obtaining accurate and comprehensive visualisation of gel morphologies.

Cryogenic scanning electron microscopy (cryo-SEM) proves to be a versatile imaging technique for frozen gels. This chapter aimed to explore the relationship between dried and hydrated gel morphology, focusing on the imidazolium gels studied in previous chapters. An optimized method for imaging these gels was developed, resulting in detailed images of gel morphology. Fibre widths were analysed by comparing conventional scanning electron microscopy (SEM) micrographs with dried/frozen gel samples containing various DPP compounds. The results showed that frozen samples generally had smaller fibre widths as a consequence of reduced bundling and drying effects. Furthermore, a concentration study using **ZnPcTS** revealed that morphological changes in these imidazolium gels are less pronounced in the hydrated state than in the dried state.

Overall, this thesis has contributed to the knowledge of soft material systems. The results of the study successfully fulfil the aim of investigating soft material systems, specifically gels. It is hoped that the results presented here will aid in the future development of functional soft materials for pharmaceutical applications.

7.2. Limitations

The work presented in the studies that comprise this thesis generally fulfils the scope of the aims and objectives as laid out in the introduction, but there is room for improvement in some respects. Specifically for Chapter 2, it would have been valuable to include a sulfonated porphyrin to for a direct comparison to **ZnPcTS**. Additionally, a comprehensive investigation into the 1,3-bis[(3-octadecyl-1-imidazolium)methyl]benzene di-chloride (**1.2Cl**) gels was lacking and could have provided insights into the role that counterions play in SO generation. Because of the lower power laser used for measuring the SO generation rate of **ZnPcSO₂Me**, a direct comparison to the highly effective SO generation of **ZnPcTS** (brought about using the 50 mW laser) was not possible.

For Chapter 3, it would have been beneficial to conduct a study on various phthalocyanines featuring different end groups. This variety would have allowed for a direct comparison of the

end group interaction with the gel lamellae. As **1.2Cl** fibre morphology is different to that of **1.2Br**, a study concerning **1.2Cl** gels could have offered perspectives on how morphology influences fluorophore diffusion. In addition, the fact that **TPPS** did not fluoresce when excited at 405 nm indicated that it was not present in the form intended, as 405 nm should match up ideally with the absorption maximum of the compound.

In Chapter 4, the molecular weight dispersity of the synthesized glycopolymers were higher than would be expected in radical addition fragmentation chain-transfer (RAFT) polymerisation. Full characterisation of the resulting gels when incorporated with **1.2Br** (including powder x-ray diffraction (PXRD) and rheology) could not be carried out as a result of time constraints. These techniques would have provided valuable insight into the glycopolymers' effect upon the microscale structure of the gels.

In Chapter 5, no firm conclusion as to why pyridine-flanked DPPs migrated into gel fibres upon gel solvent evaporation was found, though it was concluded that it was the presence of the pyridine groups that caused the effect. It was also not possible to correlate any **ZnPcTS** diffusion seen with TIRF microscopy as the requisite signal-to-noise was not achievable.

In Chapter 6, the imidazolium gels that were studied in the previous chapters on CLSM were focused on for comparison with cryo-SEM. The conclusions drawn about drying effects on imidazolium gel morphology cannot necessarily be extended to other gel systems. A thorough investigation into changes in morphologies between gel samples prepared *via* alternate freezing methods (slush freezing, metal-mirror freezing, plunge freezing) had the potential to provide valuable insights into how sample preparation affects morphology and whether gel properties observed under electron microscopy remain consistent across different preparations.

7.3. Further work

The imidazolium gel containing photosensitizer requires examination of its antimicrobial activity under *in vitro* conditions. Additionally, it is crucial to explore methods to reduce or eliminate the ethanol component of the gel, either through the addition of an additive or an alternative cosolvent. This is particularly important for *in vitro* studies as ethanol itself tends to kill bacteria, making it difficult to assess the actual effects of the SO. It would also be valuable to investigate the potential of other photosensitizers prone to aggregation to determine if the **1.2Br** gel functions as a system that can universally limit the aggregation of photosensitizers.

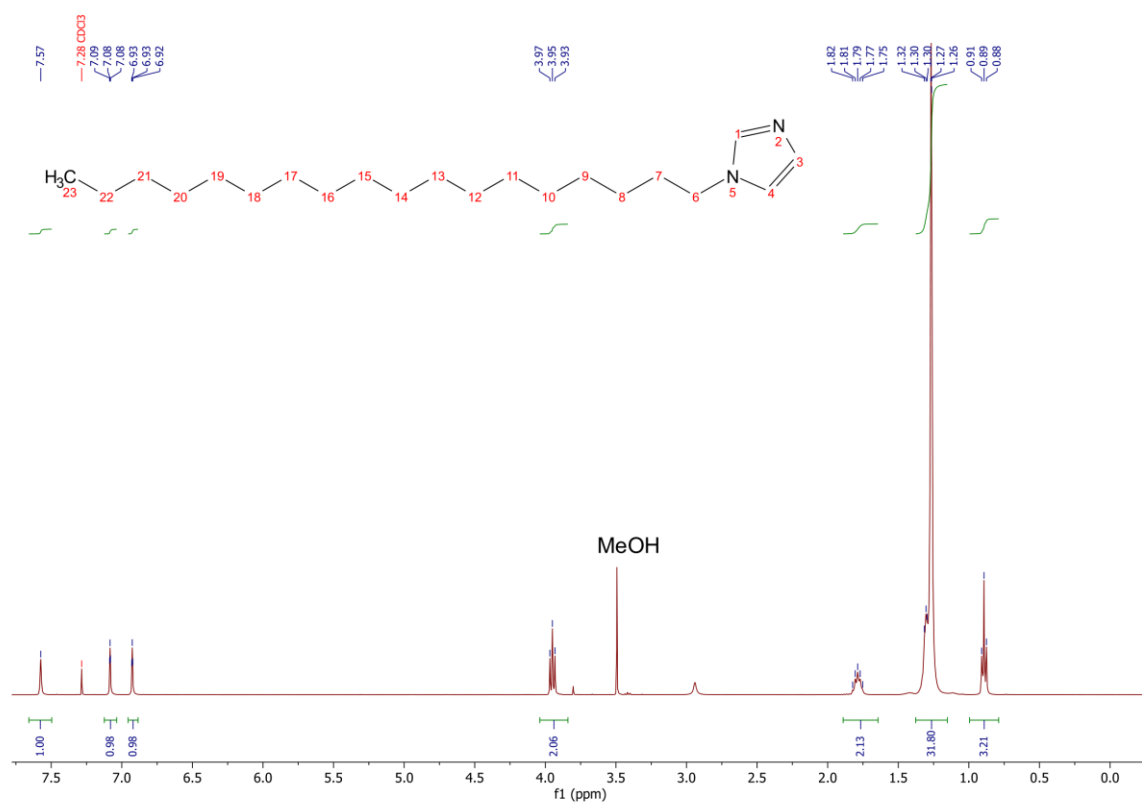
There are many options for further manipulating fluorophore diffusion in the imidazolium gel systems studied in this work. Spiroyrans are photochromic compounds which can undergo photoinduced transformations from the non-fluorescence spirocyan form to the fluorescent merocyanine form. Should a spirocyan derivative be localized in the gel fibres, disruption of morphology could occur upon this conformational change which could be used to influence fluorophore diffusion. Introducing a cationic azo molecular switch into the gel could provide insights into its impact on diffusion dynamics of incorporated fluorophores. The introduction of different fluorophores could be used to investigate further the reasons for which diffusion occurs. Zinc phthalocyanine tetracarboxylic acid would be an important molecule to investigate as it would provide further insight into the extent to which electrostatic effects between fluorophore and gel are responsible for fluorophore diffusion. For comparison with the confocal studies, DPPs could present interesting fluorophores to investigate using TIRF. As the DPPs studied were predominantly neutral, diffusion through fibres would be likely. It would also be beneficial to observe the migration of pyridyl DPPs into gel fibres using TIRF microscopy.

As mentioned previously, a full characterisation study of the glycopolymer gels is needed to better understand the morphological disruption seen in SEM and TIRF microscopy. Planned work that could not be conducted because of time constraints include the synthesis of a sulfated galactose monomer for the preparation of further glycopolymers. As each repeating unit of the sulfated glycopolymer would possess an anionic group, it is imagined that the electrostatic interactions between polymer and gel would be significantly greater. It is possible to make use of the propargyl group at the end of **CTA1** by employing click chemistry to attach a fluorescent moiety. Doing this would allow for the visualisation and localisation of the glycopolymer within the larger gel structure. In addition, multichannel experiments could be conducted on the TIRF microscope to track both the incorporated fluorophore molecules and fluorescent glycopolymers.

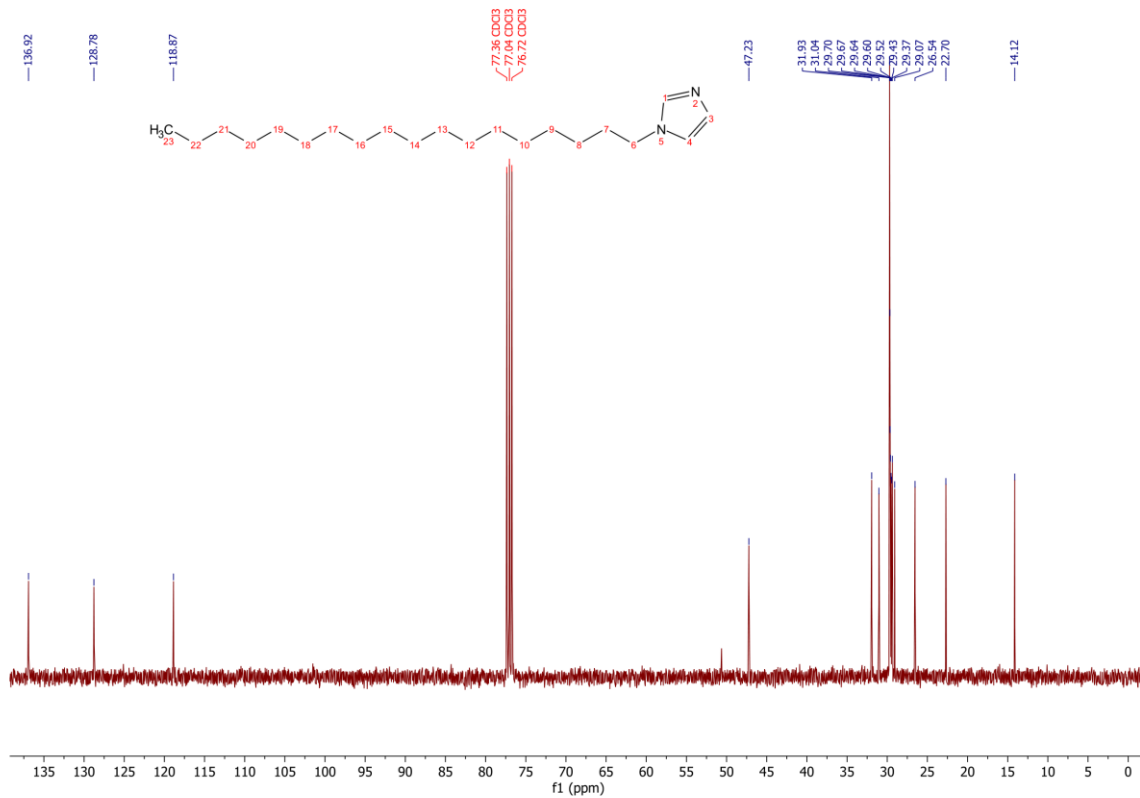
Optical tweezers use highly focused laser beams to manipulate microscale objects. They have been used to investigate the microrheology of hydrogels. Employing such a technique on the imidazolium gels studied here could provide a unique opportunity to compare their microrheological properties to their microrheological counterparts. In addition, confocal microscopy offers the change to visualize gel formation *in situ*.

A comprehensive and robust study involving all of the samples imaged on the confocal microscope is needed. It is crucial to examine other pyridyl DPPs to determine if the trend of thicker fibres continues, and therefore determine whether the effect is exclusive to this subclass of fluorophore. Recent research has focused on investigating the influence of sample preparation on gel morphology. Assessing such effects on the morphology of the imidazolium gels under investigation would be advantageous. Performing a cryo-SEM study of the Glycopolymer@Gels is recommended, as the drying effects observed in Chapter 6 might be more pronounced in conventional SEM analysis. Cryo-SEM would therefore provide a closer representation of the native morphology.

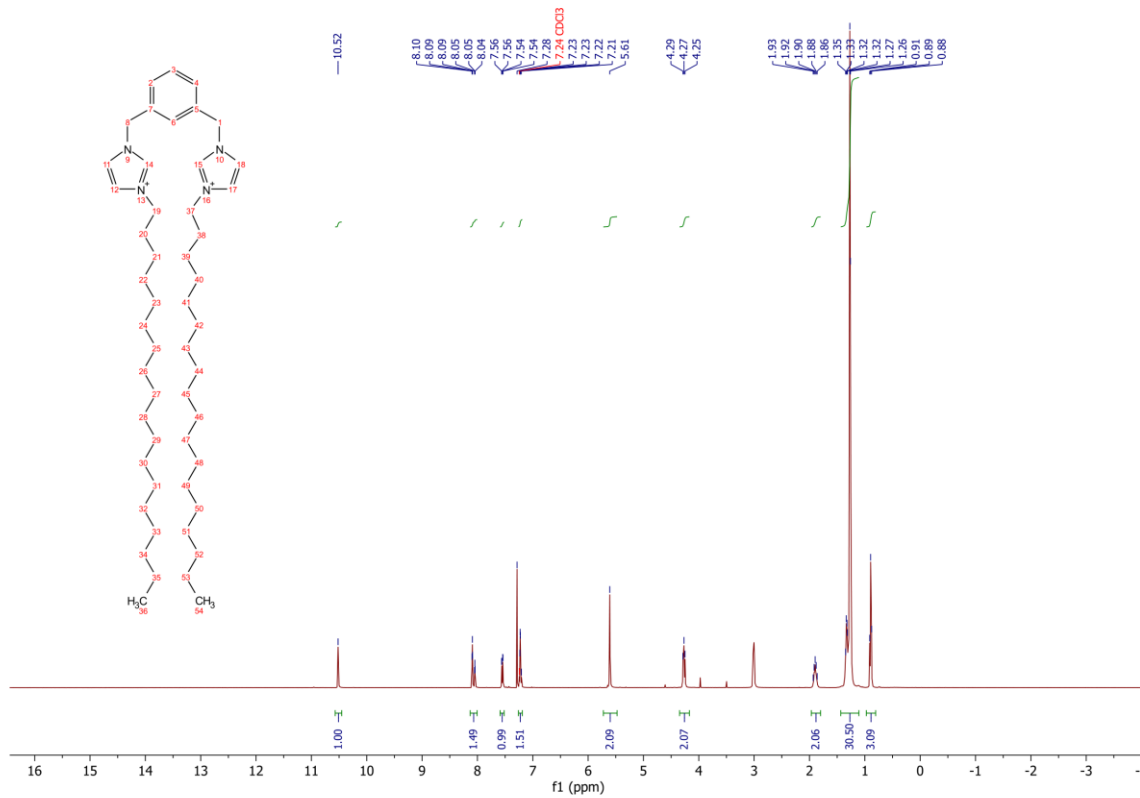
Appendix



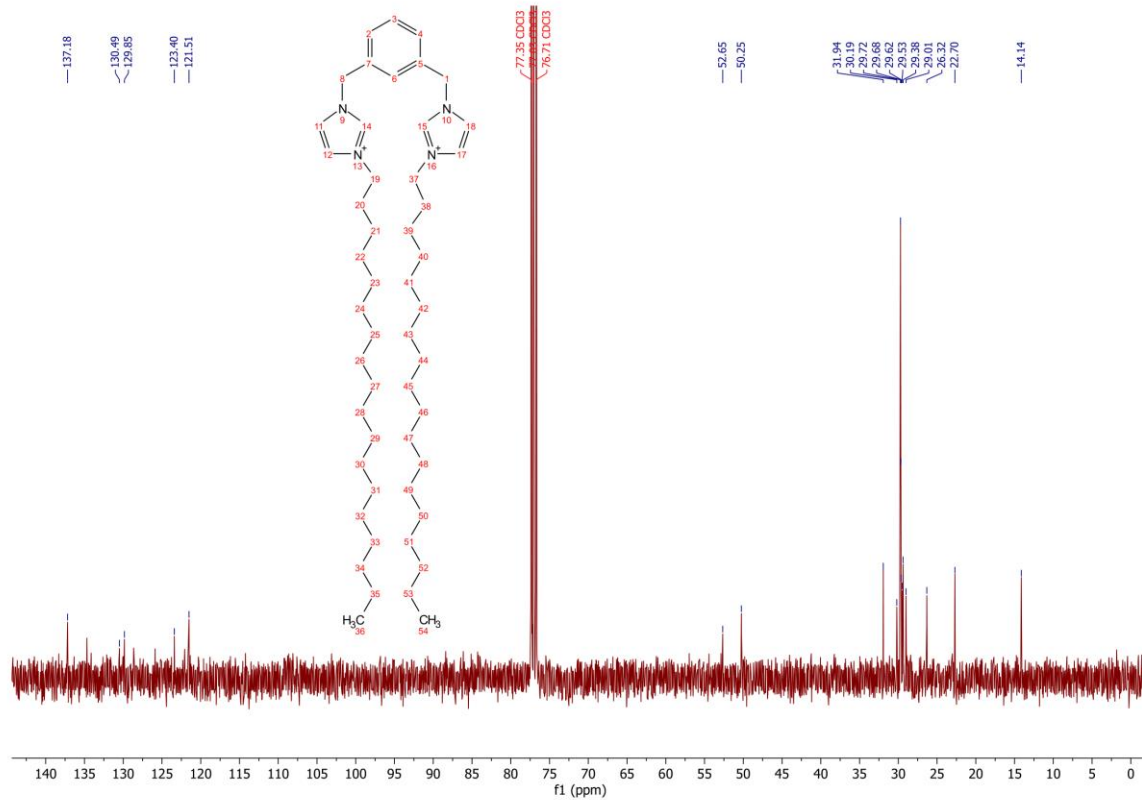
*1*¹H NMR of 1-octadecyl-1H-imidazole



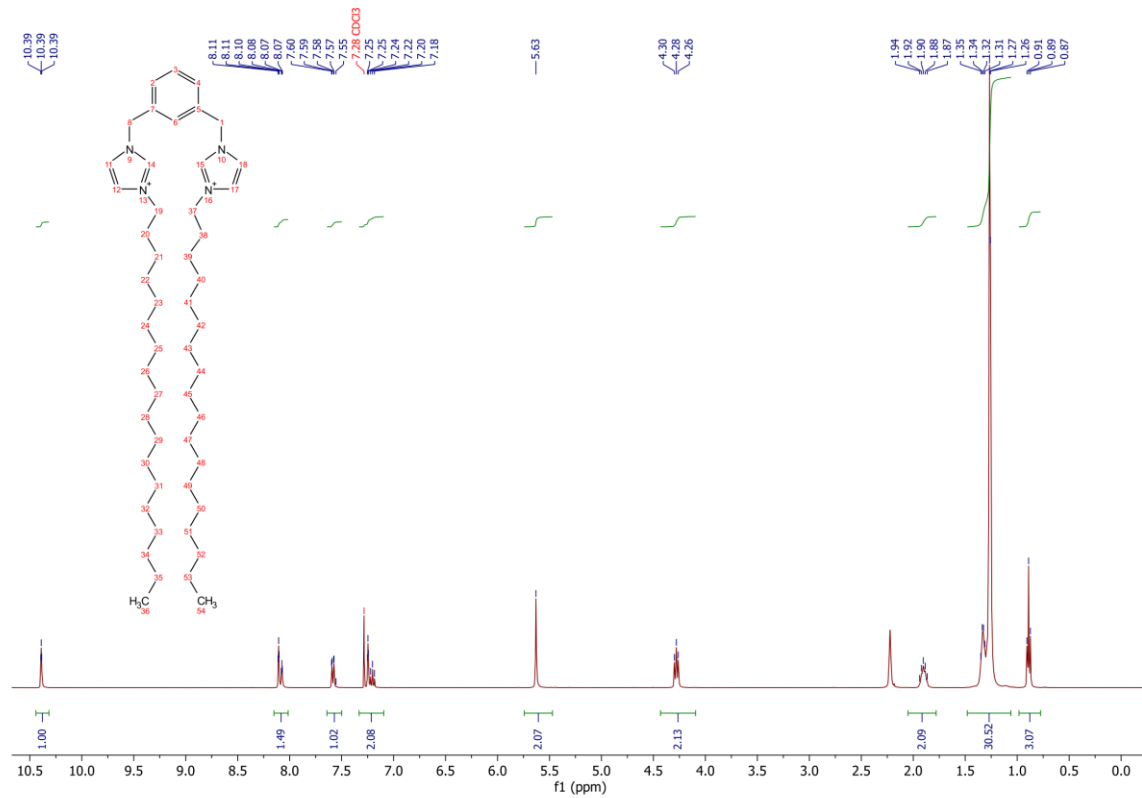
A2 ^{13}C NMR of 1-octadecyl-1H-imidazole



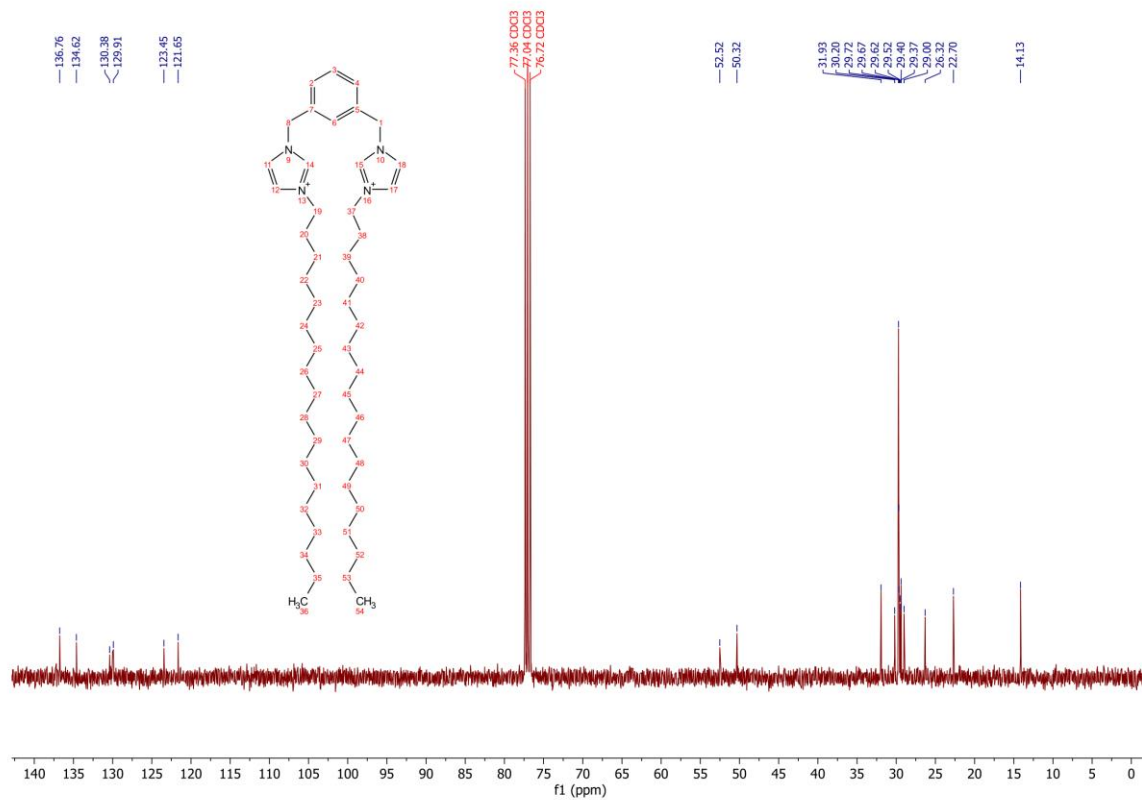
A3 ^1H NMR of 1.2CI



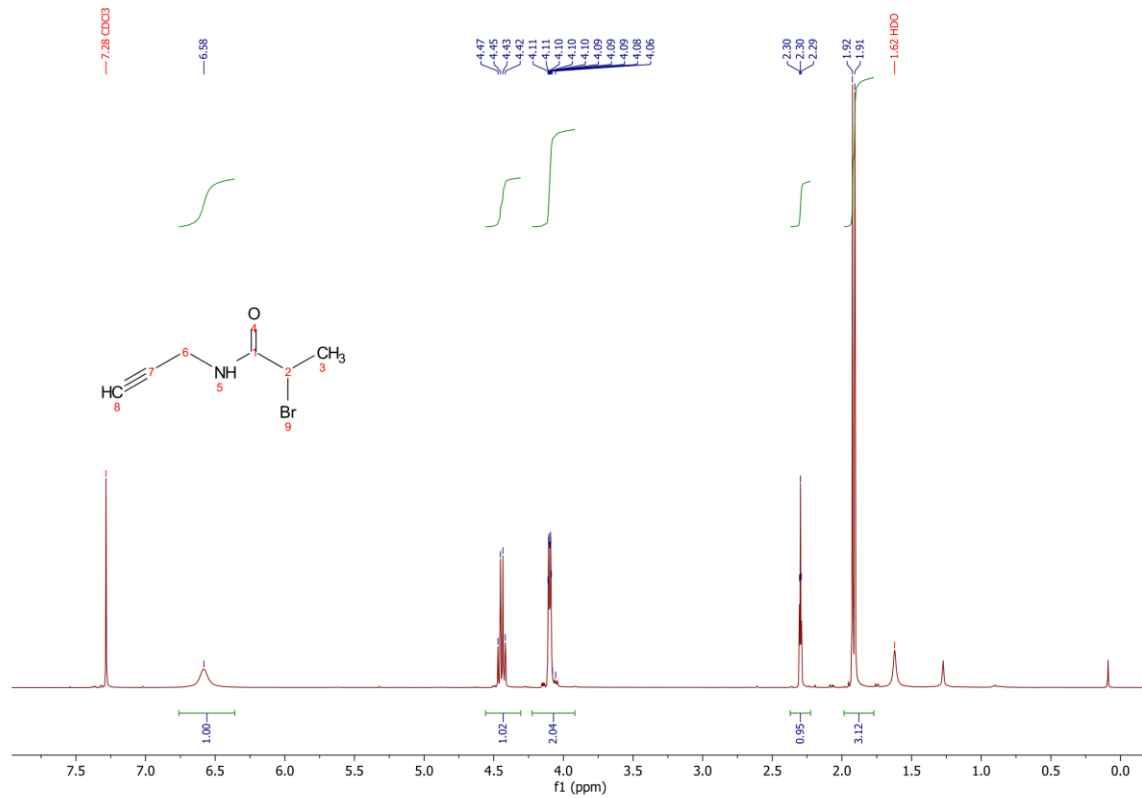
A4 ¹³C NMR of 1.2Cl



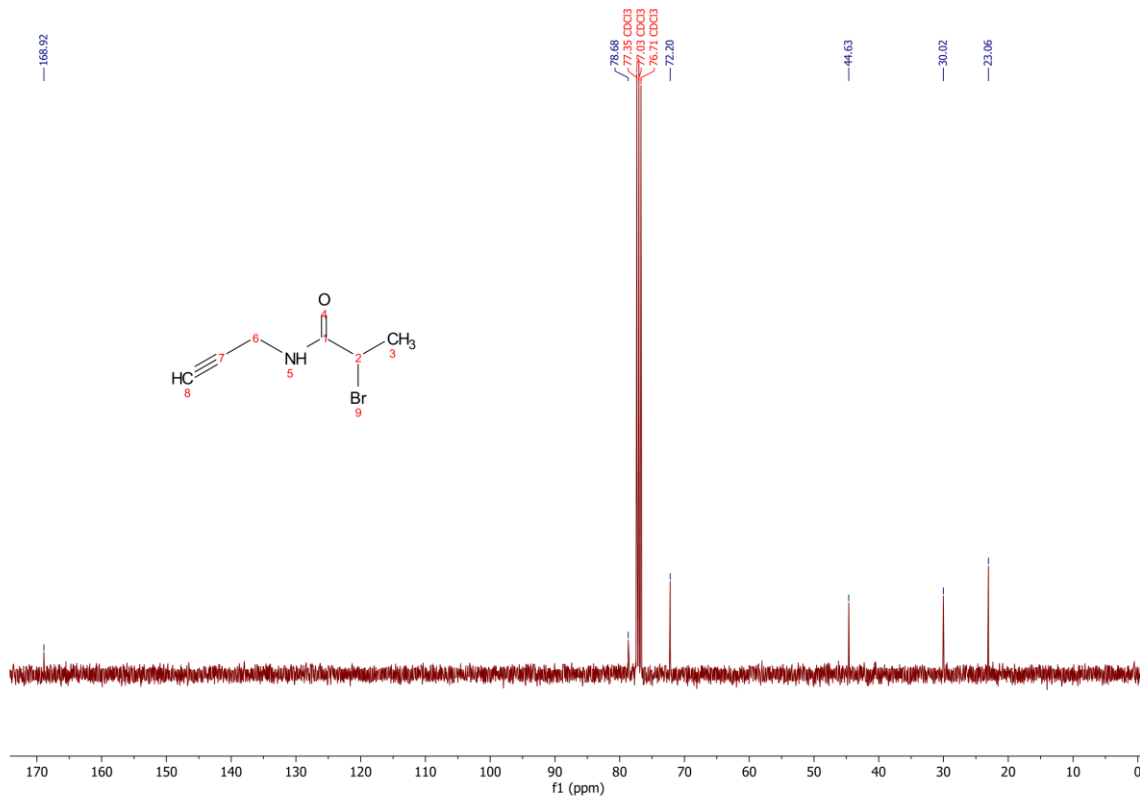
A5 ¹H NMR of 1.2Br



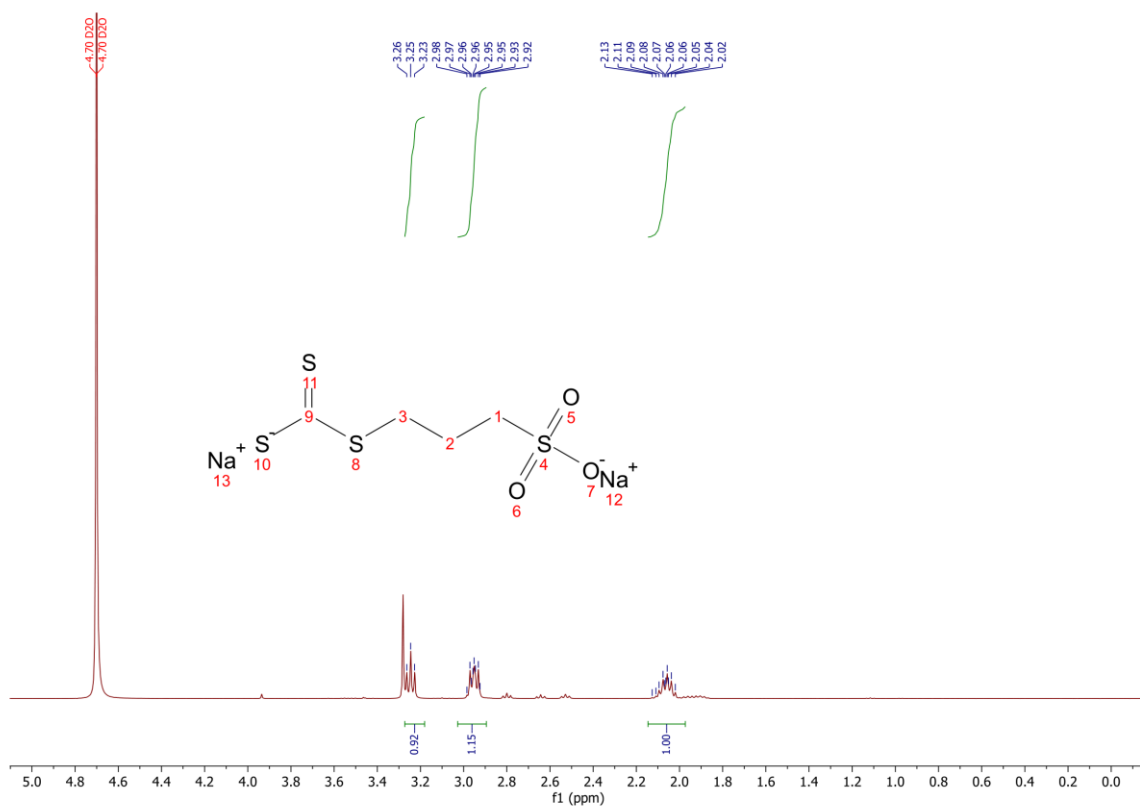
A6 ¹³C NMR of 1.2Br



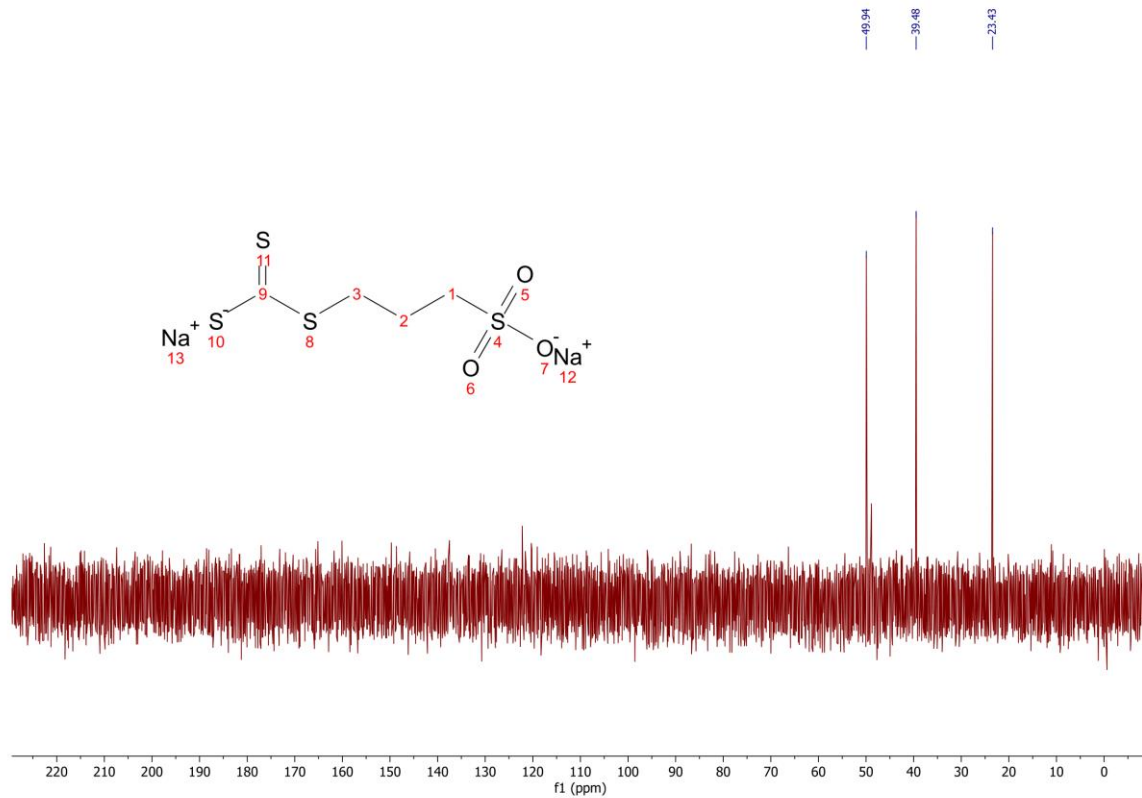
A7 ¹H NMR of SSP1



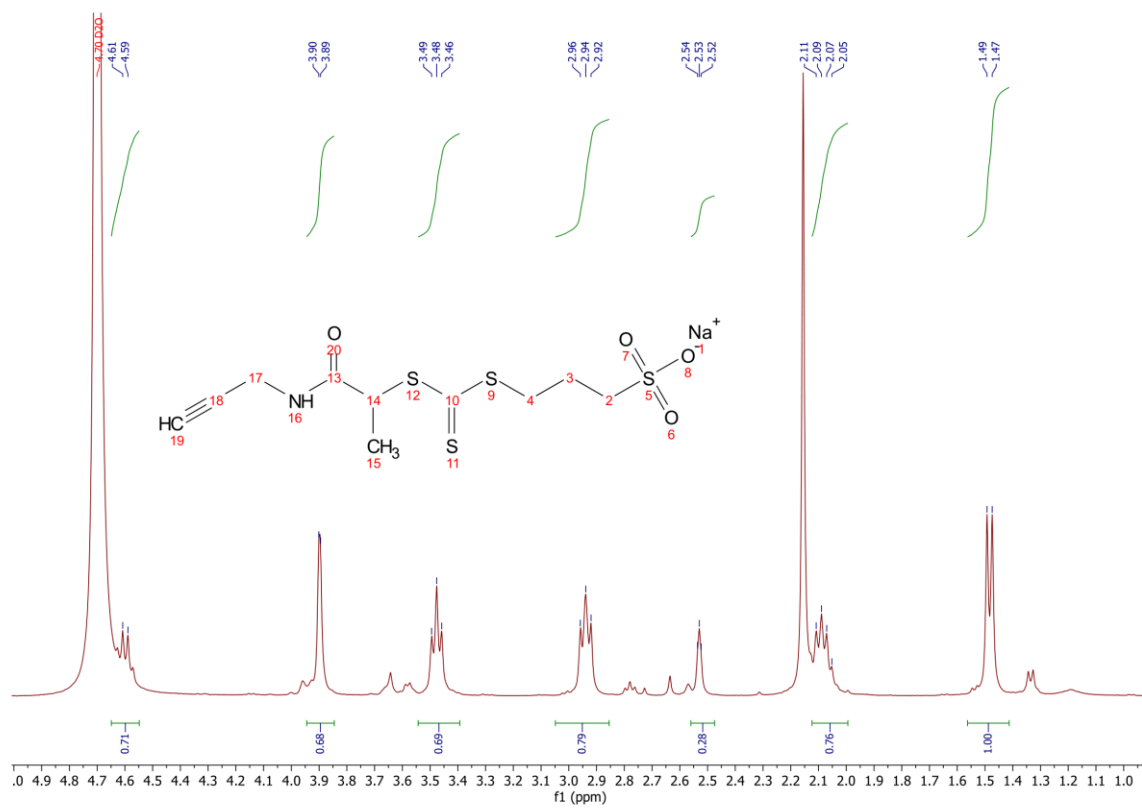
A8 ^{13}C NMR of *SSP1*



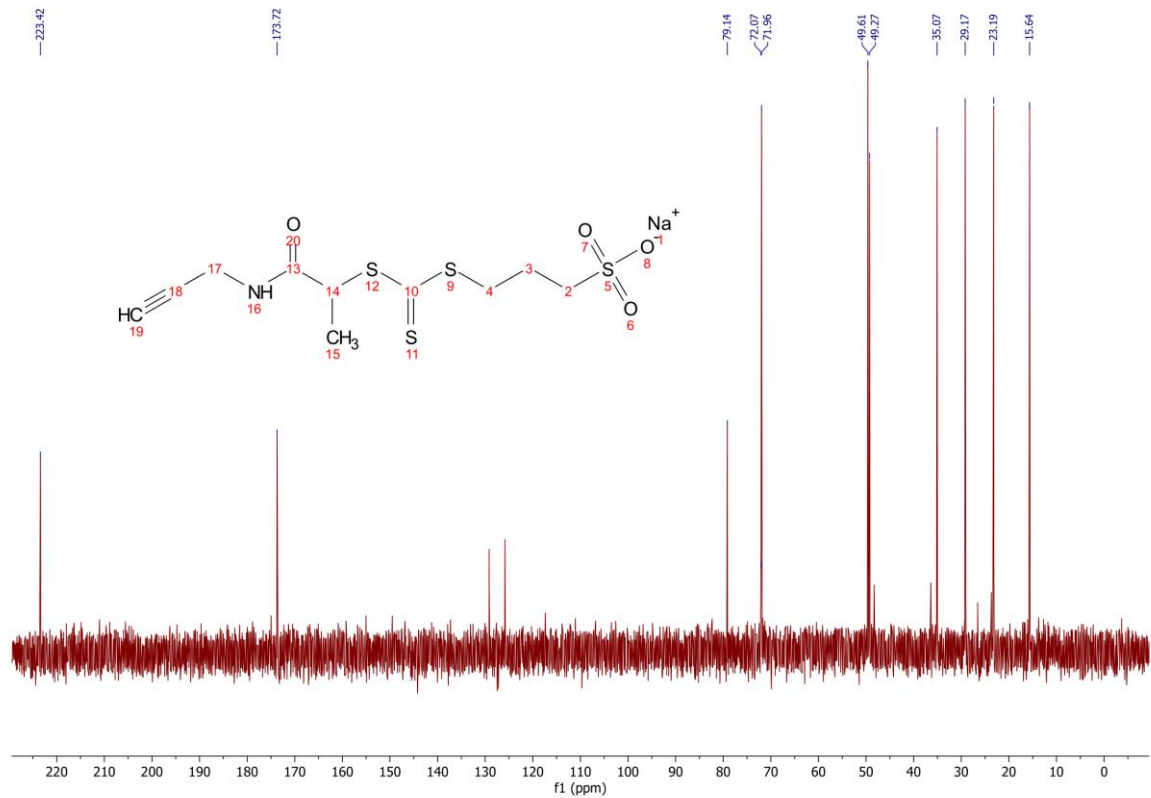
A9 ^1H NMR of *SSP2*



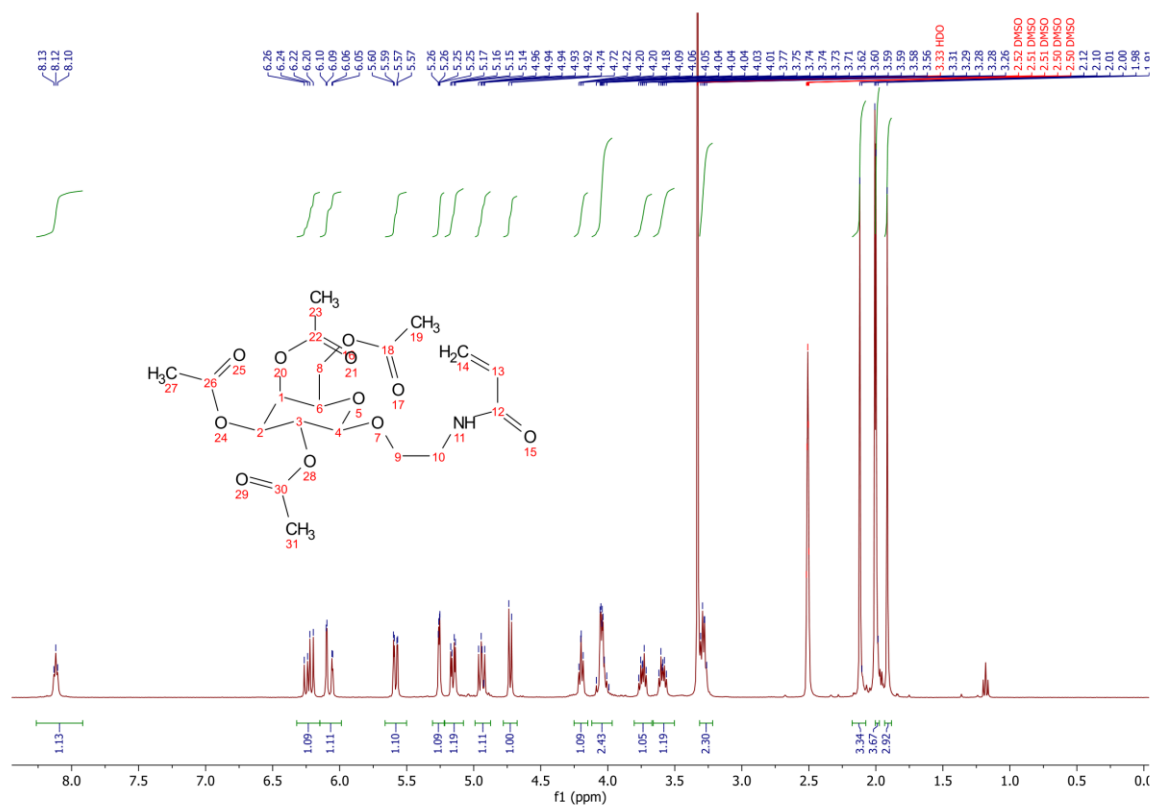
A10 ¹³C NMR of SSP2



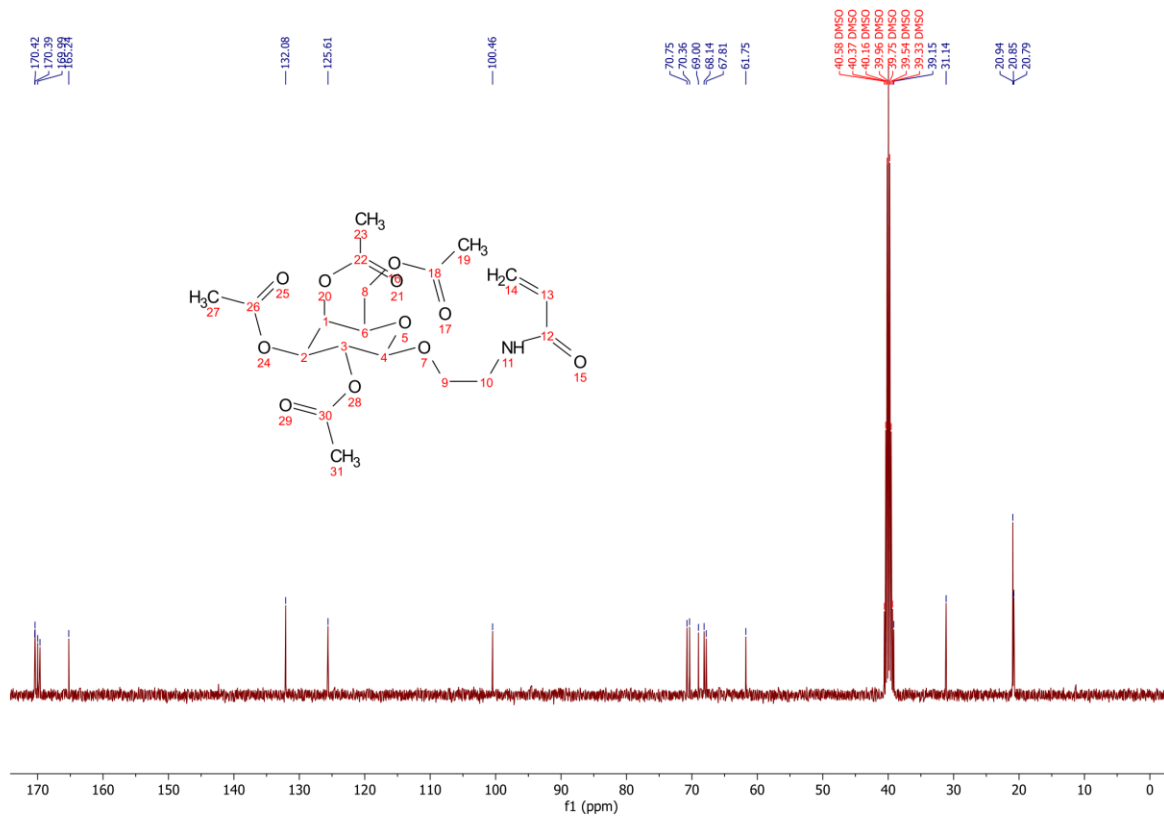
A11 ¹H NMR of CTAI



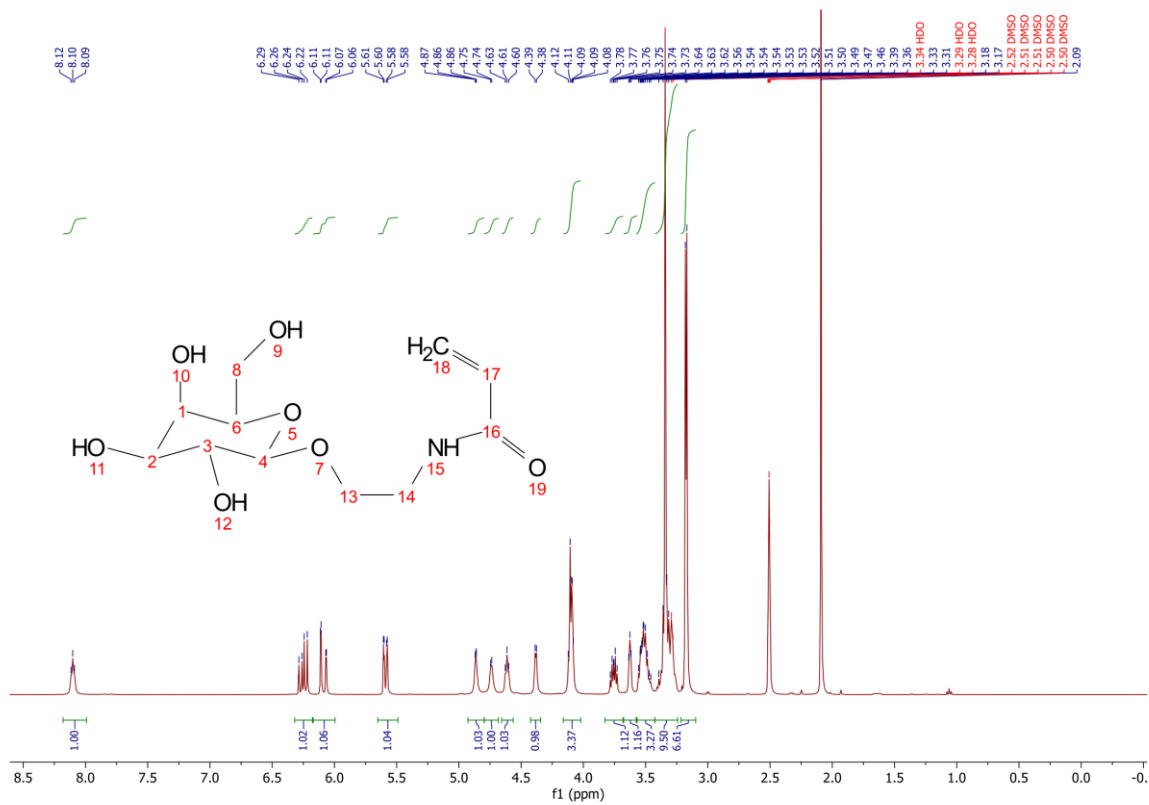
A12 ^{13}C NMR of CTA1



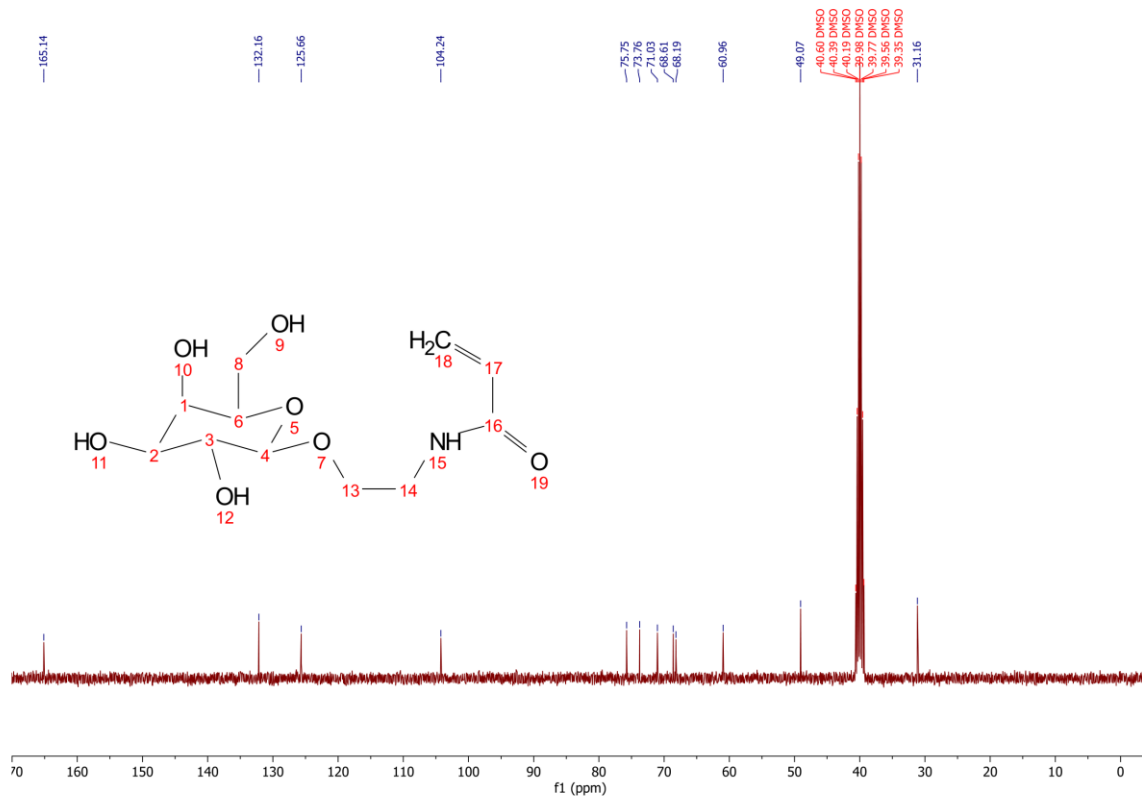
A13 ^1H NMR of SSM1



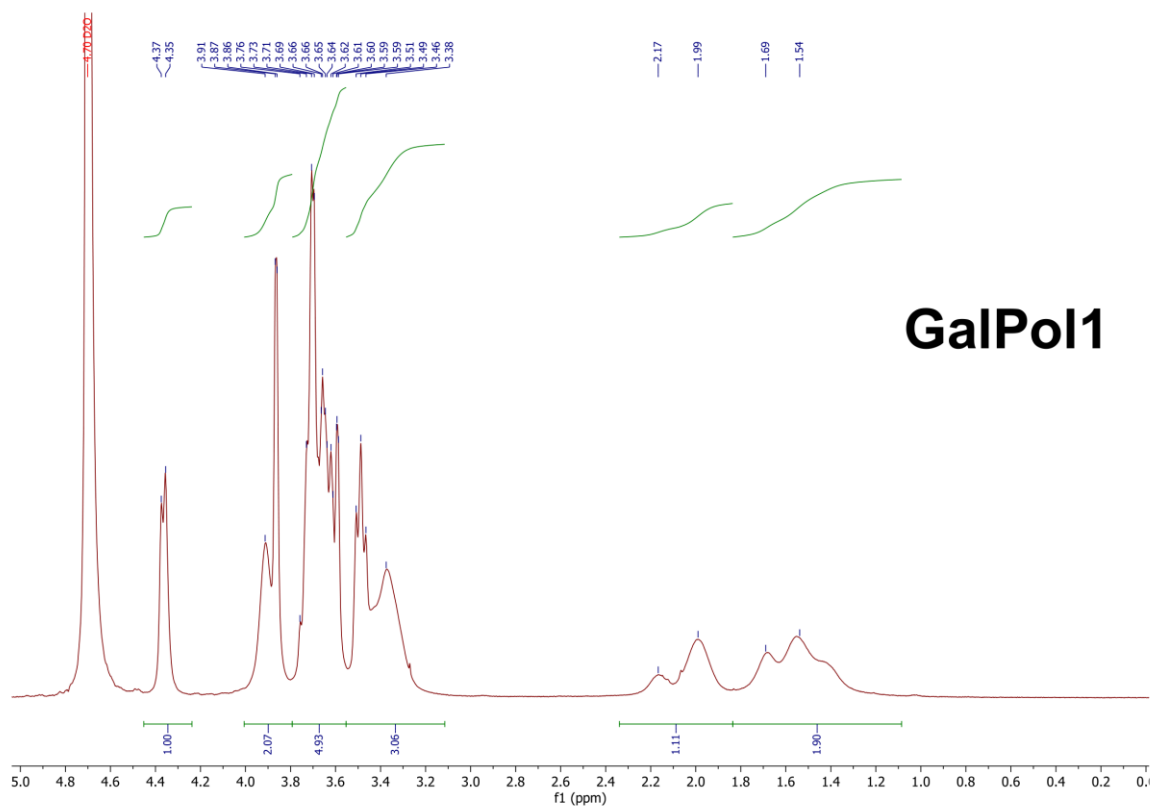
A14 ^{13}C NMR of SSMI



A15 ^1H NMR of GalMon

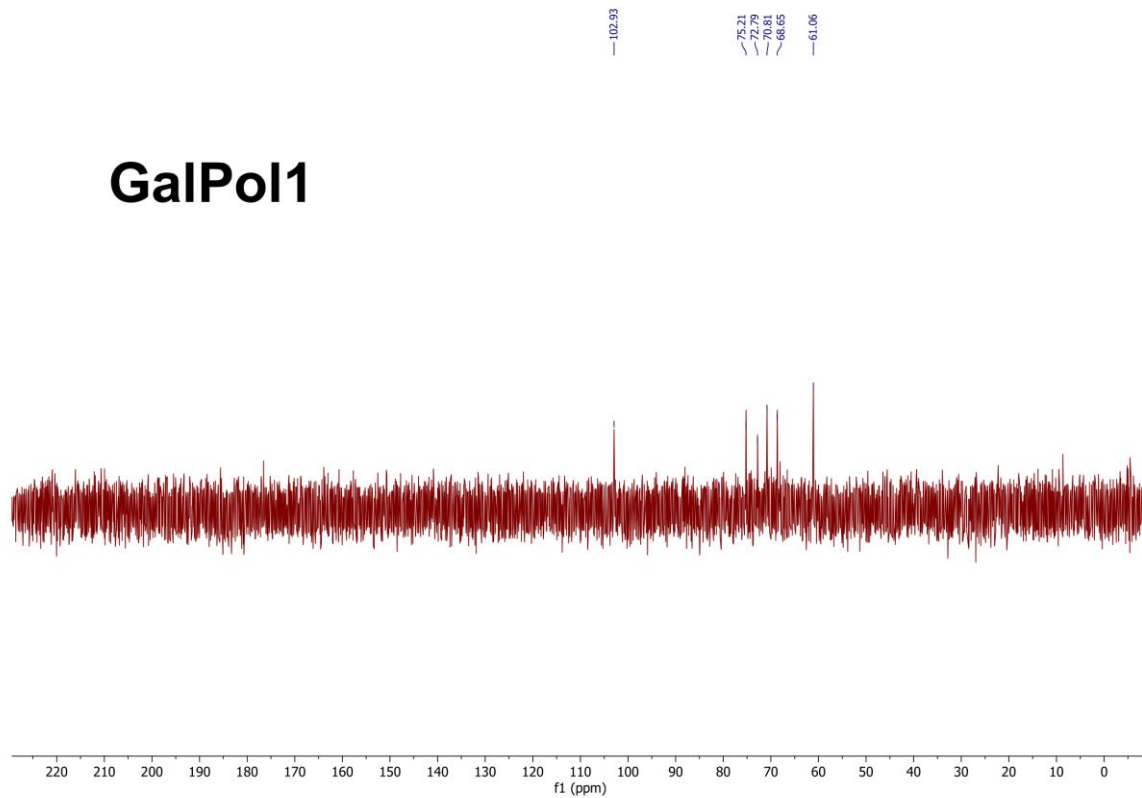


A16 ^{13}C NMR of GalMon

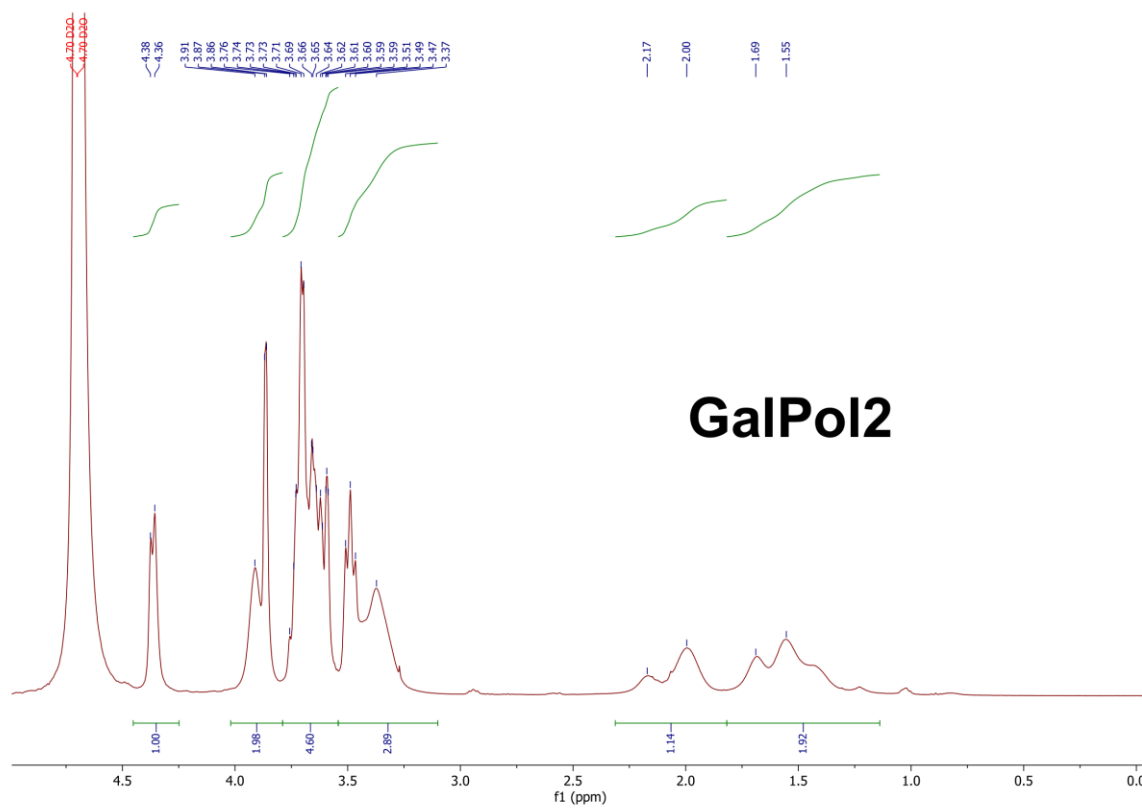


GalPol1

A17 ^1H NMR of GalPol1

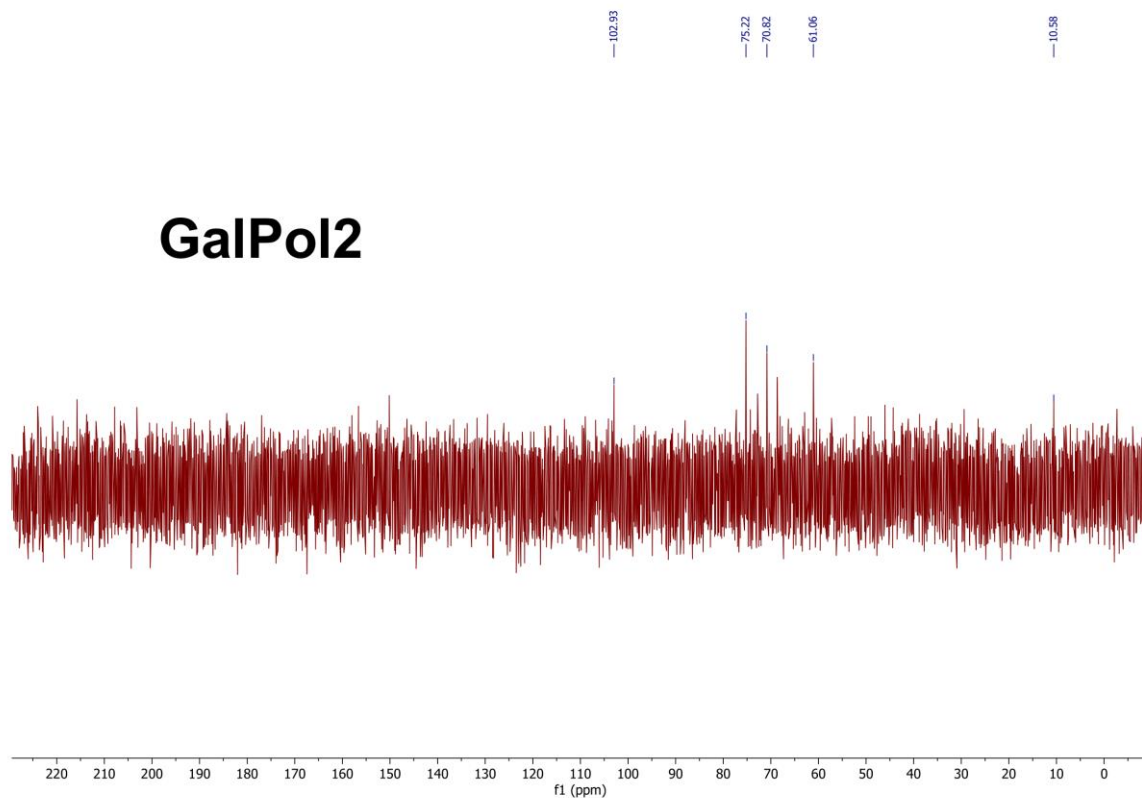


A18 ^{13}C NMR of GalPol1

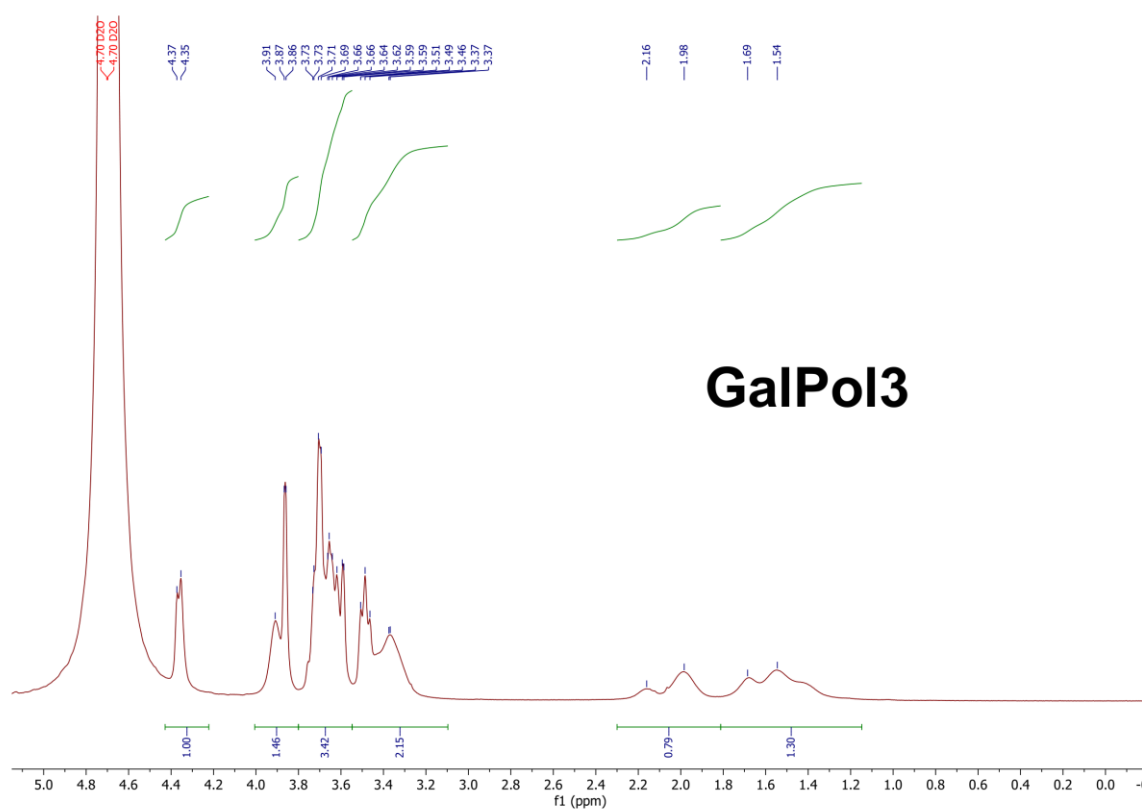


A19 ^1H NMR of GalPol2

GalPol2



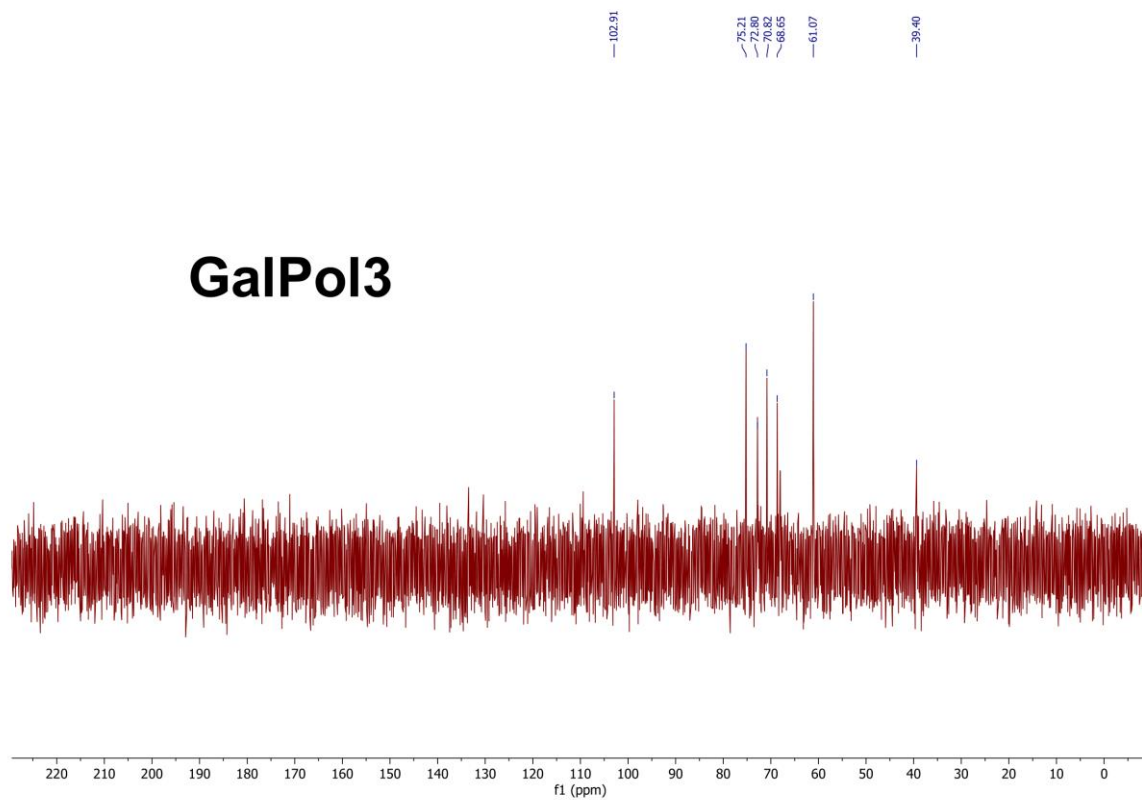
A20 ^{13}C NMR of GalPol2



GalPol3

A21 ^1H NMR of GalPol3

GalPol3



A22 ¹³C NMR of GalPol3